UC Irvine

UC Irvine Electronic Theses and Dissertations

Title

Turbulent Fluid Dynamics of Wildland Fire-Atmosphere Interactions

Permalink

https://escholarship.org/uc/item/7rn3096j

ISBN

9798291559680

Author

Desai, Ajinkya Subhash

Publication Date

2025-08-26

Copyright Information

This work is made available under the terms of a Creative Commons Attribution License, available at https://creativecommons.org/licenses/by/4.0/

Peer reviewed|Thesis/dissertation

eScholarship.org Powered by the California Digital Library
University of California

UNIVERSITY OF CALIFORNIA,
IRVINE

Turbulent Fluid Dynamics of Wildland Fire-Atmosphere Interactions

DISSERTATION

submitted in partial satisfaction of the requirements
for the degree of

DOCTOR OF PHILOSOPHY

in Civil and Environmental Engineering

by

Ajinkya Desai

Dissertation Committee:
Associate Professor Tirtha Banerjee, Chair
Assistant Professor Angela Jean Rigden
Distinguished Professor Efi Foufoula-Georgiou
Professor James T Randerson
Professor Jasper Vrugt

2025

Chapter 2 © 2022 Ajinkya Desai (Springer Nature)
Chapter 3 © 2023 Ajinkya Desai (Elsevier B.V.)
Chapter 4 © 2024 Ajinkya Desai (Springer Nature)
All other materials © 2025 Ajinkya Desai

DEDICATION

To all the beings and forces in the Universe
that are guided by love, compassion, and respect for balance...

TABLE OF CONTENTS

Page

LIST OF FIGURES **v**

LIST OF TABLES **xii**

ACKNOWLEDGMENTS **xiii**

VITA **xv**

ABSTRACT OF THE DISSERTATION **xviii**

1 Introduction **1**

2 Investigating the turbulent dynamics of small-scale surface fires **6**
2.1 Background 6
2.2 Methods 11
2.3 Results 14
2.3.1 Flow field and Streamlines 14
2.3.2 Coherent Structures 19
2.3.3 Length, Time, and Velocity Scales 29
2.3.4 Turbulent Kinetic Energy Budget 33
2.4 Summary and Future Work 37

3 Features of turbulence during wildland fires in forested and grassland environments **43**
3.1 Background 43
3.2 Theory 48
3.3 Data Overview 53
3.4 Results 54
3.4.1 Surface fires under a tall vegetation canopy 54
3.4.2 Grassland Surface Fire 68
3.5 Discussion 75
3.6 Summary and Future Work 79

4 Investigating fire–atmosphere interaction in a forest canopy using wavelets **93**
4.1 Background 93
4.2 Data Overview 98

4.3 Theory and Methodology . . . 101
4.3.1 Coherent Structures . . . 101
4.3.2 Wavelet Transform and Analysis . . . 103
4.4 Results and Discussion . . . 109
4.4.1 Temperature Scalograms . . . 109
4.4.2 Scale-based Signal Reconstruction: Ramp–cliff Structures . . . 112
4.4.3 Cross-Wavelet Coherence Analysis: Turbulent Fluxes . . . 123
4.5 Conclusions and Future Work . . . 136

5 Investigating buoyant plume dynamics during wind-driven wildland fires over plant canopies using Large-Eddy Simulations (LES) 142
5.1 Background . . . 142
5.2 Computational Setup . . . 146
5.3 Results . . . 149
5.3.1 Mean velocity and temperature profiles . . . 149
5.3.2 Streamtubes and vortex tubes . . . 152
5.3.3 Momentum Fluxes and Quadrant Analysis . . . 160
5.4 Conclusions and Future Work . . . 164

6 Scaling analysis for buoyant plumes over wildland fires 169
6.1 Background . . . 169
6.2 Methods . . . 173
6.2.1 Obtaining Dimensionless (π) Groups . . . 174
6.3 Results . . . 177
6.3.1 Consistency with scaling laws from prior studies . . . 177
6.3.2 Plume centerline slope: scaling from LES . . . 187
6.4 Conclusions and Future Work . . . 195

7 Conclusions and Future Work 199

Bibliography 204

Appendix A Chapter 3 222

Appendix B Chapter 4 230

Appendix C Chapter 6 258

LIST OF FIGURES

Page

2.1 a) Post burn photograph of burn area and b) the tripod housing the FLIR SC660 and GoPRO HERO3 cameras. 14

2.2 The magnitude of horizontal velocity in the domain at time $t =$ (a) 100 s, (b) 110 s, (c) 175 s, (d) 247.5 s, (e) 300 s, and (f) 350 s. The red asterisk indicates the ignition point (IP). The white and black circles in (c)-(f) indicate the coordinates of the fixed points formed around $t = 247.5$ s in (d). [Generated using MATLAB R2021a] 16

2.3 Horizontal velocity ($\mathbf{u}_\mathrm{H}$) vectors overlaid on color contours of u_H at $t =$ (a) 100 s and (c) 110 s along with streamlines overlaid on horizontal velocity ($\mathbf{u}_\mathrm{H}$) vectors at $t =$ (b) 100 s and (d) 110 s. The red asterisk indicates the IP. Arrows have been scaled by 1.5. [Generated using MATLAB R2021a] 17

2.4 Color contours of the surface temperature (T_s) with overlaid vectors of horizontal velocity ($\mathbf{u}_\mathrm{H}$) at $t =$ (a) 100 s and (b) 247 s, demonstrating the entrainment of colder ambient air. Color contours of vertical velocity (w) and vectors of horizontal velocity ($\mathbf{u}_\mathrm{H}$) at $t =$ (a) 100 s and (b) 247.5 s, demonstrating the influx of colder ambient air from the region of downdraft. Arrows have been scaled by 1.5. Red asterisk indicates the IP. White and black circles represent FP1 and FP2, respectively. [Generated using MATLAB R2021a] 18

2.5 An isoparametric view of the total velocity ($\mathbf{u} = u\hat{\mathbf{i}} + v\hat{\mathbf{j}} + w\hat{\mathbf{k}}$) vectors plotted 4.18 cm above the surface of the fuel bed and zoomed into the active combustion region of the domain at $t = 100$ s. Red arrows indicate updrafts ($w > 0$), while blue arrows indicate downdrafts ($w < 0$). [Generated using MATLAB R2021a] 18

2.6 Cross-correlation contours of (a) u velocity (r_{11}), (b) v velocity (r_{22}), and (c) vertical velocity (r_{33}) plotted close to the IP (red asterisk). [Generated using MATLAB R2021a] 20

2.7 Horizontal vorticity vectors at t = (a) 100 s (dashed curved arrows represent vortices) and (e) 247.5 s (dashed rectangle highlights the region around FP1 and FP2), and vortex lines for t = (b) 100 s (black dashed line represents $y = 1.1$ m) and (d) 247.5 s (zoomed in around FP1 and FP2). (c) Magnitude of $\boldsymbol{\omega}_{\mathrm{H}}$ plotted along with a schematic diagram of the circulation in the vertical plane as indicated by the vortex tubes in (b), at $y = 1.1$ m. (f) Vortex lines (thick black solid) isolating the vorticity field around the fixed points. Color contours of the magnitude of $\boldsymbol{\omega}_{\mathrm{H}}$ with overlaid horizontal velocity ($\mathbf{u}_{\mathrm{H}}$) vectors (black arrows, scaled by 1.5) at t = (g) 100 s and (h) 247.5 s. Red asterisk represents the IP. [MS PowerPoint 365 used to generate arrows in (a) and (c); all panels generated using MATLAB R2021a] 22

2.8 (a) A schematic diagram showing the kinked vortex tubes (not to scale), (b) helicity (H), and (c) net vorticity vectors ($\boldsymbol{\omega} = \omega_x\hat{\mathbf{i}} + \omega_y\hat{\mathbf{j}} + \omega_z\hat{\mathbf{k}}$) demonstrating that eddies precess alternately away from (red arrows) and toward (blue arrows) the surface at $t = 100$ s. Pairs of counter-rotating vortices are shown in (a). Black asterisk in (b) represents the IP. [MS PowerPoint 365 used to create (a); (b) and (c) generated using MATLAB R2021a] 26

2.9 (a) The horizontal turbulent flux ($\overline{u'v'}$), (c) $u'v'$, (e) u, $\overline{u}$ (thick solid line), and u', and (g) v, $\overline{v}$ (thick solid line), and v' at FP1. (b) The horizontal turbulent flux ($\overline{u'v'}$), (d) $u'v'$, (f) u, $\overline{u}$ (thick solid line), and u', and (h) v, $\overline{v}$ (thick solid line), and v' at FP2. Dashed vertical lines in (e) and (g) represent t = 158 s, 198 s, 309 s, and 322 s. Dashed vertical lines in (f) and (h) represent t = 174 s, 184 s, 301 s, and 353 s. [Generated using MATLAB R2021a] 28

2.10 Energy spectrum ($fS(f)$) for the time-varying u signal at (a) the IP, (b) FP1, and (c) FP2, and u_* computed at (d) the IP, (e) FP1, and (f) FP2. [Generated using MATLAB R2021a] 30

2.11 (a) A schematic diagram showing the major axis tracked at two instances of time elapsed since ignition to compute the corresponding distances of the heading and rear edges of the fire-front from the IP and (b) the variation of the heading and rear edge RoS with time. [MS PowerPoint 365 used to create (a); (b) generated using MATLAB R2021a] 33

2.12 (a) TKE (black solid) and MKE (blue dashed), (c) TKE_{sp}, (e) TKE_{tr}, and (g) $TKE_{\mathrm{tr_V}}$ (magenta dashed) and $TKE_{\mathrm{tr_H}}$ (green solid) at FP1. (b) TKE (black solid) and MKE (blue dashed), (d) TKE_{sp}, (f) TKE_{tr}, and (h) $TKE_{\mathrm{tr_V}}$ (magenta dashed) and $TKE_{\mathrm{tr_H}}$ (green solid) at FP2. Vertical dashed lines in (e) and (f) correspond to t = 150 s, 200 s, 235 s, and 284 s. Color contours of u_{H} at t = (i) 317.7 s (white cross represents FP3 and black cross represents FP4) and (k) 350 s (white square represents FP5 and black square represents FP6). TKE_{tr} at (j) FP3 (blue solid line) and FP4 (red dotted line), and (d) FP5 (green solid line) and FP6 (magenta dotted line). [All panels generated using MATLAB R2021a] 34

2.13 A brief illustration of the (pre- and post- fixed point formation) flow dynamics in the presence of the flame. Figure is not to scale. [Created in MS PowerPoint 365] 39

3.1 (i) Ambient wind velocity recorded by nearby AmeriFlux towers. One-hour moving means of the measured (ii) streamwise velocity ($\overline{u}$), (iii) cross-stream velocity ($\overline{v}$), (iv) vertical velocity ($\overline{w}$), and (v) temperature ($\overline{T}$) for the following cases: (a) NJ2011, (b) NJ2012, (c) West Tower (NJ2019), and (d) Control Tower (NJ2019). Vertical dotted lines indicate ignition times. Vertical dashed lines delineate FFP times in (a), (b), and (c), and the West Tower FFP time in (d). 82
3.2 Total horizontal velocity ($u\hat{\mathbf{i}}+v\hat{\mathbf{j}}$) wind-rose statistics for (i) pre-FFP, (ii) FFP, and (iii) post-FFP times at (a) $h = 20\,\mathrm{m}$ and (b) $h = 3\,\mathrm{m}$ for NJ2011, and for (c) $h = 20\,\mathrm{m}$ and (d) $h = 3\,\mathrm{m}$ for NJ2012. Colors represent classes of wind speed, while 0° represents the positive streamwise direction. 83
3.3 Total horizontal velocity ($u\hat{\mathbf{i}} + v\hat{\mathbf{j}}$) wind-rose statistics for (i) pre-FFP, (ii) FFP, and (iii) post-FFP times at (a) $h = 20\,\mathrm{m}$ and (b) $h = 3\,\mathrm{m}$ at the West Tower for NJ2019, and (c) $h = 20\,\mathrm{m}$ and (d) $h = 3\,\mathrm{m}$ at the Control Tower for NJ2019. Colors represent classes of wind speed, while 0° represents the positive streamwise direction. 84
3.4 (i) $\overline{u'w'}$, (ii) $\overline{v'w'}$, TKE budget terms for (iii) $h = 20\,\mathrm{m}$ (iv) $h = 10\,\mathrm{m}$, and (v) $h = 3\,\mathrm{m}$ for the following cases: (a) NJ2011 (b) NJ2012 (c) West Tower (NJ2019), and (d) Control Tower (NJ2019). Vertical dotted lines indicate ignition times. Vertical dashed lines delineate FFP times in (a), (b), and (c), and West Tower FFP time in (d). 85
3.5 MKE budget equation terms for (a) NJ2011, (b) NJ2012, (c) West Tower (NJ2019), and (d) Control Tower (NJ2019), at $h =$ (i) 20 m, (ii) 10 m, and (iii) 3 m. Vertical dotted lines indicate ignition times. Vertical dashed lines delineate FFP times in (a), (b), and (c), and West Tower FFP time in (d). . 86
3.6 Pre-ignition vertical profiles of the (a) mean streamwise velocity (U), (b) mean cross-stream velocity (V), (c) temperature (T_m), and (d) Mean Kinetic Energy ($(U^2 + V^2 + W^2)/2$) for TX2006. 87
3.7 Total horizontal velocity ($u\hat{\mathbf{i}} + v\hat{\mathbf{j}}$) wind-rose statistics for (i) pre-FFP, (ii) FFP, and (iii) post-FFP times at $h =$ (a) 42 m, (b) 28 m, (c) 10 m, and (d) 2 m for TX2006. Colors represent classes of wind speed, while 0° represents the positive streamwise direction. 88
3.8 For TX2006: (a)(i) One-minute moving means of the TKE and (ii) vertical fraction of TKE (r); (b) turbulent fluxes, i.e. (i) $\overline{u'w'}$, (ii) $\overline{v'w'}$, and (iii) $\overline{u'v'}$ at all four heights; (c) TKE budget terms at $h =$ (i) 42 m, (ii) 28 m, (iii) 10 m, and (iv) 2 m. Black dotted vertical line indicates ignition time; black dashed vertical lines delineate FFP time. 89
3.9 A brief summary of the turbulent processes in the 2011 sub-canopy backing fire (NJ2011) along with profiles of the TKE budget equation terms for a time instant in the (i) post-FFP period and (iii) pre-FFP period. Arrows are not to scale. (Vector figures of the pine tree, black bush, green bush, and flame taken from *www.vecteezy.com/free-vector/nature*) 90

3.10 A brief summary of the turbulent processes in the 2019 sub-canopy heading fire (NJ2019) along with profiles of the TKE budget equation terms for a time instant in the (i) post-FFP period and (iii) pre-FFP period. Arrows are not to scale. (Vector figures of the pine tree, black bush, green bush, and flame taken from *www.vecteezy.com/free-vector/nature*) 91
3.11 A brief summary of the turbulent processes in the 2006 grassland fire (TX2006) along with profiles of the TKE budget equation terms for a time instant in the (i) FFP period and (iii) pre-FFP period. Note that post-FFP profiles are not shown here. Arrows are not to scale. (Vector figures of the green grass and the flame taken from *www.vecteezy.com/free-vector/grass* and *www.vecteezy.com/free-vector/flame*, respectively) 92

4.1 A height-wise summary of the (a) mean streamwise velocity ($\overline{u}$), (b) turbulent momentum flux ($\overline{u'w'}$), (c) mean temperature ($\overline{T}$), and (d) turbulent heat flux ($\overline{w'T'}$) within (i) 1526:30–1532:30 LT and (ii) 1534–1540 LT at both, the West and Control Towers. The two sub-durations fall within the stipulated FFP time. 100
4.2 Schematic illustrations of the technique used to compute the ramp duration, ramp slope, and cliff slope of (a) a fire-modulated ramp–cliff structure at the West Tower and (b) a ramp–cliff structure in no-fire conditions at the Control Tower 107
4.3 Measured temperature at the West Tower at h = (a) 3 m (T_3) and (b) 20 m (T_{20}) along with the magnitude scalograms of the temperature signal at the West Tower at h = (c) 3 m and (d) 20 m and magnitude scalograms of the temperature signal at the Control Tower at h = (e) 3 m and (f) 20 m for the 30-minute duration comprising 5 minutes pre-FFP, 20 minutes during FFP (between red dashed lines), and 5 minutes post-FFP at the West Tower . . . 110
4.4 Reconstructed temperature signal at $h = 20$ m in scales ranging from 3 s to 90 s for (a) 1520–1550 LT and (b) 1526–1532:30 LT at the West Tower (where fire influence is experienced) as well as for (c) 1520–1550 LT and (d) 1526–1532:30 LT at the Control Tower (no-fire conditions). In (a) and (c), red dashed vertical lines delineate the stipulated FFP time at the West Tower, and blue dashed lines delineate the sub-duration plotted in (b) and (d), respectively. In (b) and (d), dashed and dash-dotted vertical lines enclose examples of ramp–cliff structures: two consecutive vertical lines with the same colour and style enclose one such observed structure. Not all structures are marked 113
4.5 Reconstructed temperature signal at $h = 3$ m in scales ranging from 3 s to 90 s for (a) 1520–1550 LT and (b) 1533:00–1540:10 LT at the West Tower (where fire influence is experienced) as well as for (c) 1520–1550 LT and (d) 1533:00–1540:10 LT at the Control Tower (no-fire conditions). In (a) and (c), red dashed vertical lines delineate the stipulated FFP time at the West Tower, and blue dashed lines delineate the sub-duration plotted in (b) and (d), respectively. In (b) and (d), dashed and dash-dotted vertical lines enclose examples of ramp–cliff structures: two consecutive vertical lines with the same colour and style enclose one such observed structure. Not all structures are marked 115

4.6 Histograms and empirical cumulative distribution functions of ramp durations associated with both, fire influence and no-fire conditions at all three measurement heights 117
4.7 Histograms of ramp slopes associated with both, fire influence and no-fire conditions, at all three measurement heights, along with the corresponding empirical cumulative distribution functions 119
4.8 Histograms of cliff slopes associated with both, fire influence and no-fire conditions, at all three measurement heights, along with the corresponding empirical cumulative distribution functions 123
4.9 Time–height cross-sections, comprising isotherms (filled) of temperature fluctuations (T') overlaid with vector arrows of $u'\hat{\mathbf{x}} + w'\hat{\mathbf{z}}$, at the West Tower for (a) 1526:30–1532:30 LT and (b) 1534–1540 LT, and at the Control Tower for (c) 1526:30–1532:30 LT and (d) 1534–1540 LT 125
4.10 Normalized time–height cross-sections comprising isotherms (filled) of temperature fluctuations (T'), overlaid with vector arrows of $u'\hat{\mathbf{x}} + w'\hat{\mathbf{z}}$, during different short time windows within the FFP time at the West Tower. Plots (a)–(f) fall within 1526:30–1532:30 LT and plots (g)–(k) fall within 1534–1540 LT 126
4.11 Magnitude-squared coherence (R^2) near the canopy top, i.e. at $h = 20\,\mathrm{m}$, for the 6-minute time window 1526:30–1532:30 LT. (a) R^2_{wT}, (c) R^2_{uw}, and (e) R^2 between $w'T'$ and $-u'w'$ at the West Tower. (b) R^2_{wT}, (d) R^2_{uw}, and (f) R^2 between $w'T'$ and $-u'w'$ at the Control Tower. Phase arrows are shown for $R^2 \geq 0.6$ in all cases: rightward-pointing arrows indicate in-phase motions; leftward-pointing arrows indicate motions out of phase by π radians. The white dashed line represents the cone of influence (COI) in all cases 129
4.12 Magnitude-squared coherence (R^2) near the canopy top, i.e. at $h = 20\,\mathrm{m}$, for the 6-minute time window 1534–1540 LT. (a) R^2_{wT}, (c) R^2_{uw}, and (e) R^2 between $w'T'$ and $-u'w'$ at the West Tower. (b) R^2_{wT}, (d) R^2_{uw}, and (f) R^2 between $w'T'$ and $-u'w'$ at the Control Tower. Phase arrows are shown for $R^2 \geq 0.6$ in all cases: rightward-pointing arrows indicate in-phase motions; leftward-pointing arrows indicate motions out of phase by π radians. The white dashed line represents the cone of influence (COI) in all cases 133
4.13 A schematic representation summarizing modulations induced by a heading sub-canopy surface fire in the ramp slope, ramp duration, and cliff slopes (i) in the earlier time window (as the fire-front approaches) and (ii) in the latter time window (during FFP) from a Lagrangian perspective (inspired by Figure 6.9 of the work by **(author?)** (1)) along with representative profiles of the mean streamwise velocity ($\overline{u}$), turbulent momentum flux ($\overline{u'w'}$), mean temperature ($\overline{T}$), and turbulent heat flux ($\overline{w'T'}$). Solid arrows represent local wind motion: thicker arrows represent stronger draughts while thinner arrows represent weaker draughts; dotted arrows represent heat transfer; colorbar, arrow length, and arrow thickness are not to scale; images of the flame and vegetation are taken from *www.vecteezy.com* 137

5.1 A schematic of the computational setup for the simulations in a canopy setting. (a) Velocity profile at the inlet. (b) Domain description; kinks along the vertical axes represent regions with vertical grid stretching. 147
5.2 Contours of the 1-h mean temperature plotted on the XZ plane $y = 500\,\mathrm{m}$ (passing through the center of the heated patch) for the (a) canopy and (b) no-canopy cases. Dashed horizontal line in (a) represents $z = h_\mathrm{c}$ 149
5.3 Color contours of the 1-h mean vertical velocity ($\overline{w}$) for the (a) canopy and (b) no-canopy cases. Grey points represent 1-h mean plume centerline (μ) in the far-field (Zone 2); vertical yellow dotted lines represent $\mu \pm s_t$ at multiple locations in the far-field; green dots represent the plume centerline in Zone 1, while white slanted dotted lines represent the plume centerline inclination. In (a), the black dashed line represents the inclination of the plume centerline in the transition zone (Zone 1(B)). 151
5.4 3-D Streamtubes colored by vorticity magnitude (s^{-1}) (a) as observed from the downstream face of the domain and (b) demonstrating the presence of CVPs (C1, C2) near the source, in the canopy case. (c) A comparison of the structure of 3-D streamtubes between the canopy and no-canopy cases. with recirculating streamtubes. A1, A2–helical patterns along the plume edges; B–secondary helical pattern; D– recirculating streamtubes 154
5.5 (a) Streamtubes, colored by ω_y, in the XZ plane passing through the center of the surface patch and (b) isosurfaces of the Q-criterion shown for the canopy and no-canopy cases 156
5.6 Vortex tubes colored by vorticity magnitude (s^{-1}). A– Vortex tubes influenced by updrafts, cross-wind; Plume-modulated and tilted hairpin vortices; C– Spiraling vortex tubes in plume; D– Vorticity intensification at plume windward edge; E– CVPs propagating downstream. Black solid arrows represent vorticity vectors and red arrows the corresponding circulation structures 158
5.7 Streamtubes for a high-aspect ratio heat source colored by $\overline{w}$. T1–tower-like regions; T2–trough-like regions; R–rotational/helical patterns 159
5.8 Turbulent momentum fluxes ($\overline{u'w'}$) in the (a) canopy and (b) no-canopy cases close to the surface. $\Delta S = E_\mathrm{s} - E_\mathrm{e}$ in the (c) canopy and (d) no-canopy cases. $\Delta S = E_\mathrm{o} - E_\mathrm{i}$ in the (e) canopy and (f) no-canopy cases. Black dots represent mean plume centerlines and colorbar units are $\mathrm{m^2 s^{-2}}$ 163
5.9 Fraction of sweeps in the (a) canopy and (b) no-canopy cases; ejections in the (c) canopy and (d) no-canopy cases; outward interactions in the (e) canopy and (f) no-canopy cases; inward interactions in the (g) canopy and (h) no-canopy cases. Blue dots represent the mean plume centerline in Zone 1 . . . 165

6.1 Contours of the 1-h mean vertical velocity ($\overline{w}$) for the (a) no-canopy and (b) canopy environments depicting the respective plume centerlines in each zone (cyan blue dots in Zones 1–1(B) and white squares in Zone 2) and their inclinations for a representative case of $H_\mathrm{patch} = 5\,\mathrm{kW}$ and $U = 2\,\mathrm{ms^{-1}}$ 189

6.2 Plot of plume centerline slope ($\Delta\overline{z}/\Delta x$) against (a) $\pi_3\pi_4$ and (b) $u_*^{(\mathrm{pl})}/u_*^{(\mathrm{up})}$ in Zones 1, 1(B), and 2 for the canopy cases. Slope i, computed from the simulation outputs, refers to the plume centerline slope in Zone i. Trend-lines represent the best fit of a power law to the data; R^2 represents the coefficient of determination 190
6.3 Plot of plume centerline slope ($\Delta\overline{z}/\Delta x$) against (a) $\pi_3\pi_4$ and (b) $u_*^{(\mathrm{pl})}/u_*^{(\mathrm{up})}$ in Zones 1–2 for the no-canopy cases. Slope i, computed from the simulation outputs, refers to the plume centerline slope in Zone i. Trend-lines represent the best fit of a power law to the data; R^2 represents the coefficient of determination 193
6.4 Plot comparing the normalized height (z_{pc}/δ) at which the plume transitions from the rise phase to the atmospheric or bent-over phase (Zone 2) between the canopy and no-canopy cases. Trend-lines for z_{pc}/δ represent power-law dependence; L_{B}/δ represents the normalized buoyancy length scale 196

7.1 Stream slices in the symmetry plane (XZ) of the two square surface patches, colored by mean vertical velocity, depicting the progression of interaction between spatially separated plumes. Colorbar units are ms^{-1} 203

LIST OF TABLES

Page

2.1 A summary of the peak frequency and the corresponding time scale for the u energy spectrum, and the computed wave number and length scale for the IP, FP1, and FP2. 29

3.1 Summary features for the prescribed sub-canopy backing fire experiments (NJ2011, NJ2012), prescribed sub-canopy heading fire experiment (NJ2019), and the prescribed heading grassland fire or FireFlux experiment (TX2006) analyzed in this study (2; 3; 4; 5). 55

4.1 Height-wise summary statistics of fire-modulated ramps and ramps in no-fire conditions. Tabulated modes are obtained directly from the data (not from the histograms) 121

4.2 Height-wise summary statistics of the slopes of fire-modulated cliffs and cliffs in no-fire conditions 122

6.1 A summary of the variables used in the dimensional analysis 175

ACKNOWLEDGMENTS

Myriad voices of experience have remarked that no one achieves success alone, emphasizing the essential role of community support in individual accomplishments. I would like to take this opportunity to express my gratitude to all those who contributed to the success of my doctoral journey and dissertation.

At the heart of my PhD journey has been the highly edifying scientific guidance that my advisor, Prof. Tirtha Banerjee, has provided me, which has improved the quality of my research by leaps and bounds, and I thank him for that. His experience in the field of fire science and mentorship have been instrumental in ensuring that I make useful and edifying contributions to our understanding of fire–atmosphere interactions. I will always be grateful for the professional growth opportunities that he has provided me, the faith and resources he has invested in me, and for generously sharing his knowledge, ideas, and advice with me.

I would like to extend my gratitude to the members of my Dissertation Committee—Dr. Angela Rigden, Prof. Efi Foufoula-Georgiou, Prof. James Randerson, and Prof. Jasper Vrugt for contributing their time, energy, and thoughtful comments and suggestions to my work. I am grateful to have been able to collaborate with Prof. Foufoula-Georgiou and Prof. Randerson on some of my research and to Prof. Vrugt for thoughtful, productive discussions on the approach researchers should take to strengthen the impact of their work.

I thank the US Forest Service officials who provided us with the prescribed burn data for my analysis. I feel honored to have been entrusted with the data and for their faith in my abilities. Moreover, I would like to thank the developers of the PALM modeling system for providing the open-source platform for my computer simulations and for responding to my queries whenever I reached an impasse. I also thank the guardians of the HPC3 Cluster for their assistance with the technical issues that I encountered. I am grateful for the support and permission that I have received from the publishers and co-authors of my PhD publications to include the latter in my dissertation.

I appreciate the affection, support, encouragement, kindness, generous help, and feedback that I have received from my friends and colleagues in the BLT Group, including Ekaterina, Antonio, Konstantinos, Somnath, Subharthi, Assaad, Shu, Alec, Janine, Margarita, and Mukesh. Their advice and help have improved the quality of my work considerably, and I am ever so grateful for that. Moreover, I thank my friends and office-mates, Jinhyuk and Ved from ESS, for their encouragement, advice, moral support, and edifying discussions. I would also like to thank my roommates, Joshua and Christian, for their patience and understanding with me when my work schedule became highly intense.

I thank my dearest old friends, Sonali Rahagude and Sayed Asad Ali, for their unwavering moral support and empathic understanding throughout the struggles of my academic journey, and, of course, their child, my beloved niece, Arzoo, for her growing and rejuvenating affection. Moreover, I thank my partner, Sharyu, for inspiring me with her academic achievements, uplifting me with her sense of humor, and supporting my ambitions with her

understanding during this past year of my doctoral journey.

I am grateful to my parents, brother, sister-in-law, cousins, aunts, and uncles for their moral support, practical guidance, and encouragement throughout my doctoral journey. In particular, I acknowledge my mother, Mrs. Sangita Desai, for all the sacrifices she has made, the care she has invested in me, and her uplifting spiritual guidance and words of comfort, which have led to this moment of success.

Prof. Banerjee is supported by the US National Science Foundation (NSF-AGS-PDM-2146520, NSF-OISE-2114740, NSF-CPS-2209695, NSF-ECO-CBET-2318718, and NSF-DMS-2335847), the University of California Office of the President (UCOP-LFR-20-653572), NASA (80NSSC22K1911), and the United States Department of Agriculture (NIFA 2021-67022-35908, and USDA-20-CR-11242306-072). I acknowledge the financial support that I received from these grants. In addition, I would like to acknowledge funding support from the Henry Samueli Endowed Fellowship, the Distinguished Public Impact Fellowship, and the Graduate Dean's Dissertation Fellowship from UCI.

Chapter 2 of this dissertation is a reprint of the materials as it appears in "Desai, A., Goodrick, S. & Banerjee, T. Investigating the turbulent dynamics of small-scale surface fires. Sci Rep 12, 10503 (2022)". Used with permission from Springer under the Creative Commons Attribution (CC-BY) license. Prof. Tirtha Banerjee directed and supervised this research, which forms the basis for the dissertation.

Chapter 3 of this dissertation is a reprint of the materials as it appears in "Desai, A., Heilman, W. E., Skowronski, N. S., Clark, K. L., Gallagher, M. R., Clements, C. B., and Banerjee, T. (2023). Features of turbulence during wildland fires in forested and grassland environments. Agricultural and Forest Meteorology, 338, 109501". Used with permission from Elsevier under the Creative Commons CC-BY-4.0 license. Prof. Tirtha Banerjee directed and supervised this research, which forms the basis for the dissertation.

Chapter 4 of this dissertation is a reprint of the materials as it appears in "Desai, A., Guilloteau, C., Heilman, W.E., Charney, J.J., Skowronski, N.S., Clark, K.L., Gallagher, M.R., Foufoula-Georgiou, E. and Banerjee, T., 2024. Investigating Fire–Atmosphere Interaction in a Forest Canopy Using Wavelets. Boundary-Layer Meteorology, 190(5), p.21." Used with permission from Springer under the Creative Commons Attribution (CC-BY) license. Prof. Tirtha Banerjee directed and supervised this research, which forms the basis for the dissertation.

VITA

Ajinkya Desai

EDUCATION

Doctor of Philosophy in Civil and Environmental Engineering **2025**
University of California, Irvine *Irvine, CA*

Master of Fine Arts in Dramatic Arts **2017**
The Old Globe Theatre/University of San Diego *San Diego, CA*

Master of Science in Engineering Sciences (Aerospace Engineering) **2015**
University of California, San Diego *San Diego, CA*

Bachelor of Technology in Aerospace Engineering **2013**
Indian Institute of Technology, Kanpur *Kanpur, UP, India*

RESEARCH EXPERIENCE

Graduate Research Assistant **2020–2025**
University of California, Irvine *Irvine, California*

Junior Research Fellow **2019–2020**
Indian Institute of Technology, Hyderabad *Hyderabad, Telangana, India*

Graduate Research Assistant **Apr–Dec 2014**
University of California, San Diego *San Diego, California*

Research Intern **May–July 2012**
Texas A&M University *College Station, Texas*

SURGE Research Intern **May–July 2011**
Indian Institute of Technology, Kanpur *Kanpur, UP, India*

TEACHING EXPERIENCE

Teaching Assistant **Winter 2021, 2022**
University of California, Irvine *Irvine, California*

Teaching Assistant **Winter, Spring 2015**
University of California, San Diego *San Diego, California*

REFEREED JOURNAL PUBLICATIONS

Okun, K., Desai, A., Parnell, P.E., Masunaga, E., Lucas, A. J., Lerczak, J., Pawlak, G., Semidiurnal inner shelf flow in the Southern California Bight. 130, e2024JC021591. **2025**
Journal of Geophysical Research: Oceans

Desai, A., Guilloteau, C., Heilman, W. E., Charney, J. J., Skowronski, N. S., Clark, K. L., Gallagher, M. R., Foufoula-Georgiou, E., and Banerjee, T., Investigating fire–atmosphere interaction in a forest canopy using wavelets, 190, 21 **2024**
Boundary-Layer Meteorology

Desai, A., Heilman, W. E., Skowronski, N. S., Clark, K. L., Gallagher, M. R., Clements, C. B., and Banerjee, T., Features of turbulence during wildland fires in forested and grassland environments, 338, 109501 **2023**
Agricultural and Forest Meteorology

Desai, A., Goodrick, S., Banerjee, T., Investigating the turbulent dynamics of small-scale surface fires, 12, 10503 **2022**
Scientific Reports

Desai, A., Vourganti, V., Vyasarayani, C.P. A note on damping in heat-exchanger tubes, 8, 352–360 **2020**
International Journal of Dynamics and Control

Vourganti, V., Desai, A., Samukham, S., Vyasarayani, C.P. Effect of nonlinear cladding stiffness on the stability and Hopf bifurcation of a heat-exchanger tube subject to cross-flow, 55, 49–68 **2020**
Meccanica

Verma, A., Desai, A., Mittal, S. Aerodynamics of badminton shuttlecocks, 41, 89-98 **2013**
Journal of Fluids and Structures

PUBLICATIONS (UNDER REVIEW)

Scholten R. C., Banerjee T., Chen Y., Delgado A., Desai A., Ke Z., Liu T., Morton D. C., Peterson D. A., Tang Q., Veraverbeke S., Zhang J., Randerson J. T., Multi-ignition fire complexes drive extreme fire years and impacts **2025**
Science Advances, AAAS

AWARDS, HONORS

Graduate Dean's Dissertation Fellowship **Jul–Sep 2024**
Graduate Division, UC Irvine

Distinguished Public Impact Fellowship **Jan–Jun 2024**
Graduate Division, UC Irvine

Henry Samueli Endowed Fellowship **Jan–Jul 2023**
Department of Civil and Environmental Engineering, UC Irvine

Kunwar Devendra Pratap Singh & Kunwarani Krishna Kumari Memorial Award, Best Senior Design Project **Jul 2013**
Department of Aerospace Engineering, IIT Kanpur

Award for Excellence in Art and Cultural Activities **Jul 2013**
IIT Kanpur

ACADEMIC SERVICES

Reviewer **Jun 2024–present**
Boundary-Layer Meteorology, Springer

Session Chair **May 2025**
HydroML Symposium, UCLA Lake Arrowhead

Mentor **Sep 2024–May 2025**
Next Gen Pathways initiative, UC Irvine

Student Committee Member **Oct 2023–May 2025**
California Fire Science Seminar Series

ABSTRACT OF THE DISSERTATION

Turbulent Fluid Dynamics of Wildland Fire-Atmosphere Interactions

By

Ajinkya Desai

Doctor of Philosophy in Civil and Environmental Engineering

University of California, Irvine, 2025

Associate Professor Tirtha Banerjee, Chair

Complex turbulence patterns emerge from the interaction of a wildland fire-front with its surrounding atmosphere in a variety of terrain and ambient conditions. This interaction, referred to as fire-atmosphere interaction, frequently begets unexpected fire behavior that is difficult to control and threatens communities residing at the boundaries of wilderness. Fire–atmosphere interactions also inform ember-driven ignitions and smoke dispersion patterns that affect respiratory health and visibility downwind. Despite the progress made in recent decades and the operational utility of several fire models, a lot still needs to be understood about fundamental fire behavior to improve model predictive capabilities and expand their range of application.

This dissertation begins with the examination of wind velocity and temperature data collected during burn experiments ranging from small scales to operational scales for the turbulence processes characteristic of the presence of a fire in vegetative environments. At small scales, the analysis is akin to the microscopic observation of a fire in its infant stages: tracking velocity vectors in the vicinity of a propagating flame at high temporal and spatial resolutions allows a meticulous examination of the characteristic organized (coherent) flow structures. Besides being able to quantify the presence of counter-rotating vortex pairs along the fire-front, which play a key role in fire spread, potential mechanisms for the interaction

between neighboring spot fires are illuminated. Next, data from operational-scale burn experiments (prescribed burns) is leveraged to differentiate between turbulence patterns during fires in grassland and forested environments, under differing ambient wind-forcing conditions. Such comparisons can help simplify the complex equations that govern fire physics, thereby expediting model predictions. A follow-up study utilizes a wavelet-based approach to track individual fire-modulated ramp-cliff-like structures in the measured temperature signal, in a forest canopy, as they evolve in time, along with their constitutive frequencies. These are known to find application in computing sensible heat fluxes within forested environments, which can be used to initialize and evaluate fire-behavior models. Given the spatial restraints on field measurements, we further attempt to investigate flow structures characteristic of buoyant-plume–canopy interaction under cross-wind forcing through large-eddy simulations (LES) using a low-complexity, 'no-flame' setup. The study replicates characteristic structures observed during field-scale experimental fires while also revealing differences in the spatial structure of the turbulent fluxes within the plume in both canopy and no-canopy environments. By varying ambient wind speeds and heat-source strength, we then attempt to construct scaling laws informing plume deflection in canopy environments.

Comprehensive knowledge of these processes can help develop improved parameterizations for the process-level phenomena in coarser-resolution, fast-running, predictive fire-behavior and plume-dispersion models. Improved models can be utilized for the careful planning of prescribed burns intended to reduce hazardous fuels and forewarning fire managers regarding conditions conducive to unexpected fire behavior, leading to efficient wildland fire management practices.

Chapter 1

Introduction

While several wildfires recorded worldwide are relatively small in terms of burnt area, the damage inflicted upon people, property, and the environment by large, severe fires is significant (6). Some examples of post-millennial fires that fit the latter description include: Portugal 2003 and 2005; Greece, Italy, and the US 2007; Australia 2009; the US 2013; Canada and Chile 2016; Portugal and the US 2017 (6), the US (California) 2018 (7; 8), US (California and Colorado) 2020, US (Hawaii, California) and Canada 2023 (9; 10), and US (California) 2025 (11). Once a rare phenomenon, mega-fires are now increasingly common in occurrence, particularly due to the aggravating global and regional weather systems (12). Current models and studies also suggest an increase in fire risk and/or burning frequency in many areas, such as the Arctic (13), tropical forests in Indonesia, India (14), and the southern Amazon, and areas of the savanna woodlands (15) of DR Congo, South Africa's northern savanna (16), tropical savannas, and tropical and temperate grasslands (17). In the United States itself, the 10-year-average year-to-date (2015-2024) statistics are 30,324 wildfires and 2,647,028 acres burned (18). In the year 2025, up to July 16, about 40,431 fires burned through 2,647,028 acres across the USA: the number of fires exceeded the 10-year-average statistic.

The United Nations Environment Programme (17) provides a list of useful strategies for mitigating wildfire risk including but not limited to a review and analysis of data collected on past events, understanding the critical factors involved (such as fuels, weather, fire behavior, etc.) and causes of ignition, improved fuel management and wildfire monitoring, and promoting integrated fire-management (with sustainable land-use). While methods of fire suppression such as fuel treatment are useful in their own right, they may not always yield the desired outcome due to the complex interaction of the fire with the surrounding atmosphere. In a computational study conducted by Banerjee et al. (19), it was found that the thinning of (dry) midstory and understory vegetation beneath a forest canopy resulted in enhanced turbulence levels, causing the rate of spread to increase and often go higher than in the (dry) dense mid-story case. Prescribed fires serve as a useful technique to eliminate hazardous surface fuels. However, these are severely limited by the poor predictability of smoke dispersion patterns (20), which represent respiratory and visbility hazards for neighboring communities, and the dangers of escape risks via ember-driven ignition (21).

Extreme fire behavior (EFB), characterized by unpredictability and dangerously rapid spread rates, presents an added challenge to fire management and mitigation. Driven by the interaction of fires with the surrounding atmosphere and terrain, EFB threatens fire managers and vulnerable communities residing in the boundaries of wilderness, i.e. the wildland-urban interface (WUI). In an experimental study of a fire entering a canyon from a flat surface, a sudden rapid increase in the fire-spread rate intensity was observed as the fire entered the canyon, despite strong winds perpendicular to the canyon axis. Among other factors, this increase was found to be due to flow circulation inside the canyon (22). At larger scales, such aberrant fire behavior is known to subject firefighters to unprecedented levels of danger resulting in fatalities (e.g. Portugal, 1985) (22). Another complex and yet, frequently observed phenomenon, is the formation of fire whirls (or fire tornadoes) that are known for their notoriously unpredictable behavior and ability to loft firebrands that cause spot-fire ignitions (23). The inclined fire whirl observed during the Freeway Complex fire in Yorba

Linda, California, in 2008 (23) is a prime example of a fire whirl that occurred in close proximity to Irvine. While these are often observed near the edges of forested environments, they occur in a variety of topographic and wind conditions and their dynamics remain relatively unexplored. These studies demonstrate that a detailed understanding of fire behavior across diverse environments is, therefore, of prime importance at present. There are multiple facets to the study of fire science including but not limited to assessing socioeconomic impacts, fire ecology, combustion science, air quality, and fire-atmosphere interaction. The pioneers of wildland fire research in the USA focused on developing mathematical equations to obtain fire-spread rates and the location of the fire-front at a given time for operational purposes, while the underlying fluid dynamics has only recently gathered attention.

The present research investigates the interaction between wildland fires and the surrounding atmosphere from a turbulence standpoint on both laboratory (small) and operational (large) scales. We aim to describe, both qualitatively and quantitatively, the organized swirling motions that characterize the complex turbulent environment of a wildland fire. A major determining factor in characterizing coherent structures and the corresponding turbulence processes is the scale. At smaller scales, the ability to be able to track velocity vectors in the vicinity of a flame at high temporal and spatial resolutions, as the fire-front evolves, provides the advantage of a meticulous examination of the coherent structures that characterize fire-induced turbulence. The analysis of large-scale fires affords a different set of opportunities and requires an alternate perspective and approach. Fire-induced heat, momentum, and scalar fluxes in grassland and forested environments are linked with the ambient atmospheric (or canopy) turbulent fluxes through a feedback mechanism: one informs the other and vice versa. Such behavior also influences smoke dispersion, impacting human health and visibility for civilians residing on the boundaries of wilderness. Furthermore, the transport of firebrands poses a severe risk of spotting up to several kilometers away from the fire-front. Since firebrands are lofted by the fire plume before they are transported horizontally by the ambient wind, fire-induced buoyancy and shear production are expected

to play a role in governing the physics of firebrand transport. This motivates an analysis of fire-induced turbulent momentum fluxes and turbulent kinetic energy (TKE) budgets in different environments (e.g., forested and grassland) and under differing wind conditions (e.g., heading and backing fires). Furthermore, a (time-) scale-based representation of turbulent quantities against their temporal evolution affords us the ability to examine how the background atmospheric turbulence is modulated by the presence of the fire. Moreover, such an analysis allows us to identify the most relevant turbulent-flux events along with their associated time scales, which in turn inform scales associated with the dispersion of smoke (and other scalars) and length scales that can be used to adapt popular turbulence models (24) for simulating fire behavior.

The system of equations governing fire-front propagation comprising chemical processes such as combustion, heat- and mass transfer, and momentum transport is highly complex (25). The interaction of the fire with the surrounding atmosphere, the topography, and the vegetation characteristics present an additional level of complexity (26). Computational simulations are limited by the computational overhead and the necessity of simplifying assumptions, making them less amenable for extended use. This encourages us to test the utility of a low-complexity, no-flame setup in a large-eddy simulation (LES) model in investigating flow patterns associated with the interaction of buoyant plumes, akin to those generated by fires, with a vegetative canopy, in cross-wind. The advantages of LES models are multifold. Such simulations allow us to characterize the aforementioned flow patterns extensively in space, which is difficult to accomplish through experiments. Moreover, these can be leveraged to investigate and isolate the effect of varied forcing conditions over a wide parametric space while limiting meteorological variability and maintaining control over the influencing variables. Therefore, a large suite of LES runs can be leveraged to quantify dependencies between plume behavior and forcing variables, facilitating the development of scaling laws for improved predictability of plume behavior.

The overall goal of this research is to provide a deeper understanding of fire and plume behavior given the context of the complex turbulent field arising out of fire-atmosphere interactions. A comprehensive understanding of fire-atmosphere feedback flow can be used to develop improved models that predict such behavior more reliably than the current ones, which must resort to simplifying assumptions, thereby limiting their range of application. Improved models will help design strategies for efficient and effective fire management, circumventing the loss of human life and property.

Chapter 2

Investigating the turbulent dynamics of small-scale surface fires

2.1 Background

While wildfire modeling has progressed significantly over the past few decades, the progress in terms of observational evidence has been slow. The interaction between the fire and the atmosphere creates a turbulent environment and very limited observations are available to characterize this turbulence as well as the characteristic coherent structures. Measurement of turbulence requires high sampling frequency in time and observations of coherent structures require substantial spatial coverage. Most of the laboratory and field scale observations published in the literature have reported detailed flame structures, which are also important for understanding fire behavior in their own right; while turbulence measurements have been limited to 'point-in-space' observations. Being able to measure both, in space and at a high frequency in time, therefore, represents a paradigm shift in our understanding of wildland fire dynamics and fire-atmosphere interaction. In this chapter, we will be reporting observations

from a particle imaging velocimetry (PIV) experiment that covers a sizeable area in space as well a high sampling frequency, as a flame starting from point ignition spreads. This allows us to track velocity vectors *in-situ* as the flame structure evolves, as well as surface temperatures, thereby providing unprecedented insights into the complex environment of turbulence in and around a wildfire.

To place this work in context, a brief discussion of the history of wildland fire experiments is warranted. Wildfire researchers have attempted to develop models characterizing wildfire spread since the 1940s. The first empirical formula for the rate of increase of the fire perimeter as a function of wind velocity and fuel moisture content was obtained by Curry and Fons (27), which later led to the development of the first fire-spread model for heterogeneous fuel beds (28). Years later, a very simple model for fire growth was obtained (29) as formulae for the rate of increase in burnt area and fire perimeter per unit time. Anderson (30) obtained a simple elliptical model for fire propagation through a grassland using Huygen's principle of wave propagation. Then, Richards (31) derived a set of first-order, nonlinear differential equations to predict the location of the fire-front at a given time for a point-source-ignition fire. The model was improved in a subsequent study (32) and a general mathematical model was developed for fire growth in heterogeneous fuel conditions (33), albeit computationally intensive. These studies provided valuable information regarding the temporal evolution of the fire perimeter (shape and location) based on some parametric shapes but were limited in that regard.

Emerging empirical and semi-empirical models based on laboratory-scale experiments by Rothermel (34) led to a comprehensive set of useful parametric equations. FARSITE (35), FlamMap (36), and BehavePlus (37) are examples of three computer applications that incorporate this model along with others (38; 39; 40; 41) to produce more extensive results on fire growth. While such models facilitate fire management decisions, they do not account for interaction between the fire and its environment (fire-induced atmospheric turbulence).

Several researchers have, therefore, taken to computational fluid dynamics (CFD) models to investigate the detailed flow dynamics underlying wildfire behavior.

WFDS (42; 43) employs the Large Eddy Simulation (LES) method to solve the governing equations for the flow, heat transfer, and chemical processes, and has corroborated several fire spread features observed experimentally. The FIRESTAR system (44) captured the interactions between surface fires and the surrounding gas flow from simulations in pine stands. Several studies (45; 46; 47; 19) have utilized FIRETEC, which employs a finite-volume solver for its system of governing equations. Alternating regions of upwash and downwash motions (48) were discovered upwind of the headfire. Streamlines were found to deviate into the flanking direction upwind of the fire-front (47). Despite their benefits, simulations are limited by the computational overhead and the necessity of simplifying assumptions. The high Reynolds number characterizing the turbulent flow demands higher grid resolution for stability and accuracy. Moreover, fire spread is a result of several simultaneous processes; the Navier Stokes equations are closely coupled with the combustion equations. It was shown in a study (49) that a 200 s simulation could take upto 6.7 hours, while a 3D model (50) was found to take 3 weeks for 2 minutes of simulation time in a $1.2\,\mathrm{m} \times 1.2\,\mathrm{m} \times 1.2\,\mathrm{m}$ domain. A Monte Carlo-based wildfire simulation module called WyoFire (51), which was recently developed for predicting the growth of wildfires in Wyoming, USA, either overestimated or underestimated the wildfire boundaries in grassland fires. Other tools such as QUIC-Fire (a fast running tool that utilizes the phenomenological feature of fire behavior learned from FIRETEC) (52) are in relatively early stages of development.

With experimental studies in the 1940s focusing mainly on quantifying the spread rate under varied conditions, Fons (28) acknowledged that understanding the physical processes involved was also necessary to extrapolate the results to more realistic situations. Thereafter, wind-driven fire experiments in shallow fuel beds showed that combustible gases sweep ahead of the head fire-front along the fuel surface indicating that convection, and not just radiation,

plays a major role in fire spread (53). Test fires conducted on large plots of land indicated that fire-whirl formation required the presence of opposing air currents and that ambient flow around the fire resembled flow around a solid object (54). Through experiments and physical reasoning, Beer (55) commented on the reliance of the spread rate on atmospheric stability and explained the presence of fire-induced wind in the absence of wind forcing. From several fire experiments conducted in sloping *Pinus halepensis* fuel beds (56), it was inferred that increased headfire spread rate and stronger whirls for a fire travelling upslope were caused by the increased strength of fire-induced wind behind the fire. Flames in spreading fires are known to intermittently burst forward to ignite fuel particles (57; 58). These are called intermittent bursts or fire bursts. Recent experiments (58) were able to explain the mechanism behind forward flame-bursts: pairs of counter-rotating vortices that advect hot gases in the direction of headfire propagation.

Although prescribed burns can supply measurements on a management scale, they pose potential risks to expensive equipment and the lives of forest personnel (especially due to wind variability) (2). This makes small-scale field and laboratory experiments vital to fire-turbulence research. In that regard, particle image velocimetry (PIV) has developed to become a very reliable technique since the term was first used in the literature in the 1980s (59; 60; 61). More accurate and high-resolution (temporal and spatial) measurements of velocity vectors in two-dimensional (2D) flow fields have reduced much conjecturing around wall-bounded turbulent flow and have provided more detailed structural pictures (61). Although the technique has been used to study flow features in premixed laminar flames (62), the effect of puffing in pool fires (63), to obtain air-entrainment rates in pool fires (64), etc., it has only recently begun to be availed to study fire spread in vegetative fuels (65). Despite the challenges due to variability in external conditions and flow seeding, PIV measurements (65) in a $10\,\mathrm{m} \times 5\,\mathrm{m}$ bed of excelsior provided useful insights on the response of the flame dynamics to wind conditions. The presence of a "plume-dominated" region followed by "wind-dominated" region (66) was observed. In the plume-dominated region,

flames act like a barrier to the wind and there is an influx of fresh air from the downwind side of the fire. In the wind-dominated region, winds accelerate near the flame region. Flow crosses the fire-front to push hot gaseous products onto unburnt fuel. In a successive study (67), PIV data was collected at a sampling frequency of 10 Hz in a 0.71 m $\times$ 0.71 m domain to study a fire propagating upslope. They concluded that a higher acquisition rate (higher sampling frequency) would facilitate a better visualization of the velocity fluctuations and fluid dynamic structures as the fire progresses in time.

This chapter attempts to highlight some of the features of the turbulent flow during a grassland fire using PIV data sampled at a high frequency of 30 Hz in the horizontal plane (top view). A point source of ignition has been used in this experiment, in which pine needles were spread by hand to mimic natural needle cast in field situations. In this work, we first report observations regarding how the ambient environment responds to the presence of a flame that spreads from point ignition. Next, we seek to explore some of the coherent structures that characterize the flow to obtain insights on the mechanism of fire spread in the absence of a preferential ambient wind-forcing direction. Another important question that we address is how fire flames at different locations along the fire-front interact with each other. The chapter is organized as follows. We begin with preliminary observations on the fire growth with the help of snapshots of the local wind velocity, streamlines, and surface temperature. The analysis is expanded further: quantities derived from the velocity data, such as cross-correlation contours, vorticity vectors, and turbulent momentum fluxes, are computed for insights into the coherent structures that characterize the fire-induced turbulent flow. Estimates of the time, length, and velocity scales at play, as well as the rate of spread (RoS) are obtained next. We then explore the role of the individual terms of the turbulent kinetic energy (TKE) budget equation in the evolution of the fire. Finally, the contribution of this work is summarized along with directions for future work.

2.2 Methods

The data analyzed in this study were collected during a burn experiment conducted by the US Forest Service, Southern Research Station (Savannah, Georgia, USA). A $4\,\mathrm{m} \times 4\,\mathrm{m}$ sand bed was constructed using all-purpose construction sand at the Whitehall Forest on the campus of the University of Georgia, in Athens. A $2.34\,\mathrm{m} \times 2.34\,\mathrm{m}$ burn area was established inside the sand bed, marked by a wooden frame (Fig. 2.1(a)). Hand-spread pine needles mimicking natural needle cast in field situations constituted the fuel. The fuel loading was approximately $370\,\mathrm{gm}^{-2}$, which was similar to fine fuel loading measured in a longleaf pine stand with a fire return interval of one to two years (68). Fuel moisture content was $4\,\%$. Grid points were spaced $4.18\,\mathrm{cm}$ apart in both the latitudinal (x) and longitudinal (y) directions. The fire was ignited at a point given by $x = 1.34\,\mathrm{m}$ and $y = 1.17\,\mathrm{m}$ and allowed to spread without any intentional external human interference.

The imaging system consisted of a 7 m-tall aluminum tripod with a FLIR (Forward Looking Infrared) SC660 (FLIR Systems Inc., Boston, MA, USA) thermal imaging system positioned directly above burn area to provide a nadir view (Fig. 2.1(b)). The FLIR system has a focal plane array of 640×480 pixels, a spatial resolution of 1.3 mrad, a sensitivity of 0.03°C, and a thermal accuracy of $\pm 2\%$. The temperature range selected for data collection during the fire was 100 - 650°C at a measurement rate of 1 Hz. Further details on FLIR specifications are found in the literature (69; 70; 71). Visual imagery was captured by a GoPRO HERO3 camera collocated with the FLIR. Resolution of the video imagery is 1920×1080 pixels and was captured at a frame rate of 30 fps.

The flow field in the vicinity of the fire was estimated by applying cross-correlation particle image velocimetry (PIV). Our PIV implementation was inspired by the work of Fujita and Hino (72), who used an unseeded PIV method to estimate river flows. In their work, Fujita and Hino had intended to use the unseeded PIV measurement technique for small ripples,

resulting from wall-bounded turbulence, on the water surface. Instead, they used the method for large-scale patterns, caused by the interaction of boil vortices generated near the river bed with the water surface, which typically occurs in high river-flow conditions. This choice was a consequence of video images being taken from a helicopter, which made it difficult to capture small ripples on the water surface. In the current study, the unseeded PIV measurement technique could be applied in slow-flow conditions since the camera was located relatively close to the fuel bed, i.e. at a height of 7 m. While the methodology of Fujita and Hino relied on patterns generated by the interaction of boil vortices with the water surface as natural unseeded tracers, we have relied on patterns generated by the fire-flames, smoke, and ash particles as our unseeded tracers. Next, the cross-correlation PIV was implemented in Python using the openpiv module (Python version 3.8.5 and Anaconda environment version 4.9.2). The interrogation window was set at 24 pixels with a window overlap of 12 pixels and a search-area size set as 2.5 times the interrogation window size. The video from the GoPRO camera was trimmed to a 2.34 m $\times$ 2.34 m area in the center of the burn area for an image size of 888×888 pixels, and split into sequential images with a time step of 1/30 of a second.

Velocity data were collected for approximately 440 s (t_T) and the sampling frequency was 30 Hz (as mentioned above). Two components of velocity were measured: the latitudinal (x) component denoted by u and the longitudinal (y) component denoted by v. Here, $u > 0$ when the latitudinal flow is eastward, i.e. in the $+x$ direction and $v > 0$ when the longitudinal component is northward, i.e. in the $+y$ direction. The vertical velocity (w) was obtained from mass conservation: the divergence of the net velocity vector ($\nabla.\mathbf{u}$) was set to zero and the resulting equation was integrated to a height equal to the cell-size in the horizontal domain (4.18 cm) as shown in the Supplementary Information. No penetration conditions were enforced at the surface, i.e. $w|_{z=0} = w_0 = 0$. We assumed that the velocity measurements were made at a height $z = 4.18$ cm from the surface ($\Delta z = 4.18$ cm). The vertical velocity component (w) so computed is said to be positive ($w > 0$) if directed

opposite to the gravitational force.

The burn experiment was conducted during the afternoon of November 15, 2017. The weather station located in Whitehall Forest recorded mean wind speeds of 0.6 and 0.5 m/s for the hours of 1700 and 1800 UTC, respectively, with the mean direction varying between 77^o and 152^o during these hours. The maximum gust recorded during these hours was 1.21 m/s. These wind speeds were measured at a standard height of 10 m above ground level (AGL) and were adjusted to obtain the wind speeds at a height of 1 m AGL by fitting a logarithmic profile. The strongest gust measured at the height of 10 m corresponds to a speed less than 0.3 m/s at a height of 1 m. Similarly, mean wind speeds at 1 m were calculated to be less than 0.16 m/s. According to their meteorological definition, calm winds are said to have speeds that are less than 0.5 m/s or 1 knot. Since the wind conditions fulfilled this criterion near the burn site, it was expected that the wind forcing would be minimal, especially close to the surface of the fuel bed. Therefore, ambient wind data were not collected for this site during the experiment. A possible alternative for ambient wind measurements has been discussed in the Supplementary Information.

Vorticity estimates were obtained at a height $z = 4.18$ cm from the surface by taking the curl of the velocity vector ($\omega_i = \epsilon_{ijk}\frac{\partial u_k}{\partial x_j}$ in indicial notation) and using the procedure described in the Supplementary Information to discretize the partial derivatives. No-slip boundary conditions were imposed at the surface ($u|_{z=0} = v|_{z=0} = 0$).

A Reynolds decomposition was applied on the horizontal and vertical velocity components ($u_i = \overline{u}_i + u_i'$, where $i = 1, 2, 3$). The mean parameters ($\overline{u}_i$) were computed from 1-minute moving averages over the time-varying signal at each point in the domain. These were utilized to compute the mean kinetic energy (MKE), given by $(\overline{u}^2 + \overline{v}^2 + \overline{w}^2)/2$, at selected neighboring points in the flow field. The fluctuating parameters (u_i') were used to compute the turbulent momentum fluxes in the horizontal plane ($\overline{u'v'}$) and vertical plane ($\overline{u'w'}$, $\overline{v'w'}$) at these points. The 1-minute moving averages of the TKE, given by $\overline{K} = (\overline{u'^2} + \overline{v'^2} + \overline{w'^2})/2$,

were also obtained. The transport and shear production terms of the TKE budget equation are analyzed at these points for insights into the transaction of TKE between them.

(a) Burn area **(b) Tripod**



Figure 2.1: a) Post burn photograph of burn area and b) the tripod housing the FLIR SC660 and GoPRO HERO3 cameras.

2.3 Results

2.3.1 Flow field and Streamlines

Figure 2.2 shows color contours of the magnitude of the horizontal velocity ($u_{\mathrm{H}} = \sqrt{u^2 + v^2}$) of the local flow in the presence of the fire at different instances of time (t) elapsed since ignition. It must be noted that the fire-front cannot be clearly delineated from the contours of u_{H} alone. Nevertheless, it can be argued that the fire-front is on the inner side of the region of large u_{H} (yellow), since the fire creates a low-pressure warmer core that draws in cooler air from the surrounding region. It can be seen that up to $t = 110\,\mathrm{s}$, the fire-front is relatively stable and defined by a closed elliptical or circular shape (Figs. 2.2(a)). Around $t = 110\,\mathrm{s}$, it can be seen that local instabilities begin to set in and the fire starts to cease being a closed curve and forms small "pockets" of fire (Fig. 2.2(b)). These "pockets" are centred at relatively fixed points, i.e. points of extremely low local horizontal wind

velocity. After residing at these fixed points for several seconds, the fire "pockets" travel to a neighboring location, drawing in air from the surrounding region of unburnt fuel. As the fire grows, neighboring "pockets" coalesce to form larger ones (Figs. 2.2(e)-(f)). These snapshots provide a clear validation of Huygen's principle of wave propagation, cited in earlier works (30; 31; 33) as a model for fire growth. According to the Huygen's principle, every point on the fire perimeter at any time t behaves as an ignition point for a local fire; the envelope of the local fires at time $t + \mathrm{d}t$ determines the new fire-front at that time. An interesting question arises regarding whether there is some form of energy exchange between two such adjacent local fires, which shall be explored later. Two fixed points that are formed at time $t = 247.5\,\mathrm{s}$ (Fig. 2.2(d)) and remain relatively fixed for several seconds thereafter are depicted using a white circle ($x = 1.05\,\mathrm{m}$, $y = 0.67\,\mathrm{m}$) and a black circle ($x = 1.59\,\mathrm{m}$, $y = 0.54\,\mathrm{m}$) in Figs. 2.2(c)-(f). Henceforth, these two fixed points are referred to as FP1 and FP2, respectively, for brevity. The time-varying signals at these points shall be used for our analysis on turbulent momentum fluxes and the TKE budget.

For the sake of brevity, we shall refer to the part of the fuel-field burnt by the fire at a certain instant of time as the "inside" of the fire and the unburnt region as the "outside" of the fire. The color contours of u_{H} have been overlaid with vectors for the horizontal velocity ($\mathbf{u}_{\mathrm{H}} = u\hat{\mathbf{i}} + v\hat{\mathbf{j}}$) alongside the corresponding streamlines in Fig. 2.3. The $\mathbf{u}_{\mathrm{H}}$ vectors (Figs. 2.3(a), 2.3(c)) indicate that the relatively still and potentially colder (as corroborated later by the surface temperature contours) air from the "outside" is drawn into the warmer "inside" of the fire. The influx of air (and thus oxygen) contributes to the combustion process and helps in sustaining the fire. However, this fire-induced local wind also appears to exert a dynamic pressure upon the fire-front, providing resistance to the fire spread rather than accelerating it. A similar observation was made by Canfield et al. (47) for wind-driven fire, wherein a low-pressure region was found to form on the downwind side of the fire-front. Moreover, Fig. 2.3(b) shows that streamlines entering the fire get curved away from the fire-core. These streamlines meet near the inner edge of the fire-front and appear to

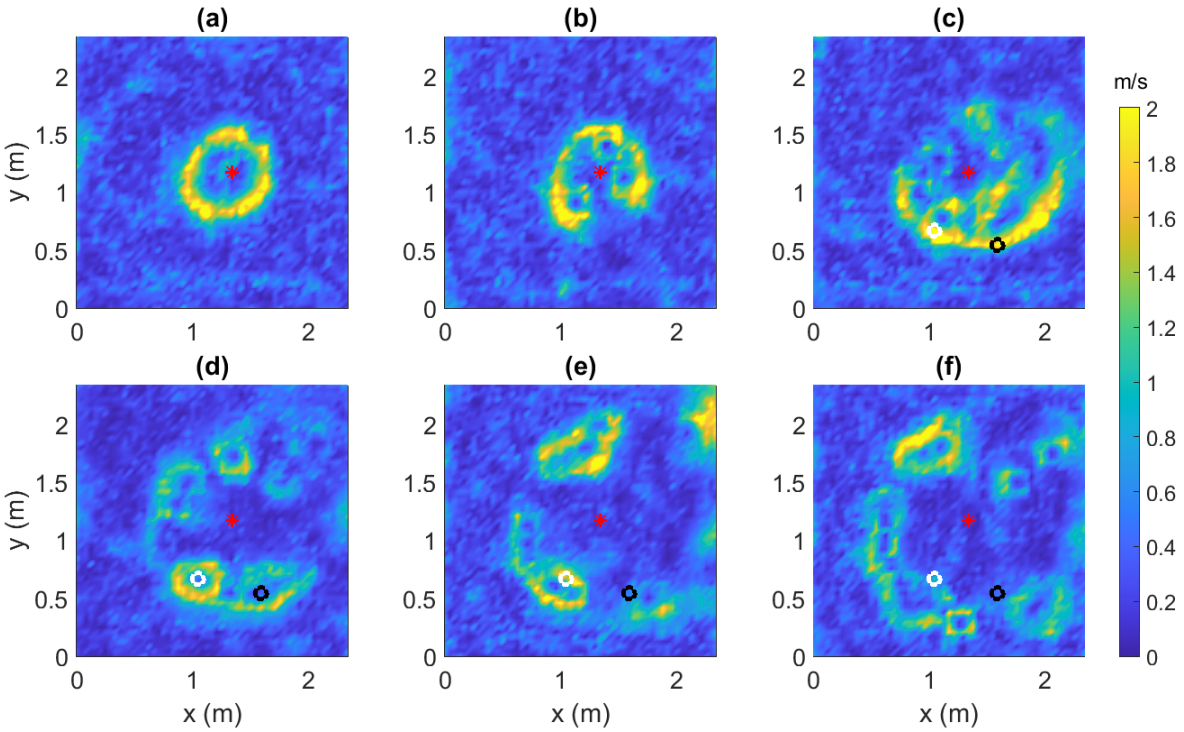


Figure 2.2: The magnitude of horizontal velocity in the domain at time t = (a) 100 s, (b) 110 s, (c) 175 s, (d) 247.5 s, (e) 300 s, and (f) 350 s. The red asterisk indicates the ignition point (IP). The white and black circles in (c)-(f) indicate the coordinates of the fixed points formed around $t = 247.5$ s in (d). [Generated using MATLAB R2021a]

shield it from the innermost core of the fire. The curving of the streamlines is indicative of a dynamic pressure differential between the inner and outer edge of the fire front (47). Additionally, the divergence of the streamlines indicate that the flow decelerates at the fire front, as also evidenced by the size of the velocity vectors. The fact that the streamlines terminate indicates that they leave the horizontal plane where the streamlines are computed. In this case, the opposing wind vectors join to form an updraft region (47) as indicated later in Fig. 2.4. Unlike observations made in some previous works that studied the behavior of a fire driven by the wind in a particular direction (47), the streamlines do not appear to drive the fire-front forward to contribute to the fire spread. Furthermore, it can be observed that when fire-pockets begin to form at time $t = 110$ s (Fig. 2.3(d)), the streamlines entering these pockets converge at the fixed points enclosed by them.

Color contours of the surface temperature (T_s) are shown in Figs. 2.4(a) and 2.4(b)

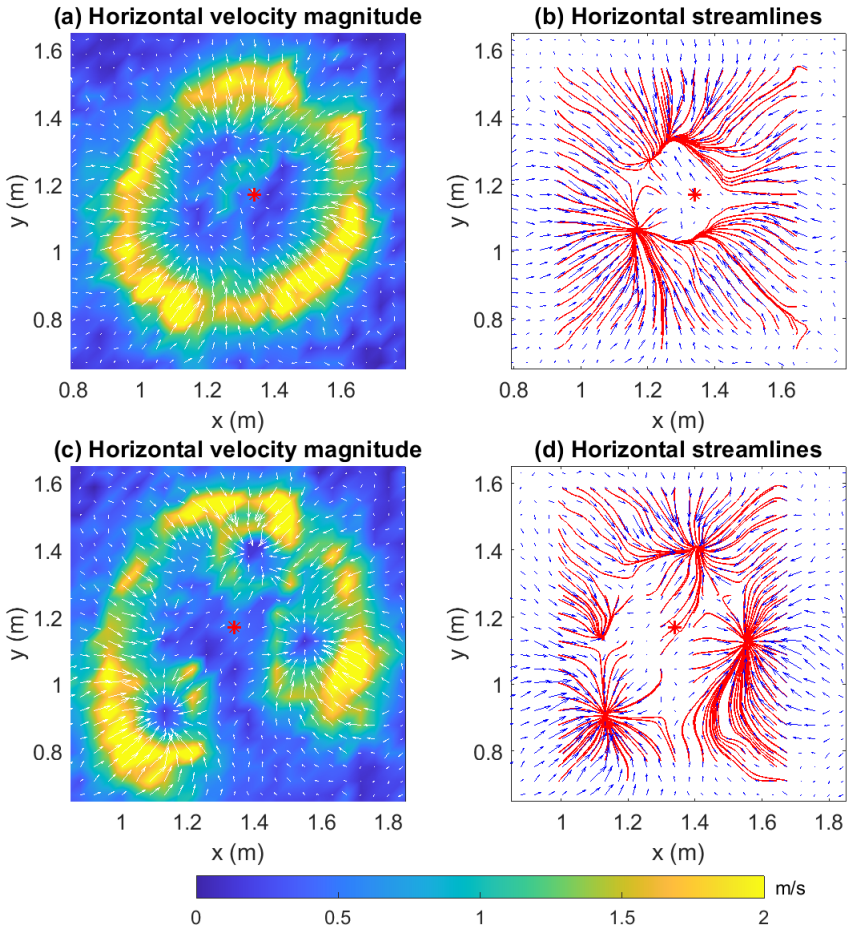


Figure 2.3: Horizontal velocity ($\mathbf{u}_{\mathrm{H}}$) vectors overlaid on color contours of u_{H} at t = (a) 100 s and (c) 110 s along with streamlines overlaid on horizontal velocity ($\mathbf{u}_{\mathrm{H}}$) vectors at t = (b) 100 s and (d) 110 s. The red asterisk indicates the IP. Arrows have been scaled by 1.5. [Generated using MATLAB R2021a]

at $t = 100\,\mathrm{s}$ and $t = 247\,\mathrm{s}$, respectively, along with overlaid vectors of horizontal velocity ($\mathbf{u}_{\mathrm{H}}$). The darkest blue regions are cooler ambient regions, while the yellow regions are high temperature regions that also include regions of active flaming. The fire-front can be delineated from the edge of the more brightly colored contours before they merge into the darkest blue (ambient temperature) regions. Although measurements of air temperature are unavailable, it is reasonable to assume that they would be lower above cooler surfaces (darkest blue regions). Thus, the influx of (cooler) ambient air into the fire-core (Fig. 2.4(a)) cools the fire-core as the fire-front expands. In some cases (Fig. 2.4(b)), contours of the highest temperature lie "outside" the fire-front. This is because the fire heats the unburnt

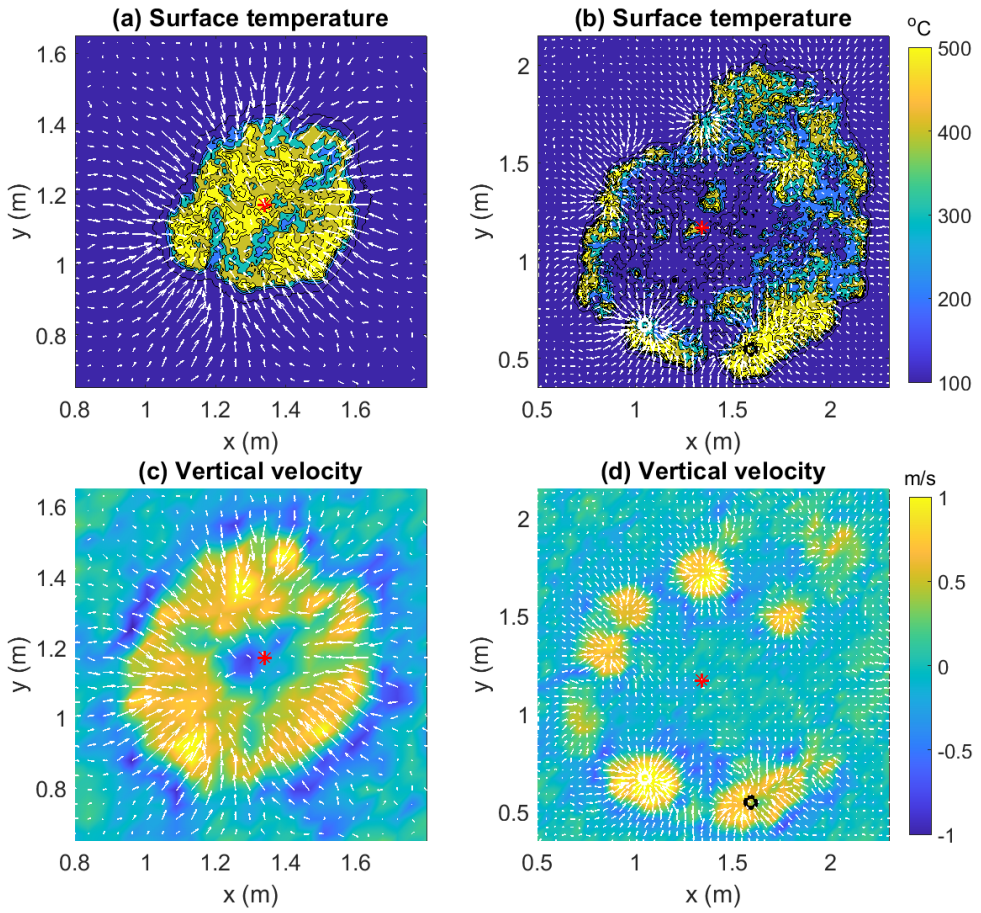


Figure 2.4: Color contours of the surface temperature (T_s) with overlaid vectors of horizontal velocity ($\mathbf{u}_\mathrm{H}$) at $t =$ (a) 100 s and (b) 247 s, demonstrating the entrainment of colder ambient air. Color contours of vertical velocity (w) and vectors of horizontal velocity ($\mathbf{u}_\mathrm{H}$) at $t =$ (a) 100 s and (b) 247.5 s, demonstrating the influx of colder ambient air from the region of downdraft. Arrows have been scaled by 1.5. Red asterisk indicates the IP. White and black circles represent FP1 and FP2, respectively. [Generated using MATLAB R2021a]

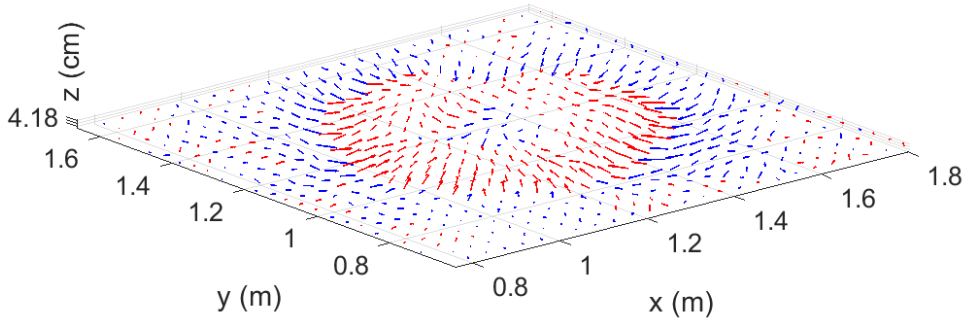


Figure 2.5: An isoparametric view of the total velocity ($\mathbf{u} = u\hat{\mathbf{i}} + v\hat{\mathbf{j}} + w\hat{\mathbf{k}}$) vectors plotted 4.18 cm above the surface of the fuel bed and zoomed into the active combustion region of the domain at $t = 100$ s. Red arrows indicate updrafts ($w > 0$), while blue arrows indicate downdrafts ($w < 0$). [Generated using MATLAB R2021a]

fuel on the outside via radiation. At ignition temperature, this fuel begins to burn, causing the fire to spread outward. Furthermore, we present color contours of the vertical velocity (w) with overlaid vectors of the horizontal velocity ($\mathbf{u}_{\mathrm{H}}$) in Figs. 2.4(c)-(d). Dark blue regions are downdraft regions, while yellow regions are those of updraft. We expect the fire-core to manifest as the region of updraft surrounded by the annular region of downdraft. This allows a clear demarcation of the fire-front. Moreover, the cooler ambient in-drafts over the downdraft region decelerate as they pass through the updraft region. The fire-front at $t = 247.5\,\mathrm{s}$, as shown in Fig. 2.4(d), affords an interesting observation. The pockets of fire at each fixed point are regions of updraft, which are separated by regions of downdraft. The envelope of the fire-perimeter of each of these pockets constitutes the fire-front, which consequentially comprises alternating regions of upwash and downwash verifying similar observations made in the literature (58; 48).

Finally, a three-dimensional flow picture is constructed from an isoparametric view of the net flow ($\mathbf{u} = u\hat{\mathbf{i}} + v\hat{\mathbf{j}} + w\hat{\mathbf{k}}$) at $t = 100\,\mathrm{s}$ as shown in Fig. 2.5. It is observed that the net velocity vectors at the fire-front are inward and upward (red arrows). We, therefore, expect the flame to be tilted inward as is characteristic of small or point-source fires that advance against the wind (in this case, fire-induced wind) (73). On the "outside" of the fire-front, the net velocity vector is inward and downward (blue arrows) indicating the presence of a downdraft region.

2.3.2 Coherent Structures

According to Jiménez (74), coherent structures in wall-bounded turbulent flows can be defined as structures "with enough internal dynamics to behave relatively autonomously from any remaining incoherent part of the flow." Indeed, coherent structures serve to provide a direction to the seemingly random nature of the flow and their study constitutes an integral

part of the analysis that makes turbulent flow during fires less mysterious. In this section, correlation contours and vorticity vectors/rollers are explored for a clearer picture of the fire structure and evolution. The eddy fluxes of momentum at the selected fixed points (FP1 and FP2) have also been explored for signatures of fire bursts (defined in the introduction).

Cross Correlation Contours

The two-point spatial correlation at time t is defined as follows (75):

$$r_{ij}(x, y, t) = \frac{\overline{u_i(x_0, y_0, t) u_j(x, y, t)}}{\overline{u_i'^2(x_0, y_0)}^{\frac{1}{2}} \, \overline{u_j'^2(x, y)}^{\frac{1}{2}}} \tag{2.1}$$

In Eq. 2.1, $(x_0,\ y_0)$ represents the IP ($x_0 = 1.34\,\text{m},\ y_0 = 1.17\,\text{m}$). Coefficients of cross-correlation with the IP are evaluated across the entire domain. Figure 2.6 presents contours of $r_{11},\ r_{22},$ and r_{33} and the IP is plotted using a red asterisk. The y-directionally (north-south)

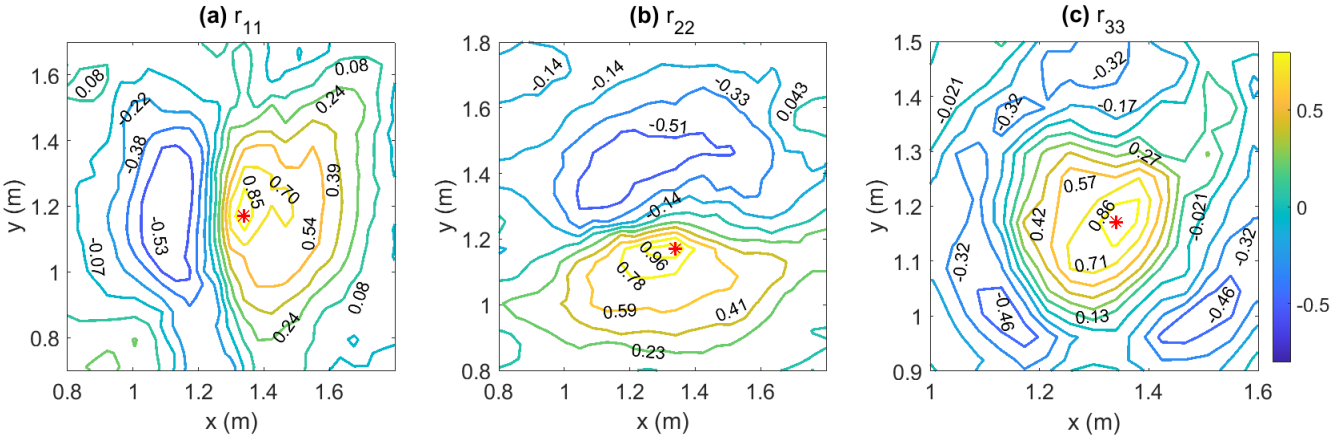


Figure 2.6: Cross-correlation contours of (a) u velocity (r_{11}), (b) v velocity (r_{22}), and (c) vertical velocity (r_{33}) plotted close to the IP (red asterisk). [Generated using MATLAB R2021a]

elongated structures of the r_{11} contours (Fig. 2.6(a)) indicate a y-directional uniformity in the u (east-west) velocity. For the first 100 s of ignition, the u velocity component remains negative ($u < 0$) at the IP (not shown here). Hence, the positively correlated contours on the

east of the IP represent *westward* u velocity ($u < 0$), while the negatively correlated contours on the west of the IP represent *eastward* velocity ($u > 0$). Similarly, the x-directionally elongated structures of r_{22} contours (Fig. 2.6(b)) indicate x-directional uniformity in the v velocity. Again, for the first 100 s of ignition, the v velocity remains positive ($v > 0$) at the IP (not shown here). The positively correlated contours on the south of the IP represent northward v velocity ($v > 0$), while the negatively correlated contours on the north of the IP represent southward v velocity ($v < 0$). We interpret the cross-correlation contours as a measure of the retainment of flow memory (recorded at the IP, in this case) across space. The y-directionally elongated r_{11} contours are indicative of the entrainment of ambient air from the eastern and western sides of the domain as a relatively quick and bulk response to ignition, the earliest sign of the presence of fire. The x-directionally elongated r_{22} contours are similarly indicative of the entrainment of ambient air from the northern and southern sides of the domain as a similar (quick and bulk) response.

Elliptical structures with decreasing values of r_{33}, where $r_{33} > 0$, can be observed with increasing distance from the IP in Fig. 2.6(c). These are interpreted as follows. Since the IP is initially a region of updraft, contours that are positively correlated with the IP are inferred to be regions of updraft. Beyond these structures, we observe contours that correlate negatively with the IP and do not encompass it. These can be interpreted as regions of downdraft beyond the fire perimeter. A shift in the direction of fire propagation towards the north-west can also be observed from the contours. This can be attributed to a shift in the direction of the local wind or heterogeneity in the fuel bed in the vicinity of the IP. Thus, contours of r_{33} give a clear picture of the evolution of the fire-front during the first minute or so.

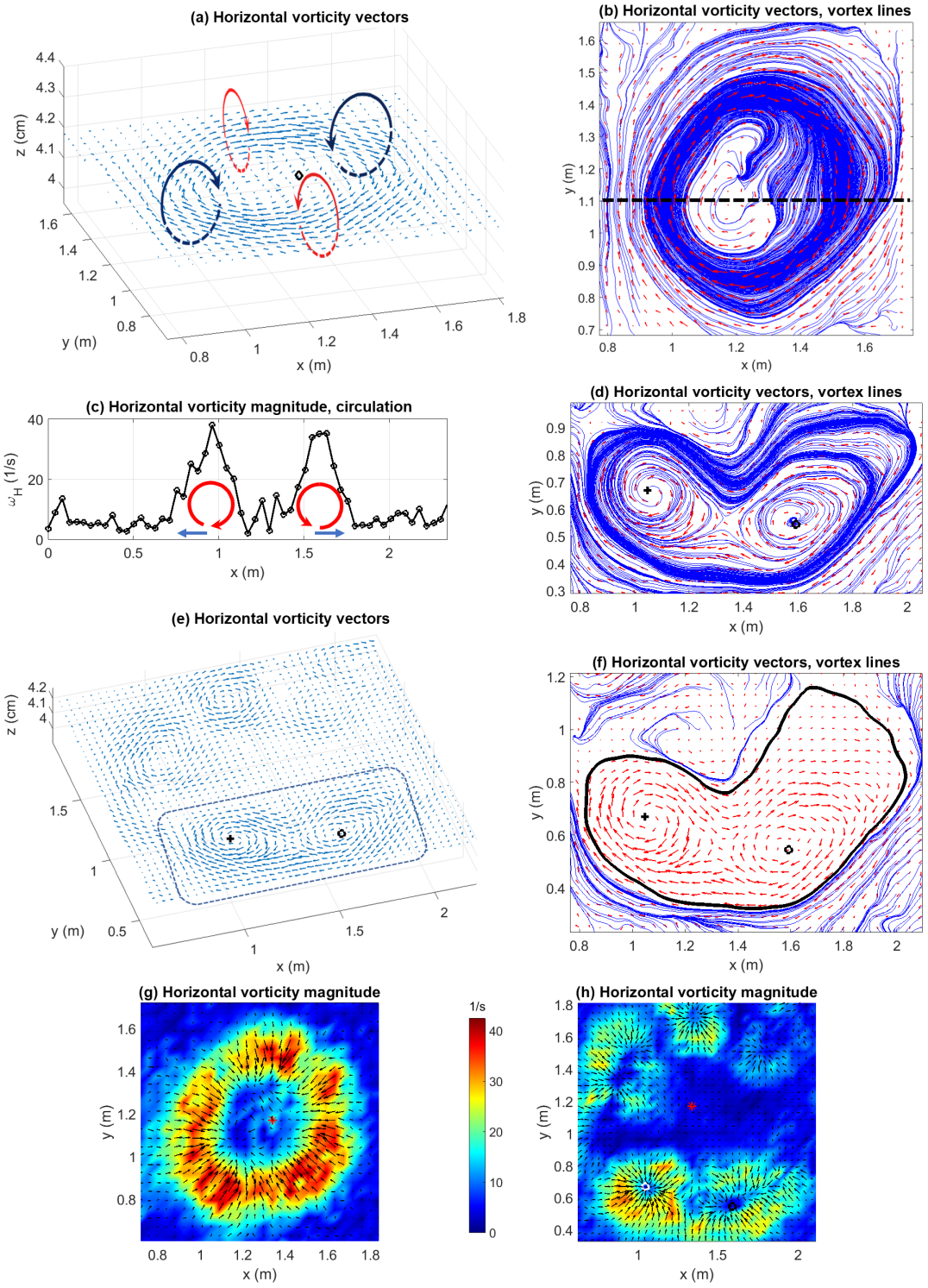


Figure 2.7: Horizontal vorticity vectors at $t =$ (a) 100 s (dashed curved arrows represent vortices) and (e) 247.5 s (dashed rectangle highlights the region around FP1 and FP2), and vortex lines for $t =$ (b) 100 s (black dashed line represents $y = 1.1$ m) and (d) 247.5 s (zoomed in around FP1 and FP2). (c) Magnitude of $\boldsymbol{\omega}_{\mathrm{H}}$ plotted along with a schematic diagram of the circulation in the vertical plane as indicated by the vortex tubes in (b), at $y = 1.1$ m. (f) Vortex lines (thick black solid) isolating the vorticity field around the fixed points. Color contours of the magnitude of $\boldsymbol{\omega}_{\mathrm{H}}$ with overlaid horizontal velocity ($\mathbf{u}_{\mathrm{H}}$) vectors (black arrows, scaled by 1.5) at $t =$ (g) 100 s and (h) 247.5 s. Red asterisk represents the IP. [MS PowerPoint 365 used to generate arrows in (a) and (c); all panels generated using MATLAB R2021a]

Vorticity and Rollers

It has been reported in the literature (58) that fire-induced counter-rotating vortices participate in fire spread by advecting hot gases towards fuel particles, causing ignition. From this experiment, it is possible to compute the vorticity as the curl of the velocity field ($\omega = \nabla \times \mathbf{u}$) and examine its spatial structure. In this section, we first look at horizontal vorticity ($\boldsymbol{\omega}_{\mathrm{H}} = \omega_x \hat{\mathbf{i}} + \omega_y \hat{\mathbf{j}}$) vectors in the domain both before and after the fire-front disintegrates. The effect of the vertical component of vorticity ($\boldsymbol{\omega}_z$) on the vortical structures is also analyzed.

Figure 2.7(a) depicts $\boldsymbol{\omega}_{\mathrm{H}}$ for $t = 100\,\mathrm{s}$. It should be noted that the vorticity here is induced by both buoyant convection and shear. The fire-induced turbulent fluctuations induce the formation of vortices as shown in Figs. 2.7(a) and 2.7(c). A simple right-hand-thumb rule can be used to determine the direction of circulation of the vortices (curved arrows that go in and out of the plane in Fig. 2.7(a)). It is important to note that the vectors plotted in Fig. 2.7(a) and 2.7(e) are not velocity vectors but vorticity vectors in the horizontal plane. The hand-drawn dashed curved arrows (Fig. 2.7(a)) show the actual circulations that result in these vorticity vectors given by $\boldsymbol{\omega}_{\mathrm{H}} = \omega_x \hat{\mathbf{i}} + \omega_y \hat{\mathbf{j}}$. Moreover, these circulation structures confirm the presence of counter-rotating vortex pairs on opposite sides reported elsewhere as a key mechanism for fire spread (58). Note that while Finney et al. (58) hypothesized the existence of these vortex pairs from images of laboratory fires, the present experiment enables us to quantify these vortices for the first time, which represents a significant advancement in the field.

Vortex lines are lines whose tangents are parallel to the local vorticity vector. As seen from Fig. 2.7(b), vortex lines originating on the outside of the fire spiral inward into the fire-front where the vorticity enhances significantly and then into the fire core where the vorticity eventually dissipates. The vortex lines drawn through each point of a closed curve

constitute the surface of a vortex tube. The spatial density of these lines increases at the fire front indicating that vortex tubes get stretched thinner at that location, before dispersing again at the fire core. To conserve circulation, when a vortex tube is stretched (thereby making it thinner), the magnitude of the vorticity has to increase, which is also confirmed by Figs. 2.7(g)-(h). A schematic of the vertical cross-section of the vortex tubes at $y = 1.1\,\mathrm{m}$ is shown in Fig. 2.7(c). If we imagine the fire-front to be located at the regions of highest vorticity magnitude, we can see how the vortices (red curved arrows) provide an outward push to hot gases that are close to the surface of the fuel bed (blue horizontal arrows). The advection of hot gases onto the unburnt fuel would result in ignition, causing the fire to spread "outward".

An example of a post-instability vortical pattern is shown in Fig. 2.7(e). Figure 2.7(e) shows the horizontal vorticity vectors for $t = 247.5\,\mathrm{s}$ with a focus on the vorticity surrounding FP1 and FP2 (black cross and black circle, respectively). The vortical pattern around a fire pocket centred at a fixed point mimics the pre-instability vortical pattern around the IP at $t = 100\,\mathrm{s}$ (Fig. 2.7(a)). Moreover, the vortices that surround FP1 are also seen to interact with the vortices that surround FP2. This indicates a possible mechanism for interaction between two such neighboring flames. Furthermore, Fig. 2.7(d) shows that the vortex lines that originate from within the fire-pocket around FP1 spiral outward and away. These vortex lines spiral inward and into the fire-pocket around FP2. The thick black solid line in Fig. 2.7(f) indicates the presence of a vortex line that separates the fixed points from the rest of the vorticity field, secluding the vortical interactions between the two fixed points from the rest of the vorticity field.

Color contours of the magnitude of the horizontal vorticity ($\boldsymbol{\omega}_\mathrm{H}$) have been shown in Figs. 2.7(g)-(h) along with overlaid arrows representing the horizontal velocity ($\mathbf{u}_\mathrm{H}$) vectors. For both, $t = 100\,\mathrm{s}$ (Fig. 2.7(g)) and $t = 247.5\,\mathrm{s}$ (Fig. 2.7(h)), regions of high magnitude of $\boldsymbol{\omega}_\mathrm{H}$ correspond to regions of higher $\mathbf{u}_\mathrm{H}$ (longer arrows). This demonstrates a strong correlation

between the strength of the vortices and the air entrained by the flame. This is an important observation in the context of fire-whirl formation discussed later.

Another feature of the vortices can be observed from the net vorticity vector ($\boldsymbol{\omega}$), i.e. from the addition of the vertical component of the vorticity to $\boldsymbol{\omega}_{\mathrm{H}}$. Vectors of the net vorticity ($\boldsymbol{\omega}$) at $t = 100\,\mathrm{s}$, shown in Fig. 2.8(c), indicate that eddies making up the vortex tubes described above precess upward (red arrows) and downward (blue arrows), alternately. This causes kinking of the resulting vortex tubes (schematic diagram in Fig. 2.8(a)). This feature is better visualized with the help of color contours of helicity. The helicity (H) at any point in the flow field is given by $H = \mathbf{u}\cdot\nabla\times\mathbf{u} = \mathbf{u}\cdot\boldsymbol{\omega}$, where "$\cdot$" represents taking the inner product. The sign of the helicity is indicative of the relative angle between $\mathbf{u}$ and $\boldsymbol{\omega}$: $H > 0$ implies that the angle is acute, while $H < 0$ indicates that the angle is obtuse. Color contours of the helicity are shown in Fig. 2.8(b), wherein alternating regions of positive helicity (red) and negative helicity (blue) are observed along the fire-front. Since the fire-front comprises updrafts (red arrows in Fig. 2.5), an acute angle with $\mathbf{u}$ indicates that $\boldsymbol{\omega}$ is pointed away from the surface (red arrows in Fig. 2.8(c)) and an obtuse angle with $\mathbf{u}$ indicates that $\boldsymbol{\omega}$ is pointed towards the surface (blue arrows in Fig. 2.8(c)). This suggests that the eddies precess upward and downward alternately, resulting in the kinking of the vortex tubes along the fire-front.

We take the opportunity to discuss the possibility of fire-whirl formation here. It is known that essential conditions for fire-whirl formation include the presence of a vorticity-generation mechanism and entrainment of air to the generated vortex column via a radial boundary layer (23). Both conditions are satisfied in the current study. It is known from Fig. 2.3(b) that the streamlines penetrating the fire-front curve away from the fire core testifying to an active $\boldsymbol{\omega}_z$ component. The vertical component of flow velocity in the vicinity of the fire-front (Fig. 2.5) would be able to direct the curving streamlines and advect (or tilt) the vorticity rollers (observed in Fig. 2.8(a)) upward, away from the surface, potentially resulting in a

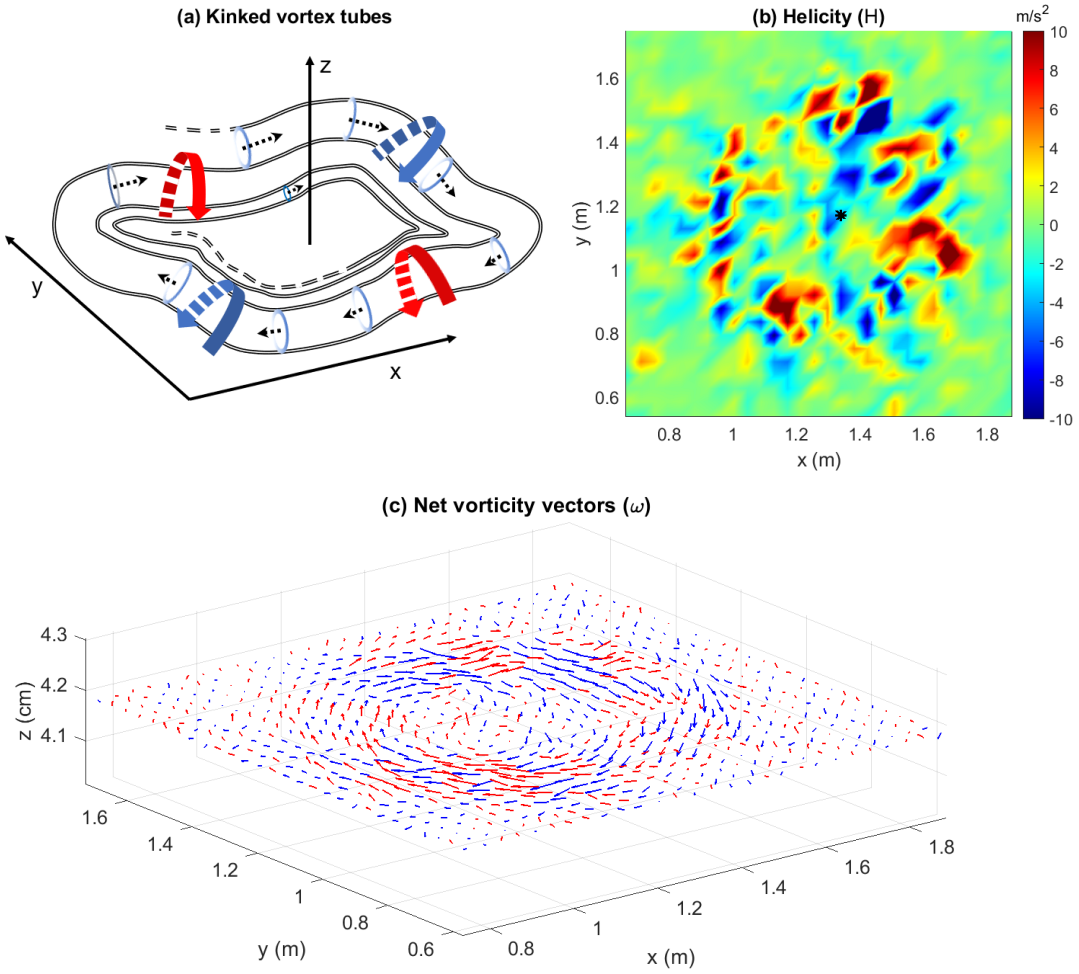


Figure 2.8: (a) A schematic diagram showing the kinked vortex tubes (not to scale), (b) helicity (H), and (c) net vorticity vectors ($\boldsymbol{\omega} = \omega_x\hat{\mathbf{i}} + \omega_y\hat{\mathbf{j}} + \omega_z\hat{\mathbf{k}}$) demonstrating that eddies precess alternately away from (red arrows) and toward (blue arrows) the surface at $t = 100\,\mathrm{s}$. Pairs of counter-rotating vortices are shown in (a). Black asterisk in (b) represents the IP. [MS PowerPoint 365 used to create (a); (b) and (c) generated using MATLAB R2021a]

fire whirl. A more complete exploration of fire whirls is anticipated in a future study, with three-dimensional data collection.

Eddy Fluxes of Horizontal Momentum

Turbulent momentum fluxes (Reynolds stresses normalized by fluid density) facilitate a re-distribution of momentum in the flow via eddies. In this section, we analyze the horizontal momentum flux ($\overline{u'v'}$) and the product of the horizontal turbulent fluctuations ($u'v'$) at the selected fixed points (FP1 and FP2) (Fig. 2.9). Let us first focus on FP1 (white circle in Fig. 2.2(d)). An increase in the magnitude of $\overline{u'v'}$ indicates the presence of the fire at or in the vicinity of this point (Fig. 2.9(a)). However, the 1-minute moving averages do not provide information regarding what the individual peaks in $u'v'$ represent. Consider the peaks in $u'v'$ at $t = 158\,\mathrm{s}$ and $t = 322\,\mathrm{s}$ (Fig. 2.9(c)). At $t = 158\,\mathrm{s}$, the mean x-directional flow is eastward ($\overline{u} > 0$, Fig. 2.9(e)), while the mean y-directional flow is northward ($\overline{v} > 0$, Fig. 2.9(g)). From Figs. 2.2(c)-(d), it can be seen that at this location, $u' < 0$ and $v' < 0$ would assist in propagating the fire away from the IP (south/west/southwest-ward), while $u' > 0$ and $v' > 0$ would combine to create the opposite effect. Therefore, $u'(> 0)$ and $v'(> 0)$ at $t = 158\,\mathrm{s}$ (Figs. 2.9(e), 2.9(g)) interact to impede the spread of the fire away from the IP at this location; this is seen as a peak in Fig. 2.9(c). A similar phenomenon is also observed at $t = 309\,\mathrm{s}$ when the mean flow supports the fire spread away from the IP ($\overline{u},\ \overline{v} < 0$), while the fluctuations resist it ($u',\ v' > 0$). At $t = 322\,\mathrm{s}$, the mean x-directional flow is westward ($\overline{u} < 0$, Fig. 2.9(e)), while the mean y-directional flow is southward ($\overline{v} < 0$, Fig. 2.9(g)). The fluctuations $u'(< 0)$ and $v'(< 0)$ at $t = 322\,\mathrm{s}$ (Figs. 2.9(e), 2.9(g)) interact to accelerate the mean flow and drive the fire south-west with sudden force away from the IP, causing a fire-burst. This phenomenon is also observed at $t = 300\,\mathrm{s}$, while burst-like peaks are also observed at $t = 148\,\mathrm{s}$, $t = 198\,\mathrm{s}$ (Fig. 2.9(c)).

At FP2 (black circle in Fig. 2.2(d)), an increase in $\overline{u'v'}$ when $150\,\mathrm{s} \leq t \leq 200\,\mathrm{s}$ or $300\,\mathrm{s} \leq$

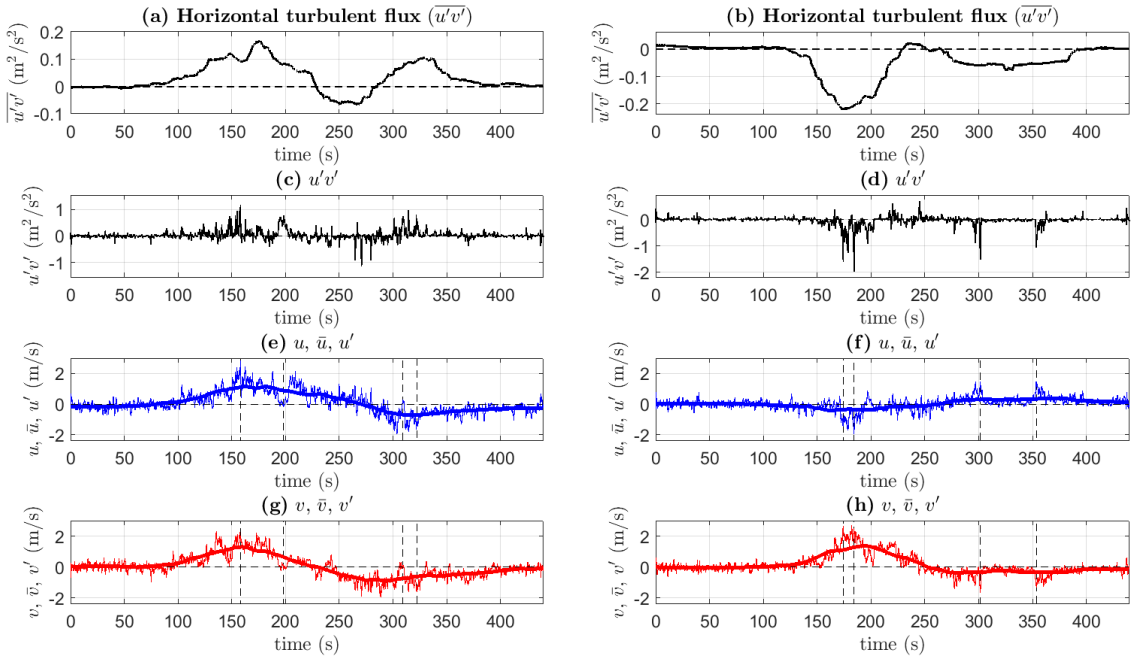


Figure 2.9: (a) The horizontal turbulent flux ($\overline{u'v'}$), (c) $u'v'$, (e) u, $\overline{u}$ (thick solid line), and u', and (g) v, $\overline{v}$ (thick solid line), and v' at FP1. (b) The horizontal turbulent flux ($\overline{u'v'}$), (d) $u'v'$, (f) u, $\overline{u}$ (thick solid line), and u', and (h) v, $\overline{v}$ (thick solid line), and v' at FP2. Dashed vertical lines in (e) and (g) represent $t = 158\,\text{s}$, $198\,\text{s}$, $309\,\text{s}$, and $322\,\text{s}$. Dashed vertical lines in (f) and (h) represent $t = 174\,\text{s}$, $184\,\text{s}$, $301\,\text{s}$, and $353\,\text{s}$. [Generated using MATLAB R2021a]

$t \leq 350\,\text{s}$ indicates the presence of the fire at or in the vicinity of this point (Fig. 2.9(b)). It can be seen from Figs. 2.2(c)-(d) that at this location, a fire-front that propagates south/east/southeast-ward spreads away from the IP. At $t = 174\,\text{s}$, 178.6 s, and $184\,\text{s}$, $u'(< 0)$ and $v'(> 0)$ (Figs. 2.9(f), 2.9(h)) interact to impede the advancement of the the fire-front (peaks in Fig. 2.9(d)) at FP2. However, at $t = 301\,\text{s}$ and $t = 353\,\text{s}$, the fluctuations $u'(> 0)$ and $v'(< 0)$ (Figs. 2.9(f), 2.9(h)) interact to drive the fire southeast via bursts (peaks in Fig. 2.9(d)). Thus, increase in the magnitude of the horizontal momentum flux ($\overline{u'v'}$) and $u'v'$ is either symptomatic of fire-bursts that occur at irregular time intervals or representative of increased turbulence-induced impediment to the fire-spread; together, they play opposing roles in the fire-spread and in determining the spread rate.

Table 2.1: A summary of the peak frequency and the corresponding time scale for the u energy spectrum, and the computed wave number and length scale for the IP, FP1, and FP2.

Point	f_p (Hz)	$\overline{U}$ (m/s)	τ_u (s)	κ (1/m)	L_u (m)
IP	0.2344	0.62	0.6791	2.3871	0.419
FP1	0.410	1.16	0.3880	2.2237	0.450
FP2	0.352	0.42	0.4527	5.3023	0.189

2.3.3 Length, Time, and Velocity Scales

An understanding of the most dominant time and length scales can provide insights regarding the fluid dynamic mechanisms that assist or impede turbulent energy transport. Owing to the high sampling frequency of the velocity signals in this study, reliable estimates of the time scales associated with high-energy eddies can be obtained from the frequency spectrum. Figure 2.10 shows plots of $fS(f)$ against f on a log-log scale, where f is the frequency and $S(f)$ is the power spectral density computed using MATLAB's *pwelch* function. Each plot in Figs. 2.10(a)-(c) represents the energy spectrum ($E(f)$) of the u velocity for a particular point in the flow field: the IP (Fig. 2.10(a)), FP1 (Fig. 2.10(b)), and FP2 (Fig. 2.10(c)). It is observed that the inertial sub-range for both the u spectrum (Figs. 2.10(a)-(c)) and v spectrum (not shown here) at all three points follows Kolmogorov's $-2/3$ scaling law (since this is the spectral density pre-multiplied by the frequency) as shown by the blue dashed lines. Note that the energy spectrum does not capture the dissipation scales.

Integral Length Scale

The peak frequency (f_p) of the energy spectra for u at the three points mentioned above correspond to the most energetic eddies. This can be utilized to obtain the integral time scale (τ_u) and integral length scale (L_u) as follows (76; 77):

$$\tau_u = \frac{1}{2\pi f_p},\ \kappa_p = \frac{2\pi f_p}{\overline{U}},\ L = \frac{1}{\kappa_p}. \tag{2.2}$$

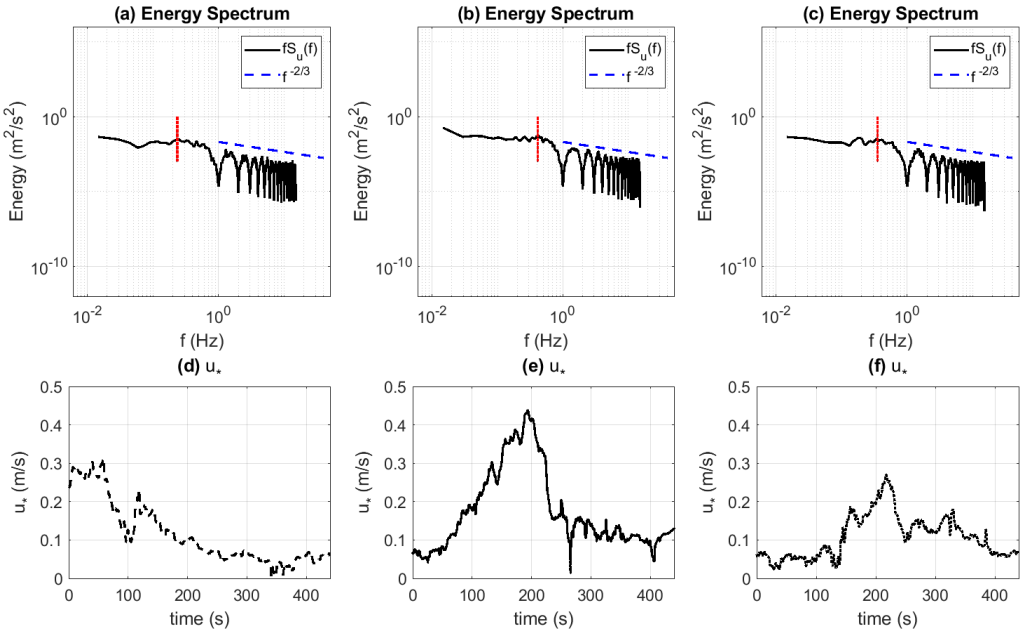


Figure 2.10: Energy spectrum ($fS(f)$) for the time-varying u signal at (a) the IP, (b) FP1, and (c) FP2, and u_* computed at (d) the IP, (e) FP1, and (f) FP2. [Generated using MATLAB R2021a]

Here, κ_p is the wave number of the most energetic eddies and $\overline{U}$ represents the largest absolute value of the moving mean $\overline{u}(t)$ for a given point. Table 2.1 summarizes the values of f_p, τ_u, κ_p, and L_u for the three points under consideration. From the table, the largest value of L_u is 0.45 m. It is, therefore, evident that the most energetic eddies have wavelengths of approximately 0.45 m ($O(10^{-1})$ m) when measured along the x direction, which is approximately $1/5^{\text{th}}$ of the domain length. The corresponding time scales range from 0.3 - 0.7 s ($O(10^{-1})$ s).

Viscous Dissipation Scales

It must be noted that at the IP, the dissipation time scale (τ_η) cannot be obtained from the energy spectrum (Fig. 2.10(a)). In order to obtain τ_η, we first compute the friction velocity

(u_*) from the 1-minute averages of $u'w'$ and $v'w'$ as follows:

$$u_*^2 = (\overline{u'w'}^2 + \overline{v'w'}^2)^{1/2} \tag{2.3}$$

The friction velocity computed from Eq. (2.3) is plotted for the IP, FP1, and FP2 in Figs. 2.10(d)-(f). For a given point, the highest values of u_* correspond to times of active combustion at that point. From a scaling perspective, we pick the largest value of u_* from Figs. 2.10(d)-(f), which is achieved at FP1 ($u_* = 0.44\,\mathrm{m/s}$ in Fig. 2.10(e)). Assuming a first-order closure model with a gradient-diffusion parameterization, where the vertical turbulent shear stress can be parameterized by a turbulent diffusivity (ν_t) and a gradient of the mean horizontal wind velocity ($\partial||\overline{\mathbf{u}}||/\partial z$)

$$u_*^2 = 0.44^2 = \nu_t \frac{\partial||\overline{\mathbf{u}}||}{\partial z} \approx \nu_t \frac{\Delta||\overline{\mathbf{u}}||}{\Delta z} \implies \nu_t \approx \frac{\Delta z}{\Delta||\overline{\mathbf{u}}||} u_*^2. \tag{2.4}$$

Here, ν_t is the eddy viscosity and "|| ||" represents computing the magnitude of a vector. We know that $\eta = \nu^{3/4}\epsilon^{-1/4}$ and $v_\eta = (\nu\epsilon)^{1/4}$, where η represents the Kolmogorov length scale, v_η is the Kolmogorov velocity scale, ϵ is the viscous dissipation rate of the TKE, and ν is the kinematic viscosity of air. From the K-ϵ turbulence model (78):

$$\nu_t = C_\mu \frac{\bar{K}^2}{\epsilon} \implies \epsilon = C_\mu \frac{\bar{K}^2}{\nu_t}, \tag{2.5}$$

where K represents the TKE and $C_\mu = 0.09$. From Eq. (2.4), we get:

$$\epsilon = C_\mu \frac{\Delta||\overline{\mathbf{u}}||\bar{K}^2}{\Delta z u_*^2} \approx 0.09 \times \frac{1.3 \times 0.4^2}{4.18 \times 10^{-2} \times 0.44^2} = 2.34\ \mathrm{m^2/s^3} \tag{2.6}$$

Here, we have used $\Delta||\overline{\mathbf{u}}|| = 1.3\,\mathrm{m/s}$ and $\bar{K} \approx 0.4\,\mathrm{m^2/s^2}$ as computed at FP1 when u_* reaches $0.44\,\mathrm{m/s}$ (Fig. 2.10(e)). The highest recorded surface temperatures are above 500°C (Figs. 2.4(a)-(b)). At 500°C, the kinematic viscosity of air (ν) is approximately 7.8×10^{-5}

m^2/s (79). This gives $\eta = 6.7 \times 10^{-4}\,m$ and $v_\eta = 0.12\,m/s$. Finally, the time-scale can be obtained using $\tau_\eta = \eta/v_\eta = 5.8 \times 10^{-3}\,s$. It is interesting to note that the value of τ_η is an order of magnitude lower than the sampling rate ($1/30\,s$), which is why the energy spectrum (Figs. 2.10(a)-(c)) does not capture the viscous dissipation scales. The sampling frequency would have to exceed $100\,Hz$ for that purpose. Furthermore, note that $v_\eta \sim 7.2\,m/min$, which is an order of magnitude higher than the RoS (0.2 - $0.3\,m/min$) discussed in the next section.

To complete the discussion on length scales, we compute the Taylor microscale (λ) using the following equation(80):

$$\lambda = \sqrt{\overline{u'^2}}\sqrt{15}\tau_\eta = 9.5 \times 10^{-3}\,m. \tag{2.7}$$

Here, we have used $\sqrt{\overline{u'^2}} \sim 0.425\,m/s$ as computed at FP1. Therefore, the Kolmogorov length scale is of $O(10^{-4})$, the Taylor microscale is of $O(10^{-3})$, and the integral length scale is of $O(10^{-1})$. Moreover, we report the Taylor Reynolds number to be $Re_\lambda = \frac{u'\lambda}{\nu} = 52$ and the turbulent Reynolds number for this study to be $Re_L = \frac{u'L}{\nu} = 2454$.

Rate of Spread

An average empirical spread-rate for this fire can be obtained from a back-of-the-envelope calculation. From Fig. 2.2(f), it can be seen that the fire-front traverses a distance of $1\,m$ from the IP ($x = 1.34\,m$) to the eastward edge ($x = 2.34\,m$) in $350\,s$ giving an average x-directional spread-rate of $0.17\,m/min$. The variation of the rate of spread with time is obtained as follows. A schematic of the location of the fire-front at two instances in time is shown in Fig. 2.11(a). As discussed earlier, the fire-front is said to be located at the periphery of the updraft region (yellow) that shares its boundary with the downdraft region

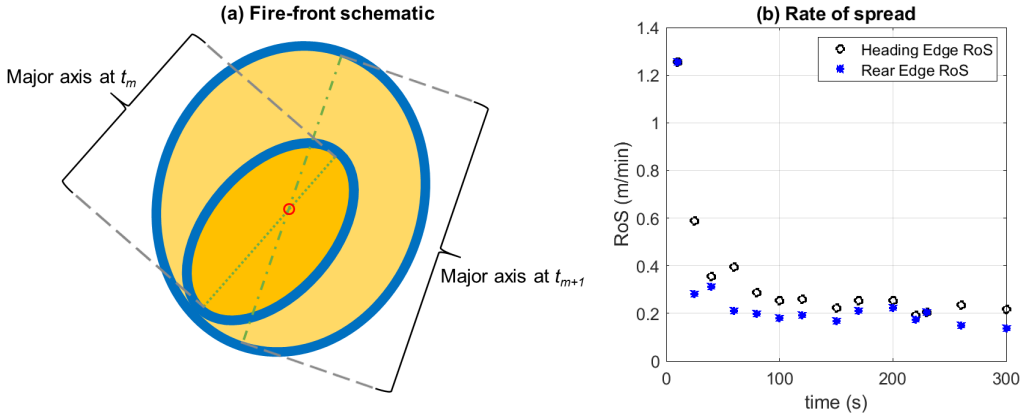


Figure 2.11: (a) A schematic diagram showing the major axis tracked at two instances of time elapsed since ignition to compute the corresponding distances of the heading and rear edges of the fire-front from the IP and (b) the variation of the heading and rear edge RoS with time. [MS PowerPoint 365 used to create (a); (b) generated using MATLAB R2021a]

(dark blue) on the outside of it. At a given time (t_m or t_{m+1}), the point on the fire-front furthest from the IP is said to be on the heading edge of the fire-front. The line joining this point to the IP gives the major axis of the ellipse (green dotted or dash-dotted lines), which intersects the ellipse again on the rear edge of the fire-front. The distances of these points from the IP at that this instant in time are used to calculate the rate of spread (RoS) of the heading and rear edges of the fire, estimates of which are shown in Fig. 2.11(b). It can be seen that after an initial transient RoS up to about $t = 50\,\text{s}$, the RoS is relatively stable between 0.2 and 0.3 m/min. This is in close agreement with the average RoS calculated above and also suggests that the fire spreads very gradually in the absence of a preferred direction for the ambient wind. Moreover, the fire must overcome both, the effects of viscous dissipation and the resistance offered by the entrained air, in order to spread "outward".

2.3.4 Turbulent Kinetic Energy Budget

We have seen that turbulent fluctuations play a role in accelerating or decelerating the fire spread via bursts or turbulence-induced impediment (eddies) at individual points on the

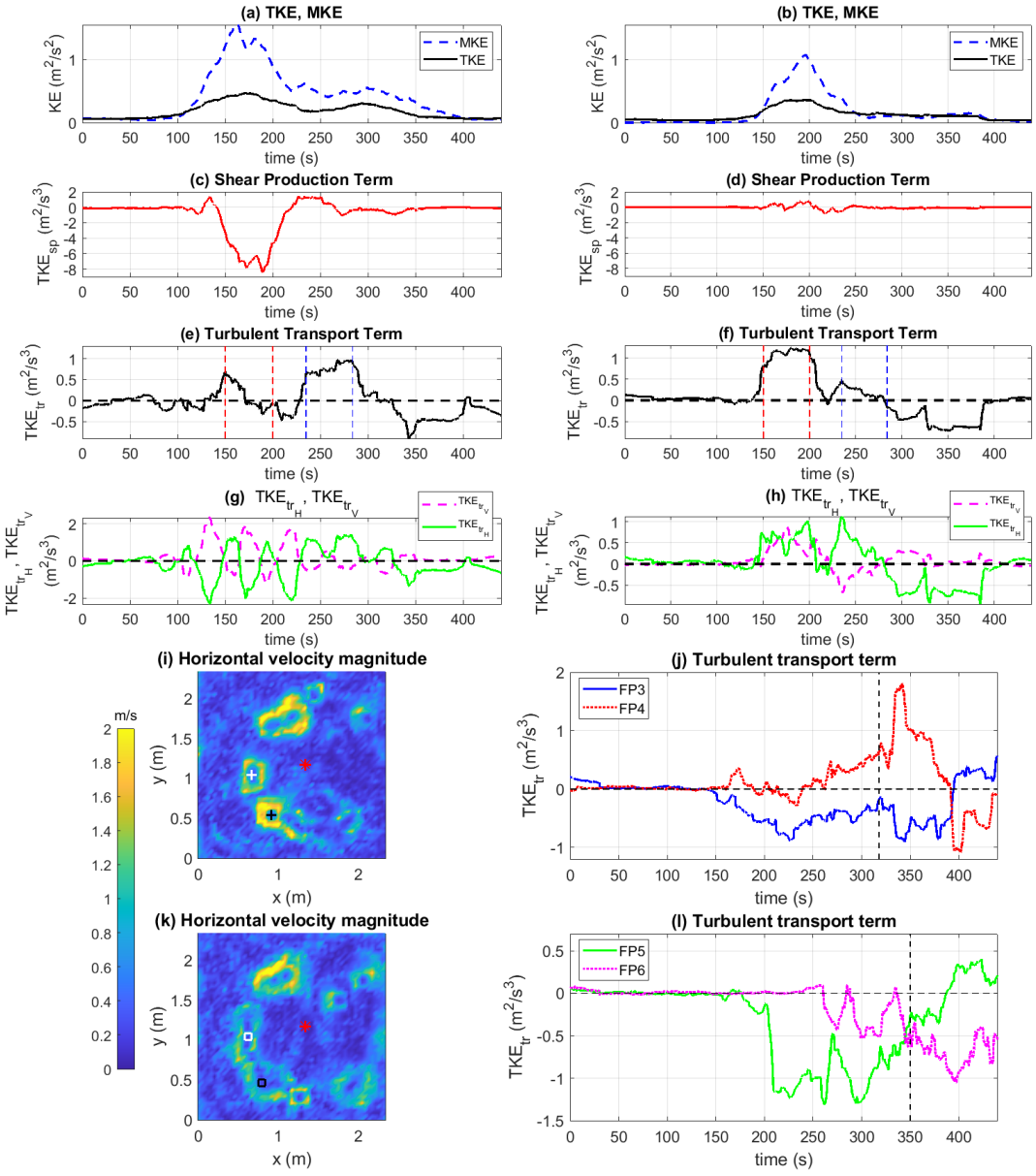


Figure 2.12: (a) TKE (black solid) and MKE (blue dashed), (c) TKE_{sp}, (e) TKE_{tr}, and (g) $TKE_{\mathrm{tr_V}}$ (magenta dashed) and $TKE_{\mathrm{tr_H}}$ (green solid) at FP1. (b) TKE (black solid) and MKE (blue dashed), (d) TKE_{sp}, (f) TKE_{tr}, and (h) $TKE_{\mathrm{tr_V}}$ (magenta dashed) and $TKE_{\mathrm{tr_H}}$ (green solid) at FP2. Vertical dashed lines in (e) and (f) correspond to $t = 150\,\mathrm{s}$, 200 s, 235 s, and 284 s. Color contours of u_{H} at $t =$ (i) 317.7 s (white cross represents FP3 and black cross represents FP4) and (k) 350 s (white square represents FP5 and black square represents FP6). TKE_{tr} at (j) FP3 (blue solid line) and FP4 (red dotted line), and (d) FP5 (green solid line) and FP6 (magenta dotted line). [All panels generated using MATLAB R2021a]

fire-front. In this section, we look at the turbulent kinetic energy (TKE) and the terms in the TKE budget equation that contribute to the rate of change of TKE. In the past, studies have compared individual terms in the TKE budget equation with each other with a view to classify the flow based on the dominating mechanism (81). The TKE budget equation is written as follows (82):

$$\frac{\partial \overline{K}}{\partial t} + \bar{u}_j \frac{\partial \overline{K}}{\partial x_j} = \delta_{i3} \frac{g}{\theta_v} \overline{u_i' \theta_v'} - \overline{u_i' u_j'} \frac{\partial \bar{u}_i}{\partial x_j} - \frac{\partial \overline{u_j' K}}{\partial x_j} - \frac{1}{\rho} \frac{\partial \overline{u_j' p'}}{\partial x_j} - \epsilon, \tag{2.8}$$

where K is the TKE, θ_v is the potential temperature (of air), and p' is the pressure perturbation. The first, second, and third terms on the right hand side are the buoyant production (TKE_{bp}), shear production (TKE_{sp}), and turbulent transport terms (TKE_{tr}), respectively. While surface temperature measurements are available in this study, air temperatures are required to compute TKE_{bp} and, therefore, the TKE_{bp} term will be analyzed in a future study. In this section, we shall be exploring TKE_{sp} and TKE_{tr} for their role in the fire spread. The time-varying signals for each term will be compared at the two selected neighboring fixed points (FP1 and FP2) to get a deeper sense of the contribution of each term to the fire evolution. All partial derivatives referred to in this section are discretized using the procedure described in the Supplementary Information.

Figure 2.12(a) shows 1-minute moving averages of the TKE ($\overline{K}$) and the mean kinetic energy (MKE, given by $(\overline{u}^2 + \overline{v}^2 + \overline{w}^2)/2$) computed at FP1, while TKE_{sp} and TKE_{tr} are shown in Figs. 2.12(c) and 2.12(e), respectively. As is known from the literature (82), TKE and MKE interact via the shear production term: $TKE_{\mathrm{sp}} < 0$ indicates a withdrawal of energy from the TKE and its addition to the MKE, while $TKE_{\mathrm{sp}} > 0$ indicates the contrary. It can be seen that the decrease in TKE_{sp} when $140\,\mathrm{s} \leq t \leq 220\,\mathrm{s}$ (Fig. 2.12(c)) causes a loss in the TKE and a corresponding gain in the MKE (Fig. 2.12(a)). Since the mean flow at FP1 opposes the spread of the fire away from the IP in this time duration, the shear production term effectually helps resist the fire-spread at this point. At FP2, $TKE_{\mathrm{sp}} \approx 0$

when $140\,\mathrm{s} \leq t \leq 220\,\mathrm{s}$ (Fig. 2.12(d)) indicating that the MKE does not increase much at the cost of the TKE. Therefore, the peak of the MKE (Fig. 2.12(b)) is much lower than that for FP1 (Fig. 2.12(a)). Relatively speaking, the shear production term does not contribute much in either assisting or resisting the fire spread at this point.

Now, let us examine the turbulent transport term (TKE_{tr}). For a closer examination, we divide it into its horizontal and vertical components:

$$TKE_{\mathrm{tr_H}} = -\frac{\partial \overline{u'K}}{\partial x} - \frac{\partial \overline{v'K}}{\partial y}; \qquad TKE_{\mathrm{tr_V}} = -\frac{\partial \overline{w'K}}{\partial z}. \tag{2.9}$$

As seen from Fig. 2.12, increased magnitudes of TKE_{tr} at FP1 (Fig. 2.12(e)) are largely a consequence of increased magnitudes of $TKE_{\mathrm{tr_H}}$, indicating that the contribution to TKE_{tr} from $TKE_{\mathrm{tr_H}}$ is much higher than the contribution of $TKE_{\mathrm{tr_V}}$ (Fig. 2.12(g)). A similar argument can be made for FP2 (Figs. 2.12(f), 2.12(h)). An interesting feature of the flow is observed upon comparing the TKE_{tr} signal at FP1 (Fig. 2.12(e)) with that at FP2 (Fig. 2.12(f)). The decreasing trend (and lower values) in TKE_{tr} for $150\,\mathrm{s} \leq t \leq 200\,\mathrm{s}$ at FP1 concurs with the increasing trend (and higher values) observed at FP2. Conversely, for $235\,\mathrm{s} \leq t \leq 284\,\mathrm{s}$, the increasing trend (and higher values) of TKE_{tr} at FP1 concurs with the decreasing trend (and lower values) at FP2. We have already seen that the horizontal TKE transport terms are the major contributors to TKE_{tr}. This suggests that TKE is exchanged between the two neighboring fixed points via a horizontal redistribution of TKE corresponding to the turbulent transport term.

The turbulent transport terms for two additional pairs of fixed points observed to have formed around $t = 317.7$ s and $t = 350$ s have been plotted in Figs. 2.12(j) and 2.12(l), respectively. The western fixed point recorded at $t = 317.7$ s is denoted by FP3 (white cross in Fig. 2.12(i)), while the eastern fixed point is denoted by FP4 (black cross in Fig. 2.12(i)). Similarly, the western fixed point recorded at $t = 350$ s is denoted by FP5 (white square in

Fig. 2.12(k)), while the eastern fixed point is denoted by FP6 (black square in Fig. 2.12(k)). At FP3 and FP4, trends in TKE_{tr} are similar until $t = 317.7$ s after which increasing trends of TKE_{tr} at FP4 concur with decreasing trends at FP3 (Fig. 2.12(j)). Similarly, increasing trends of TKE_{tr} at FP5 concur with decreasing trends of TKE_{tr} at FP6 as seen from Fig. 2.12(l) after $t = 350$ s suggesting the possibility of TKE exchange between these two fixed points via the turbulent transport terms.

The analysis above has implications for kinematic fire-growth models based on Huygen's principle (31; 33). While such models have provided a useful framework for predicting the shape and location of the fire perimeter at a given time from ignition, not much was known about the interaction of fires along the fire-front. The analysis above suggests that adjacent local fires can interact via the turbulent transport terms. Moreover, the horizontal turbulent flux at each point on the fire perimeter plays a significant role in the fire spread at a given time during its evolution, as seen above.

2.4 Summary and Future Work

In this chapter, we have analyzed quasi-two-dimensional PIV data sampled at a high frequency (30 Hz) during a laboratory-scale burn experiment in a relatively small domain (2.34 m $\times$ 2.34 m) under calm ambient wind conditions (and the lack of a preferential wind-forcing direction). The turbulent Reynolds number is reported to be approximately 2454. Observations from this study are illustrated briefly in Fig. 2.13. Horizontal velocity vectors and thermal data captured by the cameras show that the fire (or more appropriately, the hot flame) draws cool air from the surrounding region (entrainment). This local wind exerts a dynamic pressure upon the fire-front, thereby offering resistance to the fire spread. Moreover, streamlines penetrating the fire-front get curved away from the fire-core, meet near the inner edge of the fire-front, and appear to shield the fire perimeter from the innermost

core of the fire. Again, the streamlines do not carry signatures of wind-driven fire spread. Rather, the fire seems to be propelled by the radially outward velocity induced close to the surface of the fuel bed by the vortices of neighboring vortex tubes. These vortex tubes, which originate on the outside of the fire and spiral inward, get stretched thinner at the location of the fire-front before dispersing again at the fire core. Correspondingly, the horizontal vorticity magnitude increases strongly at the fire perimeter, and then reduces near the fire core where the vorticity eventually dissipates. Moreover, circulation structures obtained from the horizontal vorticity vectors confirm the presence of counter-rotating vortex pairs on opposite sides reported elsewhere as a key mechanism for fire spread (58). While Finney et al.(58) observed these vortex pairs from images of laboratory fires, the present experiment enables us to quantify these vortices for the first time, which is a significant contribution of this study.

Additionally, vortices that comprise the vortex tubes, precess alternately toward and away from the surface of the fuel bed, causing the vortex tubes to be kinked. The strong updraft observed at the location of the fire-front would advect the kinked vortex tubes vertically upward. In the presence of the active vertical vorticity component observed here or in the event of tilting of the vortex tubes, this can result in a fire whirl (albeit weaker than whirls observed in large-scale fires). Moreover, the presence of vorticity and radial entrainment are known to provide conditions that are conducive to the formation of fire whirls (23).

The integral length scale obtained from the spectral analysis suggests that the most energetic eddies have wavelengths of approximately a fifth of the domain length ($O(10^{-1})\,\mathrm{m}$) when measured along the x direction. In addition, increase in the magnitude of turbulent fluxes of horizontal momentum signal the presence of either fire bursts that assist the fire spread or fire-spread-impeding horizontal eddies. The overall consequence of the processes at play (including radiative heat transfer) is that the fire spread is relatively gradual, with a RoS of approximately 0.2 - $0.3\,\mathrm{m/min}$. Time-dependent RoS values have also been obtained, which

can be used as geometric parameters in well-documented kinematic models such as the first-order growth models of Richards (31; 32; 33).

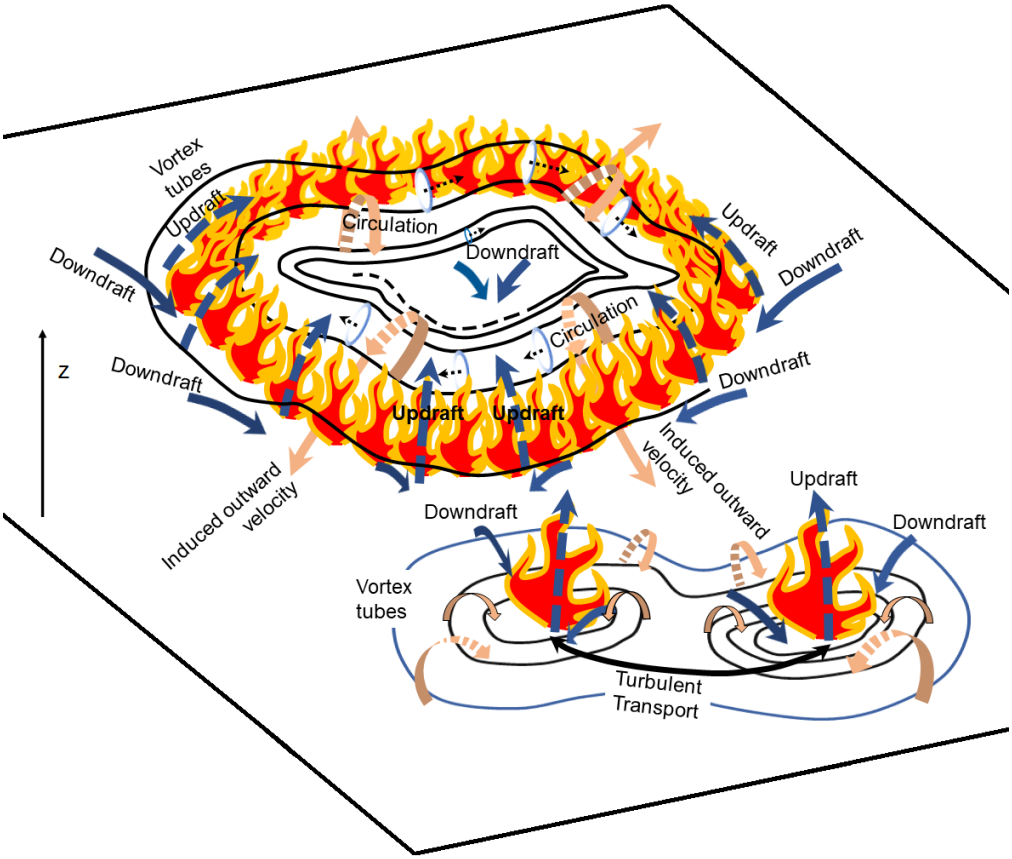


Figure 2.13: A brief illustration of the (pre- and post- fixed point formation) flow dynamics in the presence of the flame. Figure is not to scale. [Created in MS PowerPoint 365]

The structure of the fire also alters in response to its increasing perimeter and the local wind conditions. Cross-correlation contours of the vertical velocity clearly show the elliptical shape of the fire perimeter in the early stages of fire-growth along with its re-orientation in response to change in the local wind conditions or fuel-bed heterogeneity. As the fire progresses, the unstable fire-front disintegrates into smaller pockets of fire. The horizontal flow around these pockets is similar to the behavior of a chaotic system in the vicinity of an attractor. In such a case, the envelope of these fire pockets constitutes the fire-front. The envelope of fire-fronts expands as the pockets relocate further away from the IP. This behaviour suggests that the wave propagation model of Richards (31) (based on Huygen's

principle) is a reasonable model for fire growth. However, such kinematic models are unable to predict the response of the fire-front to instabilities, which can be clearly observed from the data analyzed in this study.

While Huygen's principle of wave propagation has been the basis of several fire-growth models, not much is known about how the local ellipses are affected by local changes in the flow. The advantage of decomposing the flow into its mean and turbulent components is that the contribution of the turbulent fluctuations in assisting or resisting fire-growth via bursts or fire-spread-impeding eddies, respectively, can be analyzed. Moreover, not much has been documented about the mechanism of energy exchange between neighboring (local) ellipses. This study presents the turbulent transport term of the TKE budget equation as a possible source of energy exchange between such ellipses. Historically, it is known that nearby fires are attracted to each other. As seen from the horizontal velocity contours, neighboring fire pockets in this study are also found to coalesce along the fire-front. The interaction between two nearby fires via the turbulent transport term provides a possible explanation for this.

At this point, we would like to address some of the limitations associated with this work. Although the wind data from a local weather station (Whitehall Forest) suggests calm ambient wind conditions, the absence of real-time ambient wind measurements makes it difficult to track the exact wind shifts that could explain the north-eastern predilection of the fire at later times during the experiment (as observed in Figs. 2.2(d)-(f)). Typically, the high variability in the local wind conditions during a burn experiment conducted in the open and the sensitivity of the fire-induced turbulence to these conditions makes it difficult to reproduce the results of such experiments exactly (65). Furthermore, considering that the pine litter used in this experiment was hand drawn, we also expect some heterogeneity in the fuel distribution, which could explain the north-eastern predilection of the fire. In addition, the vertical component of velocity is obtained by using zero divergence in the velocity field and is available only at one height above the surface of the fuel bed. The absence of vertical

resolution for this data, i.e. the (quasi-) two-dimensional nature of the measurements makes it difficult to establish the presence of fire whirls more concretely.

Despite its limitations, this experiment was unique in its ability to collect high frequency PIV data during a burn experiment, notwithstanding the challenges associated with measuring the velocity field in the presence of a flame (65). The ability to resolve both in time (with a high frequency) and in space has allowed us to quantify some of the canonical features reported previously by different studies of fire behavior in small-scale surface fires (such as the influx of ambient air into the fire core (66; 65) , the acceleration of the wind across the fire-front (66; 65), and the presence of counter-rotating eddies (58)) and find additional fire behavior trends that have not been reported elsewhere. Therefore, from this perspective, we have been able to "reproduce" some of the canonical features reported in previous studies, while also contributing additional insights. Moreover, this study is able to provide insights into fire behavior while circumventing the issues associated with damage to equipment or personnel life during large-scale field experiments or prescribed burns.

We have seen that upon the onset of instability, the fire disintegrates into smaller pockets concentrated around fixed points. In a subsequent study, a nonlinear bifurcation analysis shall be conducted to investigate the stability behaviour of a grassland fire where the fixed points can be treated as chaotic attractors. After remaining relatively static for a certain amount of time, the fixed points relocate further away from the ignition point as discussed above. In time, neighboring fixed points coalesce leading to larger pockets of fire concentrated at a locus of fixed points. These can be treated as different modes of post-instability behaviour. The results of this analytical work can be compared with the fire behaviour documented above. Furthermore, owing to the need for repeatability, the authors are planning on conducting a similar laboratory-scale burn experiment in the open, in the near future. Moreover, a laboratory-scale burn experiment with three-dimensional data collection would facilitate further analysis of potential fire whirls and is currently anticipated. Since fire-

fighters train to track fire behavior from one moment to the next, we hope that this work will assist them in accomplishing the same via a broader understanding of fire dynamics.

Chapter 3

Features of turbulence during wildland fires in forested and grassland environments

3.1 Background

Fire-induced turbulence has a considerable impact on scalar dispersion and momentum transport both during and after the passage of the fire-front across the fuel in wildland fire environments. The dispersion of scalars such as smoke in turn affects visibility and human health, especially for residents in the wildland-urban interface, while the transport of firebrands (embers) poses a severe risk of spotting up to several kilometers away from the fire-front (83). Moreover, fire behavior is closely linked with the ambient turbulence (canopy turbulence in the forested environments). Depending on the environment, turbulence in the canopy or the atmospheric boundary layer demonstrably affects fire spread rates (84; 85), occasionally in unexpected ways. With a deep necessity to understand fire-induced turbulence both in

grassland and forested environments, fire simulations (45; 44; 42; 86) as well as *in-situ* measurements from burns on small as well as management scales (87; 88; 89; 90; 81; 5; 91) have gained importance. However, the excessive computational overhead involved in simulating fires in forested and grassland environments (49; 50) make them less amenable for extended use. While a fast-running simulation platform like QUIC-fire (52) is able to circumvent this issue, its wind solver (QUIC-URB) outputs the time-averaged flow field, which makes it difficult to analyze the turbulence-driving fire behavior. Given these constraints on computational models, careful examination of observed data from burn experiments can be useful in investigating the coherent motions that characterize fire-induced turbulence. Such examination can potentially also allow for the simplification of the governing equations describing fire behavior based on the relative importance of the different terms involved. In the past, empirically derived models (35; 36; 37) based on the widely used model by Rothermel (34) have been successful in simplifying the complex set of governing (thermal, chemistry, fluid flow) equations for successful operational use via the parameterization of several physical quantities. However, these models are based on laboratory experiments so that their application on management scales is limited. Another limitation is their inability to provide insights into the complex turbulent environment arising from fire-atmosphere interaction.

Despite their usefulness in understanding the physics underlying fire-induced turbulence, studies relying on experimental data have only recently gathered momentum because of the high risk of damage posed to equipment during data collection in the presence of a flame (2). Here, we review the key findings of some of the few leading empirical studies that attempted to untangle the complex dynamics underlying fire-atmosphere interaction. Recent studies by Heilman et al. (90; 4) explored turbulent kinetic energy (TKE) levels at different heights of a 20-m measurement tower, the energy spectrum of the velocity components, and patterns in the turbulent heat and momentum fluxes for two different backing surface fires in the New Jersey Pinelands National Reserve (forested environment), one of high intensity in 2011 and the other of lower intensity in 2012. For the higher intensity fire, fire-induced TKE

near the canopy top was found to be much more substantial compared to the lower heights, making turbulent diffusion of smoke near the canopy top more important than mixing at lower heights within the canopy. Analysis of 1-minute averaged turbulent momentum fluxes showed that vertical turbulent fluxes contributed 40-80% to the net momentum flux before, during, and after fire-front-passage (FFP) (4). The relative contribution of the vertical turbulent heat and momentum fluxes to the net heat and momentum fluxes was found to be highest at the mid-canopy height when compared to near the surface or the canopy top. Estimates of the turbulence anisotropy obtained by Heilman et al. (81) demonstrated the significance of horizontal velocity perturbations over vertical velocity perturbations pre- and post-FFP as well as during FFP periods at all measurement heights. Analysis of the relative contribution of the terms in the TKE budget equations showed that shear production was higher than the buoyancy production at all measurement heights within the overstory vegetation layer pre- and post-FFP. Furthermore, the turbulent transport term resulted in a loss of TKE at all measurement heights during FFP in 2011, while its effect was found to be greatly diminished in the lower-intensity 2012 burn. In a separate study, Heilman et al. (91) studied the contribution to turbulent fluxes of sweep-ejection events before, during, and after the passage of a heading (wind-driven) surface fire-front through a network of 20-m measurement towers during an operational burn in the New Jersey Pine Barrens (under the U.S. Department of Defense–Strategic Environmental Research Program (SERDP)). It was found that pre-FFP and post-FFP periods were characterized by sweeps and ejections, while FFP periods were characterized by sweeps and outward interactions (convection involving the upward flux of wind with high horizontal momentum). These studies encapsulate some of the most recent turbulence analyses on experimental surface fires in forested regions.

The FireFlux experiment was a pioneering study on fire–atmosphere interactions in a grassland fire and set a benchmark for similar studies in the future (3). It comprised a heading (wind-driven) experimental grassland fire conducted at the Houston Coastal Center in Texas on 23 February, 2006. Temperature and velocity measurements taken during the experiment

by a 43-m instrumented tower were utilized by Clements et al. (3) for a first-order analysis. Derived quantities such as the velocity spectra, turbulent momentum fluxes, and TKE were analyzed to comment on the turbulence levels induced by the fire-front passage. The turbulence intensity generated by the fire was found to be four to five times greater than the ambient atmospheric turbulence. Furthermore, turbulent fluxes demonstrated a downward transfer of high momentum downstream of the fire-front. Heilman et al. (5) took the analysis further with their study of sweep-ejection-like events, which also included results from the three prescribed fires in the New Jersey Pinelands described above. Their focus was on examining how the frequencies of occurrence of sweep-ejection-like events and their contributions to the mean vertical turbulent fluxes of heat and momentum were modulated by the vicinity or presence of the fire. Contrary to conditions in the absence of surface fires, it was found that ejections were completely dominant in their contribution to heat-flux events and outward interaction events substantially overshadowed the contribution of sweeps and ejections to momentum-flux events in both environments. The most frequent events during FFP were heat-flux inward interaction events (flux of warmer air towards the surface) and momentum-flux outward interaction events (explained above) in grassland and forested environments, respectively.

As seen above, previous empirical and semi-empirical studies (92; 81) have taken a keen interest in exploring turbulent fluxes and terms of TKE budget equation pre-, during, and post-FFP for insights into the dominant physical processes characterizing fire-induced turbulence. However, the interpretation of coherent structures inferred from the turbulent fluxes and the TKE budget terms is sensitive to the averaging scheme employed to decompose turbulent signals into the mean and turbulent fluctuations from the mean. Additionally, the effect of the fire on the mean kinetic energy (MKE) budget terms remains to be explored using the existing data. Furthermore, several differences in the fire-turbulence behaviour between surface fires in forested and grassland environments remain to be articulated. For instance, we expect the nature of the turbulent transport term to be different, considering

that it assumes different levels of importance within the canopy and in the open atmospheric boundary layer in no-fire conditions (93). Heilman et al. (4) also reflected on the need to understand differences in the behavior of turbulent fluxes for backing and heading fires across all the measurement heights in the canopy. Evidently, there is a need to unify and synthesize observations from burn experiments that have already been conducted via an inter-comparison to develop an over-arching description of the process involved.

The analyses presented by Clements et al. (2; 3) and Heilman et al. (90; 81; 4; 5; 91) for four experimental management-scale burns (one grassland fire; two understory backing fires; one understory heading fire) conducted in Texas in 2006 (FireFlux), in the New Jersey Pinelands National Reserve in 2011 and 2012, and in the New Jersey Pinelands National Reserve in 2019 (SERDP) are synthesized and re-investigated in this study. Here, we aim to fill the gaps in the previous analyses on these data regarding the coherent motions arising out of fire-atmosphere interaction when juxtaposed with the background canopy (canopy-scale) turbulence or open atmospheric turbulence, depending on the surface-fire environment. High-frequency 10-Hz measurements in the case of the sub-canopy fires and 20-Hz measurements in the case of the grassland fire for velocity and temperature are utilized. We first introduce the data by exploring the slowly-varying parts of the velocity components and temperature for changes occurring in the flow over relatively longer time scales. We then investigate pre-, during, and post- FFP wind-rose statistics for a visual representation of the combined changes induced by the presence of the fire and ambient wind shifts. Finally, we compute the turbulent fluxes and terms of the TKE budget equation; we comment on the effect of the former on the latter and on the physical significance of both. From these quantities, computed at different heights above ground level (AGL), we seek insights into the more persistent coherent structures, the key fire-spread mechanisms, and the dominant turbulence generation and TKE redistribution processes, along with the relevant vertical length scales. Another important and relatively unexplored question of interest is the effect of FFP on the terms of the MKE budget equation, which is investigated here for the sub-canopy surface

fires. We aim to draw a comparison of insights among all the three scenarios considered here: heading surface fire beneath the canopy, backing surface fire beneath the canopy, and heading surface fire in a grassland. We set up the analysis in Section 3.2 and provide a brief background on the data sets in Section 3.3. In Section 3.4.1, we compare results from the sub-canopy fires and in Section 3.4.2, we highlight the attributes that distinguish the grassland fire from the sub-canopy surface fires, thereby synthesizing the key insights from each of the three scenarios considered here. As with most data collected from prescribed burns, the current data were also occasionally influenced by wind variability. We take the opportunity to comment on the effect such variability may have on the fire while simultaneously attempting to summarize the general features that broadly characterize each scenario.

3.2 Theory

All components of the velocity (u_i in the index notation) and the temperature (T) are decomposed into a relatively slowly-varying component and a fluctuating component: $u_i = \overline{u}_i + u_i'$ and $T = \overline{T} + T'$. Here, the overbar represents time averaging and the quantities marked with prime are the fluctuating terms. The overbar is chosen to represent 1-hour moving averages in the case of the sub-canopy surface fires, while it is chosen to represent 1-minute moving averages in the case of the grassland fire. We represent the streamwise (x), cross-stream (y), and vertical (z) components of velocity at height h by u_{h}, v_{h}, and w_{h}, respectively. We define the streamwise direction (x) as the direction in which the fireline propagates in the case of a heading fire and the direction opposite to fireline propagation in the case of a backing fire. Notwithstanding noticeable variability in the streamwise winds (as expected during a management-scale burn), the wind speeds are the highest in the streamwise direction for the most part, especially at the beginning of each experiment. While the direction of the ambient wind may change (relative to the cardinal directions), both the

streamwise and cross-stream directions remain fixed over the course of a burn experiment. Similarly, T_{h} represents the temperature at height h. No penetration and no-slip conditions at the surface imply that $w_0 = u_0 = v_0 = 0$. Also, h_{c} denotes the approximated mean canopy height in the case of the sub-canopy surface fires ($h_c = 20\,\mathrm{m}$).

Next, the TKE budget equation is written as follows (82):

$$\frac{\partial \overline{e}}{\partial t} + \overline{u}_j \frac{\partial \overline{e}}{\partial x_j} = \delta_{i3} \frac{g}{\theta_{\mathrm{v}}} \overline{u_i' \theta_{\mathrm{v}}'} - \overline{u_i' u_j'} \frac{\partial \overline{u}_i}{\partial x_j} - \frac{\partial \overline{u_j' e}}{\partial x_j} - \frac{1}{\rho} \frac{\partial \overline{u_j' p'}}{\partial x_j} - \varepsilon, \tag{3.1}$$

where e is the TKE, θ_{v} is the virtual potential temperature of air (approximated here as the moving mean of the temperature, $\overline{T}$), p' is the pressure perturbation, and ε is the TKE dissipation rate. The first, second, and third terms on the right-hand side are the buoyant production (TKE_{bp}), shear production (TKE_{sp}), and turbulent transport terms (TKE_{tr}), respectively. The fourth term on the right-hand side is the pressure correlation term (not computed in this analysis). Due to the absence of data varying along the streamwise (x) and cross-stream (y) directions for most of the datasets in this study, we cannot compute the following terms: (i) $-\overline{u'w'}\frac{\partial \overline{w}}{\partial x} - \overline{v'w'}\frac{\partial \overline{w}}{\partial y}$ in TKE_{sp} and (ii) $-\frac{\overline{u'e}}{\partial x} - \frac{\overline{v'e}}{\partial y}$ in TKE_{tr}. However, it must be noted that horizontal gradients may be substantial near the fire-fronts. As seen from term (ii), these gradients may drive turbulent transport in the horizontal direction, which can affect fire spread and the interaction between different points along the fire-front (as seen by Desai et al. (87) in small-scale surface fires). These gradients may also capture the effects arising from horizontal heterogeneity in the fuel (and, thereby, in fuel combustion). Given the limitations of the current data, we can only compute the $\partial/\partial z$ terms in TKE_{bp}, TKE_{sp}, and TKE_{tr}.

Since the passage of the fire-front causes a shift in the mean velocity component as well ($\overline{u}_i$), we also study the terms of the MKE budget equation in this work. The MKE budget

equation is written as (82):

$$\frac{\partial(0.5\overline{u}_i^2)}{\partial t} + \overline{u}_j \frac{\partial(0.5\overline{u}_i^2)}{\partial x_j} = -g\overline{w} + \overline{u_i' u_j'} \frac{\partial \overline{u}_i}{\partial x_j} - \frac{\partial(\overline{u_i' u_j'} \overline{u}_i)}{\partial x_j} - \frac{\overline{u}_j}{\overline{\rho}} \frac{\partial \overline{p}}{\partial x_j} + \nu \overline{u}_i \frac{\partial^2 \overline{u}_i}{\partial x_j^2}, \tag{3.2}$$

where the first term on the right-hand side represents the increase in MKE due to gravitational acceleration of vertical motions, the second term represents the interaction between TKE and MKE through shear ($-TKE_{\text{sp}}$) and accounts for the loss of MKE to TKE and vice versa, and the third term represents transport of turbulent fluxes by the mean velocity. It must be noted that the transport term in Eq. (3.2) represents the transport of turbulent fluxes by the mean velocity rather than the transport of MKE by turbulent fluctuations. The fourth and fifth terms on the right-hand side (not computed in this analysis) represent the production of MKE due to the acceleration of the mean flow by pressure gradients and the molecular dissipation of mean motions (82), respectively. Again, due to the absence of streamwise and cross-stream data resolution, we shall only compute the vertical partial derivatives ($\partial/\partial z$) in each of these terms (where applicable).

We take this opportunity to comment on the choice of 1-hour moving averages in the analysis of the sub-canopy surface fires. Moving averages are computed in this work, instead of block averages, in order to preserve the resolution of the data and the smoothness of the signal. The selection of a 1-hour time period for computing the moving averages can be explained as follows. It has been documented in the literature (94) that relatively long time periods (up to an hour) are reasonable in computing eddy fluxes. To quote from Chapter 2 of the Handbook of Micrometeorology (94): "Eddy fluxes need to be formed over a sufficiently long time that any motions that contribute to the transport can be sampled adequately. In practice, this has meant that eddy fluxes have been calculated over time periods up to an hour in duration, sufficient for several of the largest planetary-boundary-layer (PBL) scale to be sampled by the measuring system." While this argument was made in the context of turbulence in the absence of a fire, it provides a reasonable estimate for the choice of the

time period of averaging in the present study. Furthermore, for the backing fires of 2011 and 2012 discussed in this study, it was found that while the time required for the firelines to pass the tower locations was of the order of minutes, the influence of the turbulence induced by the firelines at the towers lasted for approximately an hour (90). One-hour moving averages generate a sufficiently smooth slowly-varying component for the velocity and temperature signals, which can be treated as the larger-scale atmospheric flow upon which the fire-induced fluctuations (u_i', T') "ride". However, it is later seen from the MKE budget terms that the fire noticeably affects the mean flow even if we use a time window as conservative as 1 hour to separate the effects of the fire from the ambient flow. This, incidentally, gives us the advantage of being able to track the "new" mean state during FFP.

Note that, in contrast to the present study, previous studies have computed block averages on the scale of a minute. Furthermore, they computed perturbations during the FFP period based on pre-FFP block means. That approach, in effect, treated all the coherent high- and low-frequency velocity and temperature variations during the FFP period as fire-induced turbulence, thereby presuming no change in the ambient atmospheric conditions during the FFP period. Moreover, the overbar terms can be very sensitive to the averaging scheme and time window. We have, therefore, included some information on the possible differences arising from using different averaging time windows in the form of a sensitivity analysis in the attached Supplementary Information.

The analysis of the grassland fire requires a slightly different approach. Only 1 hour of experimental data are available for the grassland fire. This makes it difficult to compute the slowly-varying parts (1-hour moving means) of the velocity components and temperature as done for the sub-canopy surface fires, which is in turn used to compute the turbulent fluctuations. Another approach to compute the fluctuations would be to remove the 1-hour block mean obtained from the entire time series. However, as seen in Table 3.1, the spread-rate and intensity of the grassland fire is one to two orders of magnitude higher than the spread-

rates and intensities of the sub-canopy surface fires. Moreover, the fire-induced turbulence intensity was found to be four to five times greater than the ambient atmospheric turbulence (3). Removing the 1-hour block mean to obtain the fire-induced turbulent fluctuations would have resulted in their underestimation during FFP. The relatively high intensity and spread-rate of the grassland fire suggests that the time scale of the influence of the fire at the measuring tower is comparatively much shorter (presumably by one to two orders of magnitude), so that fire-induced changes can be considered entirely as turbulence without attributing any change to the mean state of the atmosphere. Therefore, in the analysis of the grassland fire, mean quantities are obtained by taking a block average of the first 40 minutes (pre-ignition time duration) of velocity and temperature data, as opposed to taking a 1-hour block average. Turbulent fluctuations are obtained by subtracting these pre-fire means (denoted by U, V, W, and T_{m} for the streamwise velocity, cross-stream velocity, vertical velocity, and temperature, respectively) from the time series for each corresponding physical quantity discussed here: $u' = u - U$, $v' = v - V$, $w' = w - W$, and $T' = T - T_{\mathrm{m}}$. Note that the absence of 1-hour moving means of the velocity and temperature data in this case hinders us from computing the MKE budget terms for the grassland fire, which could have been useful for comparison with the sub-canopy surface fires. Next, we recast Eq. (3.1) (the TKE budget equation) for the grassland fire as follows:

$$\frac{\partial \overline{e}}{\partial t} + U_j \frac{\partial \overline{e}}{\partial x_j} = \delta_{i3} \frac{g}{T_{\mathrm{m}}} \overline{u_i' T'} - \overline{u_i' u_j'} \frac{\partial U_i}{\partial x_j} - \frac{\partial \overline{u_j' e}}{\partial x_j} - \frac{1}{\rho} \frac{\partial \overline{u_j' p'}}{\partial x_j} - \varepsilon, \tag{3.3}$$

Here, 1-hour moving means of the velocity components and temperature, i.e. $\overline{u}_i$ ($\overline{u}$, $\overline{v}$, $\overline{w}$) and $\overline{T}$, of Eq. (3.1) have been replaced by the pre-fire means, i.e. U_i (U, V, W) and T_{m}, in Eq. (3.3). Furthermore, the overbar in Eq. (3.3) represents 1-minute moving means. Moving means are computed as opposed to block averages to smoothen the time series associated

with each term in order to facilitate drawing inferences on coherent structures. Moreover, for the high-spread-rate, high-intensity grassland fire (one to two orders of magnitude higher than those for the sub-canopy surface fires as seen from Table 3.1) a sufficiently short time scale must be defined for the averaging process to isolate the influence of the fire at the measuring tower. Since the time duration pre-, during, and post-FFP is 2 minutes each, a time scale longer than say, 4 minutes, would obfuscate the details of the turbulence pre-, during, and post-FFP upon averaging. The averaging time scale is chosen to be 1 minute in order to be consistent with an earlier publication by Clements et al. (3).

3.3 Data Overview

As mentioned above, tower-based data from four experimental fires are used in this study. We refer to the 2011 and 2012 backing surface fires beneath the canopy in the New Jersey Pinelands National Reserve (NJPNR) as NJ2011 and NJ2012, the 2019 heading surface fire beneath the canopy in the NJPNR as NJ2019, and the heading surface fire from the FireFlux experiment in the grasslands of Texas (Houston Coastal Center) as TX2006. The 2019 burn unit is located at the Silas Little Experimental Forest within NJPNR, New Lisbon, New Jersey. For the sub-canopy burns, averaged half-hourly ambient wind velocity data in the streamwise and cross-stream directions are taken from nearby AmeriFlux towers: the Cedar Bridge Tower for NJ2011 and the Silas Little Experimental Forest Tower for NJ2012 and NJ2019. These data are provided by Clark (95; 96) and Heilman et al.(91); they are shown in Fig. 3.1 for reference and comparison with the 1-hour moving means of the measured horizontal velocity components.

For NJ2011, NJ2012, and TX2006, experimental burn data obtained from a single meteorological tower are studied in each case. For NJ2019, data obtained from two meteorological towers, i.e. the West Tower and a Control Tower, are studied for the entirety of this chapter.

The Control Tower is located outside the burn unit, 185 m away from its northern edge (91). This can also be seen in Figure 1 of ref. (91), which describes the burn unit and the location of the measurement towers. Measurement heights for each burn are shown in Table 3.1. It must be noted that the fuel consumption during the forest (sub-canopy) burns differed from each other. While NJ2011 occurred in a pine-dominated region, NJ2012 and NJ2019 occurred in an oak-dominated region. Although fuel loading of the forest floor was similar in both cases, consumption was relatively low in the oak-dominated burns. This is typical of hardwood-dominated forests: fuel consumption is usually less than that in forests with more pine trees and saplings.

For a complete description of the burn experiments, including but not limited to detailed illustrations of the burn plots, their ignition lines, and the respective directions of fireline propagation relative to the ambient winds, we refer the reader to the works of Clements et al. (2; 3), and Heilman et al. (90; 81; 4; 5; 91). Most of the important features of these four sets of data are summarized in Table 3.1. Note that although the pre-, during, and post-FFP periods indicated in Table 3.1 bear some similarity to the corresponding periods defined in the works mentioned above, they are not exactly the same.

3.4 Results

3.4.1 Surface fires under a tall vegetation canopy

Mean Velocity and Temperature

We first focus on the mean velocity components of the backing surface fires, NJ2011 and NJ2012 (Figs. 3.1(a)-(b)). In both years, $\overline{u}_{20}$ follows similar patterns as the ambient streamwise wind velocity (Figs. 3.1(a)(i) and 3.1(b)(i)). In 2011, it is seen that $\overline{u}_{10}$ and $\overline{u}_{3}$ are of

Table 3.1: Summary features for the prescribed sub-canopy backing fire experiments (NJ2011, NJ2012), prescribed sub-canopy heading fire experiment (NJ2019), and the prescribed heading grassland fire or FireFlux experiment (TX2006) analyzed in this study (2; 3; 4; 5).

Feature	**NJ2011**	**NJ2012**	**NJ2019**	**TX2006** (FireFlux)
Date	20 March 2011	6 March 2012	13 March 2019	23 February 2006
Location	New Jersey Pinelands	New Jersey Pinelands	New Jersey Pinelands	Houston Coastal Center
Plot Size	107 ha	97 ha	11 ha	40 ha
Overstory Vegetation	Pitch Pine, Mixed Oak	Pitch/Shortleaf Pine, Mixed Oak	Mixed Oak, Pitch/ Shortleaf Pine	-
Measurement Heights (AGL)	3 m, 10 m, 20 m	3 m, 10 m, 20 m	3 m, 10 m, 20 m	2 m, 10 m, 28 m, 42 m
Overstory Vegetation Height	18-23 m	18-23 m	$\approx$ 19 m	-
Understory/ Grass Vegetation	Blueberry, Huckleberry, Scrub Oak	Blueberry, Huckleberry, Scrub Oak	Blueberry, Huckleberry, Bear, Blackjack, Oak sedges, Mosses	Tall-grass prairies: Big and Little Bluestem, Long Spike Tridens
Understory/ Grass Vegetation Height	1.0 m	0.7 m	1.5 m	1.5 m
Surface Fuel Loading	1.485 kg m^{-2}	1.104 kg m^{-2}	1.347 kg m^{-2}	1.08kgm^{-2}
Ambient Wind Direction	NE-SE (45-135°)	SW-NW (225-315°)	SW (228°)	NE (45°)
Fire Intensity	325 kWm^{-1}	52 kWm^{-1}	179 kW/m	3200 kWm^{-1}
spread-rate	1.50 m min^{-1}	0.33 m min^{-1}	1.7 m min^{-1}	40.8 m min^{-1}
Flame Length	1.0 m	0.5 m	<2 m	5.1 m (2 m near tower base)
Fuel Consumption	696 gm^{-2}	507 gm^{-2}	337.7 gm^{-2}	972 gm^{-2}
Time of ignition	08:55 EST (09:55 EDT)	09:30 EST	14:45 LT	12:43 LT
Stipulated pre-FFP time	13:35-14:05 EST (14:35-15:05 EDT)	14:52-15:22 EST	14:50-15:20 LT	12:44:00-12:46:00 LT
Fire-front-passage (FFP) time	14:05-14:35 EST (15:05-15:35 EDT)	15:22-15:52 EST	15:20-15:50 LT	12:46:00-12:48:00 LT
Stipulated post-FFP time	14:35-15:05 EST (15:35-16:05 EDT)	15:52-16:22 EST	15:50-16:20 LT	12:48:00-12:50:00 LT

similar magnitude during the daytime before FFP (Fig. 3.1(a)(ii)), since the canopy elements provide a momentum sink to the ambient wind. The average plant area density in the lower

half of the canopy was much higher for the 2011 burn plot as compared to the 2012 burn plot (81), making this effect stronger in 2011. Moreover, the mean streamwise shear ($\partial\overline{u}/\partial z$) is the highest at $h = 20\,\mathrm{m}$ where $\overline{u}$ is the highest among the three heights. The high mean streamwise shear and the inflection point near the canopy top should lead to the formation of canopy-scale eddies at $h = 20\,\mathrm{m}$, the most dominant of which are known to be sweep-like momentum-flux events (93). This is also true for NJ2012. The intermittent increase in $\overline{u}_{20}$ is attributed to intermittent gusts for both years; however, the magnitude of $\overline{u}_{20}$ throughout the day is higher in 2012 than in 2011, which is conducive to the higher spread-rate observed for NJ2011. Next, note the pronounced increase in the mean cross-stream wind speed at all heights during and after FFP (1405 EST onwards) in 2011. This increase is most pronounced at $h = 20\,\mathrm{m}$ (in $\overline{v}_{20}$), where cross-stream wind speeds exceed $2.5\,\mathrm{ms^{-1}}$. According to Heilman et al. (90), ambient winds (with magnitudes less than $2.5\,\mathrm{ms^{-1}}$ during the experiment) varied between northeasterly and southeasterly (while the cross-stream direction is N-S), suggesting higher energy in the streamwise (westward) direction. Moreover, the ambient cross-stream wind velocity (Fig. 3.1(a)(i)) shows a decreasing trend pre-, during and post-FFP at the measurement tower. This suggests that the increase in $\overline{v}_{20}$ is affiliated with the fire, as opposed to ambient wind conditions. Additionally, it is worth mentioning that there was some pine crown torching scattered throughout the stand during the NJ2011 burn, which was evident from a post-burn visual inspection. In particular, there was an area dominated by pitch pine within 15-20 m of the measurement tower that crowned in addition to surface combustion. This would have induced strong horizontal velocity gradients, contributing to the observed increase in $\overline{v}_{20}$ during and after FFP in 2011.

In 2012, $\overline{u}_{20}$ demonstrates the presence of intermittent gusts (as mentioned above) from the late morning through early evening. Intermittent gusts are also observed in $\overline{v}_{20}$ during the early and late evening (after 1400 LT). We shall allude to this again in Section 3.4.1. Unlike in NJ2011, the mean cross-stream wind velocity ($\overline{v}$) does not exhibit a very obvious response to the fire-presence (1522 EST onwards). Rather, $\overline{v}_{20}$ follows the ambient cross-stream wind

velocity pattern as seen in Fig. 3.1(b)(i). This is due to the lower intensity of NJ2012 compared to the NJ2011 and lack of crown torching in the former. Other observations regarding the mean streamwise and cross-stream wind for both backing fires have already been documented in previous works (90; 81; 4).

In both years, the mean vertical velocity ($\overline{w}$) during the daytime before FFP is an order of magnitude lower than the magnitudes of $\overline{u}$ and $\overline{v}$ (Figs. 3.1(a)(iv) and 3.1(b)(iv)); this is expected because of no subsidence (or no penetration at the surface). However, for the more intense NJ2011, $\overline{w}_{20}$ shows a marked increase during FFP, followed by a marked decrease to the negative side after FFP. The mean vertical wind is also seen to sink at $h = 3\,\mathrm{m}$ and $10\,\mathrm{m}$ after FFP. This is indicative of the strong effects of fire-induced buoyancy causing an outflux of hot air into the atmosphere aloft, followed by a compensatory influx of air from above the canopy that gathers sufficiently high momentum under gravitational acceleration for the mean vertical wind to sweep through the upper canopy (from $h = 10\,\mathrm{m}$ to $20\,\mathrm{m}$) before slowing down near the surface ($h = 3\,\mathrm{m}$). An influx of ambient air is also seen near the canopy top ($\overline{w} < 0$) during and post-FFP in 2012 without being preceded by a strong outflux, due to the lower intensity of NJ2012.

We now present our observations on the sub-canopy heading fire, i.e. NJ2019 (Figs. 3.1(c)-(d)). Peaks are observed in $\overline{u}$ at the West Tower (Fig. 3.1(c)(ii)), at all heights during FFP (between 1520 and 1550 LT). A similar peak is observed for $\overline{u}_{20}$ at the Control Tower (Fig. 3.1(d)(ii)) around that time. However, the peak in $\overline{u}_{20}$ is higher at the West tower, indicating that some increase is attributed to FFP. This is followed by a decreasing trend in $\overline{u}_{20}$ during FFP as the mean streamwise wind interacts with the ambient westward-moving sea breeze from the Atlantic coast (as noted by Heilman et al. (91)), which has a component in the negative streamwise direction. This decrease in $\overline{u}_{20}$ is also observed at the Control tower during that time (after 1520). After 1600 LT, the ambient winds undergo a southerly shift (Figs. 3.1(c)(i) and 3.1(d)(i)). Following this shift, $\overline{u}_{20}$ becomes very low in magnitude

at both the West and Control Towers, and increased magnitudes of the mean cross-stream wind velocity ($\overline{v}$) are seen at all heights, at both towers, after 1600 LT, i.e. sometime after FFP at the West Tower.

Again, the mean vertical velocity at both, the Control and West towers is an order of magnitude lower than the horizontal components (Figs. 3.1(c)(iv) and 3.1(d)(iv)); however, an increase in magnitude is seen for $\overline{w}_3$ at the West tower both during FFP (downward between 1520 and 1550 LT) and after FFP (upward after 1600 LT). Since the magnitudes of $\overline{w}_{10}$ and $\overline{w}_{20}$ are relatively low during those times, we expect this to represent a redistribution of mean kinetic energy within the canopy itself. The air seems to accelerate under gravity as it sinks to $h = 3\,\mathrm{m}$ during FFP (1520 to 1550 LT). This is followed by strong updrafts, as seen from the larger magnitude of $\overline{w}_3$, due to buoyancy from residual fuel combustion after FFP (after 1600 LT and onward). Contrarily, the mean vertical wind accelerates downward under gravity at the Control Tower after 1600 LT, following an influx of ambient wind from the atmosphere aloft. We will revisit the mean vertical velocity when we discuss the MKE budget terms in Section 3.4.1.

Wind-Rose Statistics

While the 1-hour moving means explored in the previous section are useful in studying the evolution of the slowly-varying mean, a first-order statistical analysis of the horizontal velocity components is required for insights into the frequency and direction of the strongest turbulent fluctuations a few minutes before, during, and after FFP. This is achieved with the help of a 2D histogram plotted on a wind compass, plotted using *WindRose* in MATLAB (97). This function groups velocity data from a time series into classes based on their magnitude, while preserving their direction relative to the positive streamwise direction. Note that zero degrees (along $\hat{\mathbf{i}}$) represents the positive streamwise direction on the wind rose in each scenario.

Interesting observations can be made from the wind-rose statistics for the backing surface fires. As seen from Figs. 3.2(a)-(b), a shift is seen at $h = 20\,\text{m}$ in 2011 from high streamwise variability pre-FFP (1335 to 1405 LT) to high cross-stream variability during FFP (1405 to 1435 LT) and post FFP (1435 to 1505 LT). This corroborates well with the increase in the magnitude of $\overline{v}_{20}$ as seen in Fig. 3.1(a)(iii). In fact, the cross-stream winds show considerable variability in the range of 6 to $12\,\text{ms}^{-1}$ during FFP as opposed to post-FFP (Fig. 3.2(a)(ii)-(iii)) suggesting that this effect is due to the presence of the flame. Comparison with the ambient cross-stream wind velocity (Fig. 3.1(a)(i)), which shows a decreasing trend during and after FFP at the measurement tower, also emphasizes that the increased cross-stream variability is attributed to fire-induced entrainment. We can also attribute this to the diversion of momentum into the cross-stream direction as the streamwise wind (from the side of the unburnt fuel) competes with the air entrained by the fire from the burnt region. Additionally, crown torching in the stand, especially within 15-20 m of the measurement tower, would have also induced strong horizontal velocity gradients near the canopy top, leading to fire-induced entrainment in the cross-stream direction near $h = 20\,\text{m}$. Note that the shift in the cross-stream direction happens late at $h = 3\,\text{m}$ (post-FFP) since it takes a while for the cross-stream wind near the canopy top to force the wind near the ground surface.

At both $h = 3\,\text{m}$ and $20\,\text{m}$ in 2012, we see a noticeable shift from high variability in the cross-stream direction pre-FFP (1452 to 1522 LT) to high variability mostly in the streamwise direction during FFP (1522 to 1552 LT) and post FFP (1552 to 1622 LT). This is attributed to the high ambient mean streamwise wind velocity as observed in Section 3.4.1. Furthermore, the relatively lower fire intensity in 2012 does not cause noticeable entrainment in the cross-stream direction during (and post-) FFP. Contrast this with the FFP period in 2011 (Figs. 3.2(a)(ii) and 3.2(b)(ii)) during which the cross-stream winds attain speeds in the range of 6 to $12\,\text{ms}^{-1}$.

We now focus on the wind-rose statistics for the heading fire, i.e. NJ2019. At the West

Tower, the pre-FFP, FFP, and post-FFP times are 1450 to 1520 LT, 1520 to 1550 LT, and 1550 to 1620 LT, respectively (Table 3.1). An increase in streamwise variability is seen at the expense of cross-stream variability at $h = 20\,\mathrm{m}$ from pre-FFP to FFP times (Fig. 3.3(a)) possibly because of entrainment of air from the upwind side of the fire at the West Tower. The considerable variability in the cross-stream direction post-FFP is, again, attributed to the ambient wind, which undergoes a southerly shift from the FFP time to post-FFP time and has a strong cross-stream component. However, we expect the strong ambient cross-steam wind to also divert some of the streamwise eddies and momentum into the cross-stream direction. This would mean that while the cross-stream gust adds its own momentum to the canopy from aloft, it also potentially diverts some of the fire-induced turbulence near the canopy top into the cross-stream direction. Moreover, the wind statistics near the surface ($h = 3\,\mathrm{m}$ in Fig. 3.3(b)) seems to mimic that of the higher height ($h = 20\,\mathrm{m}$) suggesting a strong forcing by the ambient post-FFP cross-stream wind.

We now compare this with the wind-rose statistics at the Control Tower (Figs. 3.3(c)-(d)) obtained for the pre-, during, and post-FFP times at the West Tower. In the absence of the fire, the wind rose at $h = 20\,\mathrm{m}$ captures only the effects of the westward-moving sea breeze and southerly shift in the ambient wind, as evident from the increasing variability in the cross-stream wind, from pre-FFP time to post-FFP time at the West Tower (Figs. 3.3(c)(ii)-(iii)). It is important to distinguish the Control Tower wind-rose statistics at $h = 3\,\mathrm{m}$ (Fig. 3.3(d)) as more disorganized from the wind-rose statistics at the West Tower for $h = 3\,\mathrm{m}$ (Fig. 3.3(b)), especially in the post-FFP period. It seems that the presence of the flame (as it passes by and departs) at the West Tower organizes the turbulence better near the surface. For this reason, we see the wind behavior for $h = 3\,\mathrm{m}$ at the West Tower mimicking that for $h = 20\,\mathrm{m}$ at the West Tower post-FFP; however, at the Control Tower, the wind behavior at $h = 3\,\mathrm{m}$ during this time is much more diffused compared to that at $h = 20\,\mathrm{m}$ despite the strong ambient cross-stream forcing near the canopy top. Furthermore, the flame accelerates the flow near the surface as depicted by the increased streamwise wind variability in the 1.5

to $3\,\mathrm{ms}^{-1}$ range at $h = 3\,\mathrm{m}$, at the West Tower (Fig. 3.3(b)). Contrarily, the strongest wind speeds near the surface, i.e. at $h = 3\,\mathrm{m}$, at the Control Tower seldom exceed $1.5\,\mathrm{ms}^{-1}$ (Fig. 3.3(d)).

Turbulent and Mean Kinetic Energy Budget Terms

TKE Budget Equation Terms: Figure 3.4 summarizes the TKE budget terms for the sub-canopy surface fires along with the turbulent fluxes ($\overline{u'w'}$ and $\overline{v'w'}$, where u' and v' represent streamwise and cross-stream velocity perturbations, respectively). With reference to Figs. 3.4(a)-(b), we draw inferences for the backing fires first. We focus first on the higher-intensity fire, i.e. NJ2011 (Fig. 3.4(a)). At $h = 20\,\mathrm{m}$, TKE_{bp} is higher than TKE_{sp} during FFP (1405 to 1435 EST), while both attain similar magnitudes and post-FFP (1435 to 1505 EST). While the effects of fire-induced buoyancy are relatively short-lived, shear production persists for a few hours after FFP. The higher-intensity fire accounts for increased buoyancy along with an increase in shear production (from pre-FFP patterns) high above the surface, i.e. near the canopy top, during FFP. Note that TKE_{sp} at $h = 20\,\mathrm{m}$ largely follows the pattern displayed by $\overline{v'w'}$ (Fig. 3.4(a)(ii)) at that height during FFP (1405 to 1435 EST)) and after FFP (1435 EST onwards), leading us to believe that it is this component of the turbulent flux that does most of the work against the mean cross-stream wind shear ($\partial\overline{v}/\partial z$), thereby contributing the most to shear production near the canopy top. This is important in the context of the increase in mean cross-stream wind speeds at $h = 20\,\mathrm{m}$ (magnitude of $\overline{v}_{20}$) after FFP as observed in Section 3.4.1. Again, crown torching near the tower may also have some contribution in the increased magnitude of $-\overline{v'w'}$, and hence, in the increase of TKE_{sp}. Streamwise momentum eddies ($\overline{u'w'}$) also play a part in modifying the fire spread. Since it is a backing fire, fluctuations given by $u' > 0$ impede the fire spread. At $h = 20\,\mathrm{m}$, sweep-like patterns, composed of perturbations given by $w' < 0$ and $u' > 0$ (contributing to $\overline{u'w'} < 0$) lead to an import of streamwise fluctuations that impede the fire spread ($u' > 0$)

into the canopy towards the lower heights. Moreover, eddies associated with $\overline{u'w'} < 0$ also act as a momentum sink for ambient wind near the canopy top. Therefore, the streamwise turbulent eddies of the canopy scale (i.e. near the canopy top) work to extract kinetic energy from the mean streamwise wind above the canopy, while also resisting the spread of the fire against the mean streamwise wind within the canopy. It must be noted here that while we may have discussed the roles of the streamwise and cross-stream momentum eddies separately, they are coupled to each other through the shear production term: the work done by one set of momentum eddies increases turbulence through shear production, which may energize another set of momentum eddies; therefore, both have an influence on each other, albeit indirectly. At $h = 10\,\mathrm{m}$ (Fig. 3.4(a)(iv)), TKE_{bp} is the most dominant, while TKE_{sp} is minimal during FFP. This suggests that the mid-canopy region (in this case, the 10 m height) is a "conduit" for the vertical motion of energy during FFP, experiencing minimum fire-induced shear. At $h = 3\,\mathrm{m}$, both TKE_{bp} and TKE_{sp} increase during FFP, while shear production persists for a few hours after FFP (similar patterns to those observed at $h = 20\,\mathrm{m}$).

Patterns observed for the lower-intensity 2012 fire are remarkably different. At all heights, buoyancy production increases in the afternoon (pre-FFP) due to incoming solar radiation. At $h = 20\,\mathrm{m}$, there is a further but only slight increase in TKE_{bp} during FFP (1522 to 1552 EST), while TKE_{sp} does not change much from the (atmospheric) daytime pattern in the canopy. This is because the effect of the lower-intensity fire is minimally experienced near the canopy top. Instead, we observe a pattern in TKE_{sp} attributed to the intermittent ambient gusts near the canopy top, as evidenced by the fact that TKE_{sp} is patterned on $\overline{u'w'}$ at $h = 20\,\mathrm{m}$, and the well-documented knowledge that turbulence is imported via sweeps from above the canopy, which are energized by ambient gusts (93). There is a noticeable increase in TKE_{bp} at both $h = 3\,\mathrm{m}$ and 10 m during FFP (1522 to 1552 EST). However, not much fire response is seen in TKE_{sp} possibly since the understory/surface vegetation provides a momentum sink to the horizontal turbulent motion induced by the lower-intensity

fire. Again, the mid-canopy region (10-m height, in this case) acts like a "conduit" for the motion of energy in the vertical direction.

We make the following observations for TKE_{tr} in 2011. With increase in w' as the fire-front approaches, which results from increased buoyancy, there is an increased loss of TKE to the above-canopy flow field via the vertical turbulent transport term. Energy loss due to this term is highest at the 20-m height, possibly due to its proximity to the above-canopy atmosphere, followed by a slightly lesser loss at the 10-m height, and finally, the least loss at the 3-m height (Fig. 3.4(a)). This is followed by a gain in energy at all three heights via the transport term, possibly by a reversal process after FFP. Again, the energy gained thus is highest at the 20-m height, lesser at the 10-m height, and least at the 3-m height. In contrast, in 2012, no loss to the above-canopy region is observed, since the fire intensity is lower and the increase in buoyancy (or in w') is not as pronounced as in NJ2011. There is a gain in TKE_{tr} pre-FFP, but a loss does not follow it, suggesting a vertical flux of TKE that stays within the canopy. The difference in the behavior of the vertical turbulent transport term between NJ2011 and NJ2012 is attributed to the higher intensity of the NJ2011 fire.

We now focus on the TKE budget for the heading fire, i.e. NJ2019 (Figs. 3.4(c)-(d)). During FFP at the West Tower, we see an increase in TKE_{sp} that is comparable with the increase in TKE_{bp} at $h = 20\,\mathrm{m}$ (Fig. 3.4(c)(iii)). Owing to the lower intensity of the fire compared to NJ2011, both TKE_{sp} and TKE_{bp} at $h = 20\,\mathrm{m}$ are of lesser magnitudes compared to those for NJ2011, but higher compared to those for NJ2012. The peak in TKE_{sp} is patterned on the peak in $-\overline{u'w'}$ during FFP (1520 to 1550 LT) and is, hence, attributed to the work done by the streamwise momentum flux against the mean streamwise shear ($\partial\overline{u}/\partial z$). The shear production starts to increase again, 1600 LT onwards; however, this is patterned on $-\overline{v'w'}$ (work done by the cross-stream turbulent flux against the mean cross-stream shear, $\partial\overline{v}/\partial z$) at $h = 20\,\mathrm{m}$ after 1600 LT. The increase in the magnitude of $-\overline{v'w'}$ is in turn due to the strong increase in the overall cross-stream velocity associated with the ambient wind, which

must have led to an influx of turbulence into the canopy from the top. Such an increase in $-\overline{v'w'}$ (and in TKE_{sp}) is also observed at the Control Tower, reinforcing the attribution to the ambient wind as opposed to fire-induced turbulence, contrary to the case of the NJ2011 fire. Another point to note is the increase in TKE_{sp} at $h = 3\,\mathrm{m}$ during FFP at the West Tower (Fig. 3.4(c)(v)). It is seen that TKE_{sp} at $h = 3\,\mathrm{m}$ is slightly higher compared to that at $h = 20\,\mathrm{m}$ (West Tower) and is attributed to the presence of the fire. In the absence of a fire, shear production is typically insubstantial near the ground surface in a canopy environment compared to that at the canopy height. As seen from Fig. 3.1(c), the presence of the fire causes an increase in the mean streamwise velocity at this height ($\overline{u}_3$) resulting in an increase in the mean streamwise shear ($\partial\overline{u}/\partial z$) near the surface. Therefore, the work done by the fire-induced streamwise eddies against the mean streamwise shear ($\partial\overline{u}/\partial z$) is relatively high near the fuel-bed surface resulting in the increased shear production. This shear production associated with the fire presence acts to increase turbulence at $h = 3\,\mathrm{m}$ at the West tower during FFP. Contrast this with the low-magnitude loss through TKE_{sp} at the Control Tower during this time, which suggests that shear weakly acts to decrease turbulence at $h = 3\,\mathrm{m}$.

We notice here, similar to the case of the backing fires, that TKE_{bp} is considerably higher compared to TKE_{sp} at $h = 10\,\mathrm{m}$ (length scales of $h_{\mathrm{c}}/2$). Again, this indicates that the mid-canopy level acts like a conduit of energy in the vertical direction during FFP. Moreover, note the loss in the turbulent transport term at $h = 10\,\mathrm{m}$ at the West Tower around the time of FFP (1520 to 1550 LT). Contrast this with the weak gain in turbulent transport at the Control Tower at this height from 1520 to 1550 LT followed by a considerable gain thereafter. The loss in TKE_{tr} at the West Tower is largely because of the expulsion of TKE to the air column above $h = 10\,\mathrm{m}$, facilitated by the introduction of fire-induced turbulence from the surface (bottom of the canopy). On the other hand, the gain in TKE_{tr} at the Control Tower is because of the influx of turbulence from the top of the canopy energized by the ambient wind from the SE. For both towers, the turbulent fluxes responsible for the

increased TKE_{tr} are of the scale of $h_{\mathrm{c}}/2$.

The behavior of the transport term is also notable at $h = 3\,\mathrm{m}$ and $20\,\mathrm{m}$. During FFP at $h = 20\,\mathrm{m}$, TKE_{tr} is relatively insubstantial. However, we see a gain in the transport term ($TKE_{\mathrm{tr}} > 0$) some time after FFP, which persists for a considerable time. This is attributed to influx of air and TKE from the atmospheric boundary layer aloft ($\overline{w'e} < 0$), following the southerly shift in the ambient wind that has a strong cross-stream component during that time. More interestingly, we see a gain in the transport term ($TKE_{\mathrm{tr}} > 0$) at $h = 3\,\mathrm{m}$ during FFP. This is because of the sinking of cooler air to this height (downward flux of turbulent kinetic energy, i.e. $\overline{w'e} < 0$) to compensate for the upward flux of warmer air due to fire-induced buoyancy ($\overline{w'T'} > 0$), resulting in a gain in TKE at this height. Overall, the turbulent transport term goes from a gain near-surface, to a loss mid-canopy, followed by inactivity near the canopy top. We expect that different heights of the air column within the canopy interact with each other through the turbulent transport term in the presence of the fire.

Mean Kinetic Energy Budget Equation Terms: The MKE shear production term ($-TKE_{\mathrm{sp}}$), the transport term (MKE_{tr}), and the MKE buoyancy production term normalized by the numerical value of acceleration due to gravity ($MKE_{\mathrm{bp}}/9.81$) are depicted for the sub-canopy backing and heading fires in Fig. 3.5. Figures 3.5(a) and 3.5(b) depict the MKE budget equation terms for NJ2011 and NJ2012, respectively. For both years, it is observed that the transport term (MKE_{tr}) and the shear production/loss term ($-TKE_{\mathrm{sp}}$) in the MKE equation follow a similar pattern while having opposite signs at all heights. At $h = 20\,\mathrm{m}$, both MKE_{tr} and $-TKE_{\mathrm{sp}}$ are patterned on the magnitude of $\overline{v'w'}$ at all times in 2011, including during and after FFP (after 1405 EST) and on the magnitude of $\overline{u'w'}$ at all times in 2012, including during and after FFP (after 1522 EST). The magnitude of MKE_{tr} increases during FFP in 2011 and increases with height for both years. At $h = 3\,\mathrm{m}$, MKE_{tr} and $-TKE_{\mathrm{sp}}$ terms cancel each other out precisely (assuming no slip at the surface). Next,

we focus on $MKE_{\mathrm{bp}}/9.81$ (which, essentially, has the numerical value of $-\overline{w}$) as shown in Fig. 3.5. This must be multiplied by 9.81 to obtain the actual numerical value of MKE_{bp}, which would be an order of magnitude higher; however, useful observations can be made from $MKE_{\mathrm{bp}}/9.81$ as well. During FFP, we see a loss in this term in 2011, due to upward flux induced by the presence of the fire, at $h = 20\,\mathrm{m}$, while there is a gain at $h = 3\,\mathrm{m}$ around the same time (1405 to 1435 EST) due to sinking of air under the influence of gravity. At $h = 10\,\mathrm{m}$, this term is not very active during FFP. However, there is a gain in this term at all heights sometime after FFP (after 1500 EST), due to the influx of sinking air into the canopy. In 2012, however, there is no loss in mean kinetic energy at any height due to this term during FFP. Rather, we see a gain at $h = 10\,\mathrm{m}$ and $20\,\mathrm{m}$ during FFP (1522 to 1552 EST) with a pronounced peak at $h = 20\,\mathrm{m}$ due to increased influx of air into the canopy from the atmosphere aloft. Since NJ2012 is less intense compared to NJ2011, mean vertical updrafts are expected to be relatively weaker during FFP in 2012. Instead, there is more of a tendency for cooler ambient air to sink into the canopy via gravitational acceleration when there is an ambient gust, manifesting as a gain through MKE_{bp} at $h = 10\,\mathrm{m}$ and $20\,\mathrm{m}$.

Observations regarding MKE_{tr} and $-TKE_{\mathrm{sp}}$ at the West and Control Towers for NJ2019 are very similar to those for NJ2011 and NJ2012. At the West Tower (Fig. 3.5(c)), MKE_{tr} and $-TKE_{\mathrm{sp}}$ follow a similar pattern while having opposite signs. At $h = 20\,\mathrm{m}$, both terms are of lower magnitude when compared to their counterparts at this height for NJ2011, owing to the comparatively lower intensity of NJ2019. Furthermore, both MKE_{tr} and $-TKE_{\mathrm{sp}}$ at $h = 20\,\mathrm{m}$ are patterned on the magnitude of $\overline{u'w'}$ during FFP (1520 to 1550 LT) and on the magnitude of $\overline{v'w'}$ after FFP (after 1600 LT). MKE_{tr} is highest in magnitude at $h = 20\,\mathrm{m}$ and lowest at $h = 10\,\mathrm{m}$, where $-TKE_{\mathrm{sp}}$ is also of the lowest magnitude. At $h = 3\,\mathrm{m}$, MKE_{tr} and $-TKE_{\mathrm{sp}}$ cancel each other out precisely (assuming no slip at the surface). Next, we observe that $MKE_{\mathrm{bp}}/9.81$ has the highest variability at $h = 3\,\mathrm{m}$ during and after FFP (1520 LT onward). During FFP (1520 to 1550 LT), an increase is seen corresponding to sinking of air at a relatively high vertical speed near the surface. This is followed by a persistent

updraft after FFP (after 1600 LT) and hence, a persistent loss in MKE_{bp}. This loss near the surface can be attributed to residual combustion after FFP, which must induce a persistent, low-frequency updraft after FFP. A similar pattern, though with lesser variability is seen at $h = 20\,\mathrm{m}$. At $h = 10\,\mathrm{m}$, the variability in $MKE_{\mathrm{bp}}/9.81$ (and hence in $\overline{w}$) is least, suggesting either a potential interception of, removal of energy from, or horizontal diversion of the sinking or rising mean wind at this height.

At the Control Tower (Fig. 3.5(d)), MKE_{tr} is patterned on the magnitude of $\overline{u'w'}$ before 1600 LT, and on the magnitude of $\overline{v'w'}$ after 1600 LT. The variability in MKE_{tr} increases with height and is lowest at $h = 3\,\mathrm{m}$, unlike at the West Tower, where it is minimal at $h = 10\,\mathrm{m}$. This shows that the transport of turbulent fluxes by the mean velocity (MKE_{tr}) decreases with proximity to the surface, as would be expected in the canopy in the absence of a fire since canopy-scale eddies give way to smaller-scale eddies near the surface. Contrary to the West Tower, we see sinking motion at $h = 3\,\mathrm{m}$ and $10\,\mathrm{m}$ after 1600 LT. We understand this to be the result of the sinking of ambient air from above the canopy (strong ambient winds as seen in Fig. 3.1(d)(i)) under the influence of gravity.

Here, we provide some additional insights on the terms of the MKE budget equation. First, we comment on the net effect of MKE_{tr} and $-TKE_{\mathrm{sp}}$. For all the canopy surface fires discussed here, MKE_{tr} is slightly higher in magnitude than $-TKE_{\mathrm{sp}}$ and opposite in sign, so that the sum of the two terms is very close to zero. This suggests the following. While the MKE and TKE exchange kinetic energy via shear production/loss ($\mp\, TKE_{\mathrm{sp}}$), the energy gained or lost by the MKE via this term is compensated by the transport of turbulent momentum fluxes by the mean velocity (MKE_{tr}). Therefore, the overall MKE tendency due to turbulent momentum fluxes becomes relatively insubstantial. Indeed, among MKE_{bp}, MKE_{sp}, and MKE_{tr}, the buoyancy production term has the most variability: it is an order of magnitude higher than the other two (because of the multiplication with 9.81). Therefore, it must be noted that the mean vertical velocity, and hence MKE_{bp}, shows a

noticeable response to the presence of the fire, both during and post-FFP. Moreover, while the combined contribution of MKE_{tr} and MKE_{sp} to the overall MKE tendency is relatively low, the contribution of MKE_{bp} is considerably higher. Thus, changes in the MKE due to variation in $\overline{w}$ cannot be ignored during a fire. Again, it must be remembered that we are limited to drawing inferences from only the terms involving vertical derivatives ($\partial/\partial z$) in the MKE budget equation (Eq. (3.2)) due to lack of data collection in the horizontal direction. Another important observation is the consistently muted behaviour of the MKE budget terms at $h = 10\,\mathrm{m}$ (mid-canopy height) in all three cases, i.e. NJ2011, NJ2012, and NJ2019. This helps us envision scales for potential circulation patterns in the mean flow as the mean wind travels in and out of the canopy during the fire.

3.4.2 Grassland Surface Fire

Mean Velocity and Temperature

Figure 3.6 depicts profiles of the pre-fire means (U, V, W, T_{m}) mentioned in Section 3.2 along with the mean kinetic energy (MKE $= 0.5(U^2 + V^2 + W^2)$) profile. The mean streamwise wind (U) increases with height (increasing profile), suggesting that $\partial U/\partial z > 0$ throughout. However, at lower heights ($h = 2\,\mathrm{m}$ and $10\,\mathrm{m}$), $\partial U/\partial z$ is more substantial compared to higher up ($h = 28\,\mathrm{m}$ and $42\,\mathrm{m}$) where $\partial U/\partial z$ is relatively much lower. Furthermore, the mean streamwise wind magnitudes are higher compared to those for the canopy fires discussed above, which is expected to affect the rate of spread and fire intensity accordingly. In contrast, the pre-fire cross-stream wind profile appears to be near-uniform (i.e. $\partial V/\partial z \approx 0$) for $h > 2\,\mathrm{m}$ up until the fire-front reaches the measuring tower. However, $\partial V/\partial z$ is relatively high near the surface, i.e. for $h \leq 2\,\mathrm{m}$. Moreover, the near-uniform pre-fire mean temperature profile suggests a near-neutral atmosphere during the burn hour. We, therefore, expect pre-ignition convective turbulence to be relatively minimal.

Wind-Rose Statistics

Figure 3.7 shows the wind-rose statistics for all four measurement heights, constructed from the pre-FFP (1244 to 1246 LT), FFP (1246 to 1248 LT), and post-FFP (1248 to 1250 LT) time intervals at the tower. We notice that the flow seems to accelerate near the surface during FFP as evidenced by the considerable variability in the 6 to 12 ms^{-1} speed range accompanied by a little variability in the 12 to 15 ms^{-1} speed range at $h = 2\,\mathrm{m}$ in Fig. 3.7(d)(ii), which is absent in the pre-FFP time duration (Fig. 3.7(d)(i)). Again, this is expected to be a consequence of fire-induced entrainment from the upwind side of the flame, which accelerates the flow predominantly in the streamwise direction. This is emphasized by the fact that the variability in the 6 to 12 ms^{-1} speed range decreases noticeably post-FFP at $h = 2\,\mathrm{m}$ (Fig. 3.7(d)(iii)), suggesting that these wind speeds attained during FFP are unlikely to be associated with ambient conditions. Similar observations can be made for $h = 10\,\mathrm{m}$ (Fig. 3.7(c)), due to its proximity with the fire plume. In other words, the fire flame and the hot air column above it acts like a pump that accelerates the flow. Another point to note is that although the wind was known to have a detectable cross-stream component during the burn experiment (2) (also corroborated by the pre-FFP wind-rose statistics at $h = 2\,\mathrm{m}$ and 10 m), the wind is dominantly aligned in the positive streamwise direction pre-FFP, during FFP, and post-FFP at the higher heights, i.e. $h = 28\,\mathrm{m}$ and 42 m (Figs. 3.7(a)-(b). We expect this to be a consequence of entrainment by the flame from the upwind side of the fire in the streamwise direction. This entrainment is experienced pre-FFP at the higher heights since the tilting of the fire plume in the direction of the wind induces strong temperature fluctuations (a high pressure differential) at the higher heights before the arrival of the fire-front at the base of the tower.

Turbulent and Mean Kinetic Energy Budget Terms

Turbulent Kinetic Energy Budget Terms: Before drawing on the TKE budget terms for inferences, we assess the 1-minute moving mean of the TKE ($\overline{e}$) and of the fraction of the vertical TKE ($r = 0.5\overline{w'^2/e}$) from Fig. 3.8(a)(i)-(ii). Note that the increase in $\overline{e}$ at $h = 28\,\text{m}$ and $42\,\text{m}$ is seen earlier than at $h = 2\,\text{m}$ and $10\,\text{m}$ as the fire-front approaches the tower due to tilting of the flame in the direction of the wind as observed by Clements et al. (2; 3). At $h = 2\,\text{m}$ and $10\,\text{m}$, $\overline{e}$ during FFP is higher than that for $h = 28\,\text{m}$ and $42\,\text{m}$, due to proximity with the fire plume, the source of the increased turbulence. In fact, $\overline{e}$ is the highest at $h = 2\,\text{m}$. Since fuels were removed around the base of the tower, $h = 2\,\text{m}$ represents the local flame height near the tower. The high value of $\overline{e}$, in conjunction with the low value of r at $h = 2\,\text{m}$ ($r \approx 0.1$) in Fig. 3.8(a)(ii), is noteworthy. This suggests that the horizontal fraction of TKE at $h = 2\,\text{m}$ is considerably higher during FFP. While this could be because of the attenuation of w' due to the proximity with the ground surface, it could also be representative of the horizontal acceleration of the flow past the flame (Fig. 3.7(d)) or increased entrainment from the upwind side. This horizontally accelerated flow causes the forward advection of hot gases onto unburnt fuel, which is responsible for the fire spread (also observed on laboratory scales by Finney et al. (58)). At $h = 10\,\text{m},\ 28\,\text{m},$ and $42\,\text{m}$, the values of r are higher than 0.3 pre-FFP, followed by values of r less than 0.2 during FFP. This is explained as follows. The tilting of the flame in the direction of the wind increases the variability in the vertical direction at the higher heights pre-FFP by virtue of buoyancy effects. During FFP, the effect of buoyancy at the higher heights, at the tower location, is greatly reduced and much of the variability is found to be in the horizontal velocity.

Let us now examine the streamwise turbulent flux ($\overline{u'w'}$) closely (Fig. 3.8(b)(i)). An increase in the magnitude of the turbulent flux pre- and during FFP, caused by the presence of the fire, is seen in Fig. 3.8(b)(i). Typically, negative $\overline{u'w'}$ ($\overline{u'w'} < 0$) in the atmospheric boundary layer (ABL) represents a momentum sink. Two possible cases that contribute to

negative $\overline{u'w'}$ (Fig. 3.8(b)(i)) are considered: sweep-like patterns, i.e. $w' < 0$ and $u' > 0$ and ejection-like patterns, i.e. $w' > 0$ and $u' < 0$. At all heights AGL, eddies associated with sweep-like patterns send streamwise fluctuations assisting in fire spread ($u' > 0$) to the lower heights, i.e. towards the flame at the surface ($w' < 0$). Therefore, the streamwise turbulent flux associated with sweep-like events at these heights assists in the fire spread, while also providing a momentum sink to the ambient mean wind. The effect of eddies associated with ejection-like patterns is explained as follows: in-drafts of air from the downwind side ($u' < 0$) are diverted away from the fire flame near the surface ($w' > 0$) so that they play more of a role in vertical transport rather than impeding the fire spread.

Next, we explore the influence of the streamwise turbulent flux on the TKE budget terms as shown in Fig. 3.8(c). First, we note that the shear production term (TKE_{sp}) at $h =$ 2 m and 10 m is patterned on $-\overline{u'w'}$ at those heights. During FFP, the increase in TKE_{sp} is highest at $h = 2$ m, followed by $h = 10$ m. At both heights, this increase is higher than that at the higher heights AGL ($h = 28$ m and 42 m). This is because shear production is a consequence of work done by the turbulent fluxes (in this case, mostly $\overline{u'w'}$) against the mean wind shear (in this case, $\partial U/\partial z$). In a grassland environment, the mean streamwise wind shear is higher closer to the ground surface, as opposed to near the top of the canopy in a forested environment as discussed in Section 3.4.1. This accounts for the high increase in TKE_{sp} at $h = 2$ m. From $h = 2$ m to 10 m, the shear production decreases with height despite the increase in $-\overline{u'w'}$ since $\partial U/\partial z$ decreases with height. Higher up, both $-\overline{u'w'}$ and $\partial U/\partial z$ decrease with height; therefore, the work done by the streamwise turbulent flux against the mean streamwise wind shear is low. This suggests that shear production is associated with work done against the mean streamwise shear by the streamwise turbulent eddies that assist in pushing the flame towards the unburnt fuel, as discussed in the previous paragraph. Since the shear production is positive ($TKE_{\text{sp}} > 0$), the work done serves to remove energy from the MKE and provide it to the TKE. The resulting increase in TKE helps in sustaining the turbulent eddies that assist in the fire spread.

We also take this as an opportunity to comment on $\overline{v'w'}$. Similar to the NJ2011 fire, cross-stream eddies do seem to strengthen in response to the fire presence during FFP. However, such strengthening is only seen at $h = 10\,\text{m}$. Furthermore, since the mean cross-stream wind shear is minimal ($\partial V/\partial z \approx 0$) at this height (Fig. 3.6(b)), the work done by the cross-stream eddies in overcoming the mean cross-stream shear is insubstantial. Consequently, the majority of shear production is associated with the work done by the streamwise eddies against the mean streamwise wind shear. Since shear production itself results in an increase in turbulence, it is possible that the cross-stream turbulent eddies at $h = 10\,\text{m}$ germinate from this increase in turbulence. In this manner, the cross-stream eddies appear to be coupled to the streamwise eddies at this height. Moreover, the presence of strong cross-stream turbulent eddies at $h = 10\,\text{m}$ is an important observation in the context of laboratory experiments documented in the literature that suggested that cross-stream eddies are vital to the advection of hot gases from the burned fuel to the unburned fuel, which effectually causes the fire to spread (58). Considering that cross-stream eddies weaken beyond this height, an estimate of the length scale associated with such eddies can also be obtained from this height. Furthermore, it is worth noting the increase in $-\overline{v'w'}$ at $h = 28\,\text{m}$ pre-FFP (Fig. 3.8(b)(ii)), which suggests a strengthening of the cross-stream eddies at the higher heights pre-FFP possibly due to the effects of flame tilting.

Additionally, we observe an increase in $-\overline{u'v'}$ during FFP (Fig. 3.8(b)(iii)) for the grassland fire. This indicates an increase in the strength of horizontal turbulent eddies induced by the presence of the flame. It is known that horizontal eddies are formed as a consequence of fire-induced entrainment in the horizontal plane (23), which is expected to be relatively intense in an open grassland environment. We further expect these to contribute to the formation of fire-whirls or dust devils, as discussed later in this section. The increase in strength of the horizontal eddies is particularly noticeable at $h = 2\,\text{m}$ and $10\,\text{m}$ and is highest at $h = 10\,\text{m}$. This provides a perspective on the length scale associated with horizontal turbulent eddies during FFP, with respect to the given flame height, in a grassland environment.

Figure 3.8(c) shows that shear production is more substantial as compared to buoyancy production during FFP at the lower heights AGL, i.e. at $h = 2\,\mathrm{m}$ and $10\,\mathrm{m}$. While the reasons for increased TKE_{sp} have been discussed above, the decreased TKE_{bp} is associated with the attenuation of the vertical velocity fluctuations (w') at these heights even during FFP due to proximity with the ground surface. However, buoyancy production is more significant compared to shear production at the higher heights AGL, i.e. $h = 28\,\mathrm{m}$ and $42\,\mathrm{m}$ pre-FFP (Fig. 3.8(c)). This suggests that while the tilting of the flame in the direction of wind induces strong vertical fluctuations at the higher heights pre-FFP, thereby causing an increase in TKE_{bp}, it does not result in increased TKE_{sp} at these heights despite the increase in the strength of the cross-stream eddies pre-FFP. Shear production at the higher heights remains insubstantial pre-FFP.

Some interesting inferences can be drawn from the very active turbulent transport term ($TKE_{\mathrm{tr}} \neq 0$) before and during FFP. Typically, in the ABL, the turbulent transport term is not very active and equilibrium exists between viscous dissipation (ε) and shear production (TKE_{sp}). At $h = 42\,\mathrm{m}$, the turbulent transport term remains relatively insubstantial and the buoyancy production term remains the only active source of turbulence generation pre-FFP. At $h = 10\,\mathrm{m}$ and $28\,\mathrm{m}$ we observe a loss in TKE_{tr} pre-FFP (and for some time during FFP), which is associated with an average upward flux of TKE caused due to buoyant updrafts induced by the tilted flame. This is followed by a gain at $h = 10\,\mathrm{m}$ and a persistent loss at $h = 28\,\mathrm{m}$ during FFP. The gain at $h = 10\,\mathrm{m}$ is attributed to an incoming flux of TKE from higher heights as the effects of fire-induced buoyancy weaken at the higher heights ($h = 28\,\mathrm{m}$) along with an incoming flux of TKE from $h = 2\,\mathrm{m}$ where fire-induced buoyant updrafts are still active during FFP. At $h = 2\,\mathrm{m}$, we see a similar pattern of loss in TKE_{tr} followed by a gain in TKE_{tr}.

So far, we have analyzed the turbulent fluxes and terms of the TKE budget equation for the primary burn in the domain. Let us now focus on the turbulent fluxes and TKE

budget 6 to 10 minutes after FFP. Some increase in $\overline{e}$ is observed at the higher heights AGL (h = 28 m and 42 m) followed by a considerable increase at the lower heights (h = 2 m and 10 m) around this time (Fig. 3.8(a)(i)). The increase in $\overline{e}$ at each of these heights coincides with a drop in r to values below 0.1, indicating that it is associated with stronger horizontal turbulent fluctuations (u', v'). We also see an increase (peaks) in $-\overline{u'v'}$ between 1254:30 and 1257:30 LT at h = 2 m and 10 m (marked by grey dash-dotted vertical lines in Fig. 3.8(b)(iii)), while $\overline{u'w'}$ and $\overline{v'w'}$ remain relatively low in magnitude at these heights emphasizing the importance of the horizontal turbulent eddies over the vertical eddies in this time duration. This corroborates well with the observations by Clements et al. (3) that associated the increase in $\overline{e}$ with the appearance of a dust devil along with horizontal turbulent eddies arising from a secondary burn of a small section of the grassland immediately upwind of the experimental plot that was ignited after the experimental (primary) burn was completed. Moreover, an increase in buoyancy production ($TKE_{\mathrm{bp}} > 0$) is also seen at h = 2 m between 1252:30 and 1254:30 LT (marked by grey dash-dotted vertical lines in Fig. 3.8(c)(iv)) despite relatively weak w'; this is because of intense fluctuations in temperature (stronger T' than during FFP for the primary burn!) around this time at h = 2 m. It appears that the combined effect of residual combustion from the primary burn, including but not limited to smoldering, and flaming combustion from the secondary burn may be responsible for the increase in TKE_{bp} at the base of the 43-m tower between 1252:30 and 1254:30 LT, while the observed dust devil (and horizontal turbulent eddies caused by the secondary burn) is mainly responsible for the increase in $\overline{e}$ at this point between 1254:30 and 1257:30 LT. Additionally, signatures of buoyancy production, such as those seen at h = 2 m, are not seen at h = 10 m, 28 m, and 42 m from 1252:30 to 1254:30 LT, possibly because fluctuations in the vertical velocity (w') are weaker compared to those during flaming combustion from the primary burn. Furthermore, although horizontal wind shear leads to the increase in $\overline{e}$ from 1254:30 to 1257:30, as suggested by Clements et al. (3), the increase in shear production (TKE_{sp}) at h = 2 m is relatively inappreciable (Fig. 3.8(c)(iv)) during

that time. This is despite the increased strength of horizontal turbulent eddies as evident from the increase in the $-\overline{u'v'}$ (Fig. 3.8(b)(iii)). A possible explanation lies in the fact that we have not considered the contribution of the work done by the horizontal eddies towards TKE_{sp} due to lack of data collection in the horizontal plane, which impedes mean wind shear calculations in the horizontal plane ($\partial/\partial x$ and $\partial/\partial y$).

3.5 Discussion

Fire-atmosphere interaction comprises several simultaneous complex phenomena including but not limited to the entrainment of ambient air, the formation of strong turbulent eddies, the introduction of fire-induced turbulence (buoyancy production, shear production) from the surface and its redistribution in the air column above (turbulent transport), the injection of ambient turbulent fluxes from the canopy top, and the redistribution of mean kinetic energy in the air column. In this section, we integrate the key processes and events that have been inferred and elaborated on in the previous section. Figures 3.9, 3.10, and 3.11 present brief summary pictures of the sub-canopy backing surface fire (high intensity), the sub-canopy heading surface fire, and the heading surface fire in a grassland, respectively.

Comparison with a no-fire situation suggests that the presence of an approaching flame (e.g., at the West Tower for NJ2019) tends to organize the turbulence near the surface in the streamwise direction, in contrast to the more disorganized flow in the absence of fire (e.g., at the Control Tower). The presence of the flame also leads to the entrainment of ambient air from both the upstream and downstream side of the fire. In some cases, wind entrained from the upwind side of the fire interacts with that from the downwind side and diverts momentum in the cross-stream direction as well. In the grassland fire, we see that the horizontal wind near the ground surface accelerates during FFP due to the presence of the flame, with high variability in the streamwise direction (Fig. 3.11). In other words, the

flame acts like a pump for the wind in the streamwise direction. Acceleration of the wind past the hot air column above the flame is also seen in the case of the sub-canopy surface fires (Figs. 3.9 and 3.10). Moreover, the increase in mean streamwise wind speed past the hot air column above the flame at higher heights in the case of the sub-canopy heading surface fire (NJ2019) suggests some coupling between fire-induced buoyancy and the corresponding mean velocity components.

In all sets of sub-canopy surface fires, turbulent eddies (either streamwise or cross-stream) are found to be strongest near the canopy top (Figs. 3.9 and 3.10): strong streamwise turbulent flux is accompanied by relatively weaker cross-stream turbulent flux and vice-versa. Furthermore, it must be noted that both are coupled with each other through shear production. The highest shear production amongst the different heights in the air column is near the canopy top, attributed to the strong turbulent flux there. For the more intense sub-canopy surface fires, shear production near the canopy top is attributed to the fire and can persist for a few hours post FFP. For the relatively lower intensity sub-canopy surface fires (e.g. NJ2012), shear production is dictated by intermittent gusts and the background canopy-scale turbulence (work done by strong turbulent eddies against the mean shear). Sub-canopy surface fires seem to be affected considerably by the turbulence near the canopy top. The injection of turbulence into the canopy via sweep-like eddies ($\overline{u'w'} < 0$) near the canopy top has different connotations for backing and heading fires: the associated streamwise eddies resist the fire spread in the case of backing fires, while they assist fire spread in the case of heading fires. For the relatively more intense sub-canopy surface fires (e.g. NJ2011), cross-stream turbulent fluxes become prominent. In the grassland fire, both cross-stream and streamwise eddies strengthen with height before attaining a maximum (in this case, at the 10-m height) and starting to weaken with height (Fig. 3.11). The strengthening of cross-stream eddies is important in the context of recent laboratory-scale experiments that suggested that cross-stream eddies advect hot gases forward onto unburnt fuel (58). Albeit on a management-scale, the strong cross-stream eddies seen here could

similarly participate in fire spread in the grassland environment and the height at which these eddies are the strongest provides the associated vertical length scale (relative to the flame height). Furthermore, we infer that the downwash from strong streamwise eddies of this scale ($\overline{u'w'} < 0$) also participates in the fire spread by pushing hot gases onto the unburnt fuel ($w' < 0$ and $u' > 0$). This is in consonance with the results of Desai et al. (87) pertaining to a small-scale grassland fire, which suggested that vortices generated from the entrained air push hot gases outward away from the flame. The near-surface wind also seems to accelerate past the flame: also an observation that matches with those from Desai et al. (87). It is noteworthy that the phenomena seen in the grassland fire from this chapter, while pertaining to a large-scale prescribed burn, conform to those from a small-scale burn experiment on grassland fires. Contrary to the case of the sub-canopy surface fires, shear production in grassland fires is highest near the surface. This shear production is correlated to the forward advection of hot gases and the upwash of indrafts from the downwind side. Shear production then decreases with height (Fig. 3.11), despite the increase in the strength of the streamwise eddies; this is because the mean streamwise wind shear reduces with height so that the work done by the streamwise turbulent eddies against the mean streamwise wind shear is low.

In the absence of a fire, the shear length scale for a canopy is typically of the order of $h_c/2$ (93). Our analysis shows that shear production increases with height in the absence of a fire (at the Control Tower in 2019). However, at length scales of half the canopy height in the presence of a surface fire, the buoyancy production far exceeds the shear production. This makes us envision the mid-canopy height as a channel for vertical transport of kinetic energy during FFP and further emphasizes the importance of length scales of $h_c/2$. In the grassland environment, vertical length scales are dictated by the height at which the turbulent eddies become the strongest during FFP ($h = 10\,\mathrm{m}$ in this case) as evidenced by the increased magnitude of the turbulent fluxes ($-\overline{u'w'}$ and $\overline{v'w'}$), seen in Fig. 3.11. The grassland fire data also show the presence of horizontal turbulent eddies that increase in strength (increase

in magnitude of $-\overline{u'v'}$) up to $h = 10\,\mathrm{m}$. We would expect this height to vary depending on the fire intensity, flame height, and wind speed. Another measure for the shear length scale in a grassland environment during FFP can be obtained from the height at which the shear production begins to drastically reduce with height; in this case, this is achieved at a height above $h = 10\,\mathrm{m}$.

It is easy to see that buoyancy production increases with height in both environments due to the increased variability in the vertical wind velocity fluctuations (w') with height. However, the height to which the buoyancy production continues to increase is determined by the fire intensity. Another notable aspect is the role of the turbulent transport term. It is a well-documented observation that the turbulent transport term is active within the canopy as opposed to the ABL aloft where equilibrium generally exists between viscous dissipation and shear production (93). This is also demonstrated by the active turbulent transport term (gain) at a height of $h_c/2$, at the Control Tower in 2019. Much like how sweeps inject turbulence into the canopy from the ABL aloft, fire injects turbulence into the canopy from the surface. For more intense surface fires beneath the canopy, it seems that while there is a gain in TKE through buoyancy production, there is a loss in TKE (mid-canopy and/or at other heights) due to expulsion of TKE to the ABL aloft via the turbulent transport term (pre- and post-FFP profiles in Figs. 3.9 and 3.10). Such an expulsion is compensated by a reversal process where there is an influx of TKE via the turbulent transport term. The transport term in the grassland fire mimics this behavior up to a certain height above the surface ($h = 10\,\mathrm{m}$ in this case) relative to the flame height (Fig. 3.11). Thus, the turbulent transport term actively participates in the vertical redistribution of TKE in the air column and its behavior can be used to determine important vertical length scales. However, it must be noted that we have not been able to include the effects of the turbulent transport terms involving horizontal gradients ($\partial/\partial x$ and $\partial/\partial y$), which necessitates the collection of data in the horizontal direction, both streamwise and cross-stream.

We have also investigated the typically unexplored terms of the MKE budget equation. The MKE budget terms within the canopy indicate that the sum of the shear production term (which is the term through which the MKE and TKE interact with each other) and transport of turbulent fluxes by mean momentum is relatively inconsequential to the MKE tendency. Rather, it is the sinking of air under gravitational acceleration or the rising of air due to buoyancy that accounts for most of the variability in the MKE tendency (Figs. 3.9 and 3.10). This also indicates that the mean vertical velocity responds to the presence of a fire and cannot be assumed to be the same as the pre-FFP mean vertical velocity.

3.6 Summary and Future Work

Studies on turbulence during management-scale experimental burns conducted in differing conditions of wind and vegetation are relatively isolated. The integrated contextual framework provided in this work represents a major stride towards the synthesis of and comparison among such studies. Through the comparison, we have reinvestigated fire-induced turbulence dynamics with the backdrop of canopy turbulence (forested environments) or ABL turbulence (grassland environment) from a fundamental standpoint. The effects of changes in ambient wind conditions on the measured data have been taken into account because of their linkage to fire behavior. While the inferences drawn here have also been informed by local meteorological conditions at the time of the burn experiments, we have successfully encapsulated the coherent patterns that broadly characterize fire-induced turbulent flow in the two environments primarily by examining turbulent fluxes and the TKE budget terms. We have also examined the terms of the MKE budget equation for all of the sub-canopy surface fire experiments. The sinking of air under gravitational acceleration or the rising of air due to buoyant updrafts accounts for most of the variability in the MKE tendency during and after fire-front passage. The "slowly-varying" mean flow responds noticeably to

the presence of the fire and cannot be equated to the pre-FFP mean flow.

In this study, major differences among three scenarios of surface fires have been highlighted: sub-canopy heading fires, sub-canopy backing fires, and heading grassland fires. Differences in the relative strength and role of the streamwise and cross-stream turbulent eddies in fire spread and the relative importance of some terms of the TKE budget over others at each of the measurement heights have been discussed, based on fire intensity and the surface-fire environment. Shear production and buoyancy production in sub-canopy surface fires are found to be more substantial near the canopy top for more intense fires, while their magnitudes decrease with decreasing fire intensity. For low-intensity sub-canopy fires, the buoyancy production is considerably lower than the shear production near the canopy top, though the latter is mostly attributed to the background canopy turbulence. In a heading grassland fire, shear production dominates buoyancy production close to the surface and appears to be inconsequential beyond a certain height relative to the flame length, while buoyancy production increases with height thereby becoming substantial further away from the surface. In all sub-canopy fires, buoyancy production seems to dominate shear production at the mid-canopy height. The turbulent transport term appears to follow a coherent pattern during fire-front passage when the fire intensity is higher, both within the canopy and in a grassland environment. For intense sub-canopy surface fires, a noticeable loss in TKE due to its expulsion to the atmospheric boundary layer aloft via the transport term is compensated by a gain due to TKE influx via the transport term. In the grassland fire, the transport term shows similar behavior until a certain height. These differences also inform the vertical length scales associated with fire-induced turbulent flow in their respective environments. While such length scales have been quantified and studied in no-fire conditions in previous studies (93), this study takes a step in the direction of quantifying length scales in the presence of a fire, which can inform smoke dispersion in different environments. The system of equations that governs fire dynamics is very complex. Model developers can utilize the knowledge of relatively important or less important terms associated with each

height (relative to the vertical length scale) to simplify their models or adjust their model complexity depending on the vegetative environment. This will lead to decreased model computational costs without loss of physical understanding. In conjunction with simplified models, the turbulence dynamics presented in this study can also be applied towards understanding the physics of ember transport (98; 99; 83; 100) and estimating the horizontal distance covered by embers lofted by the fire plume before they land to generate spot fires.

Another step in the direction of simplifying the governing equations would involve parameterizing fire-atmosphere interactions via a modified flux-gradient approach (K theory). The authors plan on using this data to obtain better estimates of the eddy diffusivity in the presence of a fire that will account for the non-local turbulence in the canopy and the coupling between shear and buoyancy. Furthermore, it must be noted that there are limitations associated with the averaging scheme used for examining coherent motions: a larger averaging window delocalizes the coherent motions in time, while a smaller window makes it difficult to separate the mean terms from the turbulent fluctuations. The findings of this study could be augmented by inferences drawn from a wavelet transform on the temperature and velocity signals, which the authors are currently working on. With the help of a suitable window in the time domain, a wavelet transform could disassemble the signal into its component frequencies while achieving the best localization in time, thereby providing insights into the corresponding coherent motions and their temporal evolution.

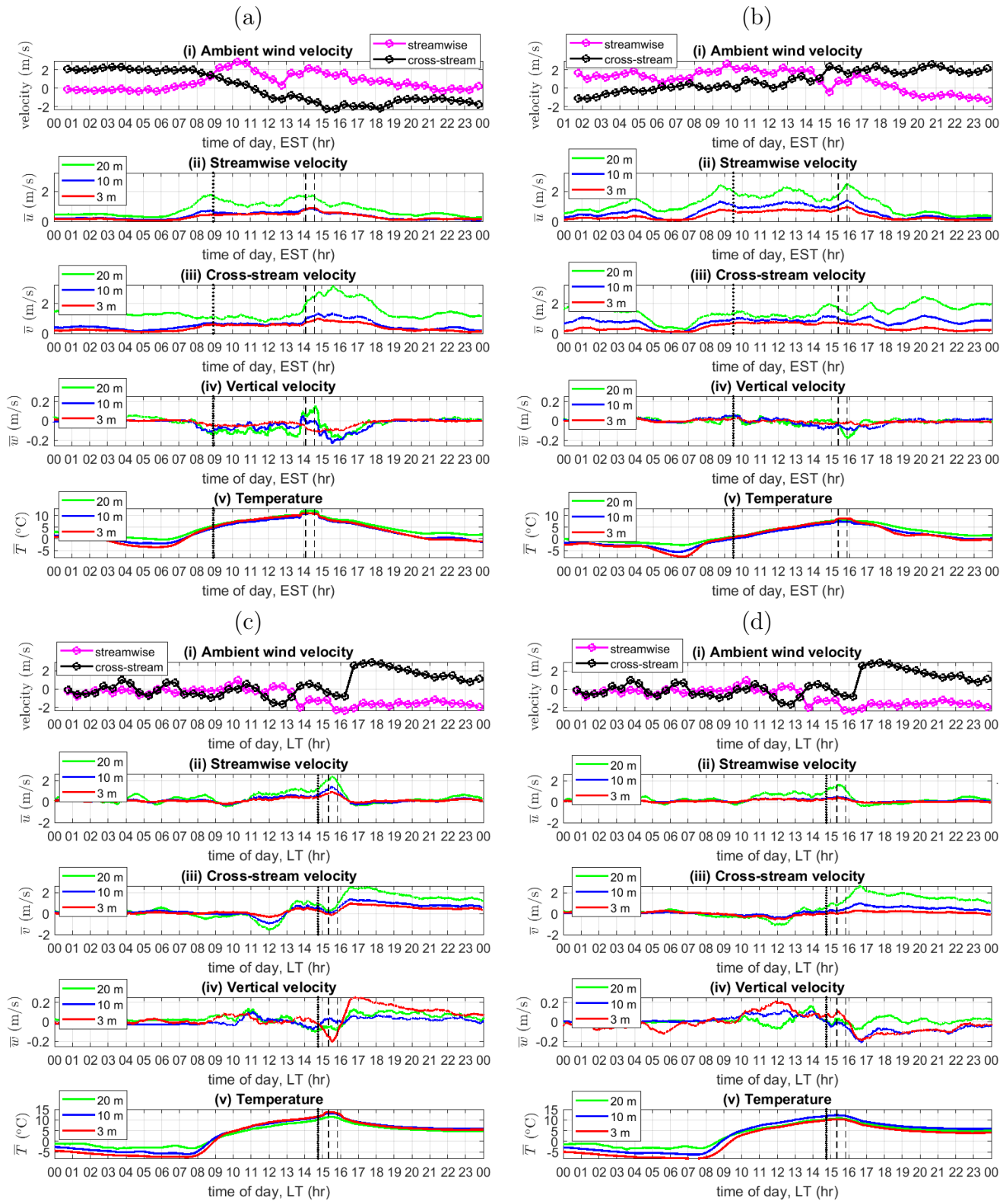


Figure 3.1: (i) Ambient wind velocity recorded by nearby AmeriFlux towers. One-hour moving means of the measured (ii) streamwise velocity ($\overline{u}$), (iii) cross-stream velocity ($\overline{v}$), (iv) vertical velocity ($\overline{w}$), and (v) temperature ($\overline{T}$) for the following cases: (a) NJ2011, (b) NJ2012, (c) West Tower (NJ2019), and (d) Control Tower (NJ2019). Vertical dotted lines indicate ignition times. Vertical dashed lines delineate FFP times in (a), (b), and (c), and the West Tower FFP time in (d).

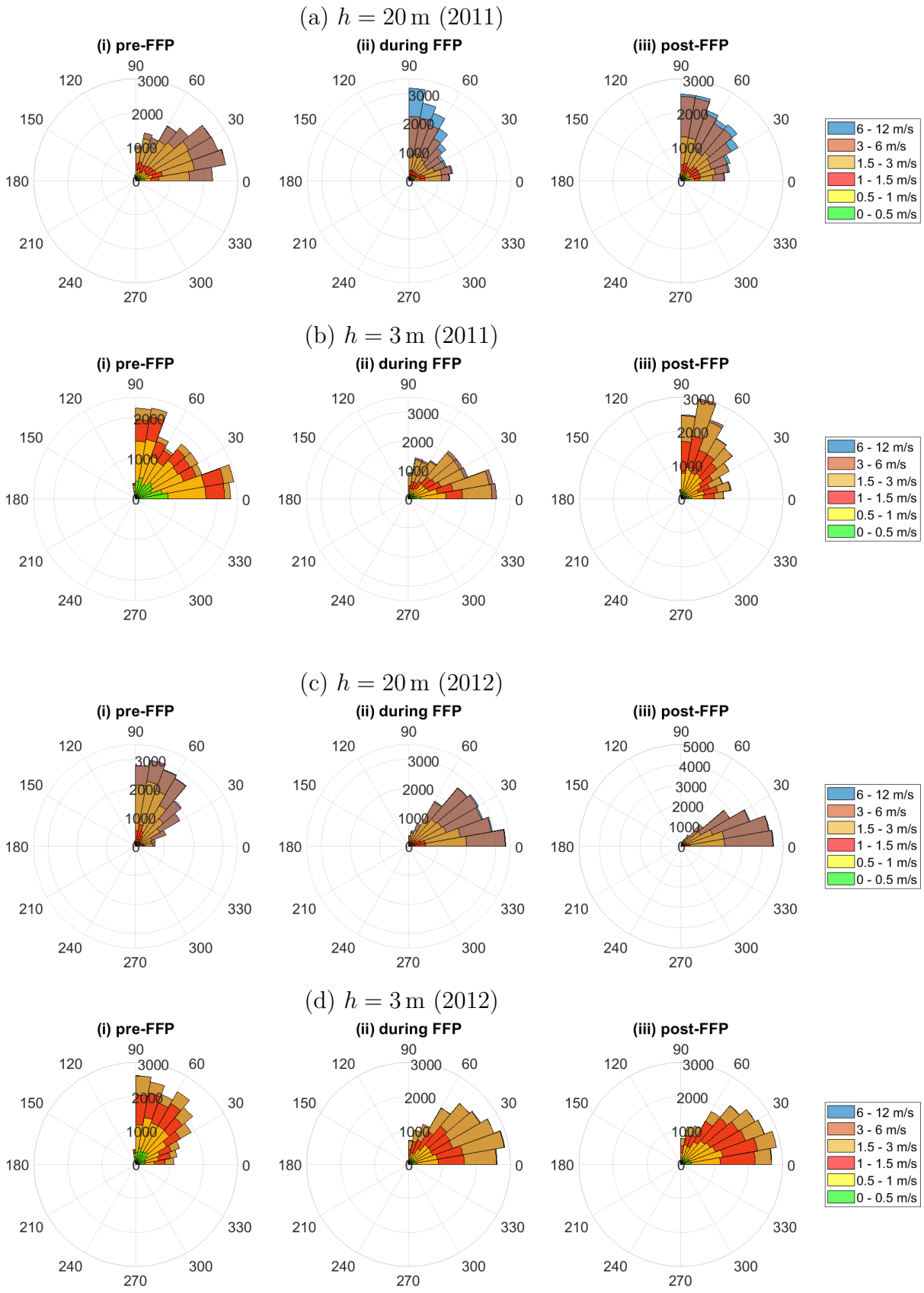


Figure 3.2: Total horizontal velocity ($u\hat{\mathbf{i}} + v\hat{\mathbf{j}}$) wind-rose statistics for (i) pre-FFP, (ii) FFP, and (iii) post-FFP times at (a) $h = 20\,\mathrm{m}$ and (b) $h = 3\,\mathrm{m}$ for NJ2011, and for (c) $h = 20\,\mathrm{m}$ and (d) $h = 3\,\mathrm{m}$ for NJ2012. Colors represent classes of wind speed, while 0° represents the positive streamwise direction.

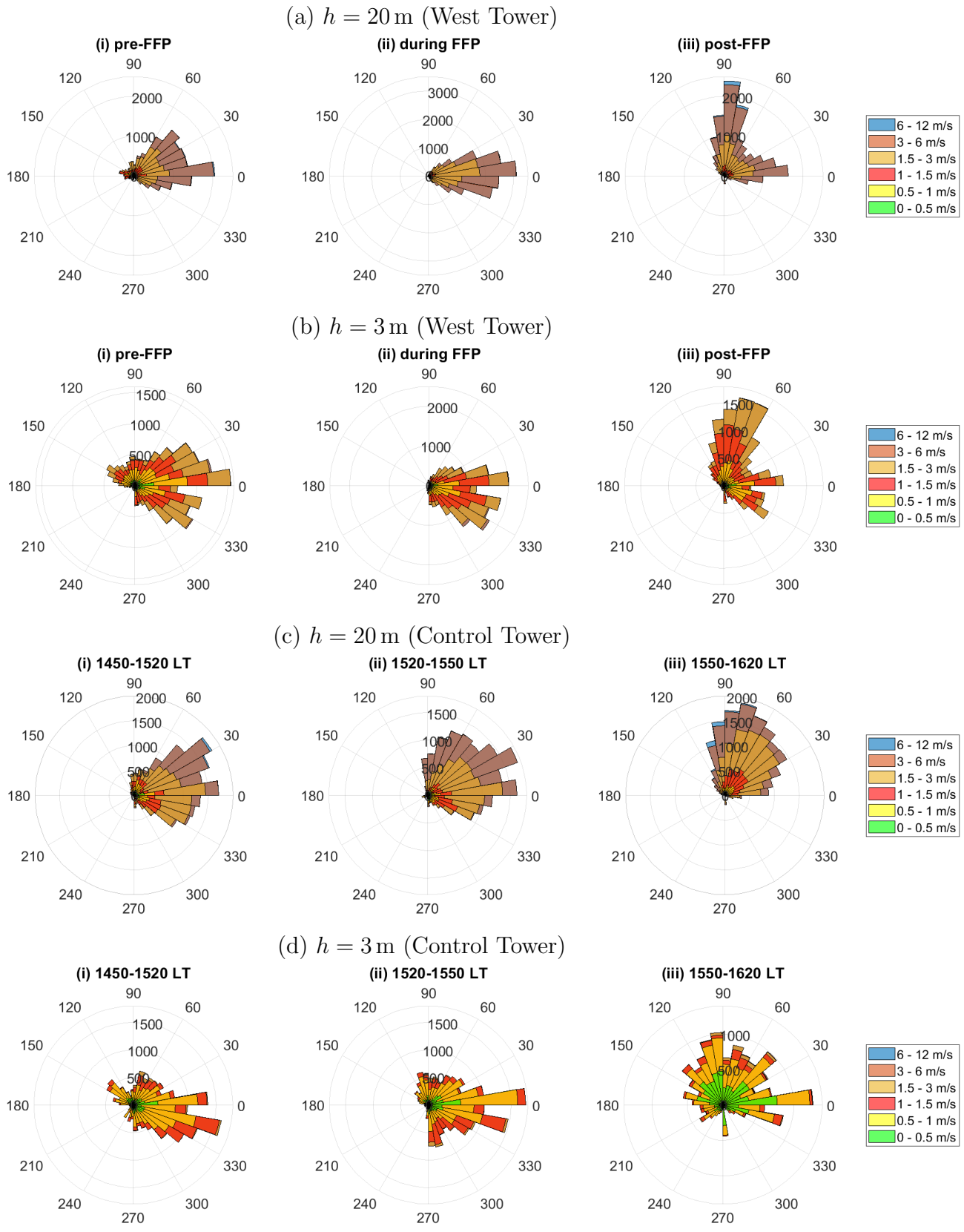


Figure 3.3: Total horizontal velocity ($u\hat{\mathbf{i}} + v\hat{\mathbf{j}}$) wind-rose statistics for (i) pre-FFP, (ii) FFP, and (iii) post-FFP times at (a) $h = 20\,\mathrm{m}$ and (b) $h = 3\,\mathrm{m}$ at the West Tower for NJ2019, and (c) $h = 20\,\mathrm{m}$ and (d) $h = 3\,\mathrm{m}$ at the Control Tower for NJ2019. Colors represent classes of wind speed, while 0^{o} represents the positive streamwise direction.

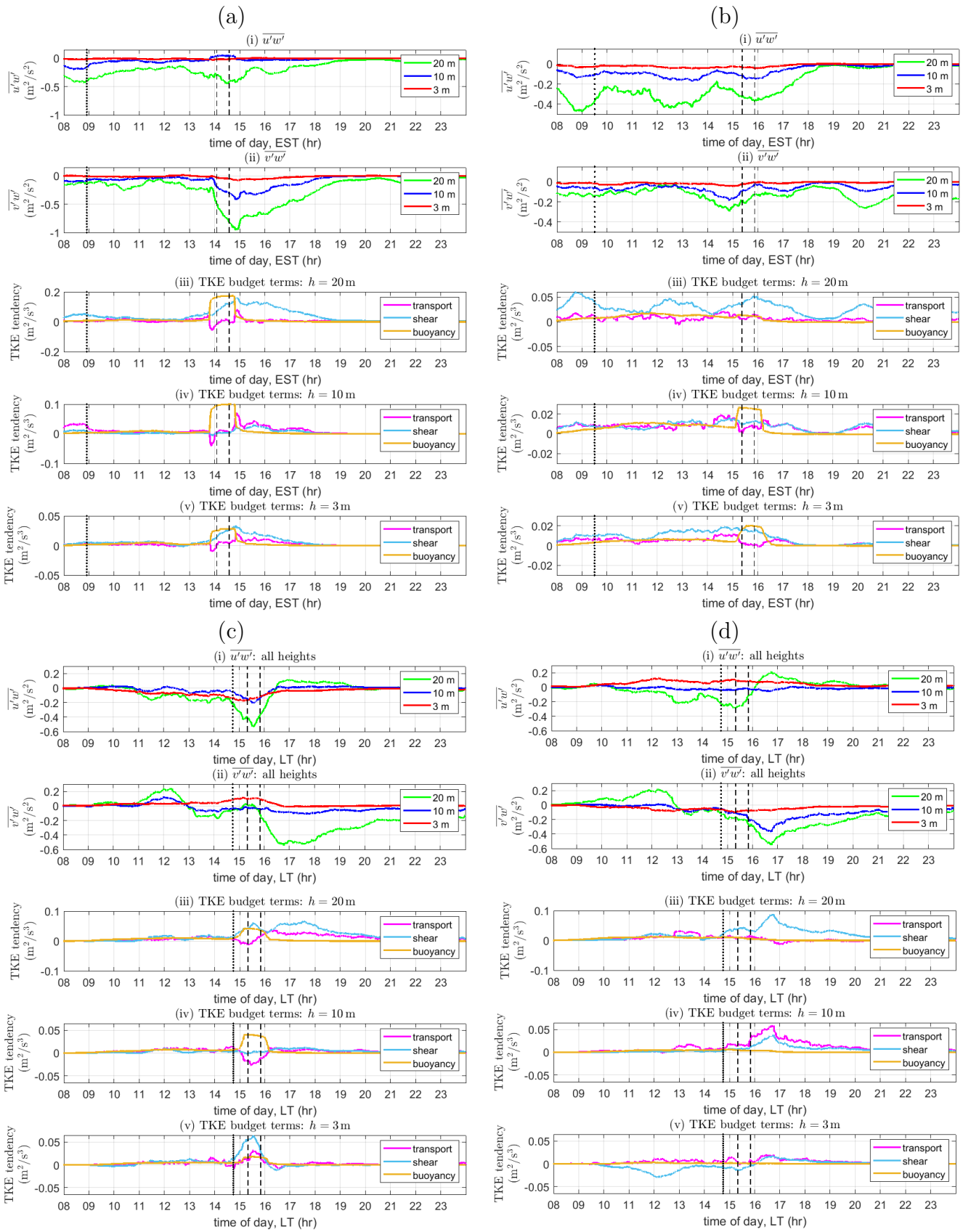


Figure 3.4: (i) $\overline{u'w'}$, (ii) $\overline{v'w'}$, TKE budget terms for (iii) $h = 20\,\mathrm{m}$ (iv) $h = 10\,\mathrm{m}$, and (v) $h = 3\,\mathrm{m}$ for the following cases: (a) NJ2011 (b) NJ2012 (c) West Tower (NJ2019), and (d) Control Tower (NJ2019). Vertical dotted lines indicate ignition times. Vertical dashed lines delineate FFP times in (a), (b), and (c), and West Tower FFP time in (d).

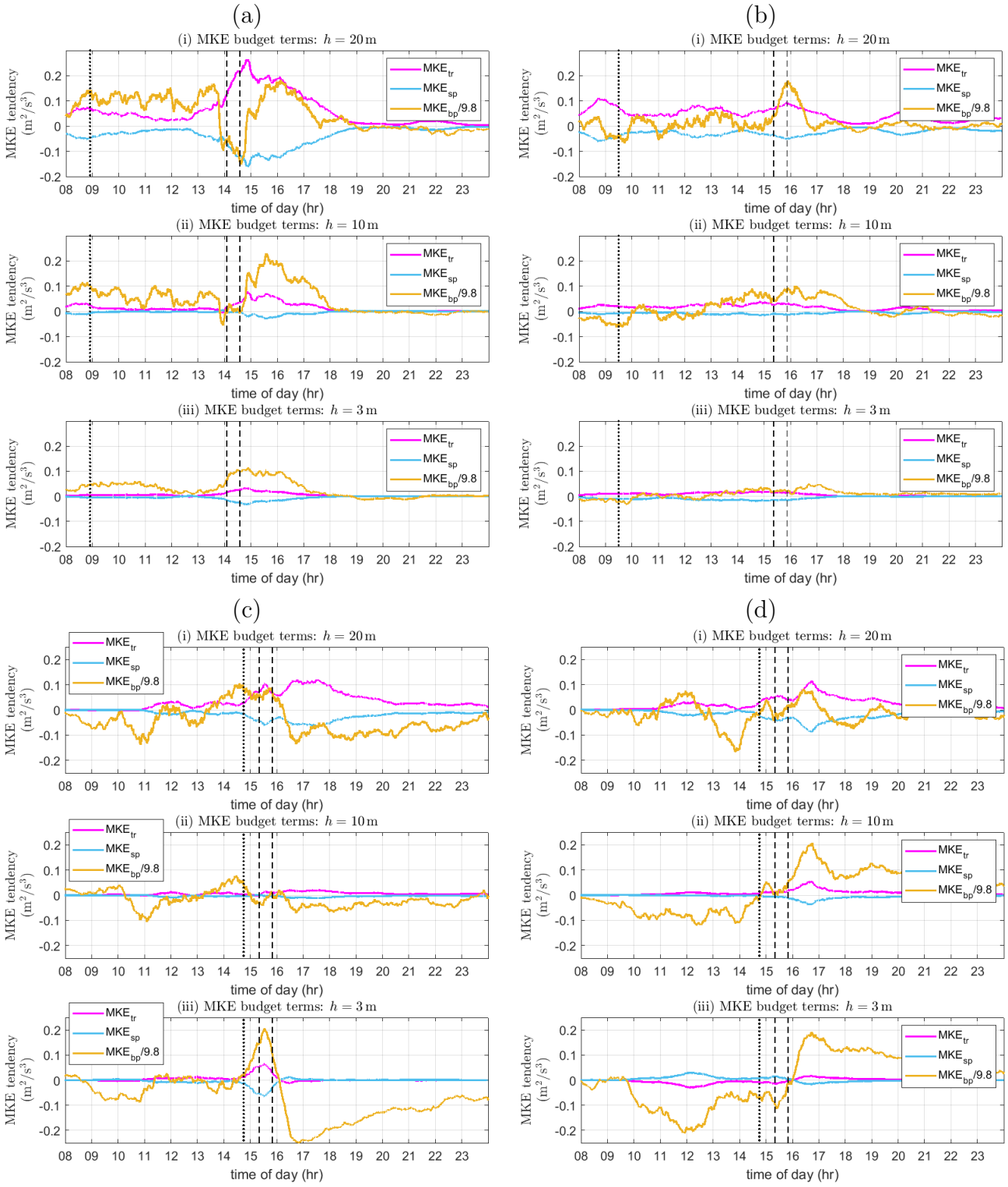


Figure 3.5: MKE budget equation terms for (a) NJ2011, (b) NJ2012, (c) West Tower (NJ2019), and (d) Control Tower (NJ2019), at $h =$ (i) 20 m, (ii) 10 m, and (iii) 3 m. Vertical dotted lines indicate ignition times. Vertical dashed lines delineate FFP times in (a), (b), and (c), and West Tower FFP time in (d).

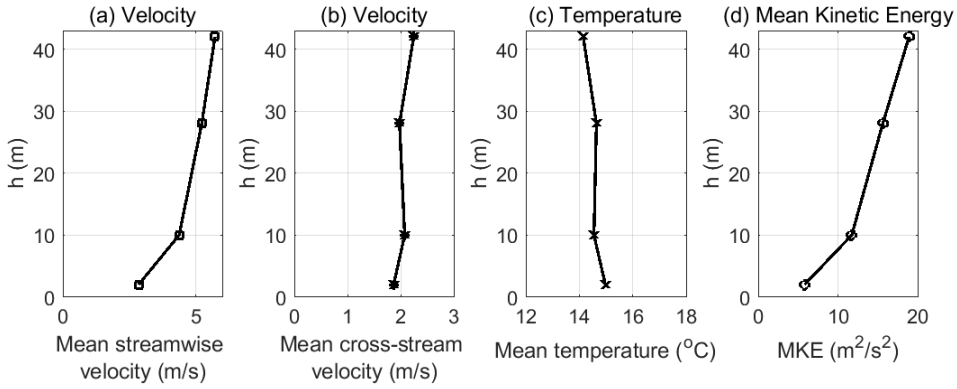


Figure 3.6: Pre-ignition vertical profiles of the (a) mean streamwise velocity (U), (b) mean cross-stream velocity (V), (c) temperature (T_{m}), and (d) Mean Kinetic Energy ($(U^2 + V^2 + W^2)/2$) for TX2006.

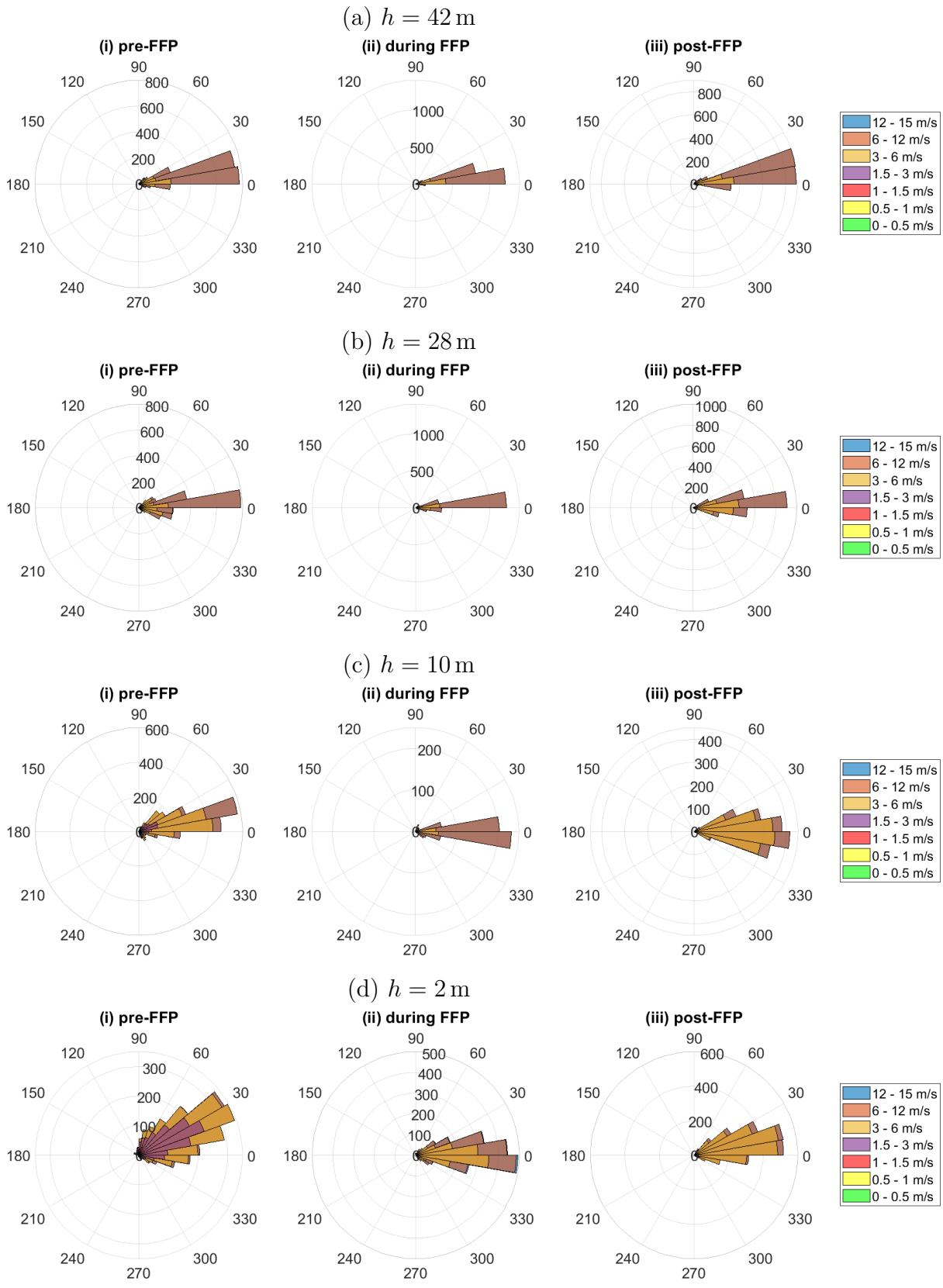


Figure 3.7: Total horizontal velocity ($u\hat{\mathbf{i}} + v\hat{\mathbf{j}}$) wind-rose statistics for (i) pre-FFP, (ii) FFP, and (iii) post-FFP times at $h =$ (a) 42 m, (b) 28 m, (c) 10 m, and (d) 2 m for TX2006. Colors represent classes of wind speed, while 0° represents the positive streamwise direction.

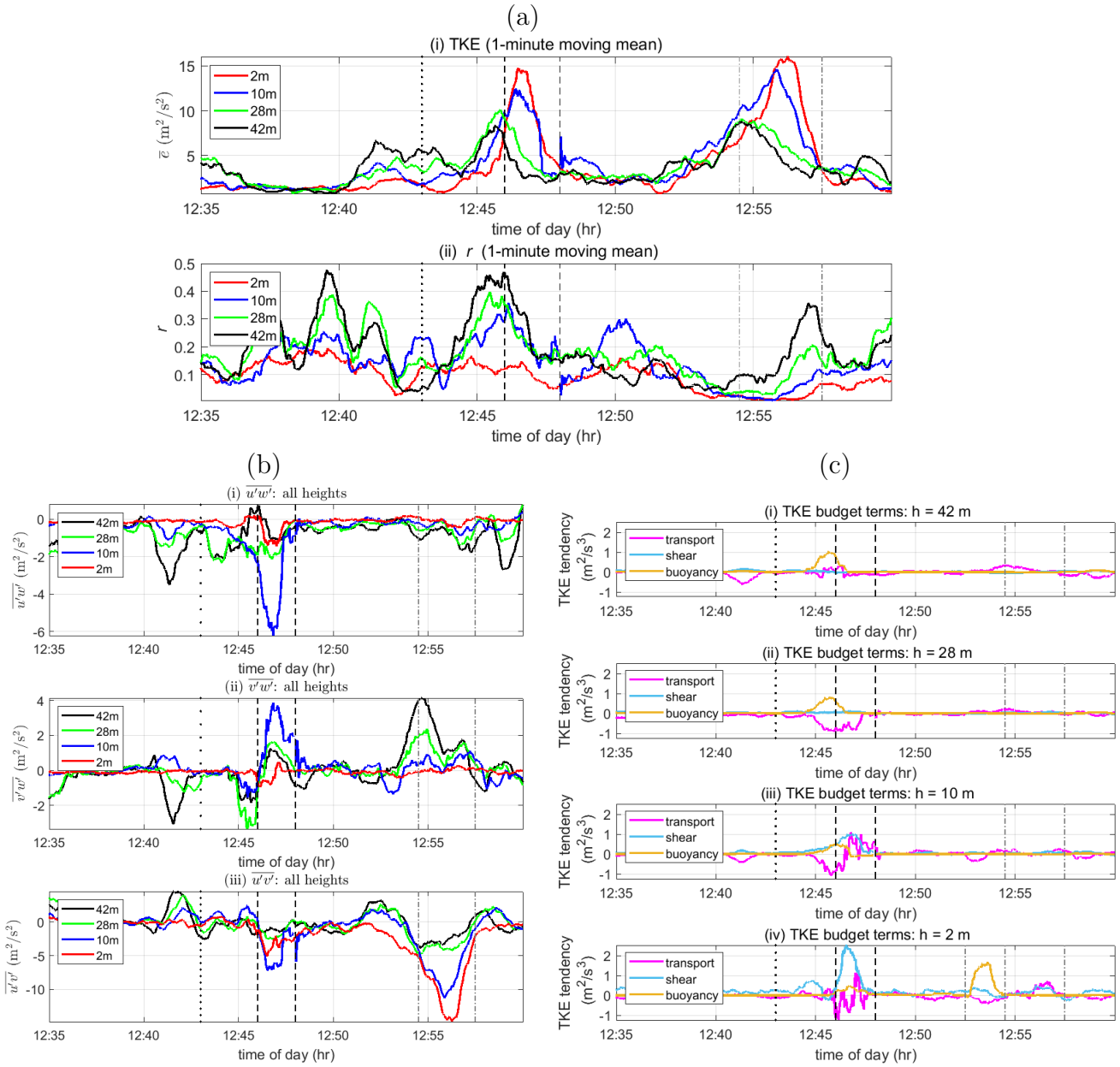


Figure 3.8: For TX2006: (a)(i) One-minute moving means of the TKE and (ii) vertical fraction of TKE (r); (b) turbulent fluxes, i.e. (i) $\overline{u'w'}$, (ii) $\overline{v'w'}$, and (iii) $\overline{u'v'}$ at all four heights; (c) TKE budget terms at h = (i) 42 m, (ii) 28 m, (iii) 10 m, and (iv) 2 m. Black dotted vertical line indicates ignition time; black dashed vertical lines delineate FFP time.

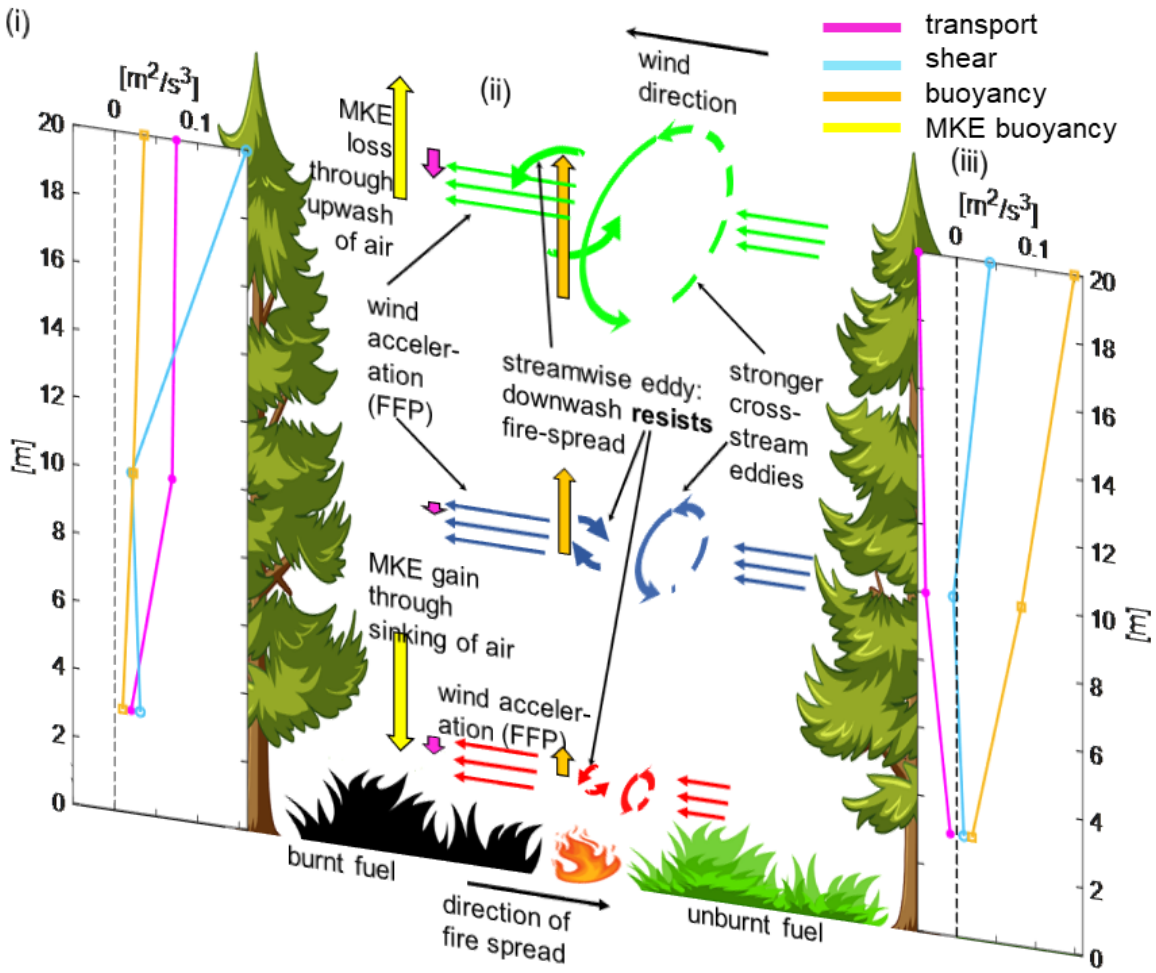


Figure 3.9: A brief summary of the turbulent processes in the 2011 sub-canopy backing fire (NJ2011) along with profiles of the TKE budget equation terms for a time instant in the (i) post-FFP period and (iii) pre-FFP period. Arrows are not to scale. (Vector figures of the pine tree, black bush, green bush, and flame taken from *www.vecteezy.com/free-vector/nature*)

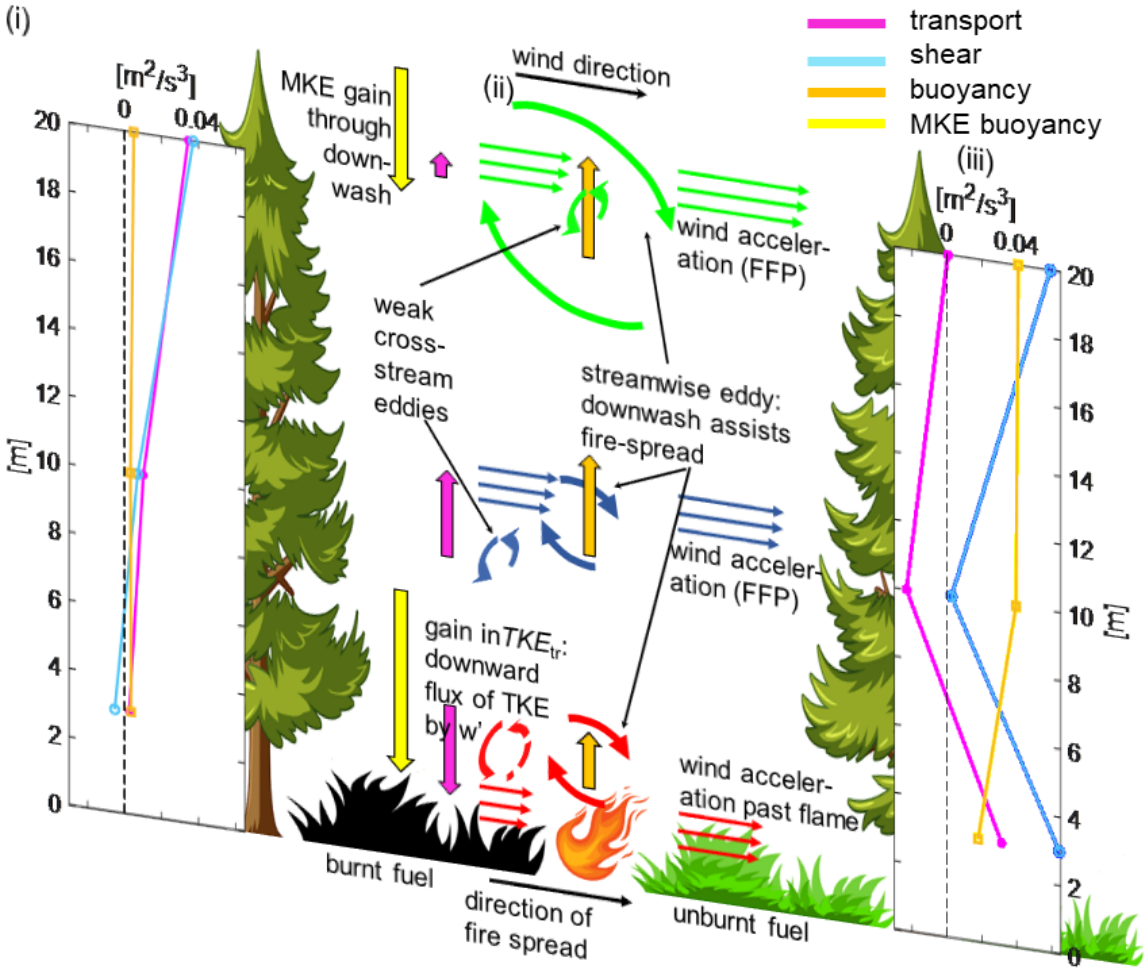


Figure 3.10: A brief summary of the turbulent processes in the 2019 sub-canopy heading fire (NJ2019) along with profiles of the TKE budget equation terms for a time instant in the (i) post-FFP period and (iii) pre-FFP period. Arrows are not to scale. (Vector figures of the pine tree, black bush, green bush, and flame taken from *www.vecteezy.com/free-vector/nature*)

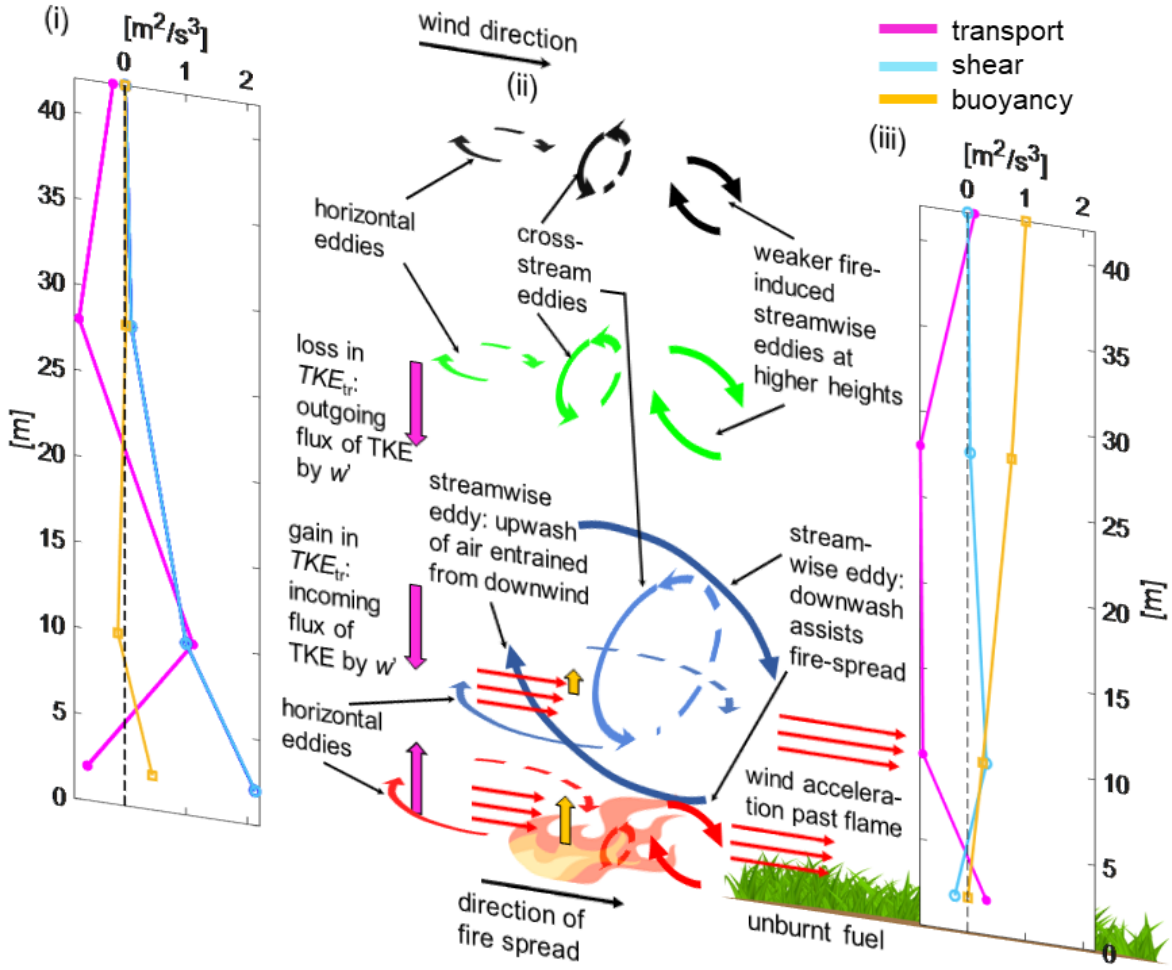


Figure 3.11: A brief summary of the turbulent processes in the 2006 grassland fire (TX2006) along with profiles of the TKE budget equation terms for a time instant in the (i) FFP period and (iii) pre-FFP period. Note that post-FFP profiles are not shown here. Arrows are not to scale. (Vector figures of the green grass and the flame taken from *www.vecteezy.com/free-vector/grass* and *www.vecteezy.com/free-vector/flame*, respectively)

Chapter 4

Investigating fire–atmosphere interaction in a forest canopy using wavelets

4.1 Background

Wildland-fire-spread behaviour in different vegetative fuel conditions is characterized to a large extent by turbulence patterns generated by the interaction between the flame and the surrounding atmosphere (55; 101; 19; 102; 85; 91). In the presence of a wildland fire in a forested environment, turbulent heat and momentum fluxes within the canopy and near the canopy top play a dominant role in modifying fire-spread rates during different stages of fire-front evolution (91). In addition, the dispersion of smoke emissions and the transport of firebrands are modulated significantly by these patterns (90; 103; 98). Increased turbulent mixing or diffusion of smoke near the canopy top compared to that near the surface greatly influences smoke out-flux from the canopy (90). The transport of firebrands is dependent

on their lofting by the buoyant plume and advection by the local wind, both of which are informed by spatial and temporal variations in patterns generated from the fire–atmosphere interplay (98; 104). Improvements in our understanding of fire-induced turbulence measurements demonstrably have bearings upon improved model predictions (101; 102; 105; 106; 37) that inform strategies for fire management operations. For instance, fast-running simulation tools such as QUIC-Fire (52), which are used for prescribed-fire planning, rely on observation-based algorithms to compute flow fields. Predictive tools for firebrand transport and smoke dispersion also rely considerably on experimental analyses to generate outputs that are more realistic (103) and consistent across different existing models for a given fire event (107). Quantifying the relevant temporal scales associated with processes observed during different stages of fire-front evolution is essential to model accuracy and evaluation. This necessitates a multi-scale analysis of turbulence measurements informed by fire–atmosphere interactions.

Despite the progress made in recent years (90; 81; 5; 105; 108), gaps exist in our understanding of the processes through which fire-induced turbulence redistributes heat and momentum within and above the forest canopy (5). While the current literature documents changes in the fraction of specific turbulent-flux events due to the passage of a fire-front, a meticulous examination of the temporal patterns of these events is currently necessary (5; 91). Furthermore, it is known that ramp–cliff structures in the temperature signal are signatures of certain organized turbulent-flux events that contribute significantly to heat transport in forested environments during no-fire conditions (109; 110; 111; 1). Ramp slopes (time rate of temperature increase along a ramp) have found application in the estimation of sensible heat fluxes within a forest canopy in no-fire conditions via the surface renewal analysis (112; 113; 1; 114). However, temporal variations in ramp–cliff structures resulting from the presence of fire are relatively less explored and warrant an investigation (90; 101; 103). Moreover, traditional methods used to infer coherent structures in the presence of a fire involve Reynolds decomposition, which entails either block averaging or computing moving averages (3; 81; 102). While these are useful in their own right, they have limitations arising

from the sensitivity of the inferred coherent motions to the averaging window; a larger averaging window delocalizes the coherent motions in time, while a smaller window makes it difficult to separate the mean terms from the turbulent fluctuations (102). Such averaging schemes either obscure the details of the finest-scale motions that characterize fire-induced turbulence or preclude the fire-induced variability in relatively longer time scales. Given that fire-induced turbulent motions are organized across a range of scales, these limitations present a critical obstacle to our understanding of them and necessitate the employment of alternative techniques.

Wavelet transforms have the principal advantage of providing information regarding the frequency content of a process as a function of time or space (115). Over the last few decades, wavelet transforms have found application in exploring diverse fundamental fluid mechanics and turbulence problems (e.g., (116; 117; 118; 119)). One of the earliest studies to employ wavelet analysis to explore turbulence within plant canopies was conducted by Collineau and Brunet (120; 121). They applied the Mexican Hat wavelet to high-frequency (16-Hz) sonic-anemometer and thermometer data collected near the canopy top in the Les Landes forest in south-western France. The method was found to be useful in obtaining an average duration scale of approximately 29 s for ramp–cliff structures in the temperature signal (121; 93). Moreover, the method was also utilized by Watanabe (122) in detecting ramp–cliff structures in the temperature output of large-eddy simulations (LES) conducted within and above a plant canopy. In another study, Gao and Li (111) applied the Mexican Hat wavelet to temperature and velocity measurements taken below, at, and above the canopy height in a deciduous forest. Patterns in the wavelet coefficients of the temperature data near the canopy top, plotted on a time–scale plane, illustrated the presence of unorganized background turbulence at time scales below 10 s and more organized plume-like structures near the 50-s time scale, which merged into low-frequency patterns at longer periods associated with large-scale atmospheric turbulent motions. Alternating updraft and downdraft regions were seen from the wavelet coefficients for the vertical velocity near the canopy top, near the

50-s time scale. Qiu et al. (123) conducted a pseudo-wavelet analysis (wherein mathematical constraints associated with a true wavelet analysis were relaxed) using the sawtooth function to identify ramp-like structures in the temperature measured in three different types of canopies. The pseudo-wavelet coefficients were utilized to obtain duration probability distributions for the ramp-like structures. The utility of wavelets in obtaining accurate estimates of turbulent fluxes was tested against the eddy covariance method by Schaller et al. (124). The study analyzed scalar turbulent fluxes obtained from 20-Hz wind and methane concentration data collected in the flat floodplains of a river by computing cross-wavelet transforms using both, the Mexican Hat and Morlet wavelets. The Mexican Hat wavelet was able to resolve short-duration turbulent events more precisely in time, owing to its better time-localization properties. Contrarily, the Morlet wavelet was better able to classify flux events on the basis of frequencies, owing to its better frequency-localization properties. In both cases, flux estimates obtained from the cross-wavelet transform were inferred to be more accurate, since the method is devoid of the steady-state assumption required for the eddy-covariance method.

While wavelets have found extensive application in investigating atmospheric turbulence in no-fire conditions (e.g., (120; 125; 111; 123; 126; 127; 128; 124; 129)), only a few studies have performed a wavelet-based analysis of fire-induced turbulence in vegetated environments. Seto et al. (88) computed the frequency spectrum for the wind velocity and temperature measured during four management-scale burn experiments, conducted over different conditions of fuel and topography, using wavelet analysis. For all four burn experiments, higher energy was registered in the velocity and temperature spectra at mid and high frequencies (above 10^{-2} Hz) during fire-front-passage (FFP) in comparison with the pre-FFP spectra. Heilman et al. (90) were able to identify the spectral frequency bands in which vertical velocity and streamwise velocity displayed peak energy values before, during, and after FFP for two backing surface fires of differing intensities (by $\mathcal{O}(1)$) in a forested environment. For the higher-intensity fire, higher energy was seen both during and post-FFP compared

to the pre-FFP spectra of the streamwise and vertical velocity components in the mid to high frequencies (above 10^{-1} Hz). In a recent study, Katurji et al. (130) obtained the time-integrated frequency spectra for sonic-anemometer data comprising streamwise and vertical wind velocity measurements taken at different heights along a meteorological tower during six experimental burns. Peak periods (time scales) for both velocity components ranged from 1 s–128 s across four burn plots and were found to increase with height from the fuel bed in each case.

Most of the aforementioned studies were able to indicate the peaking frequencies associated with FFP using wavelet analysis because of its ability to provide better smoothed spectral and co-spectral estimates compared to Fourier transforms in fluid flows (131; 88; 132). However, not many studies have utilized wavelets to explore the evolution of coherent structures associated with the measured data before, during, and after FFP. Moreover, the highly transient nature of fire-induced disturbances and the presence of intermittency rationalize the application of a wavelet-based time–frequency analysis to fire-induced turbulence measurements. In this study, we apply wavelet analysis to high-frequency sonic-anemometer data collected during a heading surface fire beneath the forest canopy to analyze coherent turbulence events in the time–frequency (or time-versus-periods) domain. The following questions encompass the major research questions that we aim to answer through this work.

(i) How does the presence of a fire impact the duration and amplitude of ramp–cliff patterns typically observed in the measured temperature signal? Moreover, are these impacts uniform across all heights within the canopy?

(ii) Does the presence of a fire enhance the degree of organization of heat- and momentum-flux-bearing eddies relative to no-fire conditions? If so, at what heights within the canopy and at which time scales?

(iii) What is the relative importance of heat-flux (thermally driven) events versus momentum-

flux (mechanically driven) events at different stages of the fire-front evolution? Is the Reynolds analogy violated by the presence of a fire? If so, is it more violated near the canopy top or in the canopy subspace?

4.2 Data Overview

Tower-based meteorological data collected during an operational prescribed burn, comprising a heading surface fire beneath the canopy in the New Jersey Pinelands National Reserve (NJPNR), conducted under the U.S. Department of Defense–Strategic Environmental Research Program (SERDP) (91; 133), are used in this analysis. The burn unit is located at the Silas Little Experimental Forest within NJPNR, New Lisbon, New Jersey, where the maximum canopy height (h_c) was approximately 20 m. On 13 March 2019, a line fire was ignited along the south-western edge of the burn unit at 1445 LT (local time = UTC − 4 h); the fireline progressed in the direction in which the ambient winds were strongest (southwesterly, 228°), i.e. the positive streamwise direction ($\hat{\mathbf{x}}$). The flame length was less than 2 m, and the fireline intensity was 179 $\mathrm{kW m^{-1}}$, with a spread-rate of 1.7 $\mathrm{m\,min^{-1}}$. A network of 20-m towers was employed to collect measurements before, during, and after fire-front-passage (FFP) across these towers. These are referred to as the South, West, East, and North Towers depending on their relative location in the burn plot (133), written here in chronological order of the arrival of the fire-front at each tower base. Additional measurements were collected by a long-term flux tower stationed within the burn unit (133). Moreover, a control tower located outside the burn unit, 185 m away from its northern edge (91), provides information regarding the local no-fire conditions during the burn experiment. It should be noted that before the arrival of the fire-front at the North Tower, a substantial shift in the ambient winds caused them to be realigned predominantly into the positive cross-stream direction ($\hat{\mathbf{y}}$). Therefore, the fire-front behaviour in relation to the ambient wind at the North Tower

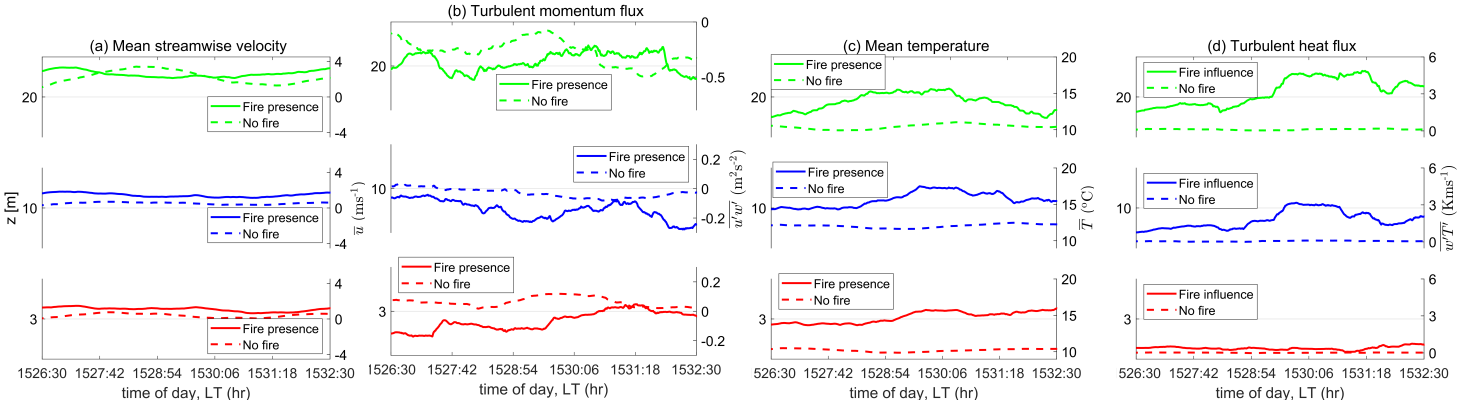
is characterized as flanking as opposed to heading at the other towers.

Data obtained from the West and Control Towers are primarily studied in this paper. The FFP time at the West Tower was reported to be 1525–1545 LT (91). Tower-mounted sonic anemometers measured air temperature (T) and east–west wind velocity, north–south wind velocity, and vertical wind velocity (w) components at 3 m, 10 m, and 20 m heights above ground level (AGL) at a sampling frequency of 10 Hz. Measured horizontal velocity components were rotated to obtain streamwise velocity (u) and cross-stream velocity (v) components. We denote the velocity components ($u,\ v,\ w$) and temperature (T) measured at height h as $u_h,\ v_h,\ w_h$, and T_h, respectively. The streamwise and cross-stream directions themselves were fixed for the entire duration of the burn experiment.

The prescribed burn experiment was conducted in the dormant season, i.e. the leaf area in the overstory vegetation was relatively low. The average plant-area density profile was highest ($0.037\,\mathrm{m^2 m^{-3}}$) at approximately $h = 12\,\mathrm{m}$ (91). A complete description of the burn experiment, including detailed illustrations of the burn plot and the ignition line, the location of the measurement towers, the type of understory and grass vegetation, and surface fuel loading, is given in refs. (5; 91; 133).

Figure 4.1 briefly summarizes the time evolution of the mean streamwise velocity ($\overline{u}$), turbulent momentum fluxes ($\overline{u'w'}$), mean temperature ($\overline{T}$), and turbulent heat fluxes ($\overline{w'T'}$) for all three measurement heights at both, the West and Control Towers, within two sub-durations that fall within the stipulated FFP time. Here, the overbar operator represents a moving average/mean (in this case, over a 2-minute moving window), while u', w' and T' denote deviations from the mean streamwise velocity ($\overline{u}$), the mean vertical velocity ($\overline{w}$), and the mean temperature ($\overline{T}$), respectively. Note that Fig. 4.1 is limited in its ability to provide information at scales shorter than the averaging window, as mentioned above; however, it serves to provide a brief overview of the data and as a good point of reference for our results. A detailed description of the heat-flux and momentum-flux events, including quadrant

(i) 1526:30–1532:30 LT



(ii) 1534–1540 LT

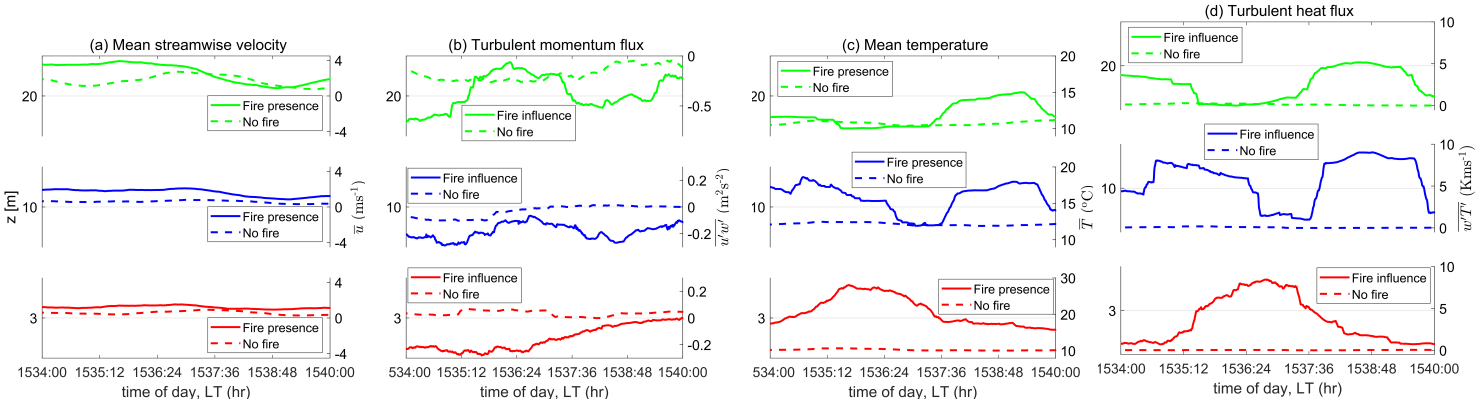


Figure 4.1: A height-wise summary of the (a) mean streamwise velocity ($\overline{u}$), (b) turbulent momentum flux ($\overline{u'w'}$), (c) mean temperature ($\overline{T}$), and (d) turbulent heat flux ($\overline{w'T'}$) within (i) 1526:30–1532:30 LT and (ii) 1534–1540 LT at both, the West and Control Towers. The two sub-durations fall within the stipulated FFP time.

analyses, pre-, during, and post-FFP is provided by Heilman et al. (91), while a first-order turbulent kinetic energy budget analysis of the current data is given by Desai et al. (102). Readers are referred to these works to obtain more context for the results presented here.

4.3 Theory and Methodology

4.3.1 Coherent Structures

Here, we first revisit the definitions of the individual heat- and momentum-flux events characteristic of the flow features in vegetative environments, which have been documented in previous works through a quadrant-analysis approach (5; 91; 134). Heat-flux events that are typically observed near the canopy top comprise warm updrafts ($w' > 0$, $T' > 0$), warm downdrafts ($w' < 0$, $T' > 0$), cool updrafts ($w' > 0$, $T' < 0$), and cool downdrafts ($w' < 0$, $T' < 0$). Among these, warm downdrafts and cool updrafts constitute counter-gradient motions and are typically less frequently observed. The streamwise momentum-flux events observed near the canopy top comprise sweeps ($u' > 0$ and $w' < 0$), ejections ($u' < 0$ and $w' > 0$), inward interactions ($u' < 0$ and $w' < 0$), and outward interactions ($u' > 0$ and $w' > 0$). In a forested environment, the strongest momentum-flux events near the canopy top typically comprise sweeps through which turbulence is imported into the canopy from the atmospheric surface layer (ASL) above in no-fire conditions, in relatively short time intervals (93; 75). The most frequent large-scale momentum-flux events comprise ejections, which are the next most important contributors to momentum-flux events (75). Generally, a coherent structure in a forested environment comprises weak ejections from the canopy top followed by a strong sweep of shorter duration into the canopy, while outward interactions and inward interactions are less frequently observed (109; 90; 91). It must be noted that while there is an overlap between the heat- and momentum-flux events as defined above, we

treat each class of events as distinct from the other in the analysis to follow (Sect. 4.4.3).

Time–height cross-sections comprising isotherms of temperature deviations from the mean and fluctuations in the velocity field (u', w') in no-fire conditions carry important information regarding heat- and momentum-flux events within and above a canopy, their interrelationship, and their mutual relationship with the temperature (micro)fronts depicted by the isotherms (109; 75). These have shown that ramp–cliff structures, both within a canopy and near the canopy top, are associated with the coherent flow features comprising predominantly of ejections and sweeps, as mentioned above (110; 109; 75). This connection is explained with help from the description given by Gao et al. (109) and Katul et al. (1) in no-fire conditions, as given below. Note that the description given by Katul et al. (1) pertains to carbon dioxide concentration in nocturnal (stable) conditions, while the explanation here pertains to temperature measurements in daytime (unstable) conditions. When a cool air parcel is swept into the canopy via a strong sweep-like downdraft from the ASL aloft in no-fire conditions, its temperature begins to increase along a ramp as it starts collecting heat from the forest surface (1). The increase in temperature along the ramp coincides with weak updrafts (mostly ejections) near the canopy top (109). The temperature of the air parcel continues to increase until the warm air parcel is finally driven out of the canopy into the ASL aloft by an ejection-like updraft. As cool air is swept into the canopy again, the measured temperature drops along a cliff. The cliff represents the sharp temperature micro-front that separates the strong sweep-like downdraft from the updraft events (109). The residence time of the air parcel within the canopy determines the time duration of the ramp structure between two consecutive occurrences of the micro-front. Ramp–cliff structures find application in the estimation of sensible heat fluxes using a method called surface renewal analysis introduced by Paw U et al. (112), which relies on the slope of the ramp structure (time rate of temperature increase along the ramp). More details regarding the procedure for accomplishing this are provided in refs. (113; 1).

4.3.2 Wavelet Transform and Analysis

Properties of the Continuous Wavelet Transform

The continuous wavelet transform (CWT) of a signal $g(t)$ is defined as (131):

$$W_g(a,b) = \frac{1}{\sqrt{a}} \int_{-\infty}^{\infty} g(t)\psi^* \left(\frac{t-b}{a}\right) \mathrm{d}t \tag{4.1}$$

Here $\psi(t)$ is called the "analyzing" wavelet, $\psi^*(t)$ is the complex conjugate of $\psi(t)$, and $\psi(\frac{t-b}{a})$ is called the wavelet function. Furthermore, b is the location parameter, a is the scale parameter (also called dilation parameter), and $W_g(a,b)$ represents the wavelet coefficient associated with scale a and location parameter b. The location parameter b controls the temporal location of the wavelet function in the time series (124). It must be mentioned that the characteristic frequency (f) associated with a wavelet of scale parameter a is given by $f = f_c/a$, where f_c is the passband centre frequency of the analyzing wavelet's power spectrum (131). This implies that the characteristic frequency of a wavelet and the associated scale have a one-to-one relation, which allows us to be able to allude to them interchangeably as we have done in the remainder of this work. The relative contribution of the energy content of $g(t)$ at scale a and location b is provided by the two-dimensional wavelet-based energy density function defined as $|W_g(a,b)|^2$ (131). A plot of $|W_g(a,b)|^2$ in the time–frequency (or time–scale) plane is referred to as the magnitude scalogram (131). The scalogram allows us to identify the temporal location and scale of the most energetic features of $g(t)$, facilitating the detection of multi-scale patterns (131; 115). Patterns in a given frequency band can be isolated by setting the wavelet coefficients outside that band to zero and performing an inverse wavelet transform using only the wavelet coefficients in the chosen frequency band (131). We refer to this technique as frequency- or scale-based signal reconstruction. The

inverse wavelet transform is given by (131; 115):

$$g(t) = \frac{1}{C_\psi} \int_{-\infty}^{\infty} \int_{0}^{\infty} W_g(a,b) \psi_{a,b}(t) \frac{\mathrm{d}a\mathrm{d}b}{a^2}, \text{where } \psi_{a.b}(t) = \frac{1}{\sqrt{a}} \psi \left(\frac{t-b}{a} \right). \tag{4.2}$$

Here, C_ψ is a normalizing constant.

An important characteristic of the wavelet transform comprises the differences in its time–frequency localization behaviour at different frequencies (or scales) in the time–frequency plane (131; 115). These differences arise from Heisenberg's uncertainty principle, according to which, "one cannot measure with arbitrarily high resolution in both time and frequency" (to quote directly from Kumar and Foufoula-Georgiou (115)): high resolution in time will always be accompanied by low resolution in frequency and vice versa. This is typically visualized with the help of Heisenberg boxes (or cells) that constitute the time–frequency plane with time along the x axis and frequency along the y axis. High-frequency features are well-resolved in time but with higher uncertainty in their frequency localization. This manifests in the scalogram as high energy density that is diffused along the frequency axis, i.e. across multiple frequencies or scales, but is well-localized in time (taller, thinner Heisenberg boxes) when analyzing higher-frequency events. Conversely, low-frequency features are well-resolved in frequency but with high uncertainty in time localization. This manifests in the scalogram as high energy density that is diffused along the time axis, i.e. across multiple time instances, but well-localized in frequency (shorter, wider Heisenberg boxes) (115).

Another practical limitation of the wavelet transform comprises its boundary effects. Wavelet coefficients computed close to the boundaries of a measured (finite) signal are contaminated by the discontinuous nature of the boundaries (edges) and must be discarded in the analysis (131). This region of "untrustworthy" wavelet coefficients becomes wider as we go higher up in scale (at lower frequencies). On the magnitude scalogram, this region manifests as a cone when the frequency axis is plotted on a logarithmic scale and is referred to as the cone

of influence (131). A detailed description of the wavelet transform along with the criteria that a function must satisfy to be classified as a wavelet, the Heisenberg boxes, the cone of influence (COI), the inverse wavelet transform, and the definition of the passband centre frequency is provided by refs. (131; 115).

Finally, we add that continuous wavelet transforms are widely-used efficient tools for analyzing time series whose spectral properties vary over time. CWT analyses can be viewed as highly redundant multi-scale analyses where the scales of interest do not need to be predefined. Even if the information carried by the wavelet coefficients is strongly correlated from one scale to the next, the continuity in scale as well as time allows us to locate the features of interest along both the scale and time axes, accurately (135). We, however, note that if the objective of the analysis is to derive a low-order parametric representation of the signal or to compress (reduce the dimensionality of) the data, redundancy is not desirable; in these cases, the use of discrete non-redundant wavelet transforms is preferable (136).

Application of the Wavelet-based Methodology

In the following section (Sect. 4.4.1), patterns in the temperature signal ($T(t)$ or simply T) are investigated using the magnitude scalogram (plot of $|W_T(a,b)|^2$ with time along the x axis and frequency along the y axis) obtained from the wavelet transform of $T(t)$ at $h = 3\,\mathrm{m},\ 20\,\mathrm{m}$ using the Mexican Hat wavelet. Given its symmetric structure, the Mexican Hat wavelet does not introduce asymmetry into the wavelet transform. The Mexican Hat wavelet prioritizes time localization over frequency localization (131; 124), making it suitable for analyzing short-lived wide-band features such as ramp–cliff structures. Furthermore, rather than for analyzing narrow-band periodic signals, the Mexican Hat wavelet is useful for identifying abrupt discontinuities (edge detection) in the signal. An abrupt discontinuity comprising a rapid switching from a high magnitude to a low magnitude in $g(t)$ manifests in the scalogram as a region of low (near-zero) energy density flanked on either side by regions of high energy

density, which spans multiple scales (131). Another pattern that can be identified by the Mexican Hat wavelet comprises a sudden increment followed by an exponential tail, which is called an exponential discontinuity (131). This manifests in the magnitude scalogram as alternating regions of high and low energy density (along the time axis) that span a range of frequencies and are well-localized in time at higher frequencies but delocalized in time at lower frequencies. The *cwtft* function of MATLAB is used for the CWT, which performs the operation presented in Eq. (4.1) for a finite time series, and the COI is computed manually. The length of the signal used for the CWT spans 30 minutes (1800 seconds) of data: 5 minutes pre-FFP, 20 minutes during FFP, and 5 minutes post-FFP. Magnitude scalograms are represented as colour contours within the COI on the time–frequency plane. The COI is obtained by computing the wavelet coefficients for a zero function ($g(t) \equiv 0$) of the same length as $T(t)$ and with artificially imposed step discontinuities at each edge where $g(t)$ is set to 1. The regions of non-zero wavelet coefficients near the edges are the regions of "untrustworthy" wavelet coefficients and their inner boundaries give us the COI.

In Sect. 4.4.2, an approximation to the original temperature signal is reconstructed in a certain frequency band using MATLAB's *icwtft* function, which performs the operation presented in Eq. (4.2) for a finite time series. As mentioned above, regions of low energy density (low $|W_g(a,b)|^2$), flanked by regions of high energy density (high $|W_g(a,b)|^2$) in the scalogram represent abrupt discontinuities in $g(t)$, when using a Mexican Hat wavelet. When the time series of the wavelet coefficients ($W_g(a,b)$) associated with an appropriate frequency/scale (a_0) is plotted alongside the reconstructed signal, the abrupt discontinuities correspond to the zero-crossings at which the wavelet coefficients transition from positive to negative ($W_g(a_0,b) = 0$, $\frac{\mathrm{d}W_g(a_0,b)}{\mathrm{d}t} < 0$). This technique, referred to as "jump detection", was utilized by Collineau and Brunet (121) to track cliffs (abrupt discontinuities) in the measured temperature ($g \equiv T$) in no-fire conditions. The time between subsequent "jumps" (cliffs) defined the event duration of a ramp–cliff structure. In the current study, we utilize the jump-detection technique to track cliffs in the reconstructed temperature signal. We extend

this technique further to track ramps in the reconstructed temperature signal. We first note that the onset of a ramp corresponds to a trough or local minimum in the time series of the wavelet coefficients $\left(\frac{\mathrm{d}W_T(a_0,b)}{\mathrm{d}t} = 0\right)$. We can then trace each ramp in the reconstructed signal between a trough (local minimum) in $W_T(a_0, b)$ and the first zero-crossing that succeeds the trough where the slope is negative, i.e. the location of the immediately successive cliff. Once an individual ramp is traced, the time duration between the onset of the ramp and the peak temperature attained along the ramp in the reconstructed temperature signal can be used to quantify the ramp duration. Note that while Collineau and Brunet (121) computed the duration of an entire ramp–cliff structure, we compute the duration of only the ramp component. Moreover, we compute the slopes of the ramp and the cliff. The peak temperature attained along the ramp and the temperature at the onset of the ramp are used to compute the ramp slope. The peak temperature and the temperature associated with the zero-crossing mentioned above are used to compute the slope of the cliff. The application of this procedure to the reconstructed temperature signals at the West and Control Towers is illustrated in Fig. 4.2.

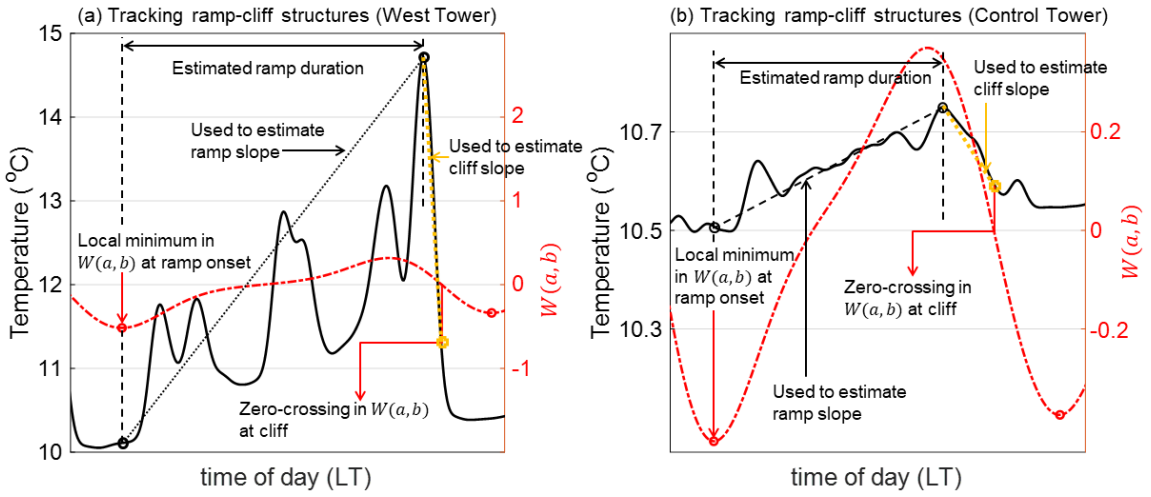


Figure 4.2: Schematic illustrations of the technique used to compute the ramp duration, ramp slope, and cliff slope of (a) a fire-modulated ramp–cliff structure at the West Tower and (b) a ramp–cliff structure in no-fire conditions at the Control Tower

Finally, to investigate the effects of FFP on heat- and momentum-flux events, we resort to a cross-wavelet coherence analysis in Sect. 4.4.3. Cross-wavelet analysis between $w(t)$ and $T(t)$ can be used to explore the scales at which fire-induced effects on the heat flux are relevant and to assess temporal variations in the most coherent heat-flux events among those mentioned above (Sect. 4.3.1). Cross-wavelet analysis between $u(t)$ and $w(t)$ can serve a similar purpose for assessing the streamwise momentum-flux events mentioned in Sect. 4.3.1. We use the Morlet Wavelet to compute the cross-wavelet coherence. Unlike the Mexican Hat wavelet, the Morlet wavelet is a complex wavelet and has the advantage of giving us information from the local relative phase between the two component time series. Moreover, the Morlet wavelet provides good frequency localization, allowing for a more accurate estimation of the scales associated with turbulent-flux events (137; 124). Obtaining the cross-wavelet coherence is a two-step process. First, we compute the cross-wavelet transform. The cross-wavelet transform (XWT) of two time series $p(t)$ and $q(t)$ is defined as $W_{pq} = W_p W_q^*$, where $*$ denotes complex conjugation (138). The cross-wavelet power is defined as $|W_{pq}|$, whereas the complex argument $\arg(W_{pq})$ is interpreted as the local relative phase between $p(t)$ and $q(t)$ in the time–frequency plane. The wavelet coherence is computed in the second step. According to Torrence and Webster (139), the wavelet coherence between two time series $p(t)$ and $q(t)$ as a function of scale ($R_{pq}(a)$) is defined as

$$R_{pq}(a) = \frac{\mathrm{S}(|W_{pq}a^{-1}|)}{\sqrt{\mathrm{S}(a^{-1}|W_p|^2)\mathrm{S}(a^{-1}|W_q|^2)}} \tag{4.3}$$

where S is a smoothing operator that comprises functions that perform smoothing along both time and scales, independently. More information about this definition is provided by Grinsted et al. (138). For our analysis, we use MATLAB's *wcoherence* function, which uses the analytic Morlet wavelet to return the magnitude-squared coherence (R_{pq}^2) as a function of time and scale. In the *wcoherence* function, a Guassian function is used for smoothing along time and a moving-average operator is used for smoothing across scales. The cross-

wavelet coherence between w and T signals on one hand, and u and w signals on the other is computed near the canopy top ($h = 20\,\mathrm{m}$) within two 6-minute-long time windows: (i) an earlier window during FFP from 1526:30 to 1532:30 LT and (ii) later during FFP from 1534:00 to 1540:00 LT. Since the large-scale eddies associated with momentum-flux events are typically the most significant near the canopy top compared to the lower heights, we restrict our coherence analysis to $h = 20\,\mathrm{m}$ in this work. However, we have included the coherence analysis within the canopy subspace (at the lower heights) in the Appendix. In regions of high coherence, the local relative phase ($\arg(W_{wT})$ and $\arg(W_{uw})$) can be used to determine the type of heat- or momentum-flux event as defined in Sect. 4.3.1.

4.4 Results and Discussion

4.4.1 Temperature Scalograms

Figure 4.3 depicts the magnitude scalograms of the measured temperature signal at the West Tower and Control Towers, at $h = 3\,\mathrm{m}$ and $20\,\mathrm{m}$, with the 20-minute FFP duration delineated by the red dashed vertical lines. The measured temperature signals at the West Tower, at $h = 3\,\mathrm{m}$ (T_3) and at $h = 20\,\mathrm{m}$ (T_{20}), are shown in Figs. 4.3(a) and 4.3(b), respectively. We first focus on the scalogram of T_3 at the West Tower. In Fig. 4.3(c), regions of high energy density attributed to the fire influence are seen during FFP (1525–1545 LT) in the highest frequency band ($f \geq 0.1\,\mathrm{Hz}$). We compare this with the highly diminished energy density in this high-frequency band in the 5 minutes pre-FFP and 5 minutes post-FFP. This suggests that some fire-induced activity is present in the high-frequency regime ($f \geq 0.1\,\mathrm{Hz}$), where ambient atmospheric temperature perturbations are considerably weaker. It is in this high-frequency band that we expect intermittent burst-like events associated with the fire, if any, to manifest as regions of high energy density that are well-localized in time and interspersed

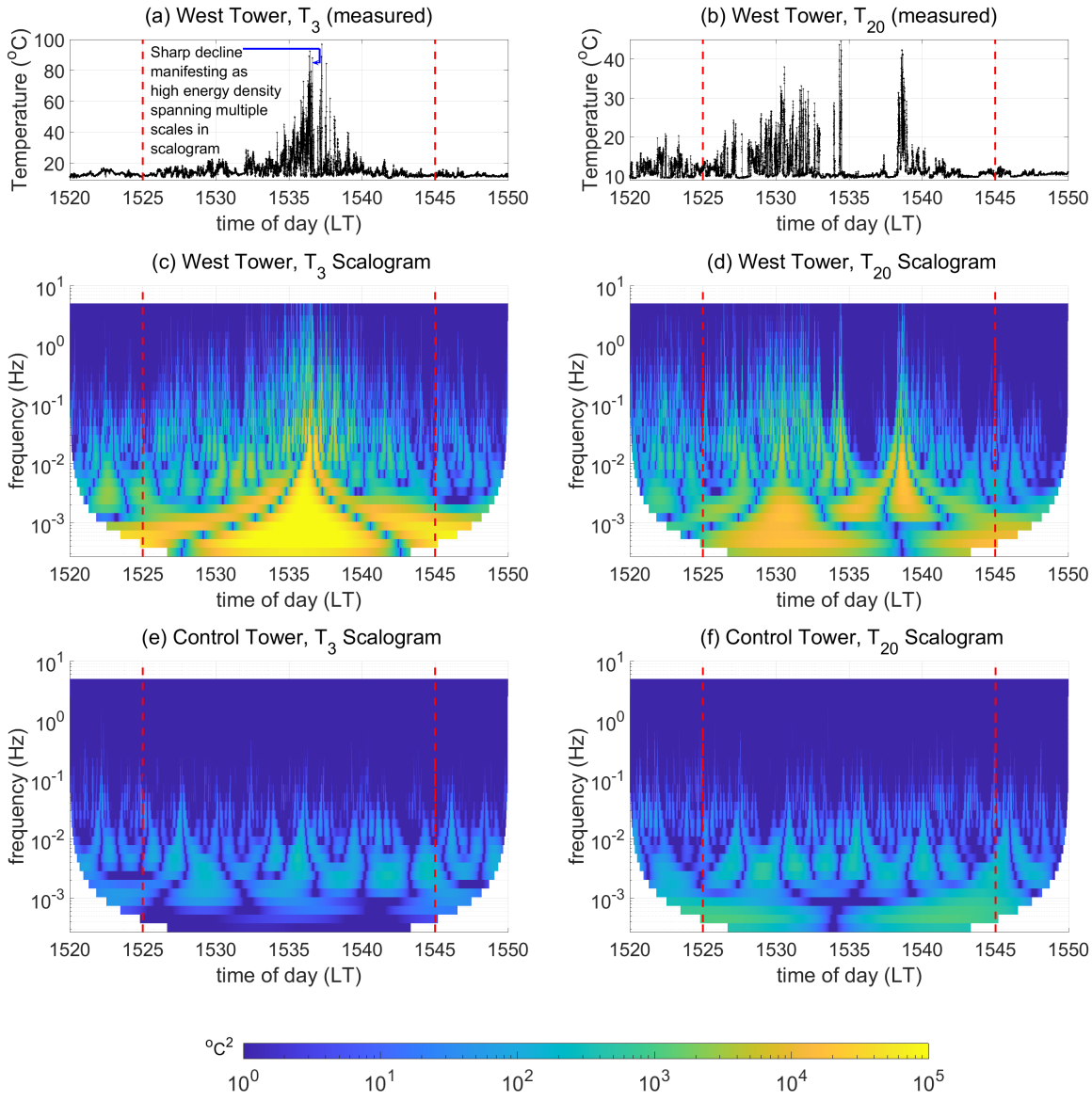


Figure 4.3: Measured temperature at the West Tower at $h =$ (a) 3 m (T_3) and (b) 20 m (T_{20}) along with the magnitude scalograms of the temperature signal at the West Tower at $h =$ (c) 3 m and (d) 20 m and magnitude scalograms of the temperature signal at the Control Tower at $h =$ (e) 3 m and (f) 20 m for the 30-minute duration comprising 5 minutes pre-FFP, 20 minutes during FFP (between red dashed lines), and 5 minutes post-FFP at the West Tower

among regions of considerably diminished energy density.

Next, a pattern of high energy density spanning a range of frequencies (multiple scales) is seen in Fig. 4.3(c): intense yellow regions corresponding to $|W_T|^2 \geq 10^4\,[^{\circ}\mathrm{C}^2]$ that alternate with blue regions corresponding to $|W_T|^2 \leq 1\,[^{\circ}\mathrm{C}^2]$ across the 20-minute FFP duration at

frequencies below 0.1 Hz, with the yellow regions becoming delocalized in time at lower frequencies. This pattern suggests that T_3 increases relatively gradually (resembling an exponential rise) to an extremely high temperature as the fire-front approaches the tower base, which is followed by a rather sharp and substantial decline. In other words, the pattern resembles a "reversed" exponential discontinuity (see Sect. 4.3.2). This pattern is also visible in the measured temperature signal (T_3) shown in Fig. 4.3(a). The highest temperature value attained before the sudden decline in T_3 can be attributed to the presence of the fire-front close enough to the base of the tower to exert the strongest influence at $h = 3\,\text{m}$. Note that this will not be exactly at the location of the tower base but a short distance ($\sim$1 ft) away (34), due to the tilting of the flame in the direction of the wind. In the mid-frequency band ($10^{-2}\,\text{Hz} < f \leq 10^{-1}\,\text{Hz}$), we see regions of near-zero energy density (dark blue regions) surrounded on either side by regions of high energy density (yellow regions). These regions (of near-zero energy density) represent sudden "cliff"-like switching in T_3 (see Sect. 4.3.2). While these cliff-like patterns are present in the measured temperature, i.e. T_3, across the entire 20-minute FFP duration (Fig. 4.3(a)), they are more evidently seen within the duration in which the strongest temperature fluctuations are recorded near the tower base (approximately 1534–1540 LT).

We now focus on the magnitude scalogram of T_{20} at the West Tower, which is shown in Fig. 4.3(d). It is easily discerned that the overall energy density in T_{20} is lower than that observed in T_3, especially across the low-frequency band ($f \leq 10^{-2}\,\text{Hz}$). This is expected due to the closer proximity of the flame to $h = 3\,\text{m}$ as opposed to $h = 20\,\text{m}$. Moreover, the tilting of the flame in the direction of the wind results in fire-induced disturbances at the higher heights before the arrival of the fire-front at the base of the tower. This manifests as the regions of increased energy density seen in the high-frequency band ($f \geq 0.1\,\text{Hz}$) earlier on (1520–1535 LT), corresponding to the increased variability in the measured temperature signal (T_{20}) within that duration as seen in Fig. 4.3(b). Furthermore, large regions of highly diminished energy density (dark blue regions), interspersed by regions of high energy density

(yellow regions) that are well-localized in time, are seen in the latter stages during FFP (1533–1545 LT) in the high-frequency band ($f \geq 0.1$ Hz) of the scalogram. This pattern is attributed to intermittent burst-like structures that are noticeably seen in T_{20} within this time duration (Fig. 4.3(b)). Again, in the mid-frequency band (10^{-2} Hz $< f \leq 10^{-1}$ Hz), we see regions of near-zero energy density (dark blue regions) flanked on either side by regions of high energy (yellow regions), which are manifestations of rapid "cliff"-like switching in T_{20}. We expect these "cliff"-like switching patterns to be associated with ramp–cliff structures that are potentially modulated by FFP.

We now compare the magnitude scalograms for the West Tower temperature signals with those for the temperature measured at the Control Tower in Figs. 4.3(e) and 4.3(f). It is immediately seen that the energy density ($|W_T|^2$) is lower than that seen for the West Tower at both heights across all the frequencies plotted in the scalograms. Moreover, in no-fire conditions, the energy density in the high-frequency band ($f \geq 0.1$ Hz), which is associated entirely with the ambient atmospheric turbulence, is considerably lower in comparison to that in the presence of a fire. However, signatures of ramp–cliff structures, associated with atmospheric (canopy) turbulence, continue to be observed in the mid-frequency band where cliffs are represented by regions of low $|W_T|^2$ flanked on either side by regions of higher $|W_T|^2$. A visual inspection shows that the cliffs are temporally further apart at the Control Tower as compared to the West Tower.

4.4.2 Scale-based Signal Reconstruction: Ramp–cliff Structures

As discussed in Sect. 4.4.1, signatures of ramp–cliff patterns are observed in the mid-frequency band of the magnitude scalograms for both T_3 and T_{20}. We, therefore, reconstruct the temperature signal within time scales (periods) ranging from 3 s to 90 s from the corresponding wavelet coefficients in the manner explained in Sect. 4.3.2. This range includes

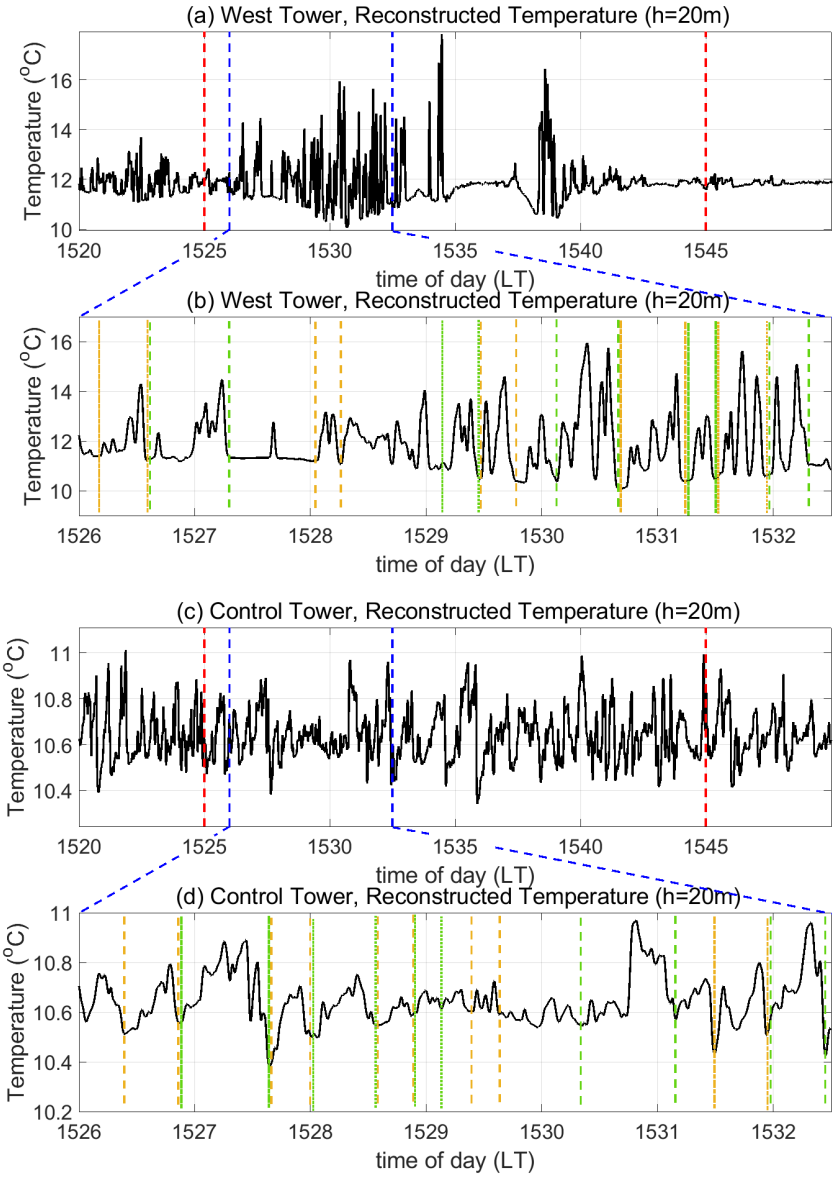


Figure 4.4: Reconstructed temperature signal at $h = 20\,\mathrm{m}$ in scales ranging from 3 s to 90 s for (a) 1520–1550 LT and (b) 1526–1532:30 LT at the West Tower (where fire influence is experienced) as well as for (c) 1520–1550 LT and (d) 1526–1532:30 LT at the Control Tower (no-fire conditions). In (a) and (c), red dashed vertical lines delineate the stipulated FFP time at the West Tower, and blue dashed lines delineate the sub-duration plotted in (b) and (d), respectively. In (b) and (d), dashed and dash-dotted vertical lines enclose examples of ramp–cliff structures: two consecutive vertical lines with the same colour and style enclose one such observed structure. Not all structures are marked

most of the mid-frequency band and some scales from the high-frequency band, which are required to be able to detect the high-frequency component of a ramp–cliff structure, i.e. the "cliff". The reconstruction in this range omits the time scales or periods shorter than

3 s (high-frequency fluctuations) and longer than 90 s (low-frequency turbulent motions), thereby acting as a band-pass filter. Figures 4.4(a) and 4.4(b) show the reconstructed temperature signal at $h = 20$ m within these time scales (periods) for the entire 30-minute duration at the West Tower and a shorter sub-duration of the FFP time (1526:00–1532:30 LT as shown by the blue dashed lines), respectively. Intermittent burst-like events are seen from 1534 LT onward. It appears that the effect of fire-induced turbulence is diminished between the burst-like events where the background canopy turbulence starts to become more effective. Owing to the tilting of the flame in the direction of the wind, we expect to see potential modulations in the ramp–cliff structures earlier on during FFP. We, therefore, focus on ramp–cliff patterns seen in the reconstructed temperature signal in an earlier sub-duration of the FFP time, i.e. from 1526:00 to 1532:30 LT, as shown in Fig. 4.4(b).

In Fig. 4.4(b), some examples of ramp–cliff structures influenced by the buoyant plume (referred to as fire-modulated ramp–cliff structures here on) are delineated using dash-dotted and dashed vertical lines. It is expected that the ramp patterns during this time will be shorter in duration, while the cliffs will be steeper compared to those in no-fire conditions. To explain this hypothesis, we return to the connection between ramp–cliffs and turbulent-flux events described in Sect. 4.3.1. When a sweep-like downdraft brings a cool air parcel into the canopy from the ASL aloft, its temperature is expected to increase along a ramp as it collects heat from the surface fire. Since the flame acts as a stronger source of heat as compared to the forest surface under no-fire conditions, the temperature of the air parcel is expected to increase more rapidly along a ramp and up to a large magnitude. Updrafts from the buoyant plume are then expected to drive the warm air parcel out of the canopy sooner than in no-fire conditions due to their increased frequency and strength, which would cause ramp durations to be shorter than in no-fire conditions. This would then be followed by a sudden decrease in temperature from the higher magnitude attained due to the fire to ambient temperature through a cool downdraft, causing the cliff to become steeper.

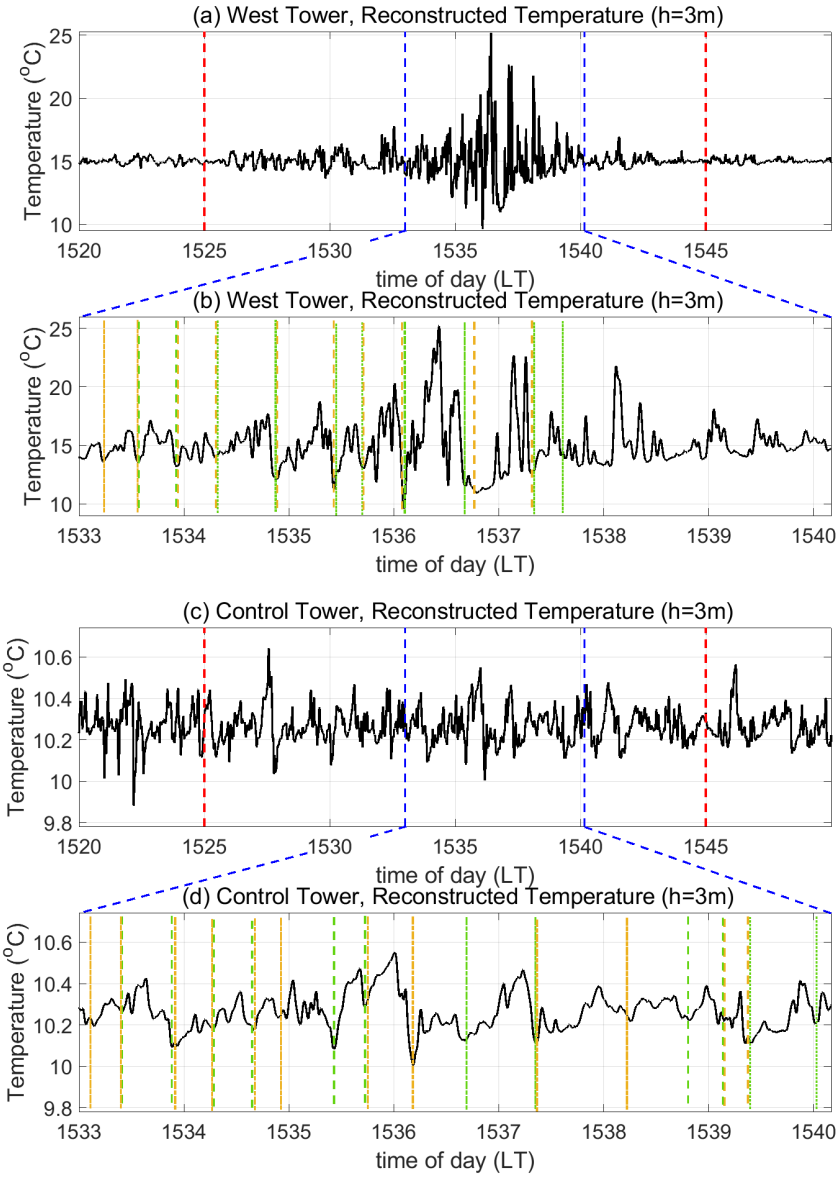


Figure 4.5: Reconstructed temperature signal at $h = 3\,\mathrm{m}$ in scales ranging from 3 s to 90 s for (a) 1520–1550 LT and (b) 1533:00–1540:10 LT at the West Tower (where fire influence is experienced) as well as for (c) 1520–1550 LT and (d) 1533:00–1540:10 LT at the Control Tower (no-fire conditions). In (a) and (c), red dashed vertical lines delineate the stipulated FFP time at the West Tower, and blue dashed lines delineate the sub-duration plotted in (b) and (d), respectively. In (b) and (d), dashed and dash-dotted vertical lines enclose examples of ramp–cliff structures: two consecutive vertical lines with the same colour and style enclose one such observed structure. Not all structures are marked

With this context, we attempt to compare Figs. 4.4(a) and 4.4(b) with the reconstructed temperature signal at the Control Tower. Figures 4.4(c) and 4.4(d) show the reconstructed temperature signal near the canopy top ($h = 20\,\mathrm{m}$) at the Control Tower, within time scales

(periods) ranging from 3 s to 90 s for the entire 30-minute duration and a shorter sub-duration of the FFP time from 1526:00 to 1532:30 LT, respectively. From a visual inspection, ramp–cliff structures can be seen in the temperature signal for the entirety of the 30-minute time duration shown in Fig. 4.4(c). The drop in temperature along a cliff is less than 1°C (less steep) due to the absence of the influence of fire at the Control Tower. Some examples of ramp–cliff structures are delineated using dash-dotted and dashed vertical lines in Fig. 4.4(d). In ramp–cliff structures of relatively higher variability, the ramps appear to be of noticeably longer duration with gradual temperature increments compared to those seen at the West Tower during this time (Fig. 4.4(b)).

Fire-modulated ramp–cliff structures can also be observed closer to the flame ($h = 3$ m), as shown in Fig. 4.5. As seen from the reconstructed temperature signal at the West Tower (Fig. 4.5(a)), the influence of the fire is strongest at $h = 3$ m from 1533 to 1540:10 LT (delineated by blue dashed lines) compared to the rest of the FFP duration. Figure 4.5(b) depicts the reconstructed temperature signal at the West Tower in this shorter sub-duration. Ramp–cliff structures with longer durations, seen from 1534 to 1535:30 LT, transform into structures with shorter durations post 1535:30 LT in Fig. 4.5(b). In contrast, several ramp–cliff structures at this height around this time are observed to be of noticeably higher durations at the Control Tower, i.e. in no-fire conditions (Fig. 4.5(d)). Moreover, temperature increments along ramps appear to be more gradual and cliffs appear to be less steep as compared to those at the West Tower.

Statistical Analysis of Ramp-like Structures

Quantitative evidence to support our hypothesis is obtained by computing a statistical distribution of the duration of the fire-modulated ramps. In order to obtain such a distribution, each ramp–cliff structure in the reconstructed temperature signal is first tracked individually using the procedure described in Sect. 4.3.2. Note that Collineau and Brunet (121)

used the peak frequency from the wavelet spectrum of the measured temperature as a_0 (see Sect. 4.3.2) to track the ramp–cliff structures in no-fire conditions. In the current analysis, the time scale associated with the peak frequency of the wavelet spectrum falls in the low-frequency band (discussed in Appendix) and exceeds the range of time scales being explored here for ramp–cliff structures. Therefore, we resort to a much shorter time scale (higher frequency compared to the peak frequency) to obtain a_0. This is justified since the time scales associated with the fire-modulated ramp–cliff structures at different heights are comparatively much shorter (refer to Appendix).

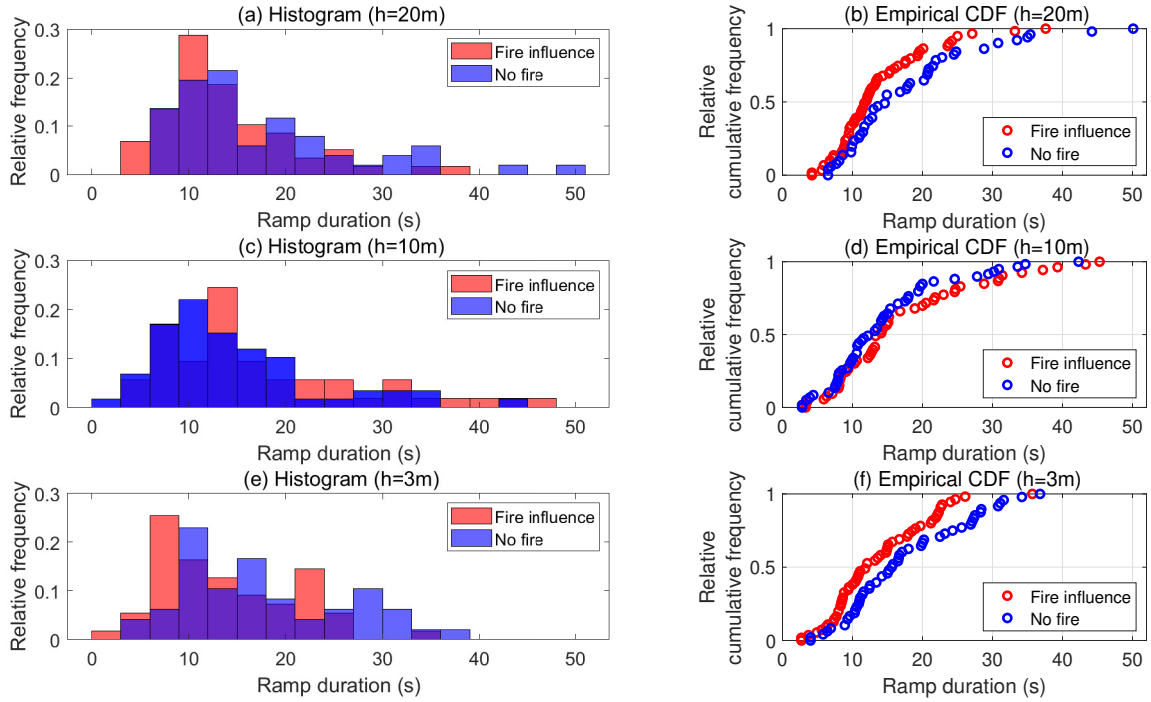


Figure 4.6: Histograms and empirical cumulative distribution functions of ramp durations associated with both, fire influence and no-fire conditions at all three measurement heights

Figure 4.6 shows histograms of the ramp durations obtained within each short sub-duration of the FFP time during which the fire influence is strongest near the canopy top (Fig. 4.6(a)), at the mid-canopy height (Fig. 4.6(c)), and near the surface (Fig. 4.6(e)). The corresponding empirical cumulative distribution functions (eCDFs) are plotted in Figs. 4.6(b), 4.6(d) and 4.6(f), respectively. The time series of wavelet coefficients ($W_T(a_0, b)$) corresponding to a time

scale of approximately 23.3 s is utilized to track ramp–cliff structures. In order to obtain a sizeable sample of ramps modulated by the fire influence at each height, reconstructed temperature signals from the South, West, East, and Flux Towers are used. Ramps are concomitantly sampled from the reconstructed temperature signals at the Control Tower to obtain a duration distribution for ramps in the background no-fire canopy conditions for comparison.

Both near the surface ($h = 3$ m) and the canopy top ($h = 20$ m), it is seen that a higher percentage of fire-modulated ramps is associated with shorter durations as compared to no-fire conditions (Control Tower). The histograms associated with the Control Tower at these heights are characterized by thicker and/or longer tails relative to the most probable durations. It must be noted that the histograms at the Control Tower are qualitatively similar to the duration distribution of ramp structures in vegetation stands obtained using a Ramp "pseudo"-wavelet by Qiu et al. (123) and in a pine forest obtained using the Mexican Hat wavelet by Collineau and Brunet (121), both in no-fire conditions. Particularly near the canopy top (Fig. 4.6(a)), where the influence of the background atmospheric canopy-scale eddies is highest in no-fire conditions, the ramp durations at the Control Tower surpass 50 s (long tail). Furthermore, near the surface (Fig. 4.6(e)), a higher percentage of ramps in no-fire conditions are seen with longer durations (thicker tail). At both heights, it is seen that the most probable durations of fire-modulated ramps are less than 10 s. The most probable fire-modulated ramp durations near the surface are observed to be shorter than those near the canopy top, due to the closer proximity of the fire to $h = 3$ m resulting in more frequent and stronger fire-induced updrafts (preceding cliffs). Furthermore, the modal duration for fire-modulated ramps is lower than the modal duration for no-fire conditions at these heights, as seen from Table 4.1. Moreover, the mean duration of a fire-modulated ramp is approximately 4 s (20%) shorter than the mean ramp duration during no-fire conditions at these heights, while the difference amounts to more than 10 s at the 95^{th} percentile. Shorter ramp durations also allow for a higher number of fire-modulated ramps be to sampled as

compared to ramps in no-fire conditions for a given time duration, as shown in Table 4.1.

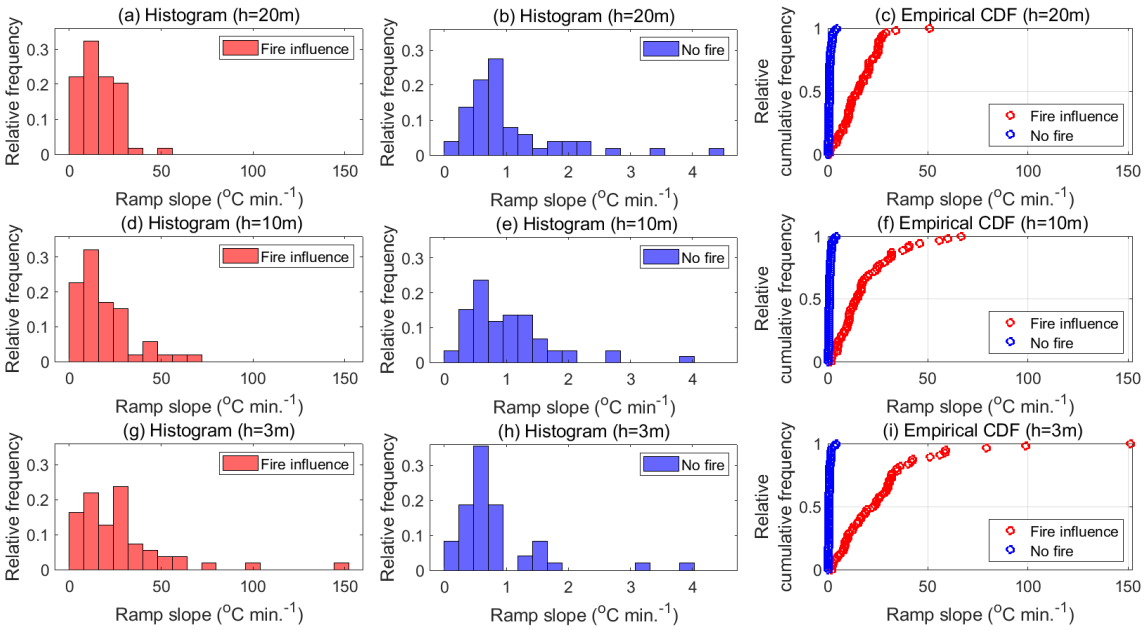


Figure 4.7: Histograms of ramp slopes associated with both, fire influence and no-fire conditions, at all three measurement heights, along with the corresponding empirical cumulative distribution functions

Interesting observations can be made for the mid-canopy height. At $h = 10\,\mathrm{m}$, it is seen that the most probable durations of fire-modulated ramps (Fig. 4.6(c)) are longer than those seen near the canopy top and the surface. In fact, near the tail end of the histogram, fire-modulated ramps with durations longer than 40 s are also seen as outliers. Moreover, Fig. 4.6(d) shows that a higher percentage of fire-modulated ramps are associated with longer durations than ramps in no-fire conditions. This is symptomatic of intermittency at the mid-canopy height. Long spells comprising weak sweep-like downdrafts that are attributed to the background canopy turbulence between strong and sudden fire-induced temperature fluctuations result in longer effective fire-modulated ramp durations. This suggests that in the time duration when the fire influence is strongest mid-canopy, the background canopy turbulence is also quite effective at this height. Given that the influence of background canopy-scale eddies that originate near the canopy top is known to extend down to the mid-canopy height in no-fire conditions (93), it is expected for the fire influence and background

canopy turbulence to interact in this manner at this height. Furthermore, as mentioned in Sect. 4.2, leaf area was relatively low in the overstory during this burn experiment. This would have allowed for higher accessibility of the background canopy-scale eddies to the mid-canopy height, reinforcing their influence at $h = 10\,\mathrm{m}$.

It must be noted that ramp durations are not the only measure of the fire influence at different heights. As seen above, it is possible to track ramps in no-fire conditions at $h = 10\,\mathrm{m}$, which have relatively shorter periods than fire-modulated ramps. However, the increase in temperature along such ramps is considerably low, so that their contribution to the heat flux is relatively insubstantial. Therefore, we need to consider another measure of the influence of the fire-front, i.e. the ramp slope. Histograms and eCDFs of the slopes of fire-modulated ramps and ramps in no-fire conditions at all three heights are shown in Fig. 4.7. The histograms show that slopes of fire-modulated ramps near the canopy top can go up to $50\,^{\circ}\mathrm{C\,min.^{-1}}$ (Fig. 4.7(a)) and of those near the surface can go up to $150\,^{\circ}\mathrm{C\,min.^{-1}}$ (Fig. 4.7(g)), while ramp slopes in no-fire conditions are bounded by $5\,^{\circ}\mathrm{C\,min.^{-1}}$ (Figs. 4.7(b) and 4.7(h)). At $h = 10\,\mathrm{m}$, it is seen that the most probable ramp slopes under fire influence (Fig. 4.7(d)) are considerably higher than in no-fire conditions (Fig. 4.7(e)). This captures the effect of strong and sudden upsurges in temperature induced by the fire even as the influence of the background canopy turbulence between these upsurges causes the effective ramp periods to increase. The eCDFs indicate that a higher percentage of fire-modulated ramps are associated with higher slopes as compared to ramps in no-fire conditions at all heights. Furthermore, as seen from Table 4.1, the ratio of the mean slope of a fire-modulated ramp to the mean slope of a ramp in no-fire conditions is highest near the surface (approx. 30) and decreases with height to about 14 near the canopy top due to decreasing proximity to the flame. This analysis suggests that fire-modulated ramps are characterized by relatively shorter durations and steeper increments to high temperatures as compared to no-fire conditions. Moreover, the values summarized in Table 4.1 can be utilized to compute sensible heat fluxes by invoking the surface renewal method (Appendix).

Table 4.1: Height-wise summary statistics of fire-modulated ramps and ramps in no-fire conditions. Tabulated modes are obtained directly from the data (not from the histograms)

	Fire-modulated ramps					No-fire ramps				
Height (h)	No. sampled	Mean duration (s)	Modal duration (s)	95th percentile duration (s)	Mean slope (°C min.$^{-1}$)	No. sampled	Mean duration (s)	Modal duration (s)	95th percentile duration (s)	Mean slope (°C min.$^{-1}$)
20 m	59	13.8	5.9	26.2	15.8	51	17.8	13.0	36.4	1.1
10 m	53	17.1	13.3	39.0	18.8	59	14.6	10.7	32.4	1.0
3 m	55	13.8	8.0	24.5	27.2	48	17.6	9.3	34.9	0.8

Statistical Analysis of Cliff-like Structures

Figure 4.8 shows the histograms and eCDFs of cliff slopes under fire influence and no-fire conditions. The histograms show that fire-modulated cliff slopes can reach magnitudes that are an order of magnitude higher compared to those of cliff slopes in no-fire conditions at all three heights. The eCDFs show that near the canopy top and the flame, approximately 50% of fire-modulated cliff slopes are above 35 °C min.$^{-1}$ in magnitude (Fig. 4.8(c)). At $h = 10$ m, approximately 50% of fire-modulated cliff slopes are above 25 °C min.$^{-1}$ in magnitude (Fig. 4.8(f)), which is much steeper than the entire range of no-fire cliff slopes at all three heights. In fact, near the flame ($h = 3$ m), the highest observed cliff-slope magnitude is approximately 600 °C min.$^{-1}$ (Figs. 4.8(g) and 4.8(i)), which represents a decline of approximately 10 °C in one second. We expect this steep slope to correspond to the sudden cooling that occurs after the fire-front has just passed by the tower base. Additionally, Table 4.2 shows that the ratio of mean fire-modulated cliff slopes to mean no-fire cliff slopes is highest near the surface (or flame) where it exceeds 30; this ratio decreases with height to approximately 15 near the canopy top. This is due to the closer proximity of the flame to $h = 3$ m which causes the temperature to rise to relatively higher values before undergoing a sudden drop to ambient conditions, as compared to the higher heights.

Table 4.2: Height-wise summary statistics of the slopes of fire-modulated cliffs and cliffs in no-fire conditions

	Fire-modulated cliffs			No-fire cliffs		
Height (h)	No. sampled	Mean slope ($^\circ$C min.$^{-1}$)	Median slope ($^\circ$C min.$^{-1}$)	No. sampled	Mean slope ($^\circ$C min.$^{-1}$)	Median slope ($^\circ$C min.$^{-1}$)
20 m	59	−40.6	−36.4	51	−2.6	−2.0
10 m	53	−40.4	−26.8	59	−1.7	−1.2
3 m	55	−61.7	−38.1	48	−1.7	−1.2

Since the drop in temperature along a cliff at a certain height is correlated to the influx of cool air via cool downdrafts, it follows that the slope of these cliffs must be associated with the strength of the cool-downdraft events. Near the surface, the presence of the flame not only results in an increased rate of temperature increase along a ramp but also induces strong buoyant updrafts causing an increased up-flux of warm air at $h = 3$ m. This upward mass flux is compensated by a down-flux of cool air during the cool-downdraft event that follows. Since the cool-downdraft event is shorter in duration compared to the warm-updraft event, the compensatory down-flux of cool air must be stronger, compared to no-fire conditions, within that short time interval. This is also in line with the increased magnitude of turbulent fluxes associated with cool downdrafts near the surface, relative to no-fire conditions, observed by Heilman et al. (5) for a high-intensity backing surface fire beneath the canopy. Near the canopy top, the presence of the buoyant plume induces stronger warm updrafts, compared to no-fire conditions, which are followed by stronger cool-downdraft events; a similar explanation can be provided for the increased strength of the stronger sweep-like downdrafts (relative to no-fire conditions) that import cool air into the canopy from the ASL aloft. However, lesser proximity from the flame at this height causes the cliffs to be less steep compared to fire-modulated cliffs near the surface.

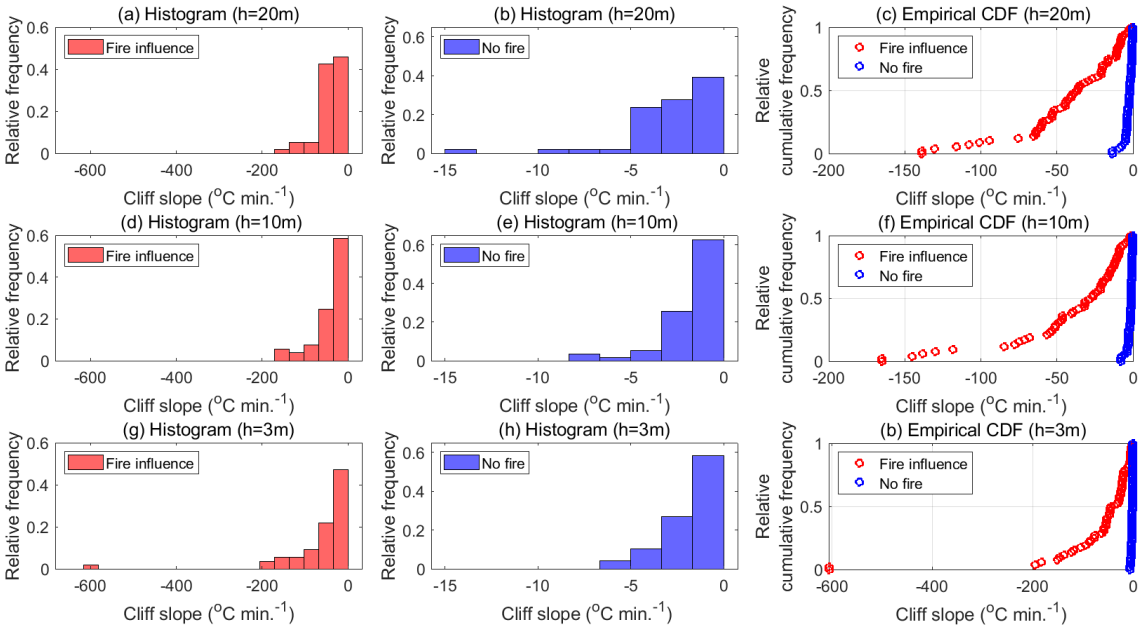


Figure 4.8: Histograms of cliff slopes associated with both, fire influence and no-fire conditions, at all three measurement heights, along with the corresponding empirical cumulative distribution functions

4.4.3 Cross-Wavelet Coherence Analysis: Turbulent Fluxes

Heat- and Momentum-flux Events

In order to establish some context for the cross-wavelet coherence analysis, we first attempt to identify heat- and momentum-flux events in the current scenario as defined in Sect. 4.3.1. Figures 4.9(a)–(b) and 4.9(c)–(d) show time–height cross-sections comprising isotherms of temperature fluctuations (T'), which are represented by the colour contours, overlaid with arrows that represent the vector sum of the streamwise horizontal and vertical velocity fluctuations ($u'\hat{\mathbf{x}} + w'\hat{\mathbf{z}}$) at the West and Control Towers, respectively. Here, fluctuating quantities (u_i', T') are obtained by subtracting one-hour moving means ($\overline{u_i}$, $\overline{T}$) from the corresponding measured quantities: $u_i' = u_i - \overline{u}$, $T' = T - \overline{T}$ (as done by Desai et al. (102)). The time–height cross-sections are depicted for two 6-minute time windows: (i) 1526:30–1532:30 LT during which the influence of the fire is strongest near the canopy top due to

the tilting of the flame in the direction of the wind and (ii) 1534–1540 LT, during which the flame is closest to the base of the West tower as discussed before. The three heights above the fuel bed are normalized by the maximum canopy height ($h_c = 20\,\mathrm{m}$). Contours of positive temperature fluctuations (warm) are depicted in shades of red, while those of negative temperature fluctuations (cool) are depicted in shades of blue. These figures are inspired by the study by Gao et al. (109) on organized turbulence structures within and above the canopy in no-fire conditions as mentioned in Sect. 4.3.1.

As seen in Figs. 4.9(a)–(b), strong temperature microfronts comprising warm isotherms (shades of red) followed immediately by cool isotherms (shades of blue) pass by the different measurement heights at the West Tower. Owing to the sudden and strong temperature fluctuations (T') induced by the presence of the fire, the warming temperature microfronts are considerably strong and frequently observed to last for relatively short time durations. This is more noticeable near the canopy top ($z/h_c = 1$) from 1526:30 to 1532:30 LT (Fig. 4.9(a)) than from 1534 to 1540 LT (Fig. 4.9(b)), due to the enhanced influence of the fire near the canopy top in the earlier time window. This suggests that fire-induced coherent heat-flux events or eddies must also be active (or organized) at relatively shorter time scales compared to no-fire conditions. Contrarily, at the Control Tower (Figs. 4.9(c)–(d)), low-temperature fronts (shades of blue) are observed to persist for longer durations and high-temperature fronts (shades of red) are seen to be relatively weaker owing to comparatively weaker temperature fluctuations ($|T'| < 2^{\circ}\mathrm{C}$). Therefore, the most coherent heat-flux events or eddies in no-fire conditions are expected to be active (or organized) mainly at relatively longer time scales. This can also be observed from the more "well-behaved" pattern of warm updrafts and cool downdrafts that persist for relatively longer durations as they occur near the canopy top ($z/h_c = 1$) at the Control Tower.

Given the variability in the temperature and velocity signals during FFP, it is difficult to see the correlation between the temperature microfronts and the velocity vectors at the West

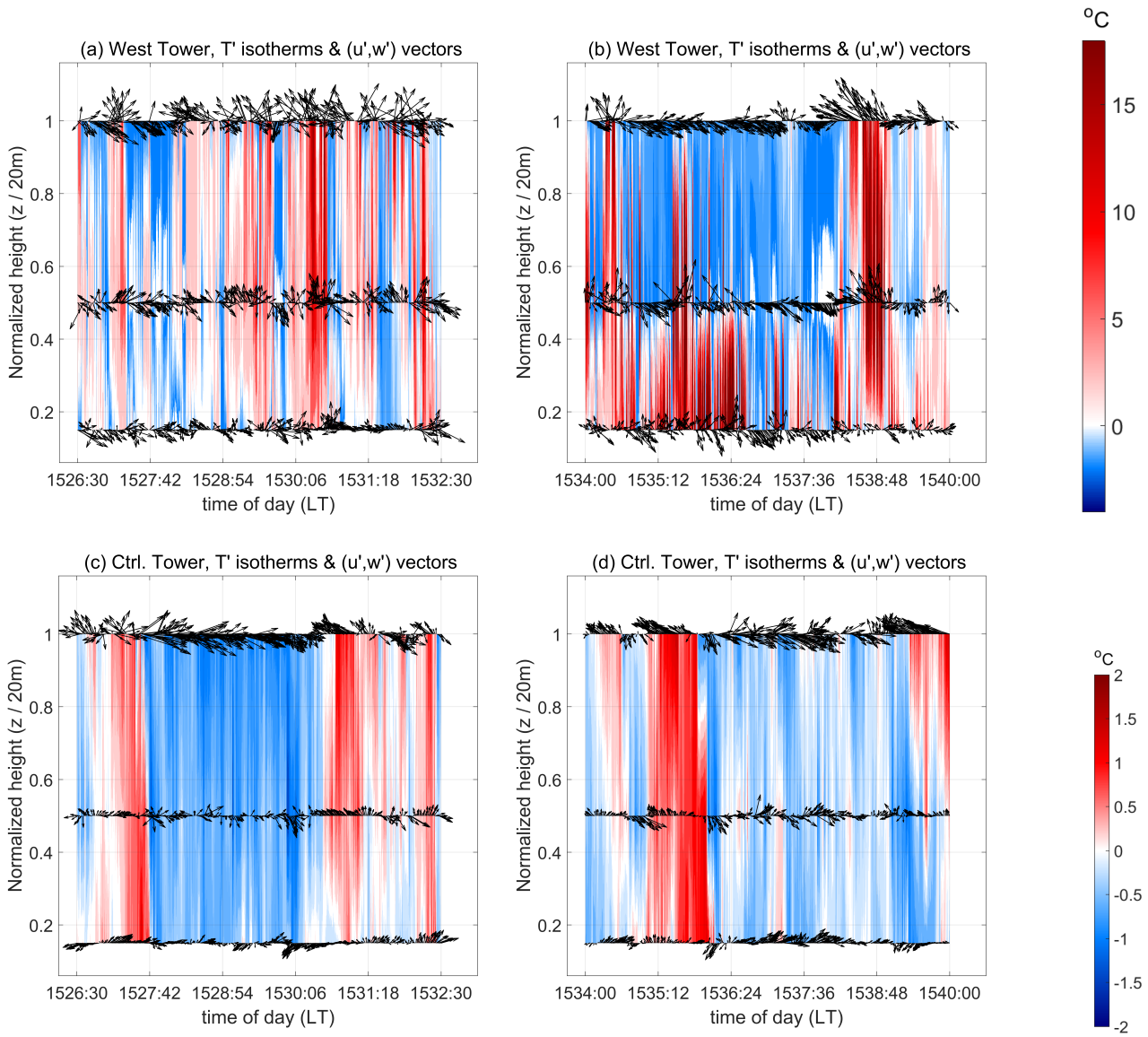


Figure 4.9: Time–height cross-sections, comprising isotherms (filled) of temperature fluctuations (T') overlaid with vector arrows of $u'\hat{\mathbf{x}}+w'\hat{\mathbf{z}}$, at the West Tower for (a) 1526:30–1532:30 LT and (b) 1534–1540 LT, and at the Control Tower for (c) 1526:30–1532:30 LT and (d) 1534–1540 LT

Tower from Figs. 4.9(a)–(b). We, therefore, present "slices" of normalized time–height cross-sections for the West Tower in Fig. 4.10. Each "slice" is of a sufficiently short duration to be able to assess possible heat- and momentum-flux events and the correlation as mentioned above. Figures 4.10(a)–(f) fall within the earlier time window (1526:30–1532:30 LT), whereas Figs. 4.10(g)–(k) fall within the latter time window (1534–1540 LT). Near the canopy top,

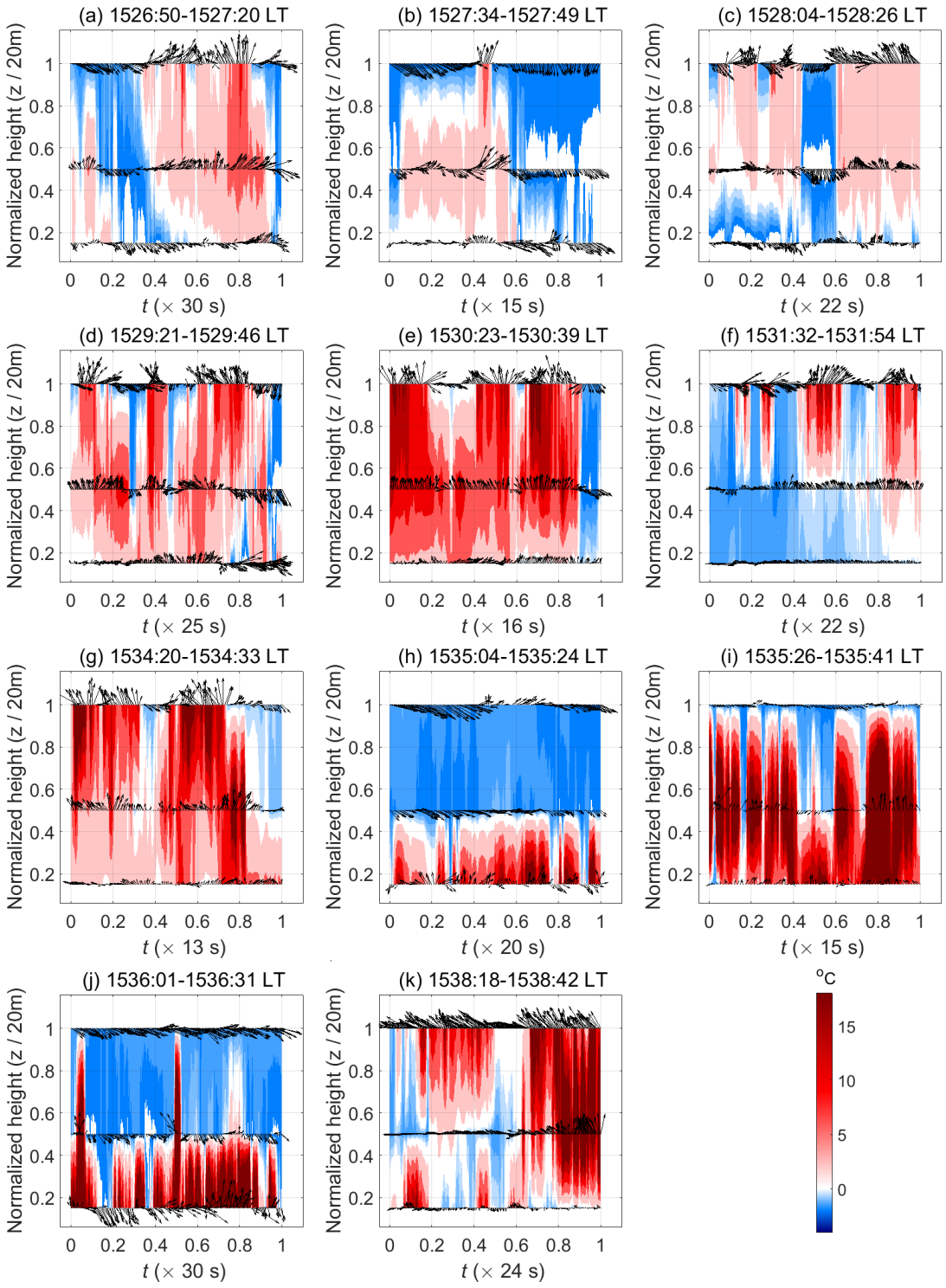


Figure 4.10: Normalized time–height cross-sections comprising isotherms (filled) of temperature fluctuations (T'), overlaid with vector arrows of $u'\hat{\mathbf{x}} + w'\hat{\mathbf{z}}$, during different short time windows within the FFP time at the West Tower. Plots (a)–(f) fall within 1526:30–1532:30 LT and plots (g)–(k) fall within 1534–1540 LT

cooler temperatures are mostly associated with downdraft events ($w' < 0$) while warmer temperatures are mostly associated with updraft events ($w' > 0$). When the influence of the fire begins to be experienced at the higher heights (Figs. 4.10(a)–(b)), persistent cool downdrafts and sweeps (of high-momentum wind) start to concede to warm updrafts and outward interactions (of high-momentum wind) and ejections (of low-momentum wind). Thereafter (Fig. 4.10(c)), cool downdrafts and sweeps switch back and forth with warm updrafts and outward interactions at shorter time scales before being followed briefly by cool downdrafts and inward interactions (of low-momentum wind), and then by more persistent warm updrafts and ejections. As the flame advances toward the tower base (Figs. 4.10(d)–(f)), the buoyancy-driven effects of the tilted flame intensify at the higher heights causing warm updrafts, ejections, and outward interactions to occur more frequently at the expense of cool downdrafts and sweeps; nevertheless, some cool downdrafts and inward interactions are also noticeably observed during this time (Figs. 4.10(d)–(e)). Both the increased strength and occurrence frequency of warm updrafts near the canopy top against typical no-fire conditions suggest that buoyancy-driven heat-flux events have considerably high variability during these times. Note that counter-gradient heat-flux motions are also briefly observed including cool updrafts in Figs. 4.10(a) and 4.10(d)–(f), as well as warm downdrafts in 4.10(c) and 4.10(e)–(f). However, these are short-lived and mostly occur as warm updrafts transition to cool downdrafts and vice versa.

As the fire approaches the tower base (after 1534 LT), warm temperature isotherms tend to coincide more noticeably with warm updrafts and ejections near the canopy top (Fig. 4.10(g)) and cooler temperature isotherms with cool downdrafts and sweeps. Strong and persistent sweeps and cool downdrafts, associated mainly with the background canopy turbulence, interspersed by weak sporadic outward interactions and cool updrafts (counter-gradient heat-flux motions) start to be seen near the cooler canopy top (Fig. 4.10(h)). When the fire-front is sufficiently near the base of the tower to induce the strongest temperature fluctuations at $h = 3\,\mathrm{m}$ (Fig. 4.10(i)), strong updrafts are seen in the warm mid-canopy region ($z/h_c = 0.5$).

These coincide with persistent sweeps and cool downdrafts near the canopy top that are relatively weaker due to the resistance provided by the strong updrafts from the mid-canopy height. A "hiatus" period then sets in near the canopy top where the cool downdrafts and sweeps continue to prevail (Fig. 4.10(j)). Finally, as the fire-front departs from the tower base, strong warm updrafts, likely associated with residual combustion, and ejections are seen near the canopy top (Fig. 4.10(k)). Since the stronger warming temperature fluctuations are experienced more frequently near the tower base compared to the canopy top after 1534 LT, we expect to see an overall diminishing influence of heat-flux events and an increasing influence of momentum-flux events near the canopy top during this latter stage of FFP (latter time window) compared to the earlier time window. Summarily, cool downdrafts, warm updrafts, sweeps, and ejections seem to be the more frequently observed events near the canopy top.

Cross-wavelet Coherence

We now turn our attention to Fig. 4.11, which depicts R^2_{wT} and R^2_{uw} along with phase arrows for $R^2 \geq 0.6$ at the West and Control Towers. These are shown at $h = 20\,\mathrm{m}$ for the 6-minute time window 1526:30–1532:30 LT. Time of day (t) starting from 1526:30 is plotted along the x axis, with the corresponding time periods (scales) along the y axis. At the West Tower (Fig. 4.11(a)), several regions of high R^2_{wT} (shades of red) are seen spanning periods from 1 s to 1 minute for this time duration. Note that during warm updrafts and cool downdrafts, turbulent fluctuations in w and T are in phase (by definition). Contrarily, these are out of phase during counter-gradient motions. The phase arrows in the region of high R^2_{wT} indicate that the measured signals w_{20} and T_{20} are in phase (rightward-pointing arrows) for the most part. This suggests that the regions of high R^2_{wT} are signatures of warm updrafts and cool downdrafts. The high R^2_{wT}, for $t \leq$ 1527:06 LT, at relatively longer periods (above 9 s), is associated with cool downdrafts that persist for more than 9 s in Fig. 4.10(a). The high R^2_{wT}

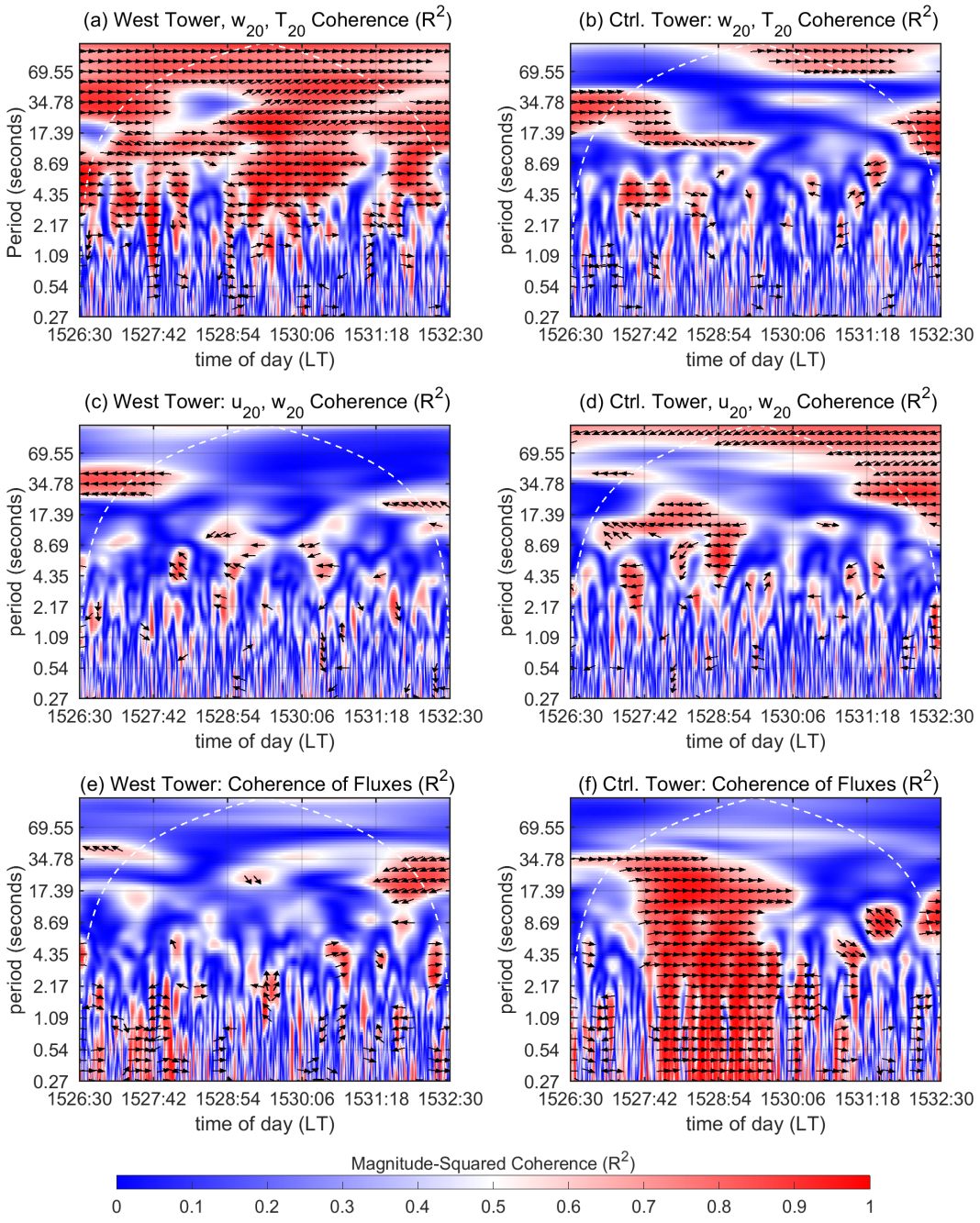


Figure 4.11: Magnitude-squared coherence (R^2) near the canopy top, i.e. at $h = 20\,\mathrm{m}$, for the 6-minute time window 1526:30–1532:30 LT. (a) R^2_{wT}, (c) R^2_{uw}, and (e) R^2 between $w'T'$ and $-u'w'$ at the West Tower. (b) R^2_{wT}, (d) R^2_{uw}, and (f) R^2 between $w'T'$ and $-u'w'$ at the Control Tower. Phase arrows are shown for $R^2 \geq 0.6$ in all cases: rightward-pointing arrows indicate in-phase motions; leftward-pointing arrows indicate motions out of phase by π radians. The white dashed line represents the cone of influence (COI) in all cases

for $t \approx 1527$:06 LT, manifesting at relatively shorter periods (above 2 s), corresponds to a brief 4-s spell of warm updrafts (that coincide with outward interactions) before being followed by another 6-s spell of warm updrafts (that coincide with ejections), as seen in Fig. 4.10(a). Around $t \approx 1527$:42 LT, relatively persistent cool downdrafts that manifest as high R_{wT}^2 at longer periods suddenly concede to short-duration warm updrafts (Fig. 4.10(b)). The relatively sudden switching causes high R_{wT}^2 to manifest at shorter periods (1 s and above). For $1527{:}42 \leq t \leq 1528{:}54$ LT, persistent warm updrafts in Fig. 4.10(c) contribute to high R_{wT}^2 for periods above 9 s, while the high R_{wT}^2 at shorter periods (above 2 s) is associated with the relatively shorter-duration cool downdrafts and warm updrafts (coinciding with outward interactions) that accompany the temperature microfronts. Overall, for $t \leq 1528{:}54$ LT, high R_{wT}^2 regions at periods ranging from 9 s to 17 s are a manifestation of persistent cool downdrafts and persistent warm updrafts (coinciding with ejections) in Figs. 4.10(a)–(c). The region of high R_{wT}^2 for $1528{:}54 \leq t \leq 1530{:}42$ LT is associated with the strong warming temperature microfronts passing through the mid-canopy height and canopy top in Figs. 4.10(d)–(e), resulting from some of the strongest fire-induced temperature fluctuations near the canopy top (Fig. 4.9(a)). A relatively lower-frequency component of heat-flux events induced by the flame is also seen at periods ranging from 35 s to minutes. Finally, high R_{wT}^2 is seen within $1531{:}18 \leq t \leq 1532{:}30$ LT corresponding to cool downdrafts and warm updrafts (coinciding with outward interactions) as shown in Fig. 4.10(f). From Fig. 4.11(a), it appears that the tilted flame induces organized heat-flux eddies near the canopy top ranging from scales of seconds up to minute scales. We expect the organized heat-flux eddies to be associated mainly with ramps (warm-updraft events) and cliffs (cool-downdraft events) observed in the temperature signal. In that regard, it is advisable to view the scales of warm-updraft events near the canopy top in association with the range of ramp durations quantified in Sect. 4.4.2.

In contrast, regions with high R_{wT}^2 (within the COI) are seen sparsely at the Control Tower during this time (Fig. 4.11(b)) for the range of scales mentioned above. Some high-R_{wT}^2

regions are seen to exist at the longer periods (above 17 s and at minute scales) and the corresponding heat-flux events can be characterized as lower-frequency events. This aligns well with the observation made from Fig. 4.9(c) that the cooling branches of the weak temperature fronts (associated with cool downdrafts) seen in no-fire conditions persist for longer durations.

Regions of high R^2_{uw} are scarce at the West Tower (Fig. 4.11(c)). This suggests that while w_{20} and T_{20} appear to cohere well at the West Tower in this time window, u_{20} and w_{20} do not seem to be well-correlated. This reflects upon the lack of variability (and organization) in momentum-flux events during this time (Figs. 4.10(a)–(f)) when temperature perturbations drive most of the coherent motions near the canopy top. In contrast to the West Tower, the high R^2_{uw} regions for $1527{:}42 \leq t \leq 1528{:}54$ LT at the Control Tower (Fig. 4.11(d)), are associated with the persistent sweeps (of high-momentum wind) occurring near the canopy top under no-fire conditions (Fig. 4.9(c)).

It is worth looking at the cross-wavelet coherence between the heat fluxes and momentum fluxes at the West and Control Towers as shown in Figs. 4.11(e) and 4.11(f), respectively. Since smoothing is accomplished in the time–frequency domain by design, we utilize $w'T'$ and $-u'w'$ rather than $\overline{w'T'}$ and $-\overline{u'w'}$ as inputs to compute the cross-wavelet coherence. Furthermore, for coherent momentum-flux events (sweeps and ejections), u' and w' are out of phase (by definition), implying that $-u'$ and w' are in phase. In that light, we utilize $-u'w'$ instead of $u'w'$, so that regions, where coherent heat-flux events correlate well with coherent momentum-flux events, manifest as "in-phase" motions (with rightward-pointing phase arrows). It can be seen that at the West Tower, heat and momentum fluxes are relatively uncorrelated (Fig. 4.11(e)), as evidenced by the low coherence at the periods at which the heat-flux events are active. The behaviour of the heat fluxes near the canopy top is typical of free convection during which momentum-flux events are considerably suppressed. This is aligned with the increased strength and proportion of warm buoyancy-driven updrafts

near the canopy top at the West Tower, as discussed earlier. Contrarily, high coherence is seen at the Control Tower for 1527:42$\leq t \leq$1530:06 LT, which corresponds to the duration in which cool air is imported ("swept") into the canopy via sweeps ($-\overline{u'w'} > 0$) as seen in Fig. 4.9(c). These sweeps are further associated with cool downdrafts ($\overline{w'T'} > 0$) observed during the same time in Fig. 4.9(c). Moreover, $w'T'$ and $-u'w'$ are seen to be in phase during this time (rightward-pointing arrows) suggesting that the coherent heat-flux events (cool downdrafts) and coherent momentum-flux events (sweeps) during this time are well-correlated and the flow is not dominated by either of the two events.

Another approach to explore the divergence of heat and momentum fluxes from each other in the presence of a fire lies in the context of potential deviations from the Reynolds analogy (140; 141). This analysis, included in the Appendix (Supplementary Information) allows us to infer the existence of strong deviations from the Reynolds analogy near the canopy top in this time window. In contrast, deviations from the Reynolds analogy near the canopy top, at the Control Tower, are found to be considerably weaker.

Interesting inferences regarding the behaviour of the turbulent fluxes can be drawn from the coherence plots in the latter time window, i.e. 1534–1540 LT. At the West Tower, regions of high R^2_{wT} are seen intermittently for periods ranging from 1 s to 17 s (Fig. 4.12(a)), mainly representing warm updrafts (e.g., in Fig. 4.10(g) for 1534:00$< t <$1534:36 LT) and cool downdrafts (e.g., in Figs. 4.10(h)-(j) for 1535:12$\leq t \leq$1535:48 LT and around $t =$1536:24 LT) near the canopy top. Notably, the high R^2_{wT} within 1538:12$< t <$1538:48 LT registers the strong warm updrafts associated with residual combustion seen in Fig. 4.10(k). In comparison, at the Control Tower (Fig. 4.12(b)), high R^2_{wT} is seen mainly at the longer periods (above 17 s and up to minutes) representing the persistent and "well-behaved" warm updrafts and the cool downdrafts accompanying the ensuing longer-duration weak cooling temperature fronts seen in Fig. 4.9(d).

Contrary to the earlier time window, regions of high R^2_{uw} are seen at the West Tower

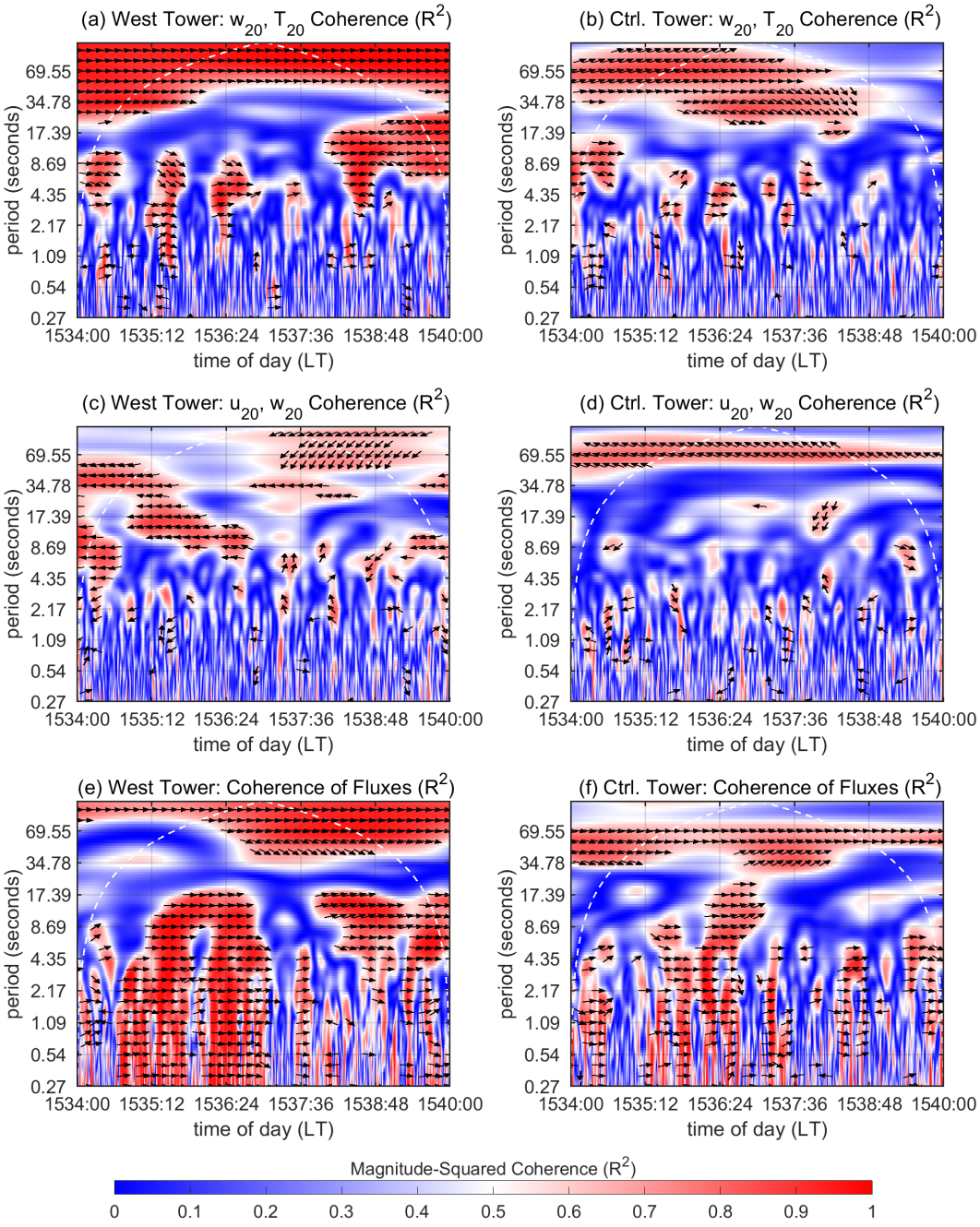


Figure 4.12: Magnitude-squared coherence (R^2) near the canopy top, i.e. at $h = 20\,\mathrm{m}$, for the 6-minute time window 1534–1540 LT. (a) R^2_{wT}, (c) R^2_{uw}, and (e) R^2 between $w'T'$ and $-u'w'$ at the West Tower. (b) R^2_{wT}, (d) R^2_{uw}, and (f) R^2 between $w'T'$ and $-u'w'$ at the Control Tower. Phase arrows are shown for $R^2 \geq 0.6$ in all cases: rightward-pointing arrows indicate in-phase motions; leftward-pointing arrows indicate motions out of phase by π radians. The white dashed line represents the cone of influence (COI) in all cases

(Fig. 4.12(c)) at periods ranging from 2 s to 35 s and above (within the COI). The (leftward-pointing) phase arrows in these regions indicate that the u and w signals are out of phase suggesting that these regions represent either ejections (e.g., in Fig. 4.10(g) for t <1534:36 LT) or sweeps. Most notable is the region of high R^2_{uw} spanning periods ranging from 8 s to 25 s for 1534:36< t ≤1536:24 LT, which corresponds to the persistent sweeps highlighted in Figs. 4.10(h)-(j). Sweeps are then registered by regions of slightly lower coherence ($0.5 \leq R^2_{uw} \leq 0.6$) at periods above 17 s for 1536:24≤ t ≤1538:12 LT. Unlike the West Tower, regions of high coherence ($R^2_{uw} \geq 0.6$) are only seen at periods of minutes and longer at the Control Tower across the entire time window, within the COI (Fig. 4.12(d)). These are associated with the background (atmospheric) canopy turbulence.

At both towers, the coherent heat-flux events and coherent momentum-flux events appear to correlate well with each other in this time window (Figs. 4.12(e)–(f)). In particular, the region of high coherence for $1534{:}36 \leq t \leq 1537{:}00$ LT at the West Tower (Fig. 4.12(e)), corresponds to the regime where cool downdrafts and sweeps are well-correlated. This suggests a relatively more congruous interaction between fire-induced flow and the background atmospheric eddies compared to the earlier time window. It appears that the influx of cool ambient air into the canopy via persistent sweeps, which are momentum-flux events, is partially a response to the outflux of warm air from the canopy due to strong warm updrafts (heat-flux events) in the earlier time window. Such an influx coincides with a duration when the influence of the flame near the canopy top is relatively diminished and strong high-temperature fluctuations are only experienced near the canopy top intermittently, hindering the organization of heat-flux eddies.

We note that it is in this later time window that an enhanced organization of heat-flux-bearing eddies is observed extensively at $h = 3$ m as evidenced by the cross-wavelet coherence computed at that height (Appendix). During this time, momentum-flux-bearing eddies are relatively less extensively organized, both in time and across time scales (under 1 minute)

near the surface. Additionally, strong deviations from the Reynolds analogy are observed near the surface. Among all heights, these deviations are found to be the strongest near the surface, due to its maximum proximity to the flame. Deviations from the Reynolds analogy at the mid-canopy height are comparatively moderated by the competing interplay between fire-induced heat fluxes and ambient momentum fluxes in both time windows. More details on the analysis leading to these inferences can be found in the Appendix (Supplementary Information). At this point, the readers are also advised that it is worth comparing our results regarding the turbulent flux events obtained from the wavelet-based analysis above against those presented in Fig. 4.1 for context and consistency.

We now take the opportunity to summarize our results pertaining to the effects that the presence of a heading surface fire has at different heights within the canopy at the different stages of fire-front propagation with the help of Fig. 4.13. As shown in Fig. 4.13, the tilting of the flame-front in the direction of the wind imposes a temporal lag in the modulation of ramp–cliff structures at different heights, as it does on the enhanced organization of heat-flux eddies, under the influence of the fire. We have, therefore, organized our findings under two stages: (i) as the fire-front approaches the tower and (ii) as the fire-front passes by the tower. The schematic representation encapsulates the steeper escalations to high temperatures along ramps over shorter durations, under the influence of the buoyant plume (and its stronger warm updrafts) at the higher heights, especially near the canopy top, as the fire approaches; this effect is present to a higher degree at the lower heights, especially near the surface, during the passage of the fire-front by the tower base, due to the closer proximity with the flame. At the mid-canopy height, ramp–cliff structures are first affected by the competing effects of ambient turbulence and the buoyant plume (Fig. 4.13(i)) and then predominantly by the stronger warm updrafts induced due to the closer proximity of the flame (Fig. 4.13(ii)). Moreover, the drop in temperature along a cliff at all heights is steeper and associated with stronger cool downdrafts compared to no-fire conditions (of which, the coherent structures near the surface in Fig 4.13(i) are an approximate representation). These modulations in

the ramp–cliff structures observed in the temperature signal are accompanied by a change in the degree of organization of flux-bearing eddies: heat-flux eddies are well-organized at relatively shorter time scales while momentum-flux eddies are not. Contrarily, the degree of organization of heat-flux and momentum-flux eddies is relatively similar at these scales in the absence of a fire. Note that while we expect some quantitative variation in the amplitudes and durations of fire-modulated ramp–cliff structures for a higher-intensity heading fire, our results will remain qualitatively consistent with the narrative captured by Fig. 4.13.

4.5 Conclusions and Future Work

Turbulent motions arising from the interaction of a propagating fire with its surrounding environment are organized at various scales. Unlike popular techniques that rely on averaging schemes, wavelet-based analyses can provide information regarding the range of temporal scales associated with the characteristic coherent structures as the fire-front evolves, overcoming a critical obstacle to the study of fire-induced turbulent motions. In this study, we have utilized wavelets to analyze the turbulence characteristics associated with a relatively low-intensity heading surface fire beneath the forest canopy. Measured temperature signals have been analyzed using the Mexican Hat wavelet, whereas turbulent fluxes have been analyzed using a complex wavelet, i.e. the Morlet Wavelet.

Patterns in the wavelet-based energy density plotted on a time–frequency plane allow us to identify specific events and structures inherent to the temperature signal at a given height. Patterns associated with the strongest temperature excursions near the surface allow us to track the FFP time at the tower base more clearly within the stipulated longer fire-front-passage duration, thereby informing our subsequent analysis. Furthermore, in the highest frequency band (0.1 to 5 Hz, which is the Nyquist frequency), some fire-induced variability is observed to be active, while the effect of atmospheric (canopy) turbulence is relatively

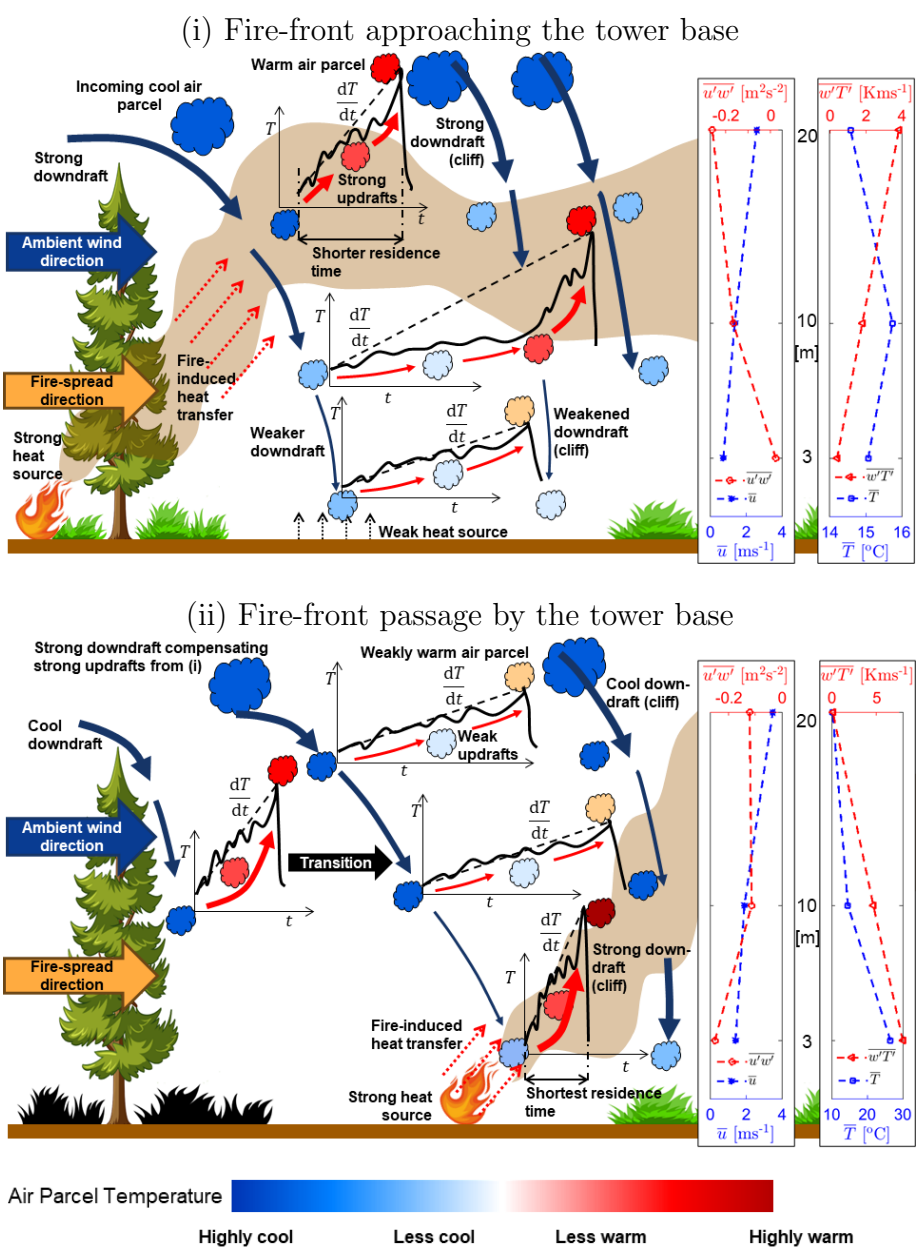


Figure 4.13: A schematic representation summarizing modulations induced by a heading sub-canopy surface fire in the ramp slope, ramp duration, and cliff slopes (i) in the earlier time window (as the fire-front approaches) and (ii) in the latter time window (during FFP) from a Lagrangian perspective (inspired by Figure 6.9 of the work by **(author?)** (1)) along with representative profiles of the mean streamwise velocity ($\overline{u}$), turbulent momentum flux ($\overline{u'w'}$), mean temperature ($\overline{T}$), and turbulent heat flux ($\overline{w'T'}$). Solid arrows represent local wind motion: thicker arrows represent stronger draughts while thinner arrows represent weaker draughts; dotted arrows represent heat transfer; colorbar, arrow length, and arrow thickness are not to scale; images of the flame and vegetation are taken from *www.vecteezy.com*

much weaker. At these scales, intermittent burst-like behaviour characterized by irregular and rapid increments in the temperature signal are observed near the canopy top. More advanced studies along the lines of the analysis by Chowdhuri et al. (142) or Allouche et al. (143) would be needed to quantify a metric for "burstiness" in the temperature signal.

The interaction of the fire with the canopy-induced sweep–ejection motions manifest in the ramp–cliff-type structures in the temperature signal, which are extracted using the wavelet-based approach as the fire-front approaches the measuring tower. This allows us to investigate the nature of fire–vegetation–atmosphere interaction compared to no-fire conditions and across the depth of the canopy sub-layer. We answer three overarching questions as described below.

(i) How does the presence of a fire impact the duration and amplitude of ramp–cliff patterns typically observed in the measured temperature signal? Moreover, are these impacts uniform across all heights within the canopy?

In response to Question (i), the presence of the fire generally shortens the ramp duration and enhances the amplitude of the ramp–cliff structures in the temperature signal. However, these impacts are not uniform across all heights within the canopy. They are strongest near the surface, owing to the maximum proximity to the flame, and weaken with height. Near the canopy top, the increase in ramp amplitudes results from the strong fire-induced buoyant updrafts. At the mid-canopy height, ramp durations increase in the presence of the fire due to the intermittent nature of the fire-plume–canopy interaction, while ramp amplitudes increase consistently because of fire-induced temperature excursions. At all heights, cliff slopes are steeper in the presence of the fire due to the sweeping motions associated with the strong downward entrainment of cooler ambient air into the canopy.

(ii) Does the presence of a fire enhance the degree of organization of heat- and momentum-flux-bearing eddies relative to no-fire conditions? If so, at what

heights within the canopy and at which time scales?

In response to Question (ii), the presence of the fire impacts the degree of organization of turbulent eddies, associated with heat- and momentum-flux events, over a range of temporal scales (periods) at all heights during FFP. Fire-induced heat-flux events (eddies) can be coherent (organized) over shorter periods compared to no-fire conditions. Under the influence of the fire, momentum-flux events (eddies) are coherent (organized) at relatively longer periods compared to heat-flux events. These observations are consistent across all heights in the canopy.

(iii) What is the relative importance of heat-flux (thermally driven) events versus momentum-flux (mechanically driven) events at different stages of the fire-front evolution? Is the Reynolds analogy violated by the presence of a fire? If so, is it more violated near the canopy top or in the canopy subspace?

In response to Question (iii), the relative importance of heat-flux-bearing eddies versus momentum-flux-bearing eddies differs between two stages of the fire-front proximity to the tower base. The first stage comprises a brief time window prior to the arrival of the fire-front at the tower base, while the second stage comprises a later time window during which the strongest fire-induced temperature excursions are recorded at the tower base. In the earlier stage, the tilting of the flame-front in the direction of the wind causes the turbulent fluxes near the canopy top to be chiefly thermally driven while momentum-flux-bearing eddies are less energetic. This is associated with enhanced organization of heat-flux-bearing eddies across a range of time scales, representing warm updrafts (at relatively longer periods) and cool downdrafts (at shorter periods). In contrast, during the later stage, heat-flux-bearing eddies near the canopy top are organized relatively intermittently and organized momentum-flux eddies start to become noticeable. These organized eddies are mainly associated with sweeps of high-momentum air from aloft, which coincide with cool downdrafts, at shorter periods, and in part with ejections of low-momentum air from the canopy subspace, which

coincide with warm updrafts, at longer periods. Note that the dynamics of the increased organization of heat-flux-bearing eddies near the canopy top is similarly observed at the mid-canopy height and near the surface, in chronological order.

To investigate the behavioural similarity between momentum-flux and heat-flux transport, we have explored adherence to the Reynolds analogy by examining deviations in the turbulent Prandtl number from unity and theoretical predictions based on the Monin-Obukhov Similarity Theory (MOST). The Reynolds analogy is distorted by the presence of the fire. The Reynolds analogy is violated the most near the surface, particularly during the later stage of the fire-front passage, due to the maximum proximity to the flame. Deviations from the Reynolds analogy at the mid-canopy height are comparatively moderated by the competing interplay between fire-induced heat fluxes and ambient momentum fluxes. Finally, deviations from the Reynolds analogy near the canopy top are found to be the least prominent compared to the lower heights within the canopy subspace.

The analysis above provides valuable insights into the characteristic temporal scales at which fire-induced turbulent motions inform smoke dispersion and firebrand transport. The mean durations, associated with coherent structures, estimated at different heights can be used to construct length scales in the manner described by Raupach et al. (93). Length scales thus obtained are necessary for estimating physical quantities used in popular one- and two-equation turbulence models for flow in forested environments (24). Differences in the observed behaviour of turbulent fluxes near the canopy top at the different stages of fire-front evolution discussed above also inform temporal variations in scalar transport and fire-spread behaviour. Insights obtained from such an analysis can be useful in testing and developing more sophisticated physics-based (e.g. LES) fire-spread, firebrand-transport, and smoke-dispersion models within forested environments. Improved predictive models can further assist in more informed and efficient fire-management operations.

In addition, our study illustrates the immense potential that wavelets carry in exploring

fire-induced turbulence measurements. Future work may involve leveraging the distinct time–frequency localization properties of different wavelets to analyze different frequency bands of a measured quantity, i.e. to make a scale-based choice of the wavelet. For instance, the Morlet wavelet with its better frequency-localization properties can be used to analyze the higher frequency bands, while the Mexican Hat wavelet with its relatively better time-localization properties can be used to analyze the lower frequency bands. Furthermore, it is worth investigating the effect of the wavelet used on event interpretation by applying other wavelets, such as the Gaussian Wave or the first derivative of a Gaussian (131), to the current data. Finally, wavelet-based techniques can be applied to other types of fire-spread scenarios such as grassland fires and backing surface fires beneath the canopy. A comparison between reconstructed signals corresponding to different scales for these scenarios could potentially reveal significant differences in the patterns of coherent structures on the basis of the surface-fire environment.

Chapter 5

Investigating buoyant plume dynamics during wind-driven wildland fires over plant canopies using Large-Eddy Simulations (LES)

5.1 Background

Turbulent structures germinate from the interaction of a buoyant plume, such as that generated by a wildland fire, with an ambient cross-wind. Although the physical implications of such structures on wildland fire behavior and spread characteristics have only recently gathered much attention, plume–cross-wind interactions have long been of interest to fluid mechanics researchers with laboratory-scale experiments representing a major source of understanding. Early laboratory experiments by Fric and Roshko (144) on the interaction of a (non-thermal) jet issued from a stationary source with cross-flow, identified the presence

of near-source shear-layer vortices and downstream counter-rotating vortex pairs (CVPs). For a similar configuration, Cardenas et al. (145) obtained two-dimensional maps of turbulent fluxes of tracers and momentum using simultaneous 2D-LIF and PIV measurements; CVPs were found to significantly influence the fluxes. Other laboratory experiments on jets-in-cross-flow, identifying CVPs and their potential formation mechanisms, such as the modulation of the near-source jet vorticity by the cross-wind, have been reviewed by Mahesh (146), while recent propagating-fire experiments in small-scale fuel beds (58; 87) have identified and quantified CVPs as key participants in fire spread. Based on similarity criteria, laboratory studies have also attempted to develop power-law scalings characterizing plume trajectories under cross-flow in the near-source and far-field regions influenced by the ratio of the momentum flux to the buoyancy flux (147; 148; 149; 150; 151; 152; 153; 149; 154; 155). Using flume experiments with a model vegetation canopy, Chung and Koseff (156) investigated the influence of canopy-induced turbulence on buoyant plumes by varying the intensity of the buoyancy source. The plume-trajectory centerline for the case with maximum turbulence was found to oscillate significantly more than the case with the lowest turbulence, with the dominant frequency corresponding to that of the Kelvin-Helmholtz rollers in the mixing layer and higher relative plume buoyancy suppressing this influence. While lab-scale analyses have been useful in their own right, they lack the complexity of more realistic, spatially evolving plume behavior in the environment. Moreover, studies investigating buoyant-plume interactions with tall vegetative canopies in the presence of cross-flow are scarce.

In-situ measurements of wind velocity and temperature from prescribed burn experiments (157) have contributed significantly to the understanding of fire-plume behavior at field scales under differing vegetative characteristics. Studies have attempted to quantify fire-plume-modulated local winds and turbulence-generation and transport mechanisms (2; 3; 90; 81; 4; 105; 5; 101), differentiate between these patterns during fires in grassland and forested environments under differing ambient wind-forcing conditions (102; 5), and track fire-modulated ramp–cliff structures in a forest canopy as they evolved temporally, along

with their constitutive frequencies (158). Observations regarding fire-modulated heat- and momentum-flux events at multiple heights (5; 91) were particularly noteworthy. Downdrafts of high horizontal momentum (sweeps) were found to dominate the intensity of momentum-flux events in forest canopy environments. However, updrafts of high horizontal momentum (outward interactions) were found to compete significantly with sweeps in their contribution to the momentum flux, while also showing a high occurrence frequency compared to no-fire conditions. Despite their usefulness, field measurements are limited by spatial localization and logistical obstacles to deploying multiple instruments while maintaining quality control (159). Furthermore, prescribed burns are limited by seasonal restrictions and weather-related uncertainties, the respiratory and visibility hazards germinating from the accompanying smoke plumes, and escape risks (160; 21); there remains a dearth of measured data during prescribed burns in forested regions (91). In addition, while the larger-scale sampling of plumes during active fires has gained momentum recently (161; 162; 163), with recent radar-based measurements providing evidence for the presence of CVPs at the fire-front (163), these observations also remain sparse.

Given the deficit in observational datasets vis-á-vis the necessity to develop reliable predictive models for active fire containment and planning prescribed burns, the majority of coupled fire–atmosphere modeling endeavors have been focused on predicting fire perimeters with a few specific observations. Mueller et al. (164) utilized the Wildland-urban interface Fire Dynamics Simulator (WFDS) to simulate a 4.25-hectare experimental surface fire in a pine forest. The study also aimed to evaluate the impact of canopy fuel structure on fire behavior. While fire spread rates showed reasonable agreement with experimentally observed values, local winds induced by the fire were underpredicted in its wake. Benik et al. (165) utilized WRF-SFIRE to simulate fire-induced circulations near the perimeter during the FireFlux2 grassland fire experiment (101). Models tracked observed fire-front locations and the vertical plume structure to high levels of accuracy; however, SFIRE relies on the Rothermel model for fire spread, which is based on laboratory experiments, and the study itself was limited to a

grassland burn. Shamsei et al. (166) attempted to recreate the 2018, complex-terrain Camp Fire using WRF-Fire. While fire propagation rate predictions showed better agreement compared to the semi-empirical FARSITE model (35), several sources of uncertainty were identified along with the need for systematic studies to demystify them in the context of fire–atmosphere feedback flow. Roberts et al. (167) attributed shortcomings in capturing these processes to the sensitivity of sensible heat fluxes during fire events to accurate estimates of fuel loading inputs. In the face of the limited predictive capabilities of existing models in predicting fire behavior, it is worth exploring the capability of models for exploring process-level fire-induced flow phenomena by systematically varying the environmental conditions (168; 169). Quantifying the near-field (close to the buoyancy source) fire-induced flow at high spatial resolution will facilitate improved parameterizations within the coarser-resolution predictive models.

However, the complex system of equations governing fire physics within the atmospheric boundary layer (ABL) makes simulations computationally intensive (25; 170; 47; 171; 172). Low-complexity models provide a practical starting point due to their reduced computational demands and can be progressively refined with added complexities and improved physical underpinnings to create reliable operational models. Although some studies have simulated cross-wind interactions with traverse jets or buoyant plumes with differing source geometries using turbulence models such as DNS or LES turbulence models in such low-complexity configurations (173; 174; 146; 175; 176; 177; 178; 179), simulations incorporating forest canopies and their comparisons with no-canopy environments remain rare. Considering the scarcity of both observations and simulations, exploring buoyant-plume–canopy–cross-wind interactions, it is necessary to establish a solid theoretical framework for plume behavior modulated by such interactions. In this study, we employ an LES model to explore interactions between a thermal plume emanating from a localized surface source with a prescribed heat flux in the presence and absence of a homogeneous forest canopy. The advantage of LES models lies in their ability to characterize the most energetic turbulent eddies accurately across space with

high spatial resolution. The key research question we intend to address through this study is: how does the presence of a tall vegetative canopy alter the near-field coherent structures and far-field plume behavior as the plume interacts with a cross-wind? Secondly, we investigate the similarities between the current, no-flame, low-complexity configuration with those involving both static and propagating fires. We start by providing a brief description of the open-source solver and the setup of our simulations in Sect. 5.2. This is followed by a set of results in Sect. 5.3, discussing physical insights into the plume flow features from the mean statistics of the velocity and temperature fields and the spatial heterogeneity in the turbulent momentum-flux events. Finally, we summarize our deductions in Sect. 5.4, while motivating and outlining pathways for future research.

5.2 Computational Setup

The Parallelized Large-Eddy Simulation Model (PALM) is utilized with its in-built plant-canopy module to study the plume–canopy interaction. PALM solves the non-hydrostatic, incompressible Navier-Stoke equations, filtered by the grid size, in Boussinesq-approximated form (180). The domain is discretized using a staggered, Arakawa C grid (181), so that scalar quantities are resolved at the center of each grid cell, while velocity components are computed at the edges, i.e. half a grid width apart from the scalars. For the advection terms in the governing (prognostic) equations, the default settings are used for discretization, i.e. an upwind-biased 5th-order differencing scheme (182) in combination with a 3rd-order Runge–Kutta time-stepping scheme after Williamson (183). PALM uses an iterative, multi-grid scheme to solve the Poisson equation for the modified perturbation pressure (184) to allow for non-cyclic boundary conditions, as discussed later in this section. For the sub-grid-scale (SGS) terms, a 1.5-order turbulence closure model after Deardorff (185) is used, where a prognostic equation is solved for the SGS turbulence kinetic energy in addition to a

(a) Inlet velocity profile (b) Domain description

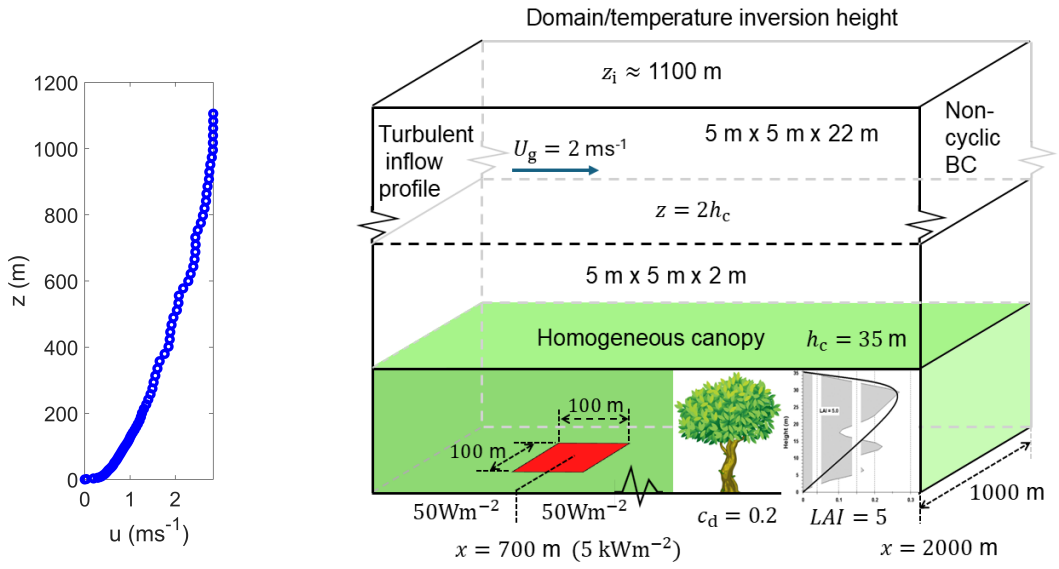


Figure 5.1: A schematic of the computational setup for the simulations in a canopy setting. (a) Velocity profile at the inlet. (b) Domain description; kinks along the vertical axes represent regions with vertical grid stretching.

gradient-diffusion parameterization for the SGS turbulent heat and momentum fluxes. More details about the PALM model and architecture can be found in the literature (184; 180).

Figure 5.1 encapsulates the computational setup for the LES run(s) in the canopy setting. The computational domain is 2 km long in the streamwise (x) direction and 1 km wide in the cross-stream (y) direction, with a homogeneous canopy up to a height ($z = h_c$) of 35 m from the surface. The cell size for the structured grid is 5 m×5 m×2 m up to $z = 2h_c$, beyond which vertical grid stretching is employed using a stretch factor of 1.08, until the maximum cell size in the vertical direction is 22 m. The higher resolution near the surface is aimed at capturing the complex turbulence patterns in the canopy sub-layer. The canopy has a drag coefficient (c_d) of 0.2 and leaf area index (LAI) of 5, with the corresponding leaf area density (LAD) profile taken from Dias-Junior et al. (186). The canopy elements are not explicitly modeled; rather, a volume-averaged effect of the porous canopy layer is considered, with the canopy drag force term in the momentum equation for the mean

velocity, accounting for the aerodynamic effects of the canopy. This is given by $f_{\mathrm{D}_i} = -c_{\mathrm{d}} LAD u_i \sqrt{u_i^2}$, where u_i represents velocity components in the index notation. Daytime atmospheric conditions are simulated with a well-mixed boundary layer, i.e. a uniform initial profile of the potential temperature with height ($\theta(z) = \theta_{\mathrm{a}} = 300\,\mathrm{K}$) up to a temperature inversion height (δ) of approximately 1.1 km. Incoming solar radiation of $1015\,\mathrm{Wm^{-2}}$ is assumed at the tree-tops (187), representative of early afternoon conditions. The ambient sensible heat flux at the forest surface was computed using a declining exponential function of the downward cumulative leaf area index (F) (188): $Q(z) = Q(h_{\mathrm{c}})e^{-\alpha F}$, where α is the extinction coefficient, taken as 0.6. Using, $Q(h_{\mathrm{c}}) = 1015\,\mathrm{Wm^{-2}}$, and $F = LAI = 5$ at $z = 0$, we get $Q(0) \approx 50\,\mathrm{Wm^{-2}}$.

Fire plume presence is simulated by a thermal plume arising from a localized region of size $100\,\mathrm{m} \times 100\,\mathrm{m}$ to which a high surface heat flux is prescribed. The surface heat flux in this region is taken to be 100 times the ambient surface sensible heat flux for the base case ($Q = 5000\,\mathrm{Wm^{-2}}$), though this factor is altered for the parametric study in Chapter 5. Fixing the heat source in space allows us to investigate the steady-state, micro-scale flow response to the plume. This approach allows us to bypass a combustion model that is highly sensitive to the accuracy of fuel-loading estimates to obtain the representative high sensible heat fluxes (167). The reduced complexity allows us to quantify the effect of plume–wind–vegetation interactions separately from the flow–combustion feedback, a need highlighted in recent literature (189). Previous studies on buoyant plumes interacting with wind shear, reviewed by Lareau et al. (163), have demonstrated the promise of this setup by capturing some characteristic flow features such as CVPs and shed vortex columns. Non-cyclic horizontal boundary conditions (BC) are used for the inlet and outlet, whereas cyclic BC are used for the lateral (cross-stream) faces of the domain. The ambient wind follows a turbulent, logarithmic profile at the inlet. This turbulent inflow profile (Fig. 5.1(a)) is achieved via a 48-hour precursor run in a smaller domain without a plant canopy, i.e. a turbulence spin-up run, with the geostrophic wind velocity (U_{g}) initialized to $2\,\mathrm{ms^{-1}}$. A

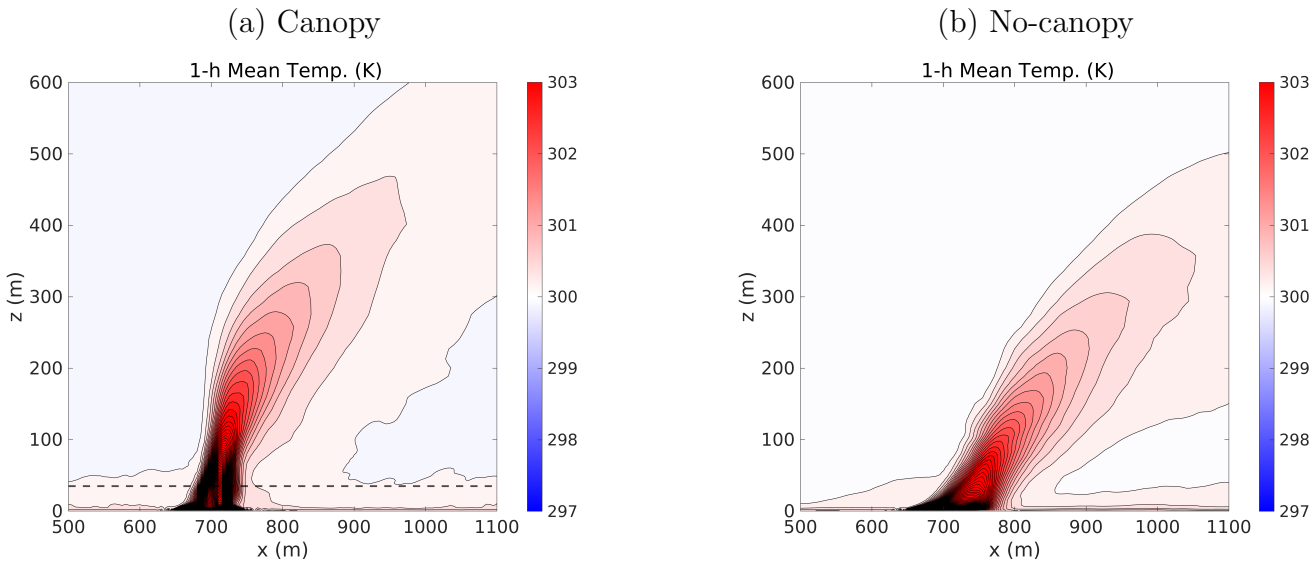


Figure 5.2: Contours of the 1-h mean temperature plotted on the XZ plane $y = 500\,\mathrm{m}$ (passing through the center of the heated patch) for the (a) canopy and (b) no-canopy cases. Dashed horizontal line in (a) represents $z = h_\mathrm{c}$

technique called the turbulence-recycling method, described by Lund et al. (190), is utilized for the main run comprising the larger domain, wherein turbulence from a cross-stream (XY) plane at $x = 220\,\mathrm{m}$ is cycled back into the inlet for 2 h of simulation time. This is followed by several restart runs with a total simulation time of 9 h. One-hour mean statistics ($\overline{u}_i, \overline{\theta}$) are computed via a block averaging over the last hour of the simulation (t = 8–9 h) and turbulent fluctuations are computed as deviations from the 1-h mean quantities: $u_i' = u_i - \overline{u}_i$ and $\theta' = \theta - \overline{\theta}$.

5.3 Results

5.3.1 Mean velocity and temperature profiles

Figure 5.2 depicts the 1-h mean potential temperature ($\overline{\theta}$) on the streamwise (XZ) plane passing through the center of the square surface patch ($y = 500\,\mathrm{m}$), for the canopy and

no-canopy cases. It is observed from the temperature contours that the warm core of the plume is more vertical in the canopy case while it deflects more strongly from the vertical in the no-canopy case. Despite the hundred-fold difference in heat flux between the heated and the ambient surface, higher temperature relative to the ambient is only observed close to the plume core ($z < 200\,\mathrm{m}$) with temperature excursions from the ambient weakening with height, becoming negligible around $z = 500\,\mathrm{m}$. More information can be gathered from Fig. 5.3, which depicts the 1-h mean vertical velocity ($\overline{w}$) on the same XZ plane for the canopy and no-canopy cases, along with the 1-h mean plume centerline. The mean plume centerline is tracked from the locus of the maximum 1-h mean vertical velocity ($\overline{w}_{\max}$). In the region near the plume source (Zone 1), $\overline{w}_{\max}$ is obtained from the maximum $\overline{w}$ across a horizontal transect in this plane at different heights. Further downstream from the plume source (Zone 2), $\overline{w}_{\max}$ is obtained from the maximum $\overline{w}$ across a vertical transect in this plane at different streamwise locations. The transition between the two zones is determined by tracking a sudden change in the local plume centerline slope beyond a certain threshold, from the green dots in Zone 1, as seen from Fig. 5.3. In the canopy case, the mean plume centerline slope in Zone 1 appears to be steeper due to the canopy drag on the plume. An additional zone above the canopy sublayer exists near the surface (Fig. 5.3(a)), where the mean plume centerline inclination transitions from the steeper inclination near the surface to a more gradual one before the onset of the far-field region. We refer to this zone as Zone 1(B). Note that the lines in Zones 1 and 1(B) depict the inclination in an approximate sense. The lines in Zone 2 are obtained using a simplex algorithm (MATLAB's *fminsearch()* function) for a linear fit (μ) to the oscillating mean plume centerline.

The spatial standard deviation (s_μ) of the far-field mean plume centerline altitude from the linear fit is approximately 20.40 m in the canopy case and 49.95 m in the no-canopy case. The 1-h mean plume centerline in the no-canopy case shows higher variability (more oscillatory behavior) compared to the canopy case. This seems to suggest that the far-field flow within the plume is more organized due to the canopy drag. Moreover, the transition

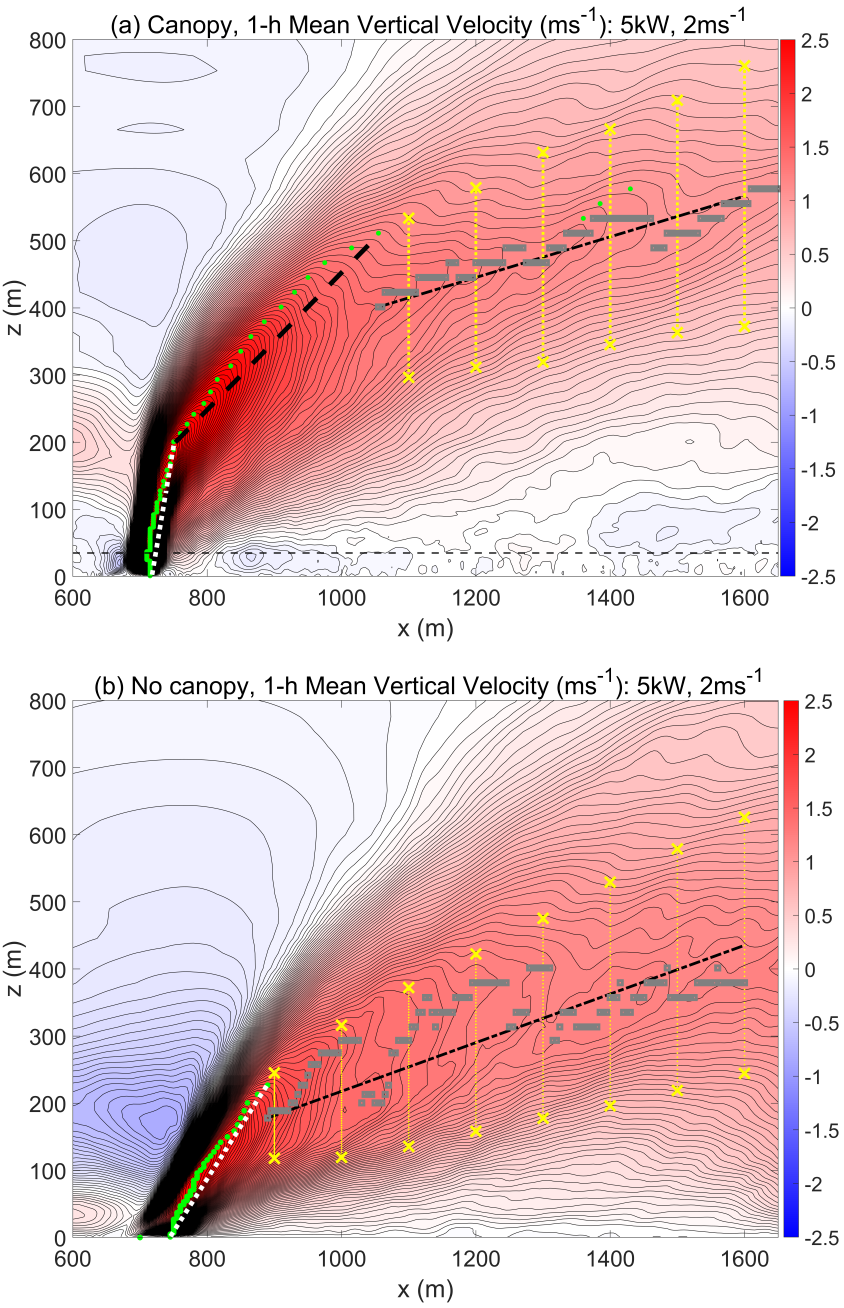


Figure 5.3: Color contours of the 1-h mean vertical velocity ($\overline{w}$) for the (a) canopy and (b) no-canopy cases. Grey points represent 1-h mean plume centerline (μ) in the far-field (Zone 2); vertical yellow dotted lines represent $\mu \pm s_t$ at multiple locations in the far-field; green dots represent the plume centerline in Zone 1, while white slanted dotted lines represent the plume centerline inclination. In (a), the black dashed line represents the inclination of the plume centerline in the transition zone (Zone 1(B)).

to Zone 2 occurs at a higher altitude ($z \approx 511\,\mathrm{m}$) in the canopy case as compared to the no-canopy case ($z \approx 227\,\mathrm{m}$), which appears to be due to the aerodynamic effects of the

canopy on the rising plume. Additionally, Fig. 5.3 depicts the variation ($\mu \pm s_t$) in the linear fit to the 1-h mean plume centerline, obtained from the standard deviation of the time series of the plume centerline altitude (s_t) at multiple streamwise locations. These locations are 100 m apart, i.e. $x = 1100\,\text{m}$–$1600\,\text{m}$ in the canopy case and $x = 900\,\text{m}$–$1600\,\text{m}$ in the no-canopy case. The time series of the plume centerline altitude at each streamwise location is obtained by tracking the height of the maximum instantaneous vertical velocity ($w_{\max}$) at that streamwise location. The time variation in the plume centerline is observed to increase along the downstream direction in the far-field, although the variance at each streamwise location appears to be similar across the canopy and no-canopy cases. It can be noted that $s_t \sim \mathcal{O}(100\,\text{m})$ at $x = 1100\,\text{m}$ in the canopy case, suggesting high variability in the time-varying trajectory of the plume centerline owing to the highly turbulent interactions between the plume and the cross-wind. The visuals above suggest that although changes in the mean air temperature are spatially limited, for the current configuration, the variability in the flow field is more extensive, warranting further investigation in the following sections.

5.3.2 Streamtubes and vortex tubes

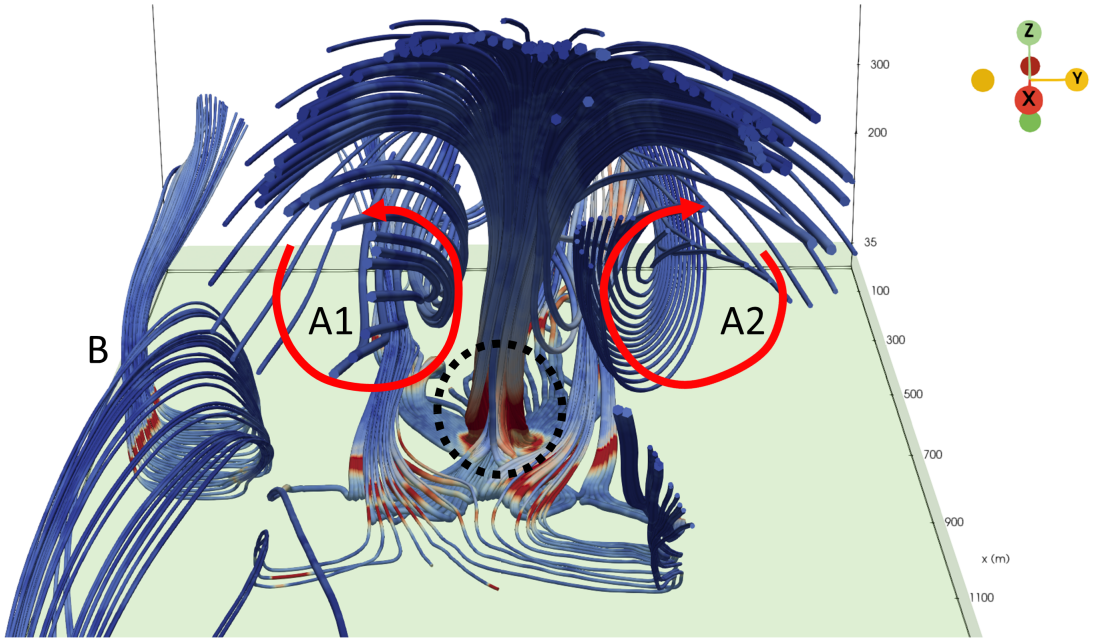
Streamtubes are bundles of streamlines that are tangent to the local flow, and can give us insights into the spatial evolution of complex flow patterns across the flow field. Figure 5.4(a) depicts the streamtubes as viewed from the downstream side of the domain, colored by vorticity magnitude. Helical patterns are observed in streamtubes along the plume edges as the plume propagates downstream (A1, A2), representative of CVPs in the far-field region. On the lateral side of the plume, streamtubes encounter a "trough-like" downdraft region, followed by a region of updraft, exhibiting circulatory motion as they propagate downstream (B). These represent additional helical patterns induced outside the path of the plume, in the flow field, by the plume presence. Close to the source of buoyancy (enclosed in a dashed line), a region of high vorticity is observed. We zoom in on this region and view it from

an alternative angle in Fig. 5.4(b). The high vorticity magnitude is found to correspond to streamtubes near the source, on either side, which rotate inward toward the source on the leeward side, resulting in CVPs (C1, C2), with their rotational axes aligned predominantly in the vertical direction ($\pm z$).

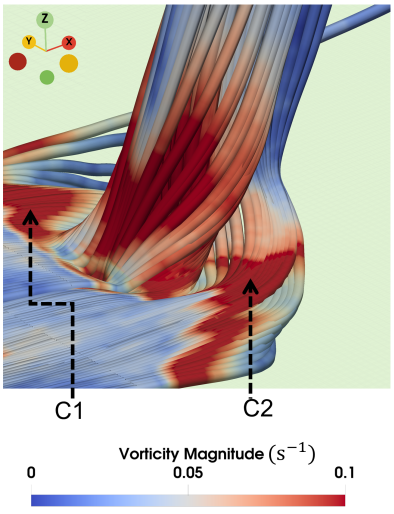
A comparison of streamtubes on the leeward side of the source between the canopy and no-canopy cases is made in Fig. 5.4(c). Two main differences can be observed. Recirculating streamtubes (D) are observed near the canopy top on the leeward side. These streamtubes represent flow that penetrates the canopy as they recirculate and the subsequent entrainment into the buoyant plume from the downstream side. Such recirculating streamtubes are absent in the no-canopy case. We explore this further from the streamtubes in the XZ plane passing through the center of the surface patch, shown for the canopy and no-canopy cases, in Fig. 5.5(a). In the canopy case, streamlines suggest flow that penetrates the canopy from both the upstream and downstream sides before being entrained by the plume updrafts. A recirculation zone is created on the leeward side and the pressure increases upstream of this zone. As the upstream flow approaches the plume, there is a consequent decrease in horizontal momentum followed by entrainment into the plume core. Owing to this decrease, the plume tilt is relatively weaker in the presence of the canopy. In contrast, entrainment into the plume from the upstream side appears to be stronger, with high horizontal momentum, in the no-canopy case. Moreover, streamtubes from aloft are seen to impinge upon the plume on the upstream side. These dynamics result in a steeper tilt in the plume in the absence of a canopy at the surface.

The streamtubes are colored by the cross-stream (y) component of vorticity (ω_y) in Fig. 5.5(a). In both cases, $\omega_y < 0$ on the windward side and $\omega_y > 0$ on the leeward side of the plume. It can be observed that the magnitude of ω_y increases within the plume, though it appears to be higher in the canopy case on both the windward and leeward sides. In the no-canopy case, the magnitude of ω_y is higher on the upstream side. The regions of increased $|\omega_y|$ in

(a) Streamtubes (leeward-side POV)



(b) Streamtubes (near source)



(c) Streamtubes (tilted side view)

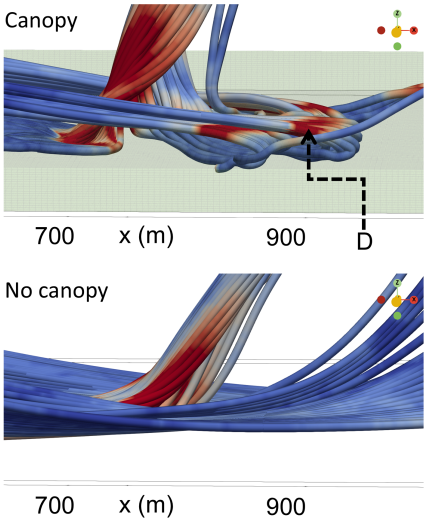


Figure 5.4: 3-D Streamtubes colored by vorticity magnitude (s^{-1}) (a) as observed from the downstream face of the domain and (b) demonstrating the presence of CVPs (C1, C2) near the source, in the canopy case. (c) A comparison of the structure of 3-D streamtubes between the canopy and no-canopy cases. with recirculating streamtubes. A1, A2–helical patterns along the plume edges; B– secondary helical pattern; D– recirculating streamtubes

both cases are associated with stronger deflection of the streamlines and increased shear.

To differentiate between regions of high vorticity and high strain, we plot iso-surfaces of the

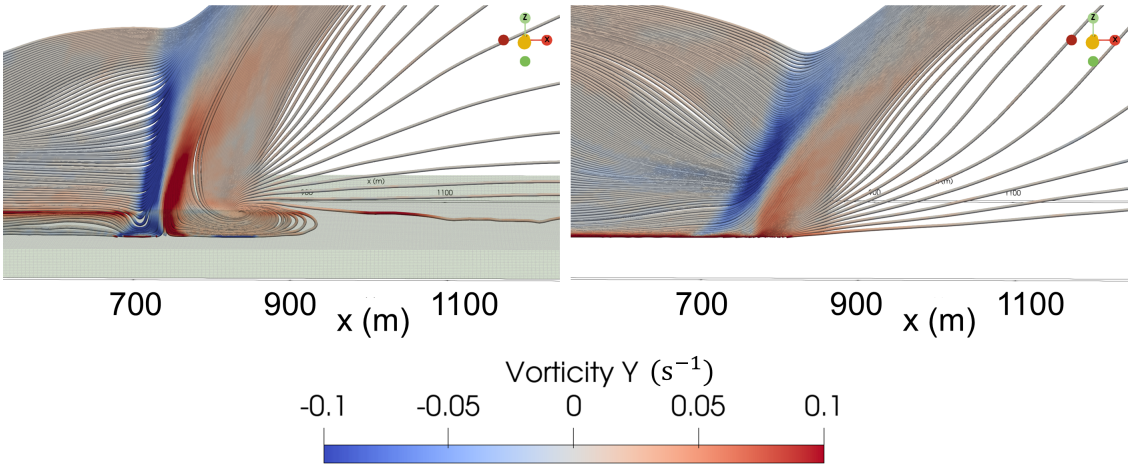
Q-criterion in Fig. 5.5(b) for both canopy and no-canopy cases. The Q-criterion is given by

$$Q = \frac{1}{2}(||\Omega||^2 - ||S||^2), \text{ where } \Omega = \frac{1}{2}\left(\frac{\partial u_i}{\partial x_j} - \frac{\partial u_j}{\partial x_i}\right) \text{ and } S = \frac{1}{2}\left(\frac{\partial u_i}{\partial x_j} + \frac{\partial u_j}{\partial x_i}\right). \quad (5.1)$$

Here, Ω is the rotation rate tensor and S represents the strain rate tensor. In Fig. 5.5(b), the dark, solid red regions ($Q > 0$) indicate rotation-dominated regions, whereas dark, solid blue regions ($Q < 0$) indicate strain-dominated regions. Note that, while the point of view is the same as in Fig. 5.5(a), the isosurfaces are 3-D. The rotation-dominated regions correspond to regions of twisting and rotating streamtubes on either side of the plume near its source in both canopy and no-canopy cases. In the no-canopy case, the rotation-dominated isosurfaces are more tilted and stretched in the downstream direction, representing the tilting and stretching of vorticity by the entrained wind. Strain-dominated regions are observed on the windward and leeward sides of the plume in the canopy case, suggesting the presence of strong shear in these regions. On the windward side, the increased strain rate appears to be associated with the deformation of fluid elements as the cross-flow impinges upon the plume and adjusts to its strong, buoyant updrafts. Conversely, on the leeward side, the increased strain rate is associated with the deformation of fluid elements as the flow transitions from the influence of strong updrafts to that of the cross-wind. Increased strain is more prominent on the leeward side in the no-canopy case.

A comprehensive picture of the circulation patterns in the flow field can be obtained from vortex tubes, i.e. bundles of lines tangent to the local vorticity vectors. Figure 5.6 represents vortex tubes colored by vorticity magnitude (s^{-1}), both within and outside the plume, in the presence of the canopy. It is observed that vortex tubes, near the canopy top, aligned in the direction transverse to the domain are lifted by plume-induced secondary updrafts (A) in the region transverse to the plume. These vortex tubes are then aligned in the streamwise direction by the cross-wind; the associated vorticity vectors, obtained from a

(a) Streamtubes: canopy (left) and no-canopy (right)



(b) Q-criterion: canopy (left) and no-canopy (right)

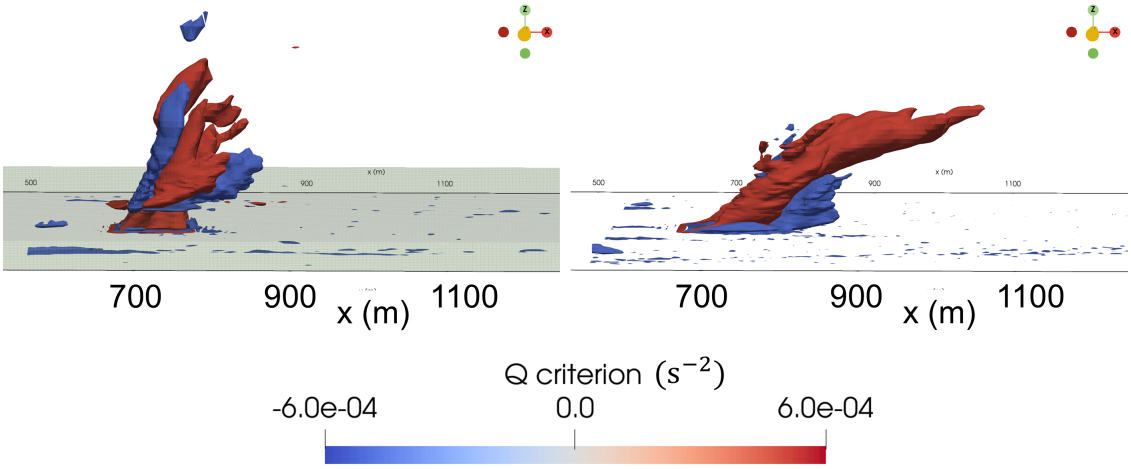


Figure 5.5: (a) Streamtubes, colored by ω_y, in the XZ plane passing through the center of the surface patch and (b) isosurfaces of the Q-criterion shown for the canopy and no-canopy cases

right-hand thumb rule, suggest circulations that direct the flow along a helical pattern, as shown by the streamlines above (B in Fig. 5.4(a)). On the leeward side of the plume, vortex tubes are tilted and stretched (B), via interaction with buoyant updrafts and the cross-wind; the corresponding vorticity vectors suggest hairpin-like vortical structures. Within the plume, vortex tubes are seen to spiral inwards into the plume core (C), resembling ring-like vortical structures and demonstrating entrainment of the surrounding vortical motions into the plume core. This is similar to vorticity entrainment as seen in tornado formation

(191), during which entrained circulation patterns respond to updrafts, resulting in whirl-like phenomena; however, the intensities of such whirl-like circulations in the current case may differ from those associated with tornado formation. On the windward side, these ring-like vortex tubes are pressed toward each other in regions where the vorticity magnitude is relatively higher (C, D). This increase in vorticity magnitude at regions where vortex tubes are more concentrated has also been observed along the fire-front in an experimental study on small-scale surface fires (192) spreading from a point ignition in calm ambient wind conditions. Finally, in the region where the plume interacts with the crosswind aloft, the circulation structures corresponding to the vortex tubes and associated vorticity vectors suggest the presence of CVPs that propagate downstream (E), which can be corroborated by the helical streamtubes seen in Fig. 5.4(a).

We take the opportunity at this point to comment on the extension of the vortical patterns observed from the current setup to intense fires. Church et al. (193) used Meteotron, an array of 105 fuel oil burners in a 140 m×140 m burn area, with a total heat output of approximately 1000 MW to generate a hot smoke plume from an intense experimental fire, which interacted with surface winds ranging from 3–5 ms^{-1}. Although the heat output in their case was 20 times more intense compared to the current case, the vortical patterns observed were similar, including the presence of CVPs near the source, horizontal vortex tubes morphing into hair-pin vortices on the leeward side of the plume, and vortex rings within the rising plume. Moreover, burners produced flames approximately 5–10 m in length, while flames are absent in the current case, indicating the relevance of our low-complexity, no-flame setup in the exploration of fire-induced turbulent flow features.

Next, we investigate the effect of the heat-source geometry. Figure 5.7 depicts streamtubes describing the interaction of the same cross-wind conditions as above with a buoyant plume emanating from a high-aspect ratio ($L_y/L_x = 25$) heat source resembling a line fire at the surface beneath a canopy. The size of the heat source is 20 m × 500 m, so that its area,

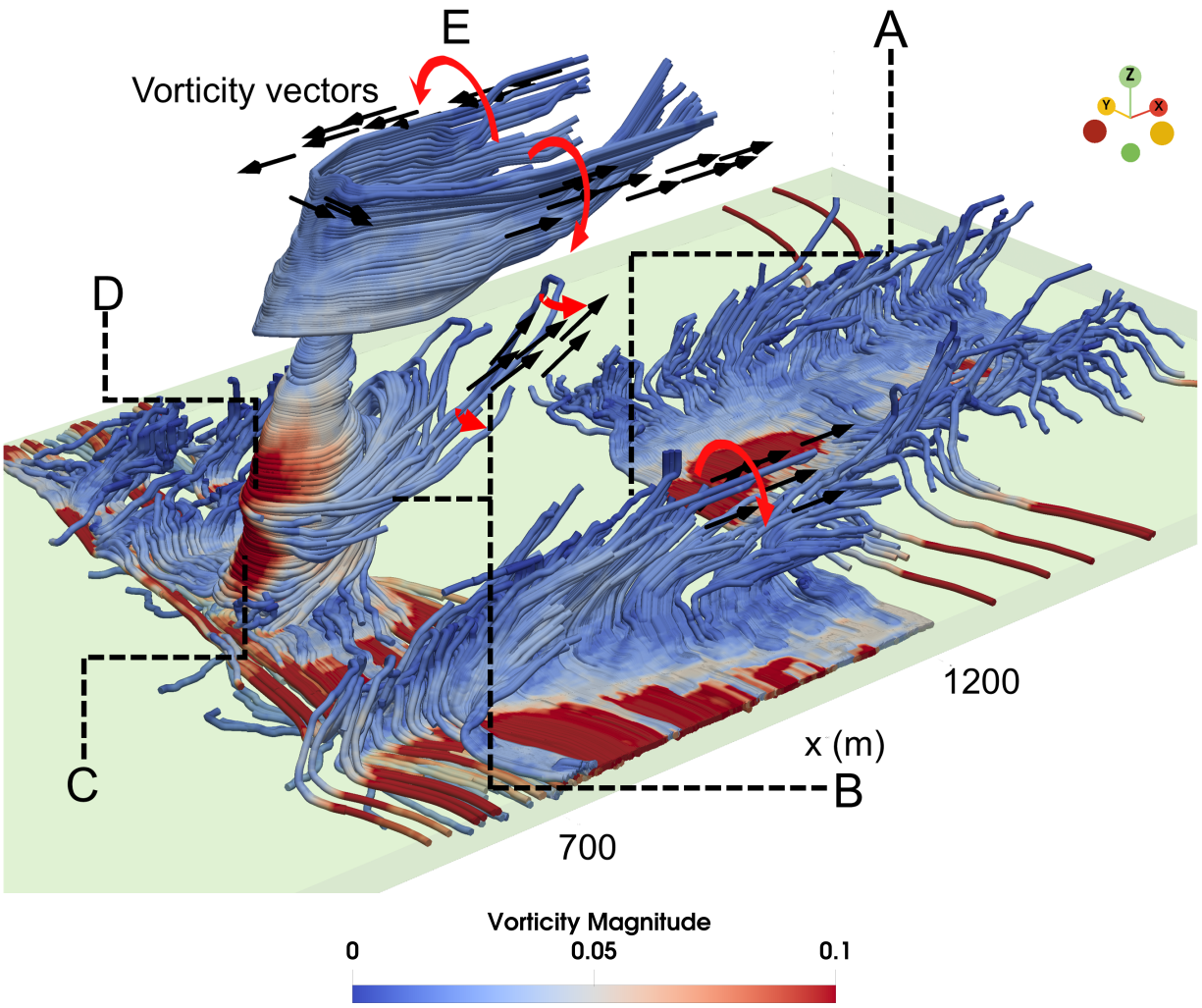


Figure 5.6: Vortex tubes colored by vorticity magnitude (s^{-1}). A– Vortex tubes influenced by updrafts, cross-wind; Plume-modulated and tilted hairpin vortices; C– Spiraling vortex tubes in plume; D– Vorticity intensification at plume windward edge; E– CVPs propagating downstream. Black solid arrows represent vorticity vectors and red arrows the corresponding circulation structures

and hence the total power output (50 MW), is the same as that for the square-shaped heat source described above. A few similarities exist with the structures seen from the square heat source, i.e. the presence of the secondary helical pattern on the transverse side of the source and helical/rotational patterns in the plume as it propagates downstream. In addition, alternating tower-trough-like structures (T1, T2) are observed in the plume. In the trough-like (T2) regions, the streamtubes resemble forward burst-like flow patterns that potentially

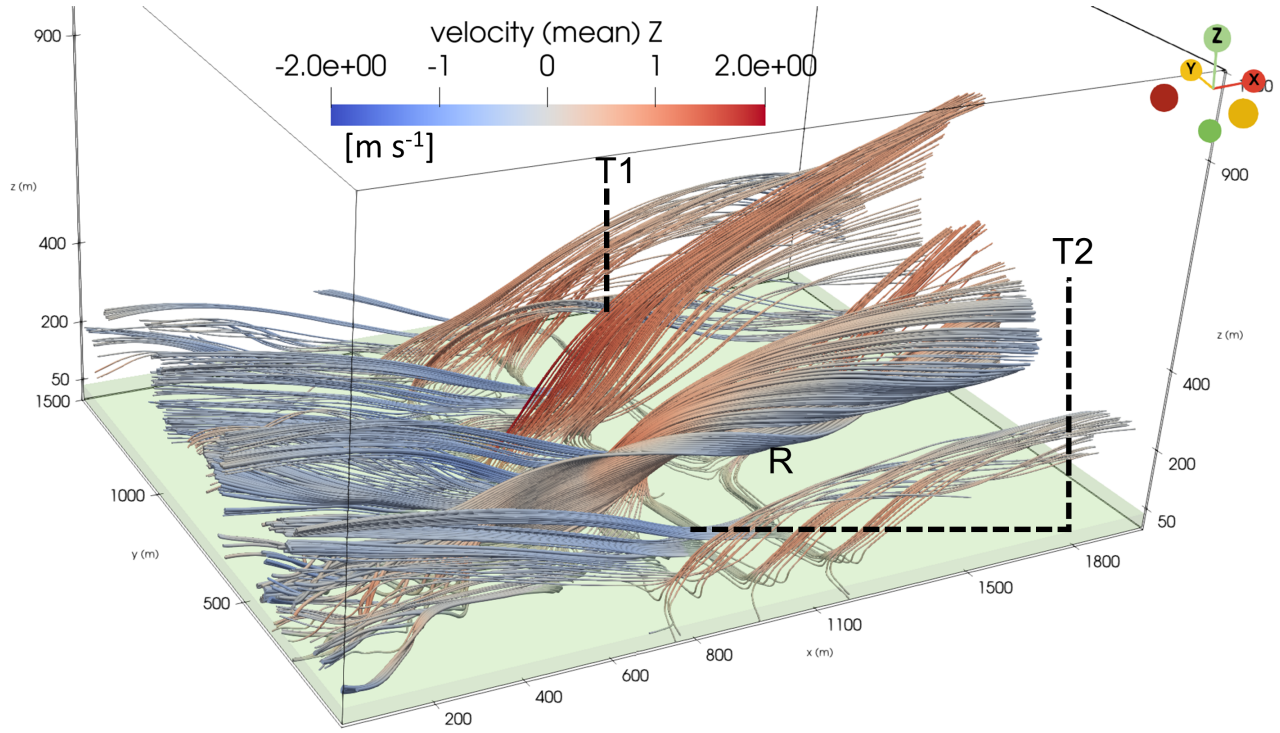


Figure 5.7: Streamtubes for a high-aspect ratio heat source colored by $\overline{w}$. T1–tower-like regions; T2–trough-like regions; R–rotational/helical patterns

transport heat downstream. In the tower-like regions (T1), the rotating streamtubes describe a helical pattern (R) in the plume as it propagates downstream. The circulation patterns in the plume are aligned in the transverse direction such that the troughs correspond to the downwash regions and the towers to the upwash regions. Such tower-trough-like regions and circulation patterns have been observed in laboratory experiments (194) and FIRETEC simulations (195) on propagating flames as well. Again, the common features between our static heat source and propagating firelines show considerable promise for the current low-complexity setup to capture much of the plume dynamics observed from otherwise more resource-intensive simulations.

5.3.3 Momentum Fluxes and Quadrant Analysis

Thus far, we have discussed the features of the mean flow field. We now focus on insights that can be obtained from the turbulent momentum-flux events near the plume source and attempt to differentiate between the canopy and no-canopy cases in that regard. Figures 5.8(a)–(b) depict the turbulent momentum flux, $\overline{u'w'}$, for the canopy and no-canopy cases, respectively, on the XZ plane passing through the symmetry axis of the heat source, with the overbar representing the 1-h block mean as discussed in Sect. 5.2. Mean plume centerlines from Zone 1 are also plotted for both cases. The regions where $\overline{u'w'} < 0$ represent regions where momentum is transported to the surface, whereas regions where $\overline{u'w'} > 0$ represent regions where momentum is injected into the atmosphere aloft. Momentum fluxes within the plume demonstrate spatial heterogeneity along with a noticeable structural difference between the canopy and no-canopy cases. In the canopy case, a clear distinction is observed between the nature of the momentum fluxes on the upstream and downstream sides of the mean plume centerline. Momentum is transported from the atmosphere aloft towards the plume source on the windward side. This region corresponds to the region where ambient wind loses its horizontal momentum as it approaches the plume, as noted in Sect 5.3.2. This region extends through the canopy, all the way to the surface. On the leeward side of the mean plume centerline, which remains relatively sheltered from the cross-wind, momentum is transported away from the source of buoyancy into the atmosphere aloft. In the no-canopy case, however, the plume region where momentum is injected into the atmosphere, by turbulent fluxes away from the buoyancy source is juxtaposed on either side by plume regions where momentum is transported to the surface/buoyancy source. Moreover, the intensity of the momentum fluxes appears to be higher in the canopy case.

Through a quadrant analysis, momentum-flux events can be categorized into sweeps (downfluxes of high momentum, i.e. $u' > 0, w' < 0$), ejections (upfluxes of low momentum, i.e. $u' < 0, w' > 0$), outward interactions (upfluxes of high momentum, i.e. $u' > 0, w' > 0$), and

inward interactions (downfluxes of low momentum, $u' < 0, w' < 0$). Of these, sweeps and ejections only contribute negative momentum fluxes, while outward and inward interactions only contribute positive momentum fluxes. Once categorized, the contribution to the net momentum flux from each of these quadrants (E) can be computed. Figures 5.8(c)–(d) depict the difference between the contribution of sweeps and ejections ($\Delta S = E_{\mathrm{s}} - E_{\mathrm{e}}$) for the canopy and no-canopy cases, respectively. In both cases, ejections dominate sweeps on the windward side of the plume (red region), whereas sweeps dominate ejections on the leeward side (blue region). However, in the canopy case, the overall effect on the leeward side is dominated by positive momentum fluxes as seen from Fig. 5.8(a), making the dominance of ejections on the windward side the more important observation. In addition, sweeps are observed to contribute more within the canopy volume on the windward side of the plume centerline. Additionally, Figs. 5.8(e)–(f) depict the difference between the contribution of outward and inward interactions ($\Delta S = E_{\mathrm{o}} - E_{\mathrm{i}}$) for the canopy and no-canopy cases, respectively. A higher momentum-flux contribution from outward interactions compared to inward interactions is observed on the windward side of the plume centerline, particularly for the no-canopy case. In the canopy case, however, outward interactions also appear to dominate on the leeward side, which is a significant observation since the overall effect is dominated by positive momentum fluxes on the leeward side. Inward interactions are observed to prevail only over a thin region along the plume centerline in both the canopy and no-canopy cases. Within the canopy volume, inward interactions prevail on the windward side; however, these are overshadowed by negative momentum fluxes as seen in Fig. 5.8(a); moreover, outward interactions prevail on the leeward side within the canopy volume (Fig. 5.8(e)). Therefore, in the canopy presence, momentum appears to be transferred toward the canopy top primarily through upfluxes of low momentum (ejections), followed by downfluxes of high momentum (sweeps) toward the buoyancy source within the canopy, on the windward side of the plume centerline. Momentum is transferred from the buoyancy source to the atmosphere aloft on the leeward side through upfluxes of high momentum (outward interactions), both within

and above the canopy subspace. The high contribution of sweeps and increased contribution from outward interactions below the canopy height, is also in agreement with observations from prescribed burns in forested environments (5; 91) as mentioned in Sect. 5.1. In fact, the increased contribution from outward interactions often competes with the contributions from sweeps and ejections in both environments (5).

Figure 5.9 shows the event fractions for each momentum-flux event near the surface/buoyancy source in both, the presence and absence of the canopy. It is observed that in the regions where the ejections dominate the momentum-flux contribution, sweeps dominate in occurrence frequency (compare Figs. 5.9(a)–(b) to Figs. 5.8(c)–(d)). Moreover, relative to sweeps, the fraction of ejections appears to be relatively suppressed (Figs. 5.9(c)–(d)). Similarly, the fraction of inward interactions appears to be higher relative to outward interactions in regions where outward interactions dominate the momentum-flux contribution, in both canopy and no-canopy cases (compare Figs 5.9(g)–(h) to Figs. 5.8(e)–(f)). Moreover, relative to inward interactions, the fraction of outward interactions is suppressed (Figs. 5.9(e)–(h)). In previous studies (5; 91), the fraction of sweeps was found to increase at all heights within the canopy as a fire-front passed by a measuring tower. Our analysis suggests an increase in sweep frequencies from the ambient above the canopy down to the canopy top (Fig. 5.9(a)), but not below. Within the canopy, ejections appear to be more frequent in our case (Fig. 5.9(c)), which is inconsistent with experimental data. Moreover, experiments have also demonstrated a higher increase in the occurrence frequency of outward interactions relative to inward interactions within the canopy, which also appears to be inconsistent with our results (Fig. 5.9(e) and (g)). However, the increase in occurrence frequency of inward interactions in the no-canopy environment (Fig. 5.9(h)) is consistent with experiments. Thus, while there is good agreement between our results and experiments for contributions from the momentum-flux events, there are inconsistencies associated with event fractions. These inconsistencies may be attributed to differing canopy densities, wind-forcing conditions (e.g., firelines backing against the wind), heat-source geometries and intensities, or insufficient observations. They

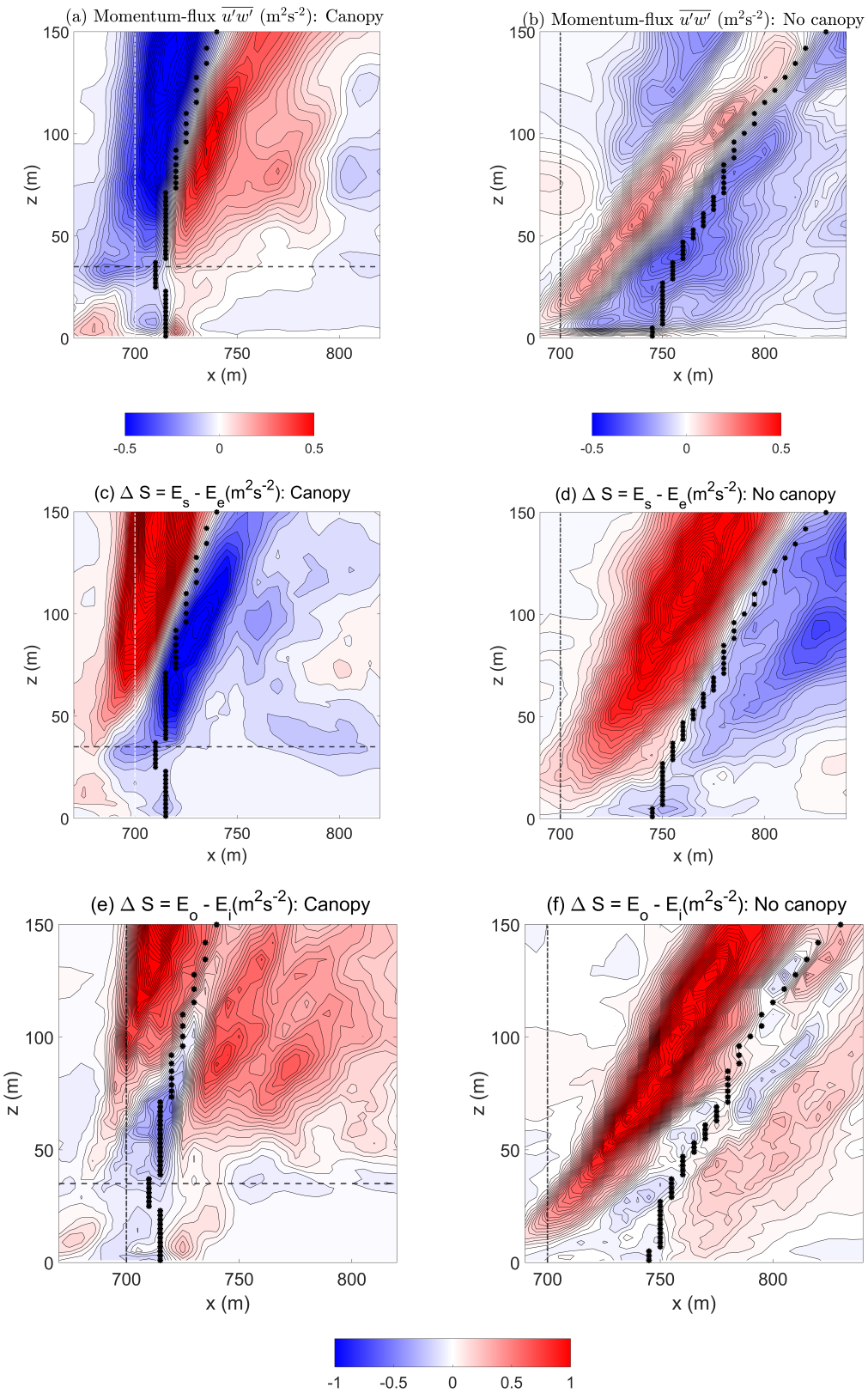


Figure 5.8: Turbulent momentum fluxes ($\overline{u'w'}$) in the (a) canopy and (b) no-canopy cases close to the surface. $\Delta S = E_s - E_e$ in the (c) canopy and (d) no-canopy cases. $\Delta S = E_o - E_i$ in the (e) canopy and (f) no-canopy cases. Black dots represent mean plume centerlines and colorbar units are m^2s^{-2}

highlight the need for more burn experiments and computational simulations over a wide range of forcing conditions and geometrical constraints, especially in canopy environments.

5.4 Conclusions and Future Work

In this study, we have investigated the flow features characteristic of the interaction of a buoyant plume with a mild cross-wind as informed by the presence of a tall, spatially homogeneous plant canopy. This is accomplished using idealized LES with a low-complexity setup sans a combustion model, in which the source of buoyancy, comprising a surface patch of a high sensible heat flux (100 times) relative to the ambient, is static. Apart from attempting to identify the key features distinguishing the effects of the canopy from no-canopy environments, we also address the usefulness of such a setup in replicating fire–atmosphere interaction features as observed in previous studies.

As the plume interacts with the crosswind, counter-rotating vortex pairs (CVPs) are formed near the source as the flow twists and rotates into the leeward side of the buoyancy source from either side. The rising plume comprises ring-like, spiraling vortical structures representing the entrainment of ambient vorticity into the plume core, akin to processes associated with tornado formation as documented in the literature. The vorticity intensifies at the windward edge, where the ring-like structures are compressed together, and tilted "hair-pin"-like vortical structures exist on the leeward side. Flow patterns aloft exhibit helical motions as the CVPs aloft propagate downstream, trailing the plume. To explore the effect of changing the source geometry, we examine the flow field surrounding a high-aspect ratio source resembling a line source of buoyancy. Tower-trough-like structures are found to exist, with forward burst-like motions in the trough regions, which potentially carry heat downstream as they penetrate the canopy. These flow features show promising consistencies with prior studies on buoyant plumes in cross-flow without canopies, propagating fires in laboratory-scale

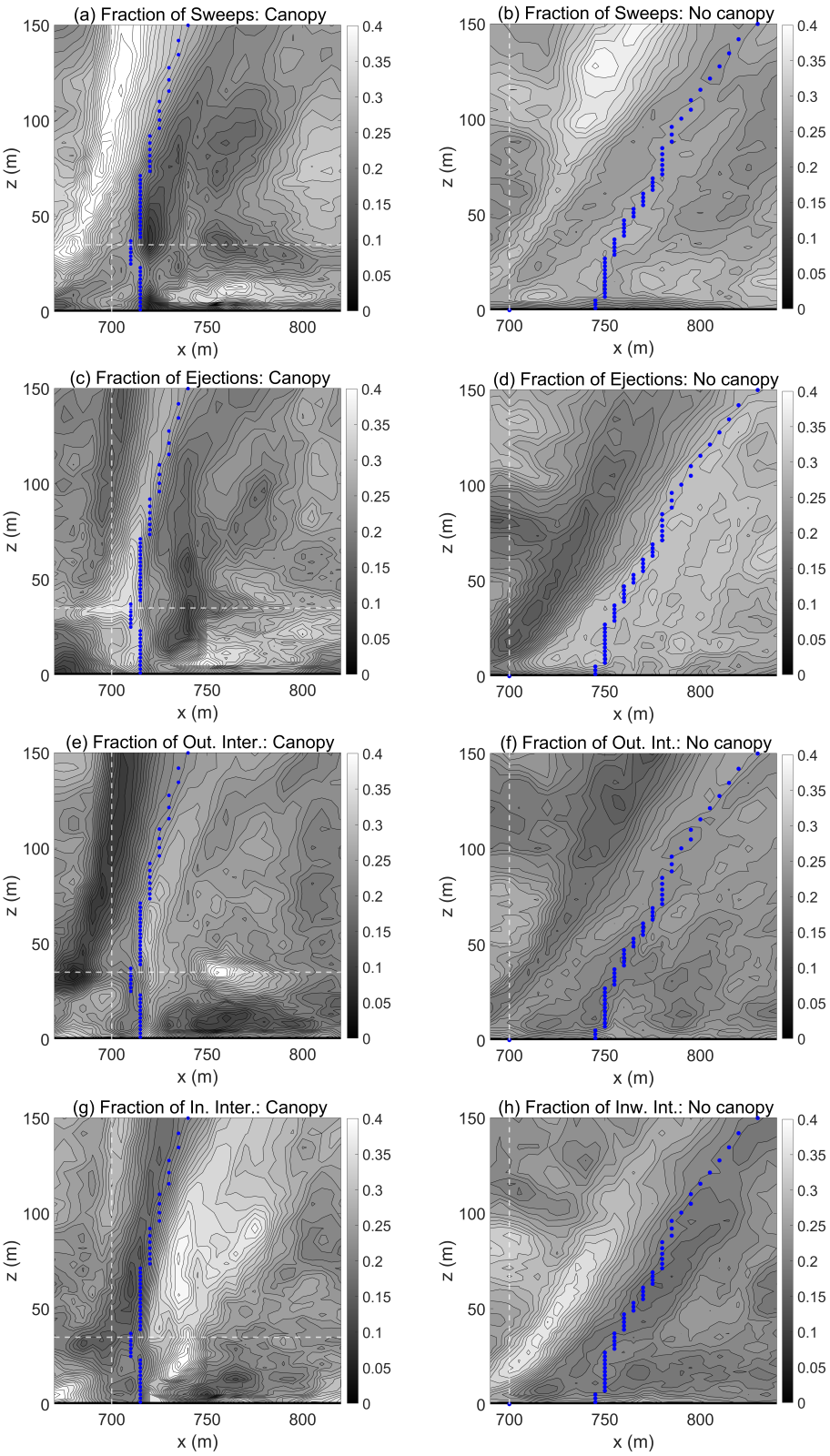


Figure 5.9: Fraction of sweeps in the (a) canopy and (b) no-canopy cases; ejections in the (c) canopy and (d) no-canopy cases; outward interactions in the (e) canopy and (f) no-canopy cases; inward interactions in the (g) canopy and (h) no-canopy cases. Blue dots represent the mean plume centerline in Zone 1

fuel beds, static fires in field-scale experiments, and FIRETEC simulations. This suggests that this simplified setup can be useful for capturing much of the plume dynamics, while circumventing the computational overhead associated with the complex system of equations governing fire spread in models and relieving the pressure on the resources deployed during controlled burns to collect extensive measurements.

Differences are observed in the plume behavior between the simulated canopy and no-canopy environments, both near the buoyancy source and in the far-field region. Near the source, the plume tilts relatively less steeply in the canopy case due to the canopy drag on the plume. Moreover, on the leeward side of the mean plume centerline, a recirculation region is formed within the canopy as air is entrained into the plume from there. As the flow approaches the region of increased pressure upstream of the recirculation, it decelerates and is entrained into the plume. In this manner, the recirculation zone obstructs the upstream flow, and two distinct regions are formed on either side of the plume centerline, with the leeward side being sheltered from the upstream flow. In contrast, no recirculation region exists in the no-canopy case, and entrainment from the upstream side of the plume centerline is stronger. The flow impinges upon the rising plume from the upstream side, and the plume tilts more steeply. The plume transitions from the rise phase to the far-field at a higher altitude in the canopy case, indicating the existence of a canopy-induced scale encompassing its aerodynamic effects on the rising plume. Moreover, the spatially oscillatory behavior of the far-field mean plume centerline is subdued compared to the no-canopy case.

The spatial distribution of turbulent momentum flux events near the buoyancy source also differs between the two environments. Above the canopy, there is downward transfer of momentum predominantly via ejections (upward fluxes of low momentum) toward the canopy top upstream of the mean plume centerline; however, sweeps (downward fluxes of high momentum) prevail within the canopy volume, upstream of the mean plume centerline. On the leeward side, sweeps dominate ejections. However, counter-gradient motions play a

more significant role in transferring momentum away from the buoyancy source, with outward interactions (upward fluxes of high momentum) being most dominant both within and above the canopy. These observations are consistent with measurements collected within tall canopies during prescribed burns. In contrast, the no-canopy environment shows a different pattern: counter-gradient motions near the surface are sandwiched between an ejection-dominated region on the upstream side and a sweep-dominated region on the downstream side. On the upstream side of the mean plume centerline, outward interactions compete with ejections–again, an observation consistent with grassland burns. The physics-based insights, obtained from our analysis, into the differences in plume behavior between canopy and no-canopy environments can be validated against experimental data and can be utilized for the development of improved parameterizations within fire- and plume-behavior models.

Notwithstanding the promise of this setup and analysis, there are limitations that need to be addressed. While our results regarding the contributions from the momentum-flux events agree with those from experiments, the inferences regarding event fractions are inconsistent with observations. These inconsistencies may be attributed to differing canopy densities, wind-forcing conditions (e.g., firelines backing against the wind), heat-source geometries and intensities, or insufficient observations. Additional computational simulations can be aimed at exploring the effects of a range of wind and buoyancy forcing conditions, source geometry, and canopy characteristics. Furthermore, a grid-sensitivity test is required to ensure the integrity of the results, regardless of the grid resolution. The effect of the domain parameters and the fetch over which the flow at the inlet adjusts to the canopy presence before encountering the plume may need to be investigated to ensure the independence of the results. Moreover, for a comparison with coherent structures observed in field-scale burns within tall canopies, the temporal resolution may need to be adjusted to match the higher sampling frequency from experiments. Future work can also involve a comparison of the steady-state features from the current analysis with the transient dynamics of propagating experimental fires in the field.

Despite its limitations, the analysis advances our knowledge regarding plume–cross-wind interactions in the presence of a canopy, which remains sparse in the literature. Moreover, it lays the foundation for the development of scaling laws characterizing plume trajectories in canopy environments as described in the next chapter.

Chapter 6

Scaling analysis for buoyant plumes over wildland fires

6.1 Background

Quantifying the dynamics of plumes emanating from surface fires is crucial for assessing respiratory and visibility hazards due to smoke, heat transfer to flammable vegetation and property in the vicinity, and for informing fire management strategies. This includes an accurate, physics-based estimation of plume trajectories under the varying influencing conditions of fire intensity, ambient wind forcing, and geometry of the burning region (196). Moreover, tall vegetative canopies significantly alter the coherent patterns associated with momentum transport and exchange with the atmosphere aloft, and turbulence intensities (93; 75; 81; 5; 102). Therefore, trajectories of plumes with heat sources beneath a tall canopy can differ substantially from those in no-canopy environments.

A large volume of early literature is dedicated to laminar and turbulent buoyant plumes emerging from point or line sources in quiescent environments (197; 198; 199; 200; 201), cap-

italizing on similarity criteria to develop scaling laws characterizing the spatially evolving plume structure. Insights from several recent studies have been aimed at strengthening the physical underpinnings and overcoming the perceived shortcomings of classical plume theory (197; 198) in relation to unsteady effects, corrections for source geometry, explosive thermals, etc.(202; 203; 204; 205; 206; 207). Additionally, over the last few decades, power-law scalings for buoyant plumes in cross flow have been developed using several experimental studies (147; 148; 149; 150; 151; 152) with the pioneering work by Briggs (147) serving as the primary reference for point sources. An early study by Raupach (208) used dimensional analysis to model bushfire plumes as a line source of buoyancy. Based on a series of assumptions, including plume self-similarity under a cross-wind and extrapolation of point-source updraft velocity behavior to line sources, they related plume angles to updraft velocity and buoyancy-source strength. Davidson (149) demonstrated that predictions of the plume trajectory from a rectified version of the two-thirds law for non-point (finite) sources, derived from conservation laws, showed improved agreement with flume experiments near the source and approached the two-thirds law downstream from the source (far-field region). Apart from validating a one-thirds law for plume rise in the near source region, with an added initial momentum at the source, and the two-thirds power law for plume rise in the far field regions, for both laminar and turbulent cross-flow, Huq and Stewart (154) demonstrated a lower plume rise in the presence of ambient turbulence using water tunnel experiments. In a subsequent analysis, based on LIF (laser-induced fluorescence) experiments on plume discharge from a finite source, Pun and Davidson (150) provided evidence supporting a three-fourths law near the plume source, referred to as the "weakly-advected-plume region", before undergoing a transition to the two-thirds law further away, called the "strongly-advected-thermal region". A recent study by James et al. (155) corroborated the one-thirds and two-thirds laws using experiments conducted on single-phase saline plumes and line thermals in cross-flow, with coefficients in good agreement from those in previous studies (209; 210). Through wind-tunnel experiments that deployed rectangular diffusion burners, Himoto et al. (196) supplemented

the literature by developing a power-law dependency of plume trajectories on dimensionless forms of not only the heat release rate and cross-wind velocity at the inlet, but also the the burner aspect ratio. The power-law model represented the experimental data to a high degree of accuracy, except close to the plume source.

Laboratory studies are limited by their scale, which can impact the physics of the observed plume behavior. Computational modeling efforts have also been invested in exploring scaling laws and have served to draw comparisons with experiments. Devenish et al. (211) compared outputs from large-eddy simulations (LES) with plume-trajectory power laws for buoyant plumes interacting with both weak and strong cross-flow under stable conditions. They found substantial evidence to support the two-thirds law for plume rise with downwind distance in strong cross-wind when analytically correcting for non-point (finite) source sizes, but little evidence for weak cross-wind. A recent LES study that incorporated similar conditions, by Cintolesi et al. (175) and direct numerical simulations (DNS), by Jordan et al. (212), on plumes with zero source-velocity interacting with a uniform cross-wind, also corroborated the two-thirds law.

While buoyant plumes interacting with a cross-wind in open (no-canopy) environments have been the focus of most previous studies, research on the added influence of vegetative canopies remains elusive. While Raupach (208) proposed scaling laws for different source geometries, the study primarily discussed the shearing effects of plant canopies qualitatively. More recently, Chung and Koseff (156) proposed scaling parameters capturing the complex interplay between buoyancy, cross-wind, and canopy turbulence, which were based on the friction velocity and the Richardson number obtained from flume experiments. Field-scale experiments (e.g. controlled pile and broadcast burn experiments) (90; 81; 4; 102) that have studied turbulent plumes originating within tall vegetative canopies, though useful in their own right, are limited by spatial localization and logistical obstacles to deploying extensive instrumentation while maintaining quality control, making the development of scaling laws

for characterizing plume dispersion on field scales an uphill task.

Dimensional analysis has found applications in several fluid mechanics problems and can be helpful in untangling the complex dynamics of turbulent flows in a variety of physical (boundary) conditions (213; 214). In this case, it presents a powerful tool to condense multiple dominant factors governing plume deflection into fewer dimensionless groups. These groups can be used to develop scaling laws governing the dependence of plume trajectories on a range of parameters, including buoyancy source strength, ambient wind forcing, and heat-source geometry, as demonstrated by many previous studies (199; 208; 196). For instance, a recent summary paper by Taherian and Mohammadian (215) attempted a dimensional analysis for a buoyant jet in cross-flow and "no-canopy" conditions, relating trajectories to a cross-flow-based densimetric Froude number, without obtaining an explicit functional relation.

In this paper, we propose scaling relationships characterizing plume rise and dispersion with a particular emphasis on canopy environments. This is accomplished via a dimensional analysis followed by a characterization of plume slopes based on a large suite of large-eddy simulations comparing buoyant plumes in canopy and "no-canopy" environments. Through such comparisons, our analysis provides insights into the relative importance of the underlying physical mechanisms informing buoyant plume trajectories, both near the surface and in the far-field, when the surface boundary conditions reflect canopy presence. Scaling laws, based on the power-law dependencies explored in our analysis, can significantly reduce the computational overhead in field-scale fire-plume and smoke behavior models (196). The analysis informs the development of improved predictive models for plume rise and smoke transport in a range of conditions, which is important for managing air quality hazards during natural and human-made disasters and when planning prescribed burns for preemptive reduction of hazardous fuels.

6.2 Methods

Starting from a summary of the primary variables involved, which may govern plume deflection, we first obtain our dimensionless groups based on the Buckingham Pi Theorem (BPT) (213; 214). We then revisit scaling laws governing the plume trajectory from some representative studies in both canopy and open environments and show that the plume centerline slope can be obtained in terms of our dimensionless (π) groups despite differences in power-law indices among various studies. Finally, we utilize outputs from a corpus of simulations in a tall-canopy environment to explore a power-law dependency between the plume slope and other non-dimensionalized parameters. These are complemented by a similar number of simulations in a "no-canopy" environment but otherwise similar computational domain, surface heat flux, heat-source geometry, and wind-forcing conditions to facilitate a comparison.

In the LES, a homogeneous canopy is simulated with a height (h_c) of 35 m, drag coefficient (c_d) of 0.2, leaf area index (LAI) of 5, and the corresponding leaf-area density (LAD) profile taken from Dias-Junior et al. (186). The canopy elements are not explicitly modeled; rather, a volume-averaged effect of the porous canopy layer is considered, with the canopy drag-force term in the momentum equation for the mean velocity accounting for the aerodynamic effects of the canopy. Fire plume presence is simulated by a thermal plume arising from a localized region of area 100 m $\times$ 100 m with a prescribed high sensible heat flux. The surface heat flux in this region is taken to be 100 times the ambient surface sensible heat flux for the base case ($H_{\text{surface}} = 50\,\text{Wm}^{-2}$, $H_{\text{patch}} = 5\,\text{kWm}^{-2}$), though this factor is increased for the parametric study in this analysis in steps of $5\,\text{kWm}^{-2}$ in the range 5–35 kWm^{-2}. The geostrophic wind speeds (U) considered include 2, 3, 5, and $7\,\text{ms}^{-1}$. The ambient wind follows a turbulent, logarithmic profile at the inlet, which morphs into a profile with an inflection point near the canopy top over some fetch. Daytime atmospheric conditions are simulated with a well-mixed layer, i.e. a uniform initial profile of the potential temperature with height, up to a temperature inversion height (δ) of approximately 1.1 km. A more comprehensive description

of the LES model and simulations can be obtained from Chapter 4.

Figure 4.13 presents a simplified, 2-D picture of the plume interacting with a cross-wind, the plume centerline trajectory transitioning from the rise phase to the entrainment phase at $(x_{\mathrm{pc}},\ z_{\mathrm{pc}})$, along with a summary of the variables/parameters involved. It can be seen that the plume centerline slope that we aim to track in the analysis to follow is given by $z_{\mathrm{pc}}/x_{\mathrm{pc}}$, which is equivalent to $\lambda_{\mathrm{pc}}/\delta$ by basic proportionality arguments. The variable λ_{pc} is the horizontal length scale representing the onset of the entrainment phase. One way of interpreting λ_{pc} is the streamwise length traversed by the plume, should the plume transition from the rise phase to the entrainment phase at the height of the inversion layer, i.e. if $z_{\mathrm{pc}} \to \delta$.

6.2.1 Obtaining Dimensionless (π) Groups

The key variables and their dimensional representations are summarized in Table 6.1. Note that we have ignored two variables, i.e. kinematic viscosity (ν) and surface roughness (z_0), since the surface roughness is much shorter compared to other relevant length scales (it can be argued that we are considering the average flow outside of the influence of the surface roughness) and the flow is at a sufficiently high Reynolds number to preclude viscous effects. We begin with a functional dependence of the response variable λ_{pc} to the geometric constraints, forcing variables, and boundary conditions of the following form: $\lambda_{\mathrm{pc}} = \mathcal{F}(\delta,\ g, \frac{\Delta H_{\mathrm{s}}}{\rho c_{\mathrm{p}}},\ u_*,\ h_{\mathrm{c}},\ L_{\mathrm{c}},\ R_{\mathrm{p}},\ U,\ \theta_{\mathrm{a}})$. Since we have 10 variables ($M_{\mathrm{d}} = 10$) and 3 fundamental dimensions ($N_{\mathrm{d}} = 3$), i.e. L, T, Θ, the number of dimensionless groups is: $M_{\mathrm{d}} - N_{\mathrm{d}} = 10 - 3 = 7$. We choose the repeating variables such that they collectively include the three fundamental dimensions:

- R_{p} - involves L

Table 6.1: A summary of the variables used in the dimensional analysis

No.	Category	Variable	Symbol	Dimensions
1	Response	Horizontal length scale, plume bend	λ_{pc}	L
2	Geometric constraint	ABL Height	δ	L
3	Forcing	Buoyancy	g	LT^{-2}
4	Forcing	Kinematic heat flux difference at surface ($\Delta H_{\mathrm{s}} = H_{\mathrm{patch}} - H_{\mathrm{ambient}}$)	$\frac{\Delta H_{\mathrm{s}}}{\rho c_{\mathrm{p}}}$	ΘLT^{-1}
5	Forcing	Friction velocity (turbulence intensity)	u_*	LT^{-1}
6	Boundary condition	Canopy height	h_{c}	L
7	Geometric constraint	Canopy drag length scale	L_{c}	L
8	Boundary condition	Effective patch radius (Patch area / Perimeter)	R_{p}	L
9	Forcing	Ambient velocity	U	LT^{-1}
10	Forcing	Ambient potential temperature	θ_{a}	Θ

- U (ambient velocity) - involves L, T
- θ_{a} (ambient temperature) - involves Θ

These repeating variables are chosen because they are relatively easy to control and can be readily determined from numerical models of fire behavior or field experiments. The formation of the π groups, based on the BPT, is presented in the Appendix for brevity and yields the following expressions.

In the canopy case: $\pi_1 = f(\pi_2, \pi_3, \cdots, \pi_6, \pi_7)$

$$\begin{aligned} \pi_1 &= f(\pi_2, \quad \pi_3, \quad \pi_4, \quad \pi_5, \quad \pi_6, \quad \pi_7), \\ \frac{\lambda_{\mathrm{pc}}}{R_{\mathrm{p}}} &= f\left(\frac{\delta}{R_{\mathrm{p}}}, \; g\frac{R_{\mathrm{p}}}{U^2}, \; \frac{\Delta H_{\mathrm{s}}}{\rho c_{\mathrm{p}}}\frac{1}{\theta_{\mathrm{a}} U}, \frac{u_*}{U}, \frac{h_{\mathrm{c}}}{R_{\mathrm{p}}}, \frac{L_{\mathrm{c}}}{R_{\mathrm{p}}}\right), \end{aligned} \tag{6.1}$$

where $L_{\mathrm{c}} = (c_{\mathrm{d}} LAD)^{-1}$ and is referred to as the canopy drag or adjustment length scale (1).

Since the integral of the leaf-area density (LAD) over height is the leaf-area index (LAI), i.e. $\int_0^{h_c} LAD \mathrm{d}z = LAI$, the adjustment length scale can be approximated using the LAI, i.e. $L_c \approx h_c (c_d LAI)^{-1}$.

In the no-canopy case, there are only five π groups: $\pi_1 = f(\pi_2, \pi_3, \pi_4, \pi_5)$:

$$\begin{aligned} \pi_1 &= f(\pi_2, \quad \pi_3, \quad \pi_4, \quad \pi_5), \\ \frac{\lambda_{pc}}{R_p} &= f\left(\frac{\delta}{R_p}, \; g\frac{R_p}{U^2}, \; \frac{\Delta H_s}{\rho c_p}\frac{1}{\theta_a U}, \frac{u_*}{U}\right), \end{aligned} \tag{6.2}$$

where the terms associated with canopy presence and characteristics are precluded. According to the linear plume rise model (Fig. 4.13), the plume slope in the rise phase for both cases is recovered as follows:

$$\frac{\delta}{\lambda_{pc}} = \frac{\delta}{R_p}\frac{1}{f}.$$

In addition, π_4 can be recast as follows:

$$\frac{\Delta H_s}{\rho c_p}\frac{1}{\theta_a U} \simeq \frac{\overline{w'\theta'}}{u_*}\frac{1}{\theta_a}\frac{u_*}{U}.$$

We know that $u_*^2 \simeq |u'w'|$. If we reasonably assume that $u' \sim u_*$, then $w' \sim u_*$. Moreover, we can argue that $\theta' \sim \Delta\theta = \theta - \theta_a$, the equation above becomes:

$$\frac{\Delta H_s}{\rho c_p}\frac{1}{\theta_a U} \sim \frac{\Delta\theta}{\theta_a}\frac{u_*}{U} \rightarrow \pi_4 \sim \frac{\Delta\theta}{\theta_a}\pi_5.$$

Moreover, we note the following. For an ideal gas, at atmospheric pressure in the environment, $p_a \approx \rho_a R \theta_a$, where the absolute temperature can be approximated to be the potential

temperature near the surface. Under thermal expansion,

$$p_{\mathrm{a}} = (\rho_{\mathrm{a}} + \Delta\rho)R(\theta_{\mathrm{a}} + \Delta\theta) \rightarrow p_{\mathrm{a}} = \rho_{\mathrm{a}} R\theta_{\mathrm{a}} \left(1 + \frac{\Delta\rho}{\rho_{\mathrm{a}}}\right)\left(1 + \frac{\Delta\theta}{\theta_{\mathrm{a}}}\right),$$
$$\Rightarrow 1 = 1 + \frac{\Delta\rho}{\rho_{\mathrm{a}}} + \frac{\Delta\theta}{\theta_{\mathrm{a}}} + \text{h.o.t.},$$
$$\Rightarrow \frac{\Delta\rho}{\rho_{\mathrm{a}}} = -\frac{\Delta\theta}{\theta_{\mathrm{a}}}.$$

Additionally, by definition of the coefficient of thermal expansion,

$$\Delta\rho = -\beta_{\mathrm{T}}\rho_{\mathrm{a}}\Delta\theta \Rightarrow \beta_{\mathrm{T}}\Delta\theta = -\frac{\Delta\rho}{\rho_{\mathrm{a}}} = \frac{\Delta\theta}{\theta_{\mathrm{a}}}.$$

Therefore,

$$\frac{\pi_4}{\pi_5} = \frac{\Delta H_{\mathrm{s}}}{\rho c_{\mathrm{p}}}\frac{1}{\theta_{\mathrm{a}} u_*} \sim \frac{\Delta\theta}{\theta_{\mathrm{a}}} \equiv -\frac{\Delta\rho}{\rho_{\mathrm{a}}} \equiv \beta_{\mathrm{T}}\Delta\theta. \tag{6.3}$$

6.3 Results

6.3.1 Consistency with scaling laws from prior studies

We show that the π groups obtained above are consistent with scaling laws for stationary sources of different geometries as obtained in previous literature. We start with power-law scalings for plume trajectories outlined in certain representative studies on buoyant plumes in cross-flow, most of which preclude the presence of a canopy, given the larger body of work under those conditions, as opposed to canopy presence. Next, through mechanistic and scaling arguments, we obtain power-law scalings for the plume centerline slope as functions of the π groups in Eqs. (6.1) and (6.2).

Line source, cross-wind, no canopy

Raupach (208) obtained the following similarity law for buoyant plumes in cross-wind, purely from dimensional considerations:

$$\frac{\overline{z}}{x} \sim \frac{B^{1/3}}{u}, \text{where } B = \int_{-\infty}^{+\infty} wg\frac{\Delta\theta}{\theta_{\mathrm{a}}}\mathrm{d}x \text{ and represents the buoyant flux per unit length.}$$

Additionally, they argued that the mean slope of the plume centerline in the rise phase is given by the ratio of the vertical velocity to the horizontal:

$$\frac{\mathrm{d}\overline{z}}{\mathrm{d}x} = \frac{w}{u}.$$

While this is a reasonable method to estimate the plume centerline slope in the rise phase and has been adopted by many studies (156), it is based on the assumption that the mean plume centerline trajectory follows the average streamline within the plume, which has been challenged in the literature (212). We relax this assumption by replacing the equality above with a similitude. Moreover, we perceive w and u as vertical and horizontal velocity scales, rather than local components of velocity, i.e. $u \sim U$. For a plume model with a linear rise phase, as shown in Fig. 4.13, we get:

$$\frac{w}{u} \sim \frac{\mathrm{d}\overline{z}}{\mathrm{d}x} \simeq \frac{z_{\mathrm{pc}}}{x_{\mathrm{pc}}} \sim \frac{B^{1/3}}{u} \Rightarrow \frac{w^3}{u^3} \sim \frac{B}{u^3}.$$

It follows that $w^3 \sim B$, which is precisely the vertical velocity scaling obtained by Raupach (208) for quiescent conditions from dimensional considerations. Thereby, Raupach's analysis assumes that the presence of a cross-wind merely alters the plume slope without changing the centerline vertical velocity behavior with height or with streamwise distance from the source from that observed in quiescent conditions. We will return to this assumption later

in our analysis. Now, using Raupach's definition of B for a line source:

$$B = \int_{-\infty}^{+\infty} wg\frac{\Delta\theta}{\theta_{\mathrm{a}}}\mathrm{d}x \sim wg\frac{\Delta\theta}{\theta_{\mathrm{a}}}L_{\mathrm{x}}.$$

Here, L_{x} represents the equivalent width of a line (high-aspect-ratio) heat source. We get:

$$w^3 \sim wg\frac{\Delta\theta}{\theta_{\mathrm{a}}}L_{\mathrm{x}} \Rightarrow \frac{w^2}{u^2} \sim \frac{gL_{\mathrm{x}}}{u^2}\frac{\Delta\theta}{\theta_{\mathrm{a}}}$$
$$\Rightarrow \frac{w}{u} \sim \sqrt{\frac{gL_{\mathrm{x}}}{u^2}\frac{\Delta\theta}{\theta_{\mathrm{a}}}}.$$

Then, noting that $u \sim U$ and, with $L_{\mathrm{x}} \sim R_{\mathrm{p}}$,

$$\frac{w}{u} \simeq \sqrt{\frac{gR_{\mathrm{p}}}{U^2}\frac{\Delta\theta}{\theta_{\mathrm{a}}}} \sim \sqrt{\frac{\pi_3\pi_4}{\pi_5}}.$$

Therefore, the plume slope is obtained as

$$\frac{\delta}{\lambda_{\mathrm{pc}}} \sim \sqrt{\frac{\pi_3\pi_4}{\pi_5}}. \tag{6.4}$$

We note here that Raupach's assumption of $w^3 \sim B$ has also been used in subsequent studies to demonstrate the equivalence of the Clark convective Froude number (F_{c}) (216; 217; 218) and Byram's energy criterion (219). Now, if we use the definition of Byram's convection number (N_{c}) in terms of the fireline intensity (I) and fireline rate of spread (r) given by:

$$N_{\mathrm{c}} = 2\frac{gI}{\rho c_{\mathrm{p}}\theta_{\mathrm{a}}(u-r)^3}, \text{ where } B = \frac{gI}{\rho c_{\mathrm{p}}\theta_{\mathrm{a}}}. \text{ For a static source, } r \to 0, \text{ and } N_{\mathrm{c}} \sim \frac{gI}{\rho c_{\mathrm{p}}\theta_{\mathrm{a}}u^3}.$$

By Nelson's formula (218), $I = \dot{m}c_{\mathrm{p}}\Delta\theta = \rho D w c_{\mathrm{p}}\Delta\theta$, where $\dot{m}$ is the mass flux rate and D is the flame depth. Using these relations,

$$N_{\mathrm{c}} \sim \frac{gD\Delta\theta}{\theta_{\mathrm{a}}u^3}w \sim \left[\frac{gD}{U^2}\right]\left[\frac{\Delta\theta}{\theta_{\mathrm{a}}}\right]\frac{w}{u} \equiv \pi_3\pi_4\pi_5^{-1}\frac{\delta}{\lambda_{\mathrm{pc}}}, \text{ where } D \equiv L_{\mathrm{x}} \equiv R_{\mathrm{p}}.$$

Using Raupach's assumption of $w^3 \sim B$, Sullivan (218) obtained the relation $N_c \sim F_c^{-3}$. If we use the definition of F_c from ref. (218), for a static source, i.e. in the limit $r \to 0$,

$$F_c^{-3} \sim \left(\frac{gD}{u^2}\frac{\Delta\theta}{\theta}\right)^{3/2} \equiv [\pi_3\pi_4\pi_5^{-1}]^{3/2}.$$

This gives us $N_c \sim \left[\sqrt{\pi_3\pi_4\pi_5^{-1}}\right]^3$, which helps us recover $\frac{\delta}{\lambda_{pc}} \sim \sqrt{\pi_3\pi_4\pi_5^{-1}}$ as obtained in Eq. (6.4). Moreover, Byram's convection number varies as the cube of the plume centerline slope in the rise phase, i.e. $N_c \sim \left(\frac{\delta}{\lambda_{pc}}\right)^3$. In this manner, we have shown that the plume centerline slope and Byram's convection number for a line source of buoyancy vary as functions of our π groups.

Point and finite sources, cross-wind, no-canopy: far-field

Davidson (149) provides the expression for the plume centerline trajectory for a finite source with equivalent radius R_s as follows, provided that the origin for $(x,\ z)$ lies at a virtual point source to which the finite source can be extrapolated:

$$\frac{\overline{z}}{L_B} \sim \left(\frac{x}{L_B}\right)^{2/3},\ \text{where } L_B = g\frac{w_s R_s^2}{U^3}\frac{\Delta\theta}{\theta_a}. \tag{6.5}$$

Here, w_s is the vertical velocity near the source and we have replaced $\Delta\rho/\rho_a$ in the original expression with $\Delta\theta/\theta_a$. The analysis corroborates similar expressions obtained from other studies (149; 150; 152; 196) for $\overline{z} >> L_B$, which is only likely to occur in the rise phase if the buoyancy source strength is "weaker" compared to the ambient wind forcing. A similar expression for the plume centerline trajectory in the entrainment phase was previously obtained by Raupach (208) for a point source in cross-wind:

$$\frac{\overline{z}}{z_{U_0}} \sim \left(\frac{x}{z_{U_0}}\right)^{2/3},\ \text{where } z_{U_0} = \frac{B}{U^3}, B = \int_{-\infty}^{+\infty} wg\frac{\Delta\theta}{\theta_a}2\pi r\mathrm{d}r \equiv g\frac{\Delta\theta}{\theta_a}w_s R_s^2.$$

Here, we have expressed the buoyancy source strength using some equivalent radius R_{s} and vertical velocity w_{s}. It follows that $z_{U_0} \equiv L_{\mathrm{B}}$. In other words, a point source is interchangeable with a finite source of the same buoyancy source strength vis-á-vis the two-thirds law for $\overline{z} >> L_{\mathrm{B}}$. Next, using Eq. (6.5), we have

$$\frac{\overline{z}^3}{L_{\mathrm{B}}^3} \sim \frac{x^2}{L_{\mathrm{B}}^2} \Rightarrow \overline{z}\left(\frac{\overline{z}}{x}\right)^2 \sim L_{\mathrm{B}}. \tag{6.6}$$

Setting $x \to \lambda_{\mathrm{pc}}$ as $\overline{z} \to \delta$, choosing $R_{\mathrm{p}} = R_{\mathrm{s}}$, and using $w_{\mathrm{s}}/U \equiv w/U \simeq \delta/\lambda_{\mathrm{pc}}$, we get

$$\left(\frac{\delta}{\lambda_{\mathrm{pc}}}\right)^2 \sim \frac{1}{\delta}\frac{g\Delta\theta}{\theta_{\mathrm{a}}}\frac{w_{\mathrm{s}}}{U^3}R_{\mathrm{s}}^2 \equiv \frac{gR_{\mathrm{s}}}{U^2}\frac{\Delta\theta}{\theta_{\mathrm{a}}}\frac{w_{\mathrm{s}}}{U}\frac{R_{\mathrm{s}}}{\delta} \Rightarrow \frac{\delta}{\lambda_{\mathrm{pc}}} \sim \frac{gR_{\mathrm{p}}}{U^2}\frac{\Delta\theta}{\theta_{\mathrm{a}}}\frac{R_{\mathrm{p}}}{\delta}.$$

This gives us the plume centerline slope in terms of the π groups as:

$$\frac{\delta}{\lambda_{\mathrm{pc}}} \sim \frac{\pi_3\pi_4}{\pi_5\pi_2}. \tag{6.7}$$

Again, Eq. (6.7) demonstrates the functional dependence of the plume centerline slope on our π groups.

Point and finite sources, cross-wind, no canopy: near-field

Lee and Chu (152) suggested the following power-law scaling close to the plume source, i.e. for $\overline{z} << L_{\mathrm{B}}$, based on previous experiments:

$$\frac{\overline{z}}{L_{\mathrm{B}}} \sim \left(\frac{x}{L_{\mathrm{B}}}\right)^{3/4}$$

In situations where the ambient cross-wind is "weak" compared to the buoyancy forcing, it is possible to have a longer buoyancy length scale L_{B}. Under such conditions, if the transition height z_{pc} as shown in Fig. 4.13 is shorter than the buoyancy length scale, i.e. $z_{\mathrm{pc}} << L_{\mathrm{B}}$,

the three-fourth law above may be applicable. In such a case,

$$\frac{\overline{z}}{L_{\mathrm{B}}} \sim \left(\frac{x}{L_{\mathrm{B}}}\right)^{3/4} \Rightarrow \left(\frac{\overline{z}}{x}\right)^{3} \sim \frac{L_{\mathrm{B}}}{\overline{z}} \tag{6.8}$$

Setting $x \to \lambda_{\mathrm{pc}}$ as $\overline{z} \to \delta$, choosing $R_{\mathrm{p}} = R_{\mathrm{s}}$, and using $w_{\mathrm{s}}/U \equiv w/U \simeq \delta/\lambda_{\mathrm{pc}}$, we get

$$\left(\frac{\delta}{\lambda_{\mathrm{pc}}}\right)^{3} \sim \frac{g}{\delta}\frac{w_{\mathrm{s}}R_{\mathrm{s}}^{2}}{U^{3}}\frac{\Delta\theta}{\theta_{\mathrm{a}}} \Rightarrow \left(\frac{\delta}{\lambda_{\mathrm{pc}}}\right)^{2} \sim \frac{gR_{\mathrm{p}}}{U^{2}}\frac{\Delta\theta}{\theta_{\mathrm{a}}}\frac{R_{\mathrm{p}}}{\delta}.$$

This gives us the plume centerline slope:

$$\left(\frac{\delta}{\lambda_{\mathrm{pc}}}\right) \sim \sqrt{\frac{\pi_3\pi_4}{\pi_2\pi_5}}. \tag{6.9}$$

In this case as well, we have demonstrated the emergence of the π groups that we have obtained in Eq. (6.2) in the expression for the functional dependency of the plume centerline slope.

Choice of R_{p} across varied source geometries

For point, line, and finite (circular) sources, we have been able to show that the plume centerline slope in the rise phase can be expressed in terms of our π groups. However, the cases differ in the power-law dependencies and combination of π groups. Notably, the slope is independent of π_2 in the case of the line source, while it varies inversely with $\sqrt{\pi_2}$ and π_2 for point/finite sources when $\overline{z} << L_{\mathrm{B}}$ and $\overline{z} >> L_{\mathrm{B}}$, respectively. This dependence of the slope on the non-dimensionalized atmospheric boundary layer (ABL) height (π_2) is attributed to the differences in the definition of the buoyancy-source strength across the two scenarios. We can propose a definition for buoyancy-source strength that unifies the scaling

for the point/finite and line sources as follows:

$$B \sim g\frac{\Delta\theta}{\theta_{\mathrm{a}}} w \times R_{\mathrm{p}}, \text{ where } R_{\mathrm{p}} = \frac{A_{\mathrm{s}}}{P_{\mathrm{s}}}. \tag{6.10}$$

Here, A_{s} and P_{s} are the buoyancy-source area and perimeter, respectively. The dimensions of buoyancy source strength are $\mathrm{L}^3\mathrm{T}^{-3}$, consistent with those for a line source. If a line source is conceived as a rectangle (of sides $L_{\mathrm{x}},\ L_{\mathrm{y}}$) with an extremely high aspect ratio ($L_{\mathrm{y}} >> L_{\mathrm{x}}$),

$$R_{\mathrm{p}} = \frac{L_{\mathrm{x}} L_{\mathrm{y}}}{2(L_{\mathrm{x}} + L_{\mathrm{y}})} \approx \frac{L_{\mathrm{x}}}{2} \text{ as } \frac{L_{\mathrm{y}}}{L_{\mathrm{x}}} \to \infty.$$

For a point or finite circular source, $R_{\mathrm{p}} = \pi R_{\mathrm{s}}^2 / 2\pi R_{\mathrm{s}} = R_{\mathrm{s}}/2$, where R_{s} is defined as above. In this manner, a source length scale R_{p} can be defined for any source geometries ranging from a point to a finite source to a line source. With this unified definition of buoyancy source strength, dimensional considerations, such as those employed by Raupach (208), suggest that $\overline{z}/x \sim B^{1/3}/U$ for each of these geometries. Following the aforementioned procedure outlined in Sect. 6.3.1 to obtain the average plume centerline slope for all these scenarios, we get the same expression as in Eq. (6.4):

$$\frac{\delta}{\lambda_{\mathrm{pc}}} \sim \sqrt{\frac{g R_{\mathrm{p}}}{U^2} \frac{\Delta\theta}{\theta_{\mathrm{a}}}} \equiv \sqrt{\frac{\pi_3 \pi_4}{\pi_5}}. \tag{6.11}$$

Infinite plane source, cross-wind, no canopy

We can now attempt to obtain a scaling for the average plume centerline slope for an infinite-plane source of buoyancy in cross-wind, which was precluded in Raupach's analysis (208). In this case, $R_{\mathrm{p}} \to \infty$ and we define the relevant length scale to be λ_{pc}. Based on the

explanation provided in Sect. 6.3.1, the buoyancy-source strength is given by:

$$B \sim g\frac{\Delta\theta}{\theta_{\mathrm{a}}} w \lambda_{\mathrm{pc}}.$$

Using $\overline{z}/x \sim B^{1/3}/u$, we get

$$\left(\frac{\overline{z}}{x}\right)^3 \sim \frac{B}{u^3} \sim \frac{g}{u^2}\frac{\Delta\theta}{\theta_{\mathrm{a}}}\frac{w}{u}\lambda_{\mathrm{pc}}.$$

Next, with $\frac{z}{x} \sim \frac{w}{u} \sim \frac{\delta}{\lambda_{\mathrm{pc}}}$,

$$\left(\frac{\delta}{\lambda_{\mathrm{pc}}}\right)^3 \sim \frac{g}{u^2}\frac{\Delta\theta}{\theta_{\mathrm{a}}}\frac{\delta}{\lambda_{\mathrm{pc}}}\lambda_{\mathrm{pc}} \Rightarrow \frac{\delta}{\lambda_{\mathrm{pc}}} \sim \left(\frac{g\delta}{U^2}\frac{\Delta\theta}{\theta_{\mathrm{a}}}\right)^{1/3} \equiv \left[\pi_2\pi_3\frac{\pi_4}{\pi_5}\right]^{1/3}. \tag{6.12}$$

Again, the average plume centerline slope is obtained in terms of our π_{i} groups. Note that with an increase in the ABL height (δ), $\pi_2\pi_3$ increases; this means that the average plume centerline slope increases (tends more towards the vertical) with a deeper inversion layer for a constant ambient velocity scale. Although this may seem counterintuitive at first glance, it is explained by the fact that the ambient wind shear (scaling), given by U/δ, is stronger (higher) for a shallower inversion layer; this leads to increased plume tilting from the vertical for a constant ambient velocity scaling, resulting in a more gradual plume centerline slope.

Canopy, cross-wind, finite source

There is a dearth of both experiments and simulations on buoyant-plume interaction with a vegetative canopy in cross-wind. As mentioned above, a unique study in that regard was conducted by Chung and Koseff (156) using flume experiments. They obtained a power-law relationship between the coefficient of variation in plume centerline trajectory ($s_\mu/\overline{z}$) and Byram's convection number, in which the velocity scaling was taken to be u_* as opposed to

U:

$$\frac{s_\mu}{\overline{z}_{\mathrm{pc}}} \sim \left(\frac{B}{u_*^3}\right)^{\beta};\ \beta < 0.$$

Here, s_μ is the standard deviation of the plume centerline computed at a location in the far-field region (156). In their analysis, $s_\mu/\overline{z}$ was also plotted as a function of the bulk Richardson number (Ri_{b}). They found that the trends were similar to those observed with B/u_*^3 and consistent with a power-law scaling. Therefore,

$$\frac{s_\mu}{\overline{z}_{\mathrm{pc}}} \sim Ri_{\mathrm{b}}^{\alpha}, \alpha < 0, \Rightarrow \frac{s_\mu}{\overline{z}_{\mathrm{pc}}} \quad \sim \left[g\beta_{\mathrm{T}}\frac{\Delta\theta}{L_{\mathrm{pl}}}\left(\frac{L_{\mathrm{RS}}}{u_*}\right)^2\right]^{\alpha}, \text{ using the definition of } Ri_{\mathrm{b}}.$$

$$\text{Therefore, } \left(\frac{B}{u_*^3}\right)^{\beta} \sim \left[g\beta_{\mathrm{T}}\frac{\Delta\theta}{L_{\mathrm{pl}}}\left(\frac{L_{\mathrm{RS}}}{u_*}\right)^2\right]^{\alpha}. \tag{6.13}$$

Here, $L_{\mathrm{pl}} = w_{\mathrm{eff}} \times f_{\mathrm{KH}}^{-1}$ (terms explained below). Established theory on canopy turbulence can be used to recast some of the physical quantities above in terms of the current variables under consideration.

Shear length scale (L_{RS}): The shear length scale, i.e. the height over which the turbulent stress is substantial within and above the canopy, has been found to be proportional to the canopy height as indicated by data across different vegetation heights (93). Hence, $L_{\mathrm{RS}} = C_0 h_{\mathrm{c}}$.

Frequency of Kelvin-Helmholtz (KH) Rollers (f_{KH}): According to Chung and Koseff (156), the frequency of KH rollers near the canopy top dictates plume centerline oscillation.

This frequency is determined by the peak spectral frequency of the vertical velocity ($f_{\mathrm{p}}(w)$), which is given by (93):

$$f_{\mathrm{KH}} \simeq f_{\mathrm{p}}(w) = \frac{U_{\mathrm{c}}}{\Lambda_{\mathrm{x}}} \approx \frac{U}{C_1 h_{\mathrm{c}}},$$

where Λ_{x} represents the horizontal wavelength of KH rollers and U_{c} represents their convection velocity. The relation $\Lambda_{\mathrm{x}} = C_1 h_{\mathrm{c}}$ is obtained from the mixing layer analogy used by Raupach (93). Therefore,

$$L_{\mathrm{pl}} = w_{\mathrm{eff}} \times f_{\mathrm{KH}}^{-1} = w_{\mathrm{eff}} \times \frac{C_1 h_{\mathrm{c}}}{U}.$$

Substituting for these terms in Eq. (6.13), and using Eq. (6.3), we get:

$$\begin{aligned}
&\left[\frac{B}{u_*^3}\right]^{\beta/\alpha} \sim \left[g\frac{\Delta\theta}{\theta_{\mathrm{a}}}\frac{1}{w_{\mathrm{eff}}\frac{C_1 h_{\mathrm{c}}}{U}}\left(\frac{L_{\mathrm{RS}}}{u_*}\right)^2\right], \text{ where } B \simeq g\frac{\Delta\theta}{\theta_{\mathrm{a}}} w R_{\mathrm{p}};\\
&\Rightarrow \left[\frac{g}{u_*^2}\frac{\Delta\theta}{\theta_{\mathrm{a}}}\frac{w}{u_*}R_{\mathrm{p}}\right]^{\beta/\alpha} \sim \left[\frac{g}{u_*^2}\frac{\Delta\theta}{\theta_{\mathrm{a}}}\frac{1}{w_{\mathrm{eff}}\frac{C_1 h_{\mathrm{c}}}{U}}L_{\mathrm{RS}}^2\right],\\
&\Rightarrow \left[\frac{U^2}{u_*^2}\frac{gR_{\mathrm{p}}}{U^2}\frac{\Delta\theta}{\theta_{\mathrm{a}}}\frac{w/U}{u_*/U}\right]^{\beta/\alpha} \sim \frac{1}{C_1}\left[\frac{gR_{\mathrm{p}}}{U^2}\frac{U^2}{u_*^2}\frac{\Delta\theta}{\theta_{\mathrm{a}}}\frac{1}{\frac{w_{\mathrm{eff}}}{U}}\left(\frac{L_{\mathrm{RS}}}{R_{\mathrm{p}}}\right)^2\frac{R_{\mathrm{p}}}{h_{\mathrm{c}}}\right]\\
&\Rightarrow \frac{w_{\mathrm{eff}}}{U}\left(\frac{w}{U}\right)^{\beta/\alpha}\left[\frac{1}{\pi_5^3}\pi_3\frac{\pi_4}{\pi_5}\right]^{\beta/\alpha} \sim \pi_3\frac{1}{\pi_5^2}\frac{\pi_4}{\pi_5}\left(\frac{L_{\mathrm{RS}}}{R_{\mathrm{p}}}\right)^2\frac{1}{\pi_6}.
\end{aligned}$$

It is reasonable to assume that the plume centerline slope, i.e. $\delta/\lambda_{\mathrm{pc}} \sim w_{\mathrm{eff}}/U \sim w/U$ and that $L_{\mathrm{RS}} \sim L_{\mathrm{c}}$. Under those assumptions, we get:

$$\begin{aligned}
&\left(\frac{\delta}{\lambda_{\mathrm{pc}}}\right)^{1+\beta/\alpha} \sim \left[\pi_3\pi_4\right]^{1-\frac{\beta}{\alpha}}\frac{\pi_7^2}{\pi_6}\pi_5^{4\beta/\alpha-3},\\
&\Rightarrow \frac{\delta}{\lambda_{\mathrm{pc}}} \sim \left(\frac{\pi_7^2}{\pi_6}\right)^{\frac{\alpha}{\alpha+\beta}}\left[\pi_3\pi_4\right]^{\frac{\alpha-\beta}{\alpha+\beta}}\pi_5^{\frac{4\beta-3\alpha}{\alpha+\beta}} \equiv \left[\left(\frac{\pi_7^2}{\pi_6}\right)^{\alpha}\left[\pi_3\pi_4\right]^{\alpha-\beta}\pi_5^{4\beta-3\alpha}\right]^{\frac{1}{\alpha+\beta}}.
\end{aligned} \tag{6.14}$$

From power-law fits to the plot of $s_\mu/\overline{z}_{\mathrm{pc}}$ against the modified Byram's convection number for various buoyancy-source strength and wind speeds, Chung and Koseff obtained $\beta = -0.22$.

From a power-law fit to the plot of $s_\mu/\overline{z}_{\mathrm{pc}}$ against Ri_{b} provided by Chung and Koseff (156) obtained using a simplex algorithm (MATLAB's *fminsearch*() function), we get $\alpha = -0.19$ with $R^2 = 0.53$ (process not shown here). Plugging these values into Eq. (6.14) gives:

$$\frac{\delta}{\lambda_{\mathrm{pc}}} \sim \left[\left(\frac{\pi_7^2}{\pi_6} \right)^{0.46} [\pi_3 \pi_4]^{-0.07} \pi_5^{0.76} \right] \tag{6.15}$$

Equation (6.15) depicts the dependence of the plume centerline slope on our π groups as intended. It is worth noting that the dependence on $\pi_3\pi_4$ is inverse and weaker compared to the dependence on π_5–π_7, suggesting that the slope is a stronger function of the canopy geometry and turbulence intensity. Albeit weak, the inverse dependence is inconsistent with an expected increase in slope for an increase in $\Delta H_{\mathrm{s}}/\rho c_{\mathrm{p}}$. Moreover, the exponents in Eq. (6.15) were obtained from the coefficient of variation in the plume centerline in the far-field region, making it difficult to characterize the plume slope closer to the source. The scale of the experiment, i.e. the shallow depth of the water tank relative to the canopy height ($4h_{\mathrm{c}}$), insufficient data points for the power-law fit, and a narrow range of wind speeds constitute other potential limitations of the analysis. These limitations emphasize the need for additional experiments and computer simulations to characterize plume deflection both near the source and in the far-field regions.

6.3.2 Plume centerline slope: scaling from LES

In this section, we investigate the dependence of the plume centerline slope ($\mathrm{d}\overline{z}/\mathrm{d}x$) on the dimensionless parameters (π groups) in Eq. (6.1). The plume centerline slope is tracked from the locus of the maximum 1-h mean vertical velocity ($\overline{w}_{\mathrm{max}}$) in the streamwise ($XZ$) plane passing through the center of the square surface patch. In the region near the plume source (Zone 1), $\overline{w}_{\mathrm{max}}$ is obtained from the maximum $\overline{w}$ across a horizontal transect in this plane at different heights. Further downstream from the plume source (Zone 2), $\overline{w}_{\mathrm{max}}$ is obtained

from the maximum $\overline{w}$ across a vertical transect in this plane at different streamwise locations. The transition between the two zones is determined by tracking a sudden change in the local plume centerline slope beyond a certain threshold, in Zone 1, as demonstrated in Fig. 6.1. Note that $\mathrm{d}\overline{z}/\mathrm{d}x$ is considered in the sense of a "best-fit line" depicting the approximate spatial trend in each zone and is better written as $\Delta\overline{z}/\Delta x$.

Canopy, cross-wind

A power-law dependence is explored between the plume centerline slope and the derived dimensionless parameters as follows:

$$\frac{\Delta\overline{z}}{\Delta x} \sim \left(\frac{gR_\mathrm{p}}{U^2}\frac{\Delta H_\mathrm{s}}{\rho c_\mathrm{p}}\frac{1}{U\theta_\mathrm{a}}\right)^{\hat{p}}\left(\frac{u_*}{U}\right)^{\hat{r}}\left(\frac{L_\mathrm{c}}{R_\mathrm{p}}\right)^{\hat{s}}. \tag{6.16}$$

Here, the first term in parenthesis on the right-hand side is $\pi_3\pi_4$, where π_3 and π_4 are grouped together based on the recurring occurrence of such grouping under the Clark convective Froude number (or equivalently, the Byram's convection number) in the literature and as shown in Sect. 6.3.1 above. Along the lines of the zones defined earlier in this section, an additional zone encompassing the canopy sublayer exists near the surface (Fig. 6.1(b)). In this zone, $\Delta\overline{z}/\Delta x$ is steep, indicating that the plume centerline is close to vertical, albeit to varying degrees, across the parametric space considered in this study. We refer to this zone as Zone 1. This is followed by a transition zone (Zone 1(B)), i.e. the region where the plume, informed by its interaction with the canopy, adjusts to the presence of the ambient cross-wind. This zone, in turn, is followed by Zone 2, where the plume centerline bends over and the influence of the ambient cross-wind strengthens relative to the effects of buoyancy.

Figure 6.2(a) shows a plot of $\Delta\overline{z}/\Delta x$ against $\pi_3\pi_4$ for Zones 1–2, with both axes scaled logarithmically. The power-law dependence between the two is represented in the form of a trend-line for each zone and takes the form: $\frac{\Delta\overline{z}}{\Delta x} = \hat{m}_\mathrm{i}\left(\frac{gR_\mathrm{p}}{U^2}\frac{\Delta H_\mathrm{s}}{\rho c_\mathrm{p}}\frac{1}{U\theta_\mathrm{a}}\right)^{\hat{p}_\mathrm{i}}$, where the index

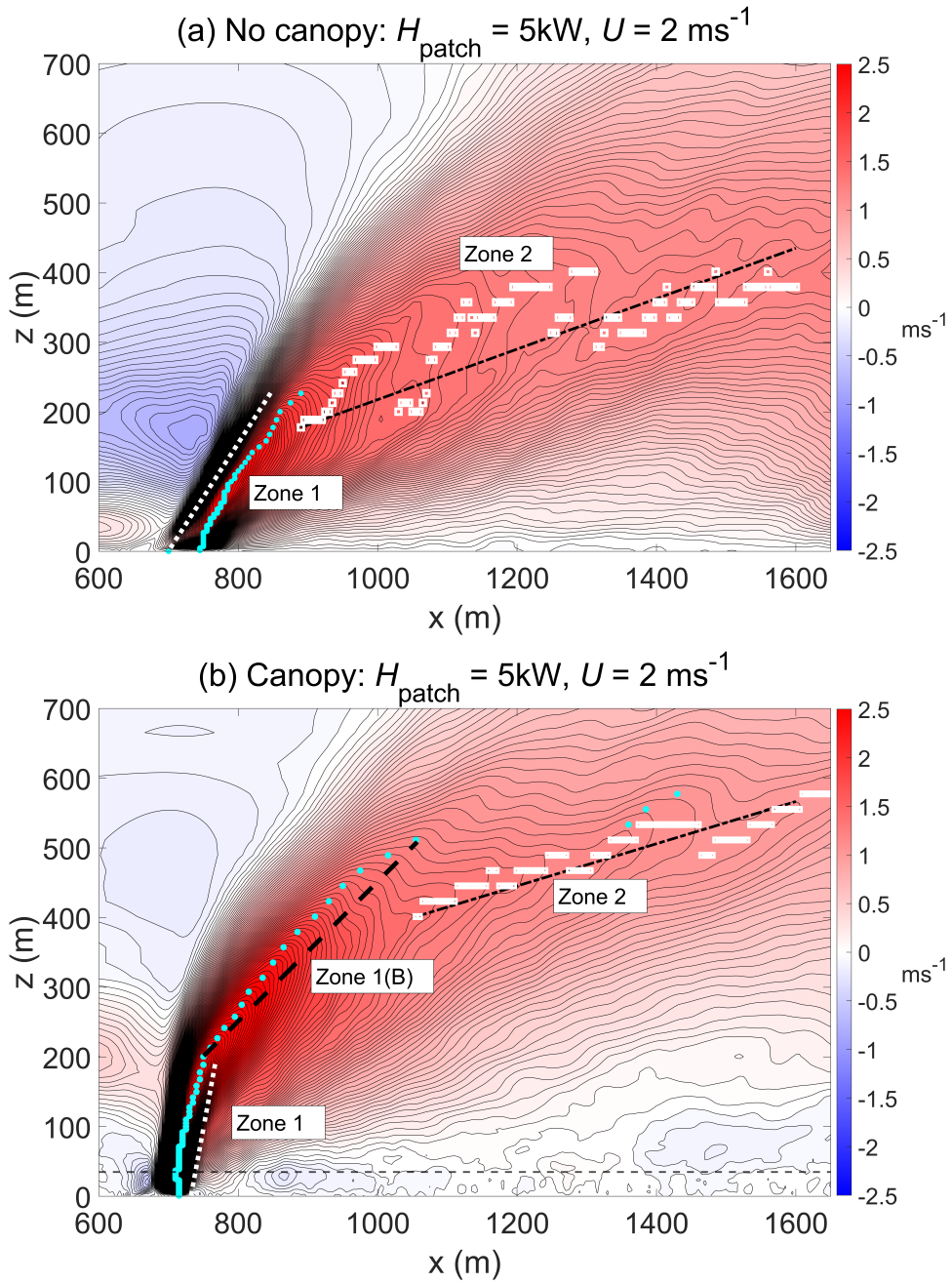


Figure 6.1: Contours of the 1-h mean vertical velocity ($\overline{w}$) for the (a) no-canopy and (b) canopy environments depicting the respective plume centerlines in each zone (cyan blue dots in Zones 1–1(B) and white squares in Zone 2) and their inclinations for a representative case of $H_{\text{patch}} = 5\,\text{kW}$ and $U = 2\,\text{ms}^{-1}$

i represents the zone number. It is observed that $\hat{m}_1 > \hat{m}_2$ by $\mathcal{O}(10^1)$ and $\hat{m}_1 > \hat{m}_3$ by $\mathcal{O}(10^2)$, suggestive of the consistently steep plume centerline slopes near the canopy across the range of $\pi_3\pi_4$. Moreover, $\hat{p}_1 \approx \hat{p}_3 >> \hat{p}_2$, suggesting a stronger dependency of the

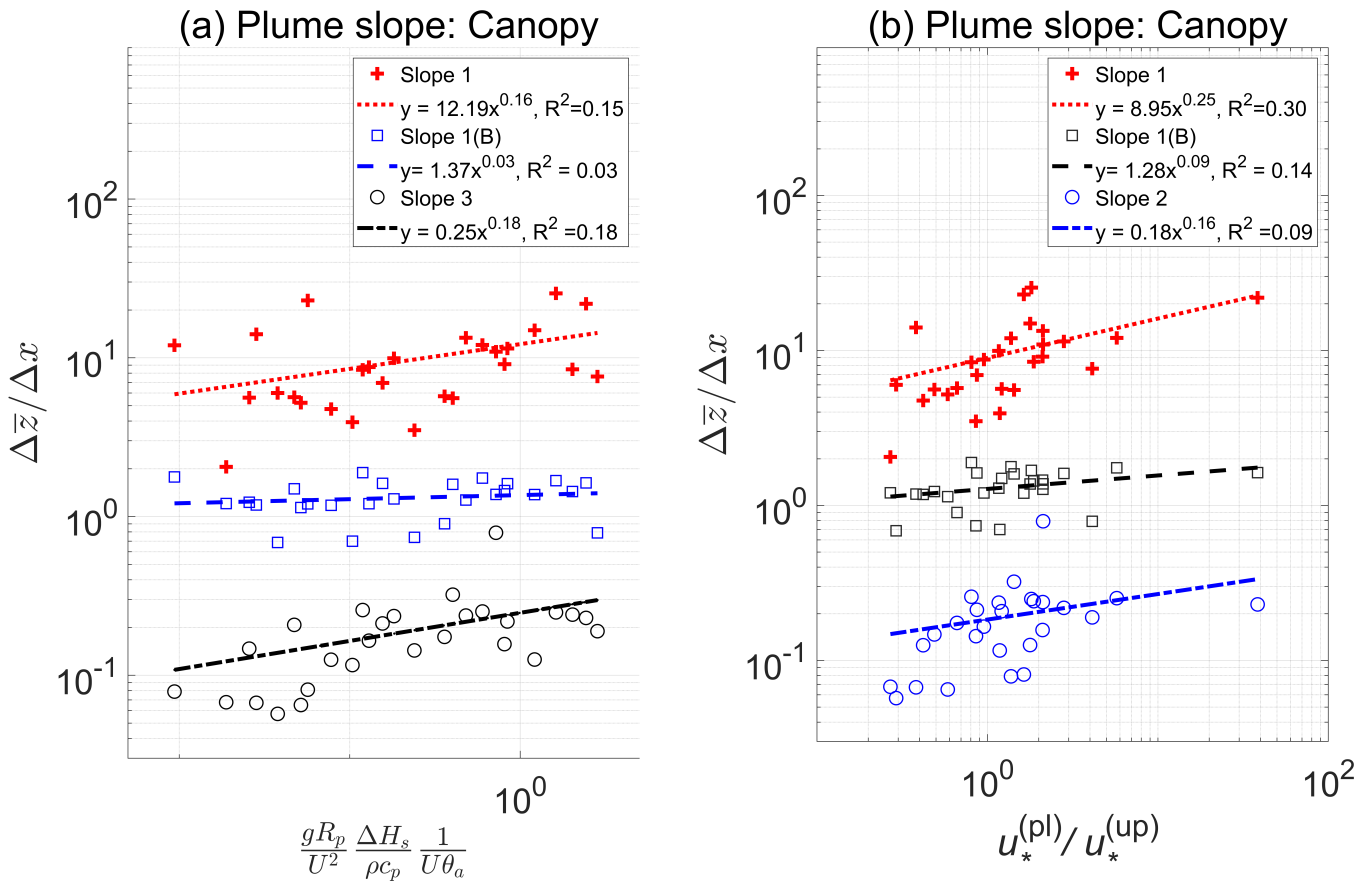


Figure 6.2: Plot of plume centerline slope ($\Delta\overline{z}/\Delta x$) against (a) $\pi_3\pi_4$ and (b) $u_*^{(\mathrm{pl})}/u_*^{(\mathrm{up})}$ in Zones 1, 1(B), and 2 for the canopy cases. Slope i, computed from the simulation outputs, refers to the plume centerline slope in Zone i. Trend-lines represent the best fit of a power law to the data; R^2 represents the coefficient of determination

plume centerline slope on $\pi_3\pi_4$ near the canopy and plume source in addition to the far-field region as compared to the transition zone. In Zones 1 and 2, the plume centerline shows an increasing trend with $\pi_3\pi_4$, with $\hat{p}_0 \approx \hat{p}_2 \approx 1/6$. The increasing trend is expected since higher values of $\pi_3\pi_4$ represent conditions in which buoyancy effects relative to the ambient forcing are stronger.

When considering the next π term, i.e. $\pi_5 = u_*/U$, the choice of location for u_* in the flow field matters. Since u_* varies spatially, i.e. upstream and downstream of the plume, it is important to consider contributions from both sides. It was discussed in Chapter 5 that the positive momentum fluxes within the plume, on the leeward side of the plume centerline,

represent upfluxes of momentum from the buoyancy source to the atmosphere aloft. It is, therefore, expected that the intensity of these momentum fluxes relative to those from an upstream location will have some bearing on the plume centerline tilt. This motivates the addition of a supplementary π term, $\hat{\pi}_5$, such that $\hat{\pi}_5 = u_*^{(\mathrm{up})}/U$, where $u_*^{(\mathrm{up})}$ represents the friction velocity at an upstream location. For the friction velocity in π_5 ($u_*^{(\mathrm{pl})}$), we choose the first grid point above the canopy top at the streamwise location within the plume where the mean vertical velocity approaches approximately $\overline{w}_{\max}e^{-1}$, where $\overline{w}_{\max}$ represents the mean vertical velocity at the plume centerline as discussed above. Similarly, $u_*^{(\mathrm{up})}$ also corresponds to the first grid point above the canopy, i.e. $z = 37\,\mathrm{m}$, and is taken at streamwise location 325 m upstream ($x = 375\,\mathrm{m}$) from the center of the heated surface patch ($x = 700\,\mathrm{m}$). This location was selected to provide sufficient fetch for the inlet wind profile to adjust to the presence of the canopy. Equation 6.16 is now rewritten as:

$$\begin{aligned}\frac{\Delta\overline{z}}{\Delta x} &\sim \left(\frac{gR_\mathrm{p}}{U^2}\frac{\Delta H_\mathrm{s}}{\rho c_\mathrm{p}}\frac{1}{U\theta_\mathrm{a}}\right)^{\hat{p}}\left(\frac{\pi_5}{\hat{\pi}_5}\right)^{\hat{r}}\left(\frac{L_\mathrm{c}}{R_\mathrm{p}}\right)^{\hat{s}} \\ &\sim \left(\frac{gR_\mathrm{p}}{U^2}\frac{\Delta H_\mathrm{s}}{\rho c_\mathrm{p}}\frac{1}{U\theta_\mathrm{a}}\right)^{\hat{p}}\left(\frac{u_*^{(\mathrm{pl})}/U}{u_*^{(\mathrm{up})}/U}\right)^{\hat{r}}\left(\frac{L_\mathrm{c}}{R_\mathrm{p}}\right)^{\hat{s}} \equiv \left(\frac{gR_\mathrm{p}}{U^2}\frac{\Delta H_\mathrm{s}}{\rho c_\mathrm{p}}\frac{1}{U\theta_\mathrm{a}}\right)^{\hat{p}}\left(\frac{u_*^{(\mathrm{pl})}}{u_*^{(\mathrm{up})}}\right)^{\hat{r}}\left(\frac{L_\mathrm{c}}{R_\mathrm{p}}\right)^{\hat{s}}.\end{aligned} \tag{6.17}$$

Figure 6.2(b) shows a plot of $\Delta\overline{z}/\Delta x$ against $u_*^{(\mathrm{pl})}/u_*^{(\mathrm{up})}$ with a trend-line that follows a power-law dependence. Again, $\Delta\overline{z}/\Delta x$ changes more gradually with $u_*^{(\mathrm{pl})}/u_*^{(\mathrm{up})}$ in Zone 1(B), i.e. the transition zone, as seen from the low value of the power-law index. Trend-lines in Zones 1 and 2 show increasing trends in the plume centerline slope. The $1/4^{\mathrm{th}}$ power law in Zone 1, which encompasses the canopy sublayer, demonstrates a stronger dependence on $u_*^{(\mathrm{pl})}/u_*^{(\mathrm{up})}$. This can be explained as follows. Higher values of $u_*^{(\mathrm{pl})}/u_*^{(\mathrm{up})}$ suggest a higher intensity of momentum transport from the buoyancy source within the canopy to the atmosphere aloft (positive momentum fluxes as mentioned above), relative to an upstream location where the plume influence is minimal and canopy-induced momentum-flux events,

comprising mainly sweeps and ejections (negative momentum fluxes) that transport higher momentum downward, are more active. This effect is more intuitively understood in Zone 1, i.e. in the vicinity of the canopy sublayer. However, this effect is also observed in Zone 2, i.e. in the far-field region of the plume, albeit to a lesser degree.

No-canopy, cross-wind

The equivalent expression to Eq. (6.17) for the no-canopy case is written as:

$$\frac{\Delta\overline{z}}{\Delta x} \sim \left(\frac{gR_{\mathrm{p}}}{U^2}\frac{\Delta H_{\mathrm{s}}}{\rho c_{\mathrm{p}}}\frac{1}{U\theta_{\mathrm{a}}}\right)^{\hat{p}}\left(\frac{u_*^{(\mathrm{pl})}}{u_*^{(\mathrm{up})}}\right)^{\hat{r}}. \tag{6.18}$$

In contrast to the canopy cases, the plume centerline follows a two-zone trajectory as seen from Fig. 6.1(a). Figure 6.3(a) shows a plot of $\Delta\overline{z}/\Delta x$ against $\pi_3\pi_4$ for Zones 1–2, with both axes scaled logarithmically. As expected, the centerline slopes are higher (steeper) close to the plume source, which is verified by the fact that $\hat{m}_1 > \hat{m}_2$ by $\mathcal{O}(10^1)$. Increasing trends are observed for the slopes as a function of $\pi_3\pi_4$ in both zones, with similar power-law indices. Note that the power laws do not match those presented in Sect. 6.3.1, where the plume centerline slope is shown to vary as a function of $\sqrt{\pi_3\pi_4}$.

The slopes in Zone 1, i.e. near the surface, are higher in the canopy versus the no-canopy cases, due to the higher drag afforded by the canopy to the rising plume- this is also reflected in the higher value of the coefficient in the canopy cases (Fig. 6.2(a)). However, the power-law indices for the trend-lines near the surface (Zone 1) are quite similar (Fig. 6.3(a)) between the canopy and no-canopy case. The far-field (Zone 2) slope in the no-canopy case follows a different power-law dependence than in the canopy case, suggesting that the far-field plume in the canopy case follows a canopy-adjusted trajectory despite the distance from the canopy. This suggests that the canopy has some "far-reaching" effects on the plume trajectory, which cannot be approximated via no-canopy boundary conditions.

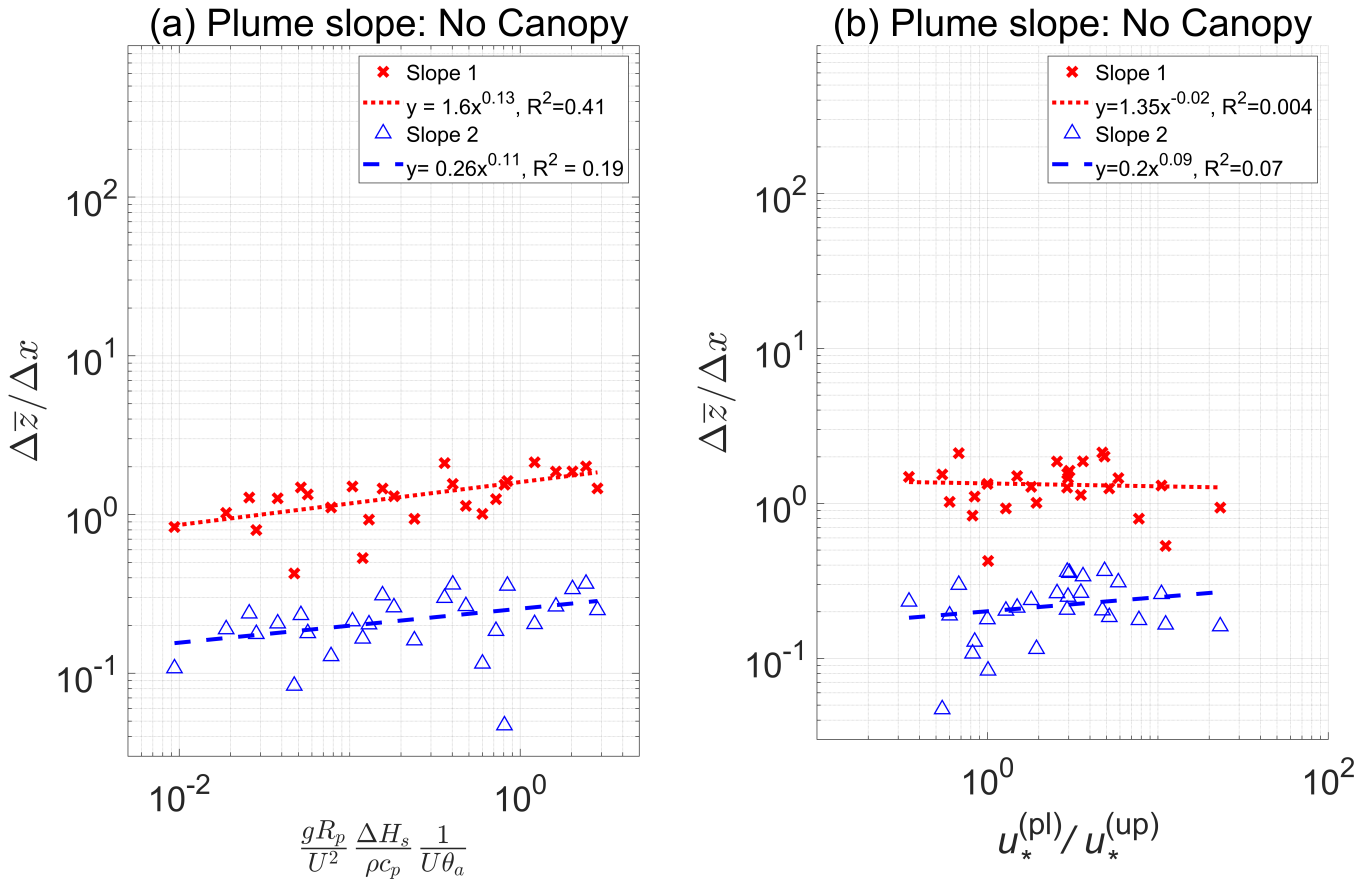


Figure 6.3: Plot of plume centerline slope ($\Delta\overline{z}/\Delta x$) against (a) $\pi_3\pi_4$ and (b) $u_*^{(\mathrm{pl})}/u_*^{(\mathrm{up})}$ in Zones 1–2 for the no-canopy cases. Slope i, computed from the simulation outputs, refers to the plume centerline slope in Zone i. Trend-lines represent the best fit of a power law to the data; R^2 represents the coefficient of determination

Figure 6.3(b) shows plots of $\Delta\overline{z}/\Delta x$ against $u_*^{(\mathrm{pl})}/u_*^{(\mathrm{up})}$ in Zones 1–2, with trend-lines that follow a power-law dependence each. Interestingly, a decreasing trend is observed in the plume centerline slope with $u_*^{(\mathrm{pl})}/u_*^{(\mathrm{up})}$, in stark contrast to the canopy case (Fig. 6.2(b)). This could be a consequence of the difference in the spatial structure of the momentum fluxes within the plume in the canopy vs. no-canopy cases. As shown in Chapter 4, the region of upward transport of high momentum (positive momentum fluxes) within the plume is juxtaposed on the windward and leeward sides by regions of downward fluxes of high momentum (negative momentum fluxes) in the no-canopy case. Therefore, higher values of $u_*^{(\mathrm{pl})}/u_*^{(\mathrm{up})}$ near the surface suggest more intense downward momentum transport, affording

higher "drag", on the leeward side of the plume. This is expected to be associated with higher plume centerline deflection from the vertical and lower plume centerline slopes near the surface. The dependence of $\Delta\overline{z}/\Delta x$ on $u_*^{(\mathrm{pl})}/u_*^{(\mathrm{up})}$ in the canopy case is stronger compared to the no-canopy case both near the surface (Zone 1) and in the far-field (Zone 2) region. This suggests a stronger influence of canopy-induced turbulence on the plume centerline behavior within the range of the parametric space considered here.

In addition to the plots on the plume centerline slopes above, we plot the height at which the plume transitions from the rise phase to the bent-over phase, normalized by the ABL height (z_{pc}/δ), in the canopy case (Zone 1(B) to Zone 2) and no-canopy case (Zone 1 to 2), as shown in Fig. 6.4. It is observed that this height increases with an increase in $\pi_3\pi_4$ as evidenced both by the data from the LES and the trend-line indicating a $1/3^{\mathrm{rd}}$ and $1/4^{\mathrm{th}}$ power-law dependence in the no-canopy and canopy cases, respectively. This is expected, since an increase in buoyancy strength relative to the ambient wind forcing, i.e. an increase in $\pi_3\pi_4$, would result in a taller rise phase and delay the onset of the bent-over phase. More importantly, the transition height in the canopy cases is consistently higher compared to the no-canopy cases, suggesting that the aerodynamic effect of the canopy delays the onset of the bent-over phase. This effect is more pronounced at lower values of $\pi_3\pi_4$, i.e. at weaker buoyancy source strengths, while the canopy effects become less prominent at higher buoyancy source strengths, i.e. for $\pi_3\pi_4 > 1$.

We also plot the normalized buoyancy length scale (L_{B}/δ) as a function of $\pi_3\pi_4$, using the definition of L_{B} from Eq. (6.5). As expected, L_{B}/δ increases as a function of $\pi_3\pi_4$. Notably, this increase is at a much faster rate compared to z_{pc}/δ, so that the ratio of the transition height to the buoyancy length scale decreases with the increase in buoyancy strength. This is consistent with the scaling laws from previous studies discussed in Sect. 6.3.1. For instance,

Eqs. (6.6) and (6.8) together suggest:

$$\begin{aligned}\left(\frac{\overline{z}}{x}\right)^3 &\sim \frac{L_{\mathrm{B}}}{\overline{z}} \text{ when } \overline{z} << L_{\mathrm{B}} \Rightarrow \frac{z_{\mathrm{pc}}}{\delta} \sim \frac{L_{\mathrm{B}}/\delta}{(\delta/\lambda_{\mathrm{pc}})^3}, \\ \left(\frac{\overline{z}}{x}\right)^2 &\sim \frac{L_{\mathrm{B}}}{\overline{z}} \text{ when } \overline{z} >> L_{\mathrm{B}} \Rightarrow \frac{z_{\mathrm{pc}}}{\delta} \sim \frac{L_{\mathrm{B}}/\delta}{(\delta/\lambda_{\mathrm{pc}})^2},\end{aligned} \tag{6.19}$$

Here, we have used $z_{\mathrm{pc}}/x_{\mathrm{pc}} \equiv \delta/\lambda_{\mathrm{pc}}$, which represents the plume centerline slope. Equation (6.19) suggests that the rate at which z_{pc} increases with an increase in the buoyancy strength relative to ambient wind forcing ($\pi_3\pi_4$) is shallower compared to the rate at which the buoyancy length scale increases, especially since the plume centerline slope ($\delta/\lambda_{\mathrm{pc}}$) also increases with $\pi_3\pi_4$ as shown above. This is also an important observation in light of the differing power-law indices (Sect. 6.3.1) based on whether $\overline{z} << L_{\mathrm{B}}$ or $\overline{z} >> L_{\mathrm{B}}$. As $\pi_3\pi_4$ increases, the assumption of $\overline{z} << L_{\mathrm{B}}$ in the rise phase of the plume becomes more questionable when deriving the power-law scaling for the plume trajectory in this phase. This becomes an added consideration and emphasizes the need for more studies to investigate the power-law dependencies across multiple scales.

6.4 Conclusions and Future Work

In this study, we have explored the dependence between the centerline slope of a buoyant plume emanating from a static source, akin to a surface fire, as it interacts with an ambient cross-wind and a set of influencing variables, including heat source strength, ambient wind speed, source geometry, and turbulence intensity, both in the presence and absence of a vegetative canopy. We have utilized the Buckingham Pi Theorem to reduce the influencing variables to a set of dimensionless parameters or π groups, primarily describing the relative strength of buoyancy to the ambient wind forcing (similar to Byram's convection number or Clark convective Froude number), the non-dimensionalized turbulence intensity,

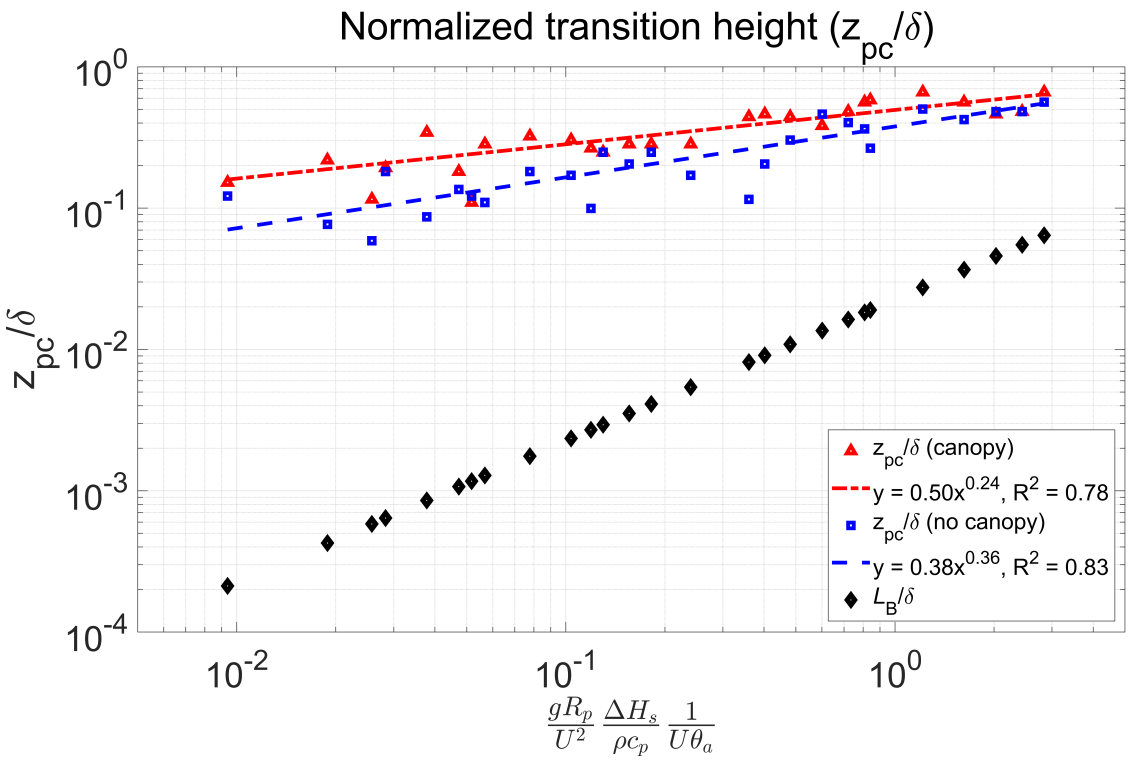


Figure 6.4: Plot comparing the normalized height (z_{pc}/δ) at which the plume transitions from the rise phase to the atmospheric or bent-over phase (Zone 2) between the canopy and no-canopy cases. Trend-lines for z_{pc}/δ represent power-law dependence; L_{B}/δ represents the normalized buoyancy length scale

and canopy length scales relative to the source geometry. Following the dimensional analysis, we have demonstrated that the plume centerline slope can be obtained using scaling laws previously reported in the literature, primarily from laboratory experiments, in terms of the π groups, thereby making them robust. Next, we have attempted to quantify the dependence of the plume centerline slope on some of the π groups, using LES results from 28 simulations with systematic variation in the ambient wind speed and heat source strength. Given the particular sparseness of scaling laws in the literature characterizing this dependence in canopy environments, we attempted to obtain power-law dependencies from the same set of simulations conducted both in the presence and absence of an idealized, homogeneous, tall vegetative canopy with features resembling those of an Amazon rain forest, facilitating a comparison.

The LES results suggest that plume centerline slopes near the surface are an order of magnitude higher in the canopy cases as compared to the no-canopy cases, owing to the drag afforded by the canopy to the rising plume. In contrast, far-field plume centerline slopes are of a similar order of magnitude in both cases. Increasing trends are observed as a function of $\pi_3\pi_4$ $\left(\frac{gR_{\mathrm{p}}\Delta H_{\mathrm{s}}}{U^3\rho c_p\theta_{\mathrm{a}}}\right)$, which encapsulates the relative strength of buoyancy to the ambient wind forcing, in both cases. Power-law indices describing this trend are similar between the two scenarios for the near-surface plume centerline slopes. However, this exponent is higher for the far-field plume centerline in the canopy case, suggesting that the far-field plume trajectory is influenced by and is more sensitive to an increase in $\pi_3\pi_4$ in the presence of the canopy.

It is found that the near-surface plume slope has a much stronger dependence on the turbulence intensity on the leeward side of the plume relative to the turbulence intensity at an upstream location ($u_*^{(\mathrm{pl})}/u_*^{(\mathrm{up})}$), in canopy as compared to no-canopy environments. This is due to the difference in the spatial structure of the momentum fluxes within the plume between the two environments close to the plume source. In the far-field region, a higher sensitivity of the plume centerline slope to an increase in $u_*^{(\mathrm{pl})}/u_*^{(\mathrm{up})}$ is also noticeable in the canopy case compared to the no-canopy case, suggesting a far-reaching influence of the canopy-induced turbulent interactions with the plume. However, this difference in sensitivity to $u_*^{(\mathrm{pl})}/u_*^{(\mathrm{up})}$ is not as palpable as it is closer to the surface.

Additionally, we have found that the height at which the rising plume transitions to the entrainment phase, in the no-canopy environment, increases with $\pi_3\pi_4$ with a one-third power law dependence. However, the rate of increase of this transition height is lower compared to that of the buoyancy length scale. This must be taken into account when employing power laws for the plume trajectory from the literature, which depend on the height of the plume centerline relative to the buoyancy length scale.

Future work is needed to address the limitations of this analysis. There are discrepancies

in power-law indices between the best fits to our LES results and experiments. These can be addressed by running more simulations over a wider range of values in the dimensionless parametric space to get more accurate estimates of the power-law indices. It may also be helpful to investigate outliers in the plume centerline slopes and the causes for their deviation from the observed trends. Model constraints such as the domain size, ABL height, or the location of the plume source may also have bearings on the plume physics, especially at the edges of the dimensionless parameter space. Uncertainties associated with the fetch over the canopy before encountering the plume may also affect the turbulence intensity, both before and after the onset of the rising plume, thereby changing the power-law scaling of the plume centerline slope. Furthermore, the dependence of the plume centerline slopes on other canopy geometry such as canopy density and height remains to be quantified. Additional simulations are required to assess the sensitivity to variations in these conditions. Moreover, the authors aspire to extend the scaling analysis to characterize the plume centerline deflection and rate of spread for propagating firelines in both canopy and no-canopy environments, in stable as well as unstable atmospheric conditions.

Notwithstanding the limitations of the present work, our analysis provides physical insights into how forcing mechanisms such as buoyancy strength, ambient wind speeds, and turbulent momentum fluxes, informed by the presence of a canopy, impact plume trajectories. Our analysis can inform the development of future scaling laws on buoyant plumes emanating from a vegetative canopy interacting with a cross-wind, which represents a gap in the literature. Such scaling laws can inform the development of improved, more efficient operational models for managing smoke hazards across a multitude of forcing conditions, which can find applications in mitigating the effects of natural and human-made disasters.

Chapter 7

Conclusions and Future Work

Complex turbulence patterns emerge from the interaction of a wildland fire-front with its surrounding atmosphere in a variety of terrain and ambient conditions, which remain to be fully characterized. Operational coarse-resolution fire-behavior models resort to simplifying assumptions regarding these interactions, limiting their predictive capabilities. Through a multi-scale analysis combining field observations and large-eddy simulations, this dissertation aims to describe the organized structures underlying fire-atmosphere interactions in both grassland and forested (canopy) settings.

In Chapter 2, high-frequency particle image velocimetry data from a small-scale grassland burn under calm wind reveal the presence of counter-rotating vortex pairs (CVPs) at the fire-front where the vorticity intensifies, which push hot gases outward, thereby causing the fire to spread. The evolving fire perimeter eventually disintegrates as the fire evolves, breaking into small "pockets" that resemble a chaotic system in the vicinity of an attractor. These localized fires interact with each other via fluxes of the turbulent kinetic energy.

Chapter 3 studies operational-scale experimental surface fires in both canopy and grassland environments, providing insights at more realistic scales. Moreover, insights into the rel-

ative significance of the processes governing turbulence production rates can help simplify the complex system of governing equations. In intense sub-canopy fires, shear production and buoyancy production are more substantial near the canopy top. At mid-canopy-height scales, buoyancy production dominates shear production, becoming the key mechanism for vertical transport of TKE. In the grassland fire, shear production dominates buoyancy production near the surface and is insignificant beyond a certain height relative to the flame length, while buoyancy production increases with height, becoming substantial further away from the surface. However, the time-averaging schemes utilized in these studies limit the determination of the characteristic finer-scale motions.

A wavelet analysis helps quantify time scales associated with fire-induced turbulent events more accurately, while also preserving their temporal signature. In Chapter 4, we isolate fire-modulated ramp–cliff structures with mean ramp durations approximately 20% shorter and both ramp and cliff amplitudes that are an order of magnitude higher compared to no-fire conditions. The increased cliff amplitudes signify intensified downdrafts penetrating the canopy, while the ramp amplitudes can be used to compute sensible heat fluxes that can be used to force and evaluate models. The characteristic time scales will help develop more reliable turbulence models in the presence of fire.

Despite their usefulness, observations are limited by spatial localization, and their database remains largely sparse. To overcome this limitation, we use low-complexity, no-flame large-eddy simulations with a fixed surface heat source and mild crosswind to examine the interaction of a buoyant plume with a homogeneous plant canopy. As described by Chapter 5, this setup, despite its simplicity, replicates key turbulent features observed near fire fronts–specifically, intensified vorticity at the windward edge and the formation of CVPs near the source that persist into the far field–supporting the utility of this approach. The plume within the canopy sub-layer tilts less steeply due to canopy drag, and a recirculation zone develops on the leeward side, obstructing upstream flow–an effect absent in the no-canopy

setting. Additionally, the transition height from the initial rise phase to the far-field regime is delayed in the canopy setting, and oscillations in the far-field plume centerline are more damped.

We then explore power-law dependencies between plume centerline slopes and dimensionless parameters encapsulating buoyancy strength relative to wind forcing (group I) and plume turbulence intensity relative to upstream (group II) using a suite of simulations in both environments as described in Chapter 6. Near-surface slopes are an order of magnitude steeper in canopy settings due to canopy-induced drag, though both environments exhibit similar sensitivity to group I. In contrast, far-field slopes in the canopy are more sensitive to this group. The turbulence intensity group has a stronger influence on near-surface slopes in canopy cases, reflecting spatial differences in the near-source momentum-flux structure between the two environments. Additionally, in the no-canopy setting, the transition height to the far-field regime follows a one-third power-law scaling with group I. Our results support the development of scaling laws for plume trajectories across varied environments and inform the improved tracking of plume trajectories.

Future work involves the modeling of interactions between multiple plumes in the absence of ambient wind forcing. Spatially separated fires are known to be attracted to each other, eventually leading to convergence and forming complex fires. This can happen in both parallel flanking fires (winds are parallel to firelines) or in coalescing fires (heading and backing firelines converge). While such behavior has been explored on laboratory scales and through modeling efforts, it remains fairly unexplored and the critical conditions beyond which the interactions intensify are unknown. Preliminary results from LES on the interaction between two plumes emerging from two static sources of heat with differing areas are presented here. The sizes of the upstream and downstream heated patches are $200\,\mathrm{m}\times200\,\mathrm{m}$ and $100\,\mathrm{m}\times100\,\mathrm{m}$, respectively, and the configuration is intended to simulate the interaction of coalescing fires. The inner edges of the heated patches are $500\,\mathrm{m}$ apart and the geostrophic

velocity at the inlet is $20\,\mathrm{cm\,s^{-1}}$. Figure. 7.1 depicts stream-slices in the flow field colored by the 10-minute mean vertical velocity at multiple instances in time. In the initial stages ($t = 0.167\,\mathrm{h}$), the plumes rise vertically given the weak ambient wind-forcing conditions. The interaction begins to set in as air is entrained by the downstream plume from the upstream plume, as observed from the streamlines. The interaction starts to intensify at $t = 0.833\,\mathrm{h}$ as recirculation regions appear between the plumes. Moreover, convection cells are formed further upstream in the domain. Around $t = 1.5\,\mathrm{h}$, the plumes are observed to merge into each other with strong wind entrainment from the upstream side for the upstream patch and from the downstream side for the downstream patch. By $t = 2.667\,\mathrm{h}$, the flow in the upstream region of the domain accelerates, with air descending swiftly toward the source of the upstream patch, causing a steeper tilt in the upstream plume. While the two plumes remain merged, they are both tilted in the downstream direction.

We plan to run the simulations for a longer time to explore potential oscillations in the merged plumes. Subsequent analyses will aim to characterize the pressure field that modulates these flow patterns and investigate the effect of varying the (i) distance between the heat sources, (ii) the geometry of each heat source, (ii) their placement relative to the wind direction, to explore interactions perpendicular to the wind direction.

This research aims to provide a comprehensive understanding of fire-atmosphere interactions in a range of environmental and meteorological conditions. This facilitates improved parameterizations of process-level phenomena, aiding in the development of efficient, physics-based predictive models over a broader application range, expanding their capabilities for wildland fire management.

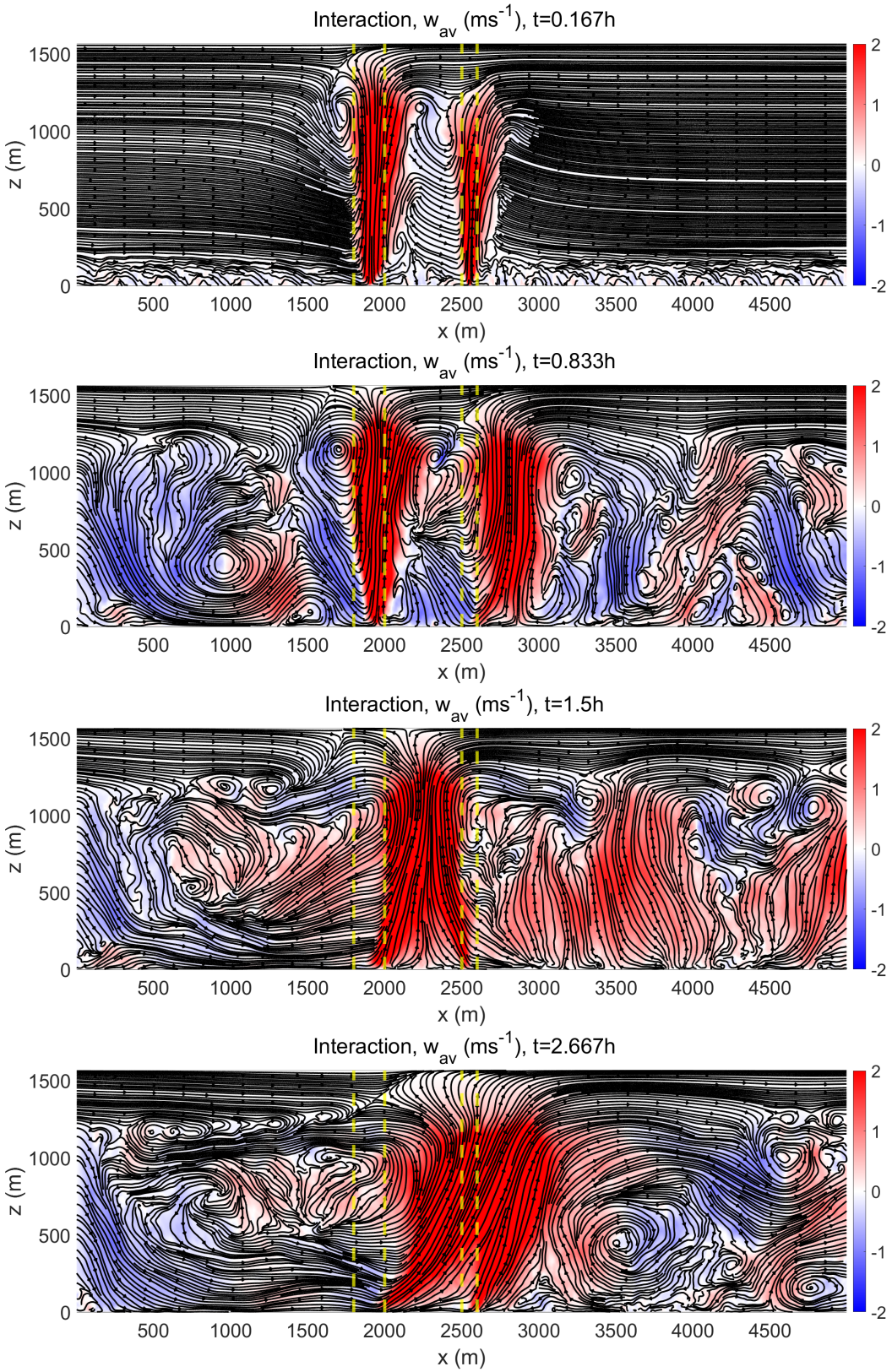


Figure 7.1: Stream slices in the symmetry plane (XZ) of the two square surface patches, colored by mean vertical velocity, depicting the progression of interaction between spatially separated plumes. Colorbar units are ms^{-1}

Bibliography

[1] G. G. Katul, D. Cava, M. Siqueira, and D. Poggi, "Scalar turbulence within the canopy sublayer," *Coherent Flow Structures at Earth's Surface*, pp. 73–95, 2013.

[2] C. B. Clements, S. Zhong, S. Goodrick, J. Li, B. E. Potter, X. Bian, W. E. Heilman, J. J. Charney, R. Perna, M. Jang, *et al.*, "Observing the dynamics of wildland grass fires: FireFlux—a field validation experiment," *Bulletin of the American Meteorological Society*, vol. 88, no. 9, pp. 1369–1382, 2007.

[3] C. B. Clements, S. Zhong, X. Bian, W. E. Heilman, and D. W. Byun, "First observations of turbulence generated by grass fires," *Journal of Geophysical Research: Atmospheres*, vol. 113, no. D22, 2008.

[4] W. E. Heilman, X. Bian, K. L. Clark, and S. Zhong, "Observations of turbulent heat and momentum fluxes during wildland fires in forested environments," *Journal of Applied Meteorology and Climatology*, vol. 58, no. 4, pp. 813–829, 2019.

[5] W. E. Heilman, T. Banerjee, C. B. Clements, K. L. Clark, S. Zhong, and X. Bian, "Observations of sweep–ejection dynamics for heat and momentum fluxes during wildland fires in forested and grassland environments," *Journal of Applied Meteorology and Climatology*, vol. 60, no. 2, pp. 185–199, 2021.

[6] F. Tedim, V. Leone, M. Amraoui, C. Bouillon, M. R. Coughlan, G. M. Delogu, P. M. Fernandes, C. Ferreira, S. McCaffrey, T. K. McGee, *et al.*, "Defining extreme wildfire events: Difficulties, challenges, and impacts," *Fire*, vol. 1, no. 1, p. 9, 2018.

[7] E. E. Knapp, Y. S. Valachovic, S. L. Quarles, and N. G. Johnson, "Housing arrangement and vegetation factors associated with single-family home survival in the 2018 camp fire, california," *Fire Ecology*, vol. 17, no. 1, p. 25, 2021.

[8] N. P. Lareau, N. J. Nauslar, and J. T. Abatzoglou, "The Carr Fire vortex: A case of pyrotornadogenesis?," *Geophysical Research Letters*, vol. 45, no. 23, pp. 13–107, 2018.

[9] T. W. Juliano, F. Szasdi-Bardales, N. P. Lareau, K. Shamsaei, B. Kosovic, N. Elhami-Khorasani, E. P. James, and H. Ebrahimian, "Brief communication: The lahaina fire disaster: How models can be used to understand and predict wildfires," *Natural Hazards and Earth System Sciences Discussions*, vol. 2023, pp. 1–7, 2023.

[10] B. Luo, C. Xiao, D. Luo, Q. Fu, D. Chen, Q. Zhang, Y. Ge, and Y. Diao, "Atmospheric and oceanic drivers behind the 2023 canadian wildfires," *Communications Earth & Environment*, vol. 6, no. 1, p. 446, 2025.

[11] M. Qiu, D. Chen, M. Kelp, J. Li, G. Huang, and M. D. Yazdi, "The rising threats of wildland-urban interface fires in the era of climate change: The los angeles 2025 fires," *The Innovation*, vol. 6, no. 5, 2025.

[12] National Geographic Society, "Megafire." `https://education.nationalgeographic.org/resource/megafire/`, 2022. Accessed: 6.1.2023.

[13] A. Descals, D. L. Gaveau, A. Verger, D. Sheil, D. Naito, and J. Peñuelas, "Unprecedented fire activity above the arctic circle linked to rising temperatures," *Science*, vol. 378, no. 6619, pp. 532–537, 2022.

[14] A. Barik and S. Baidya Roy, "Climate change strongly affects future fire weather danger in indian forests," *Communications Earth & Environment*, vol. 4, no. 1, p. 452, 2023.

[15] Y. Useni Sikuzani, M. Mpanda Mukenza, H. Khoji Muteya, N. Cirezi Cizungu, F. Malaisse, and J. Bogaert, "Vegetation fires in the lubumbashi charcoal production basin (the democratic republic of the congo): Drivers, extent and spatiotemporal dynamics," *Land*, vol. 12, no. 12, p. 2171, 2023.

[16] M. V. Singo, H. Chikoore, F. A. Engelbrecht, T. Ndarana, T. P. Muofhe, I. L. Mbokodo, F. M. Murungweni, and M.-J. M. Bopape, "Projections of future fire risk under climate change over the south african savanna," *Stochastic Environmental Research and Risk Assessment*, vol. 37, no. 7, pp. 2677–2691, 2023.

[17] A. Sullivan, E. Baker, and T. Kurvits, "Spreading like wildfire: The rising threat of extraordinary landscape fires," tech. rep., A UNEP Rapid Response Assessment, United Nations Environment Programme, Nairobi, 2022.

[18] N. National Interagency Fire Center, "National Fire News year-to-date statistics," 2021.

[19] T. Banerjee, W. Heilman, S. Goodrick, J. K. Hiers, and R. Linn, "Effects of canopy midstory management and fuel moisture on wildfire behavior," *Scientific Reports*, vol. 10, no. 1, pp. 1–14, 2020.

[20] G. Williamson, D. M. S. Bowman, O. F. Price, S. Henderson, and F. Johnston, "A transdisciplinary approach to understanding the health effects of wildfire and prescribed fire smoke regimes," *Environmental Research Letters*, vol. 11, no. 12, p. 125009, 2016.

[21] S. Li, J. A. Baijnath-Rodino, R. A. York, L. N. Quinn-Davidson, and T. Banerjee, "Temporal and spatial pattern analysis of escaped prescribed fires in california from 1991 to 2020," *Fire Ecology*, vol. 21, no. 1, p. 3, 2025.

[22] D. X. Viegas, A. Rodrigues, A. Abouali, M. Almeida, and J. Raposo, "Fire downwind a flat surface entering a canyon by lateral spread," *Fire Safety Journal*, vol. 122, p. 103349, 2021.

[23] A. Tohidi, M. J. Gollner, and H. Xiao, "Fire whirls," *Annu. Rev. Fluid Mech.*, vol. 50, pp. 187–213, 2018.

[24] G. G. Katul, L. Mahrt, D. Poggi, and C. Sanz, "One-and two-equation models for canopy turbulence," *Boundary-Layer Meteorology*, vol. 113, no. 1, pp. 81–109, 2004.

[25] A. Grishin, "General mathematical model for forest fires and its applications," *Combustion, Explosion and Shock Waves*, vol. 32, no. 5, pp. 503–519, 1996.

[26] R. R. Linn and P. Cunningham, "Numerical simulations of grass fires using a coupled atmosphere–fire model: basic fire behavior and dependence on wind speed," *Journal of Geophysical Research: Atmospheres*, vol. 110, no. D13, 2005.

[27] J. R. Curry and W. L. Fons, "Forest-fire behavior studies," *Mechanical Engineering. 62: 219-225*, vol. 62, pp. 219–225, 1940.

[28] W. L. Fons, "Analysis of fire spread in light forest fuels," *Journal of Agricultural Research*, vol. 72, no. 3, pp. 93–121, 1946.

[29] C. V. Wagner, "A simple fire-growth model," *The Forestry Chronicle*, vol. 45, no. 2, pp. 103–104, 1969.

[30] D. Anderson, E. Catchpole, N. De Mestre, and T. Parkes, "Modelling the spread of grass fires," *The ANZIAM Journal*, vol. 23, no. 4, pp. 451–466, 1982.

[31] G. D. Richards, "An elliptical growth model of forest fire fronts and its numerical solution," *International Journal for Numerical Methods in Engineering*, vol. 30, no. 6, pp. 1163–1179, 1990.

[32] G. D. Richards, "The properties of elliptical wildfire growth for time dependent fuel and meteorological conditions," *Combustion Science and Technology*, vol. 95, no. 1-6, pp. 357–383, 1993.

[33] G. D. Richards, "A general mathematical framework for modeling two-dimensional wildland fire spread," *International Journal of Wildland Fire*, vol. 5, no. 2, pp. 63–72, 1995.

[34] R. C. Rothermel, *A mathematical model for predicting fire spread in wildland fuels*, vol. 115. Intermountain Forest & Range Experiment Station, Forest Service, US Department of Agriculture, 1972.

[35] M. A. Finney, *FARSITE, Fire Area Simulator–model development and evaluation*. No. 4, US Department of Agriculture, Forest Service, Rocky Mountain Research Station, 1998.

[36] M. A. Finney, "An overview of FlamMap fire modeling capabilities," in *Andrews, Patricia L.; Butler, Bret W., comps. 2006. Fuels Management-How to Measure Success: Conference Proceedings. 28-30 March 2006; Portland, OR. Proceedings RMRS-P-41. Fort Collins, CO: US Department of Agriculture, Forest Service, Rocky Mountain Research Station. p. 213-220*, vol. 41, 2006.

[37] P. L. Andrews, "Current status and future needs of the BehavePlus fire modeling system," *International Journal of Wildland Fire*, vol. 23, no. 1, pp. 21–33, 2014.

[38] F. A. Albini, *Computer-based models of wildland fire behavior: a user's manual*. Intermountain Forest and Range Experiment Station, Forest Service, US Department of Agriculture, 1976.

[39] C. E. V. Wagner, "Conditions for the start and spread of crown fire," *Canadian Journal of Forest Research*, vol. 7, no. 1, pp. 23–34, 1977.

[40] J. H. Scott and E. D. Reinhardt, *Assessing crown fire potential by linking models of surface and crown fire behavior*. No. 29, US Department of Agriculture, Forest Service, Rocky Mountain Research Station, 2001.

[41] R. C. Rothermel, *Predicting behavior and size of crown fires in the Northern Rocky Mountains*, vol. 438. US Department of Agriculture, Forest Service, Intermountain Forest and Range, 1991.

[42] W. Mell, M. A. Jenkins, J. Gould, and P. Cheney, "A physics-based approach to modelling grassland fires," *International Journal of Wildland Fire*, vol. 16, no. 1, pp. 1–22, 2007.

[43] W. Mell, A. Maranghides, R. McDermott, and S. L. Manzello, "Numerical simulation and experiments of burning douglas fir trees," *Combustion and Flame*, vol. 156, no. 10, pp. 2023–2041, 2009.

[44] D. Morvan, J.-L. Dupuy, E. Rigolot, and J.-C. Valette, "FIRESTAR: a physically based model to study wildfire behaviour," *Forest Ecology and Management*, no. 234, p. S114, 2006.

[45] R. Linn, J. Reisner, J. J. Colman, and J. Winterkamp, "Studying wildfire behavior using FIRETEC," *International Journal of Wildland Fire*, vol. 11, no. 4, pp. 233–246, 2002.

[46] F. Pimont, J.-L. Dupuy, R. R. Linn, and S. Dupont, "Validation of FIRETEC windflows over a canopy and a fuel-break," *International Journal of Wildland Fire*, vol. 18, no. 7, pp. 775–790, 2009.

[47] J. Canfield, R. Linn, J. Sauer, M. Finney, and J. Forthofer, "A numerical investigation of the interplay between fireline length, geometry, and rate of spread," *Agricultural and Forest Meteorology*, vol. 189, pp. 48–59, 2014.

[48] T. Banerjee, T. Holland, K. Solander, M. Holmes, and R. Linn, "Identifying characteristics of wildfire towers and troughs," *Atmosphere*, vol. 11, no. 8, p. 796, 2020.

[49] J. J. Colman and R. R. Linn, "Separating combustion from pyrolysis in HIGRAD/FIRETEC," *International Journal of Wildland Fire*, vol. 16, no. 4, pp. 493–502, 2007.

[50] X. Zhou, S. Mahalingam, and D. Weise, "Experimental study and large eddy simulation of effect of terrain slope on marginal burning in shrub fuel beds," *Proceedings of the Combustion Institute*, vol. 31, no. 2, pp. 2547–2555, 2007.

[51] C. W. Ott, B. Adhikari, S. P. Alexander, P. Hodza, C. Xu, and T. A. Minckley, "Predicting fire propagation across heterogeneous landscapes using WyoFire: A Monte Carlo-driven wildfire model," *Fire*, vol. 3, no. 4, p. 71, 2020.

[52] R. R. Linn, S. Goodrick, S. Brambilla, M. J. Brown, R. S. Middleton, J. J. O'Brien, and J. K. Hiers, "QUIC-fire: A fast-running simulation tool for prescribed fire planning," *Environmental Modelling & Software*, vol. 125, p. 104616, 2020.

[53] R. C. Rothermel and H. E. Anderson, *Fire spread characteristics determined in the laboratory*, vol. 30. Intermountain Forest & Range Experiment Station, Forest Service, US Department of Agriculture, 1966.

[54] C. M. Countryman, *Mass fires and fire behavior*, vol. 19. Pacific Southwest Forest and Range Experiment Station, Forest Service, US Department of Agriculture, 1964.

[55] T. Beer, "The interaction of wind and fire," *Boundary-Layer Meteorology*, vol. 54, no. 3, pp. 287–308, 1991.

[56] J.-L. Dupuy, J. Maréchal, D. Portier, and J.-C. Valette, "The effects of slope and fuel bed width on laboratory fire behaviour," *International Journal of Wildland Fire*, vol. 20, no. 2, pp. 272–288, 2011.

[57] G. Byram, H. Clements, E. Elliott, and P. George, "An experimental study of model fires.," tech. rep., Southern Forest Fire Lab, Macon, GA, 1964.

[58] M. A. Finney, J. D. Cohen, J. M. Forthofer, S. S. McAllister, M. J. Gollner, D. J. Gorham, K. Saito, N. K. Akafuah, B. A. Adam, and J. D. English, "Role of buoyant flame dynamics in wildfire spread," *Proceedings of the National Academy of Sciences*, vol. 112, no. 32, pp. 9833–9838, 2015.

[59] C. J. Pickering and N. A. Halliwell, "Laser speckle photography and particle image velocimetry: photographic film noise," *Applied optics*, vol. 23, no. 17, pp. 2961–2969, 1984.

[60] R. J. Adrian, "Scattering particle characteristics and their effect on pulsed laser measurements of fluid flow: speckle velocimetry vs. particle image velocimetry," *Applied optics*, vol. 23, no. 11, pp. 1690–1691, 1984.

[61] R. J. Adrian, "Twenty years of particle image velocimetry," *Experiments in Fluids*, vol. 39, no. 2, pp. 159–169, 2005.

[62] D. L. Reuss, R. J. Adrian, and C. C. Landreth, "Two-dimensional velocity measurements in a laminar flame using particle image velocimetry," *Combustion Science and Technology*, vol. 67, no. 4-6, pp. 73–83, 1986.

[63] S. Tieszen, T. O'hern, R. Schefer, E. Weckman, and T. Blanchat, "Experimental study of the flow field in and around a one meter diameter methane fire," *Combustion and Flame*, vol. 129, no. 4, pp. 378–391, 2002.

[64] X. C. Zhou, J. P. Gore, and H. R. Baum, "Measurements and prediction of air entrainment rates of pool fires," in *Symposium (International) on Combustion*, vol. 26, pp. 1453–1459, Elsevier, 1996.

[65] F. Morandini, X. Silvani, and A. Susset, "Feasibility of particle image velocimetry in vegetative fire spread experiments," *Experiments in fluids*, vol. 53, no. 1, pp. 237–244, 2012.

[66] F. Morandini and X. Silvani, "Experimental investigation of the physical mechanisms governing the spread of wildfires," *International Journal of Wildland Fire*, vol. 19, no. 5, pp. 570–582, 2010.

[67] F. Morandini, X. Silvani, D. Honoré, G. Boutin, A. Susset, and R. Vernet, "Slope effects on the fluid dynamics of a fire spreading across a fuel bed: PIV measurements and OH* chemiluminescence imaging," *Experiments in fluids*, vol. 55, no. 8, p. 1788, 2014.

[68] R. D. Ottmar and R. Vihnanek, "Stereo photo series for quantifying natural fuels. volume VI: Longleaf, pocosin and marshgrass types in the Southeastern United States," tech. rep., PMS 835. Boise, ID: National Wildfire Coordinating Group, National Interagency Fire Center, 2000.

[69] J. K. Hiers, J. J. O'Brien, R. Mitchell, J. M. Grego, and E. L. Loudermilk, "The wildland fuel cell concept: an approach to characterize fine-scale variation in fuels and fire in frequently burned longleaf pine forests," *International Journal of Wildland Fire*, vol. 18, no. 3, pp. 315–325, 2009.

[70] E. L. Loudermilk, J. J. O'Brien, R. J. Mitchell, W. P. Cropper, J. K. Hiers, S. Grunwald, J. Grego, and J. C. Fernandez-Diaz, "Linking complex forest fuel structure and fire behaviour at fine scales," *International Journal of Wildland Fire*, vol. 21, no. 7, pp. 882–893, 2012.

[71] J. J. O'Brien, E. L. Loudermilk, B. Hornsby, A. T. Hudak, B. C. Bright, M. B. Dickinson, J. K. Hiers, C. Teske, and R. D. Ottmar, "High-resolution infrared thermography for capturing wildland fire behaviour: RxCADRE 2012," *International Journal of Wildland Fire*, vol. 25, no. 1, pp. 62–75, 2015.

[72] I. Fujita and T. Hino, "Unseeded and seeded PIV measurements of river flows videotaped from a helicopter," *Journal of Visualization*, vol. 6, no. 3, pp. 245–252, 2003.

[73] P. A. Werth, B. E. Potter, C. B. Clements, M. A. Finney, J. A. Forthofer, S. S. McAllister, S. L. Goodrick, M. E. Alexander, and M. G. Cruz, "Synthesis of knowledge of extreme fire behavior: volume I for fire managers," 2011.

[74] J. Jiménez, "Coherent structures in wall-bounded turbulence," *Journal of Fluid Mechanics*, vol. 842, 2018.

[75] J. Finnigan, "Turbulence in plant canopies," *Annual Review of Fluid Mechanics*, vol. 32, no. 1, pp. 519–571, 2000.

[76] E. K. Webb, *Autocorrelations and energy spectra of atmospheric turbulence*. No. 5, Commonwealth Scientific and Industrial Research Organization, 1955.

[77] A. J. Puga, *Characteristics of the velocity power spectrum as a function of Taylor Reynolds number*. PhD thesis, UC Irvine, 2016.

[78] W. Jones and B. E. Launder, "The prediction of laminarization with a two-equation model of turbulence," *International journal of heat and mass transfer*, vol. 15, no. 2, pp. 301–314, 1972.

[79] Engineers Edge, "Viscosity of air, dynamic and kinematic." `https://www.engineersedge.com/physics/viscosity_of_air_dynamic_and_kinematic_14483.htm`, 2018. Accessed: 2021-06-20.

[80] S. B. Pope, *Turbulent flows*. Cambridge University Press, 2000.

[81] W. E. Heilman, X. Bian, K. L. Clark, N. S. Skowronski, J. L. Hom, and M. R. Gallagher, "Atmospheric turbulence observations in the vicinity of surface fires in forested environments," *Journal of Applied Meteorology and Climatology*, vol. 56, no. 12, pp. 3133–3150, 2017.

[82] R. B. Stull, *An introduction to boundary layer meteorology*, vol. 13. Springer Science & Business Media, 2012.

[83] W. Thurston, J. D. Kepert, K. J. Tory, and R. J. Fawcett, "The contribution of turbulent plume dynamics to long-range spotting," *International Journal of Wildland Fire*, vol. 26, no. 4, pp. 317–330, 2017.

[84] R. Sun, S. K. Krueger, M. A. Jenkins, M. A. Zulauf, and J. J. Charney, "The importance of fire–atmosphere coupling and boundary-layer turbulence to wildfire spread," *International Journal of Wildland Fire*, vol. 18, no. 1, pp. 50–60, 2009.

[85] T. Banerjee, "Impacts of forest thinning on wildland fire behavior," *Forests*, vol. 11, no. 9, p. 918, 2020.

[86] E. Mueller, W. Mell, and A. Simeoni, "Large eddy simulation of forest canopy flow for wildland fire modeling," *Canadian Journal of Forest Research*, vol. 44, no. 12, pp. 1534–1544, 2014.

[87] A. Desai, S. Goodrick, and T. Banerjee, "Investigating the turbulent dynamics of small-scale surface fires," *Scientific Reports*, vol. 12, no. 1, p. 10503, 2022.

[88] D. Seto, C. B. Clements, and W. E. Heilman, "Turbulence spectra measured during fire front passage," *Agricultural and Forest Meteorology*, vol. 169, pp. 195–210, 2013.

[89] W. E. Heilman, S. Zhong, J. J. Charney, *et al.*, "Development of modeling tools for predicting smoke dispersion from low-intensity fires," 2013.

[90] W. E. Heilman, C. B. Clements, D. Seto, X. Bian, K. L. Clark, N. S. Skowronski, and J. L. Hom, "Observations of fire-induced turbulence regimes during low-intensity wildland fires in forested environments: implications for smoke dispersion," *Atmospheric Science Letters*, vol. 16, no. 4, pp. 453–460, 2015.

[91] W. E. Heilman, K. L. Clark, X. Bian, J. J. Charney, S. Zhong, N. S. Skowronski, M. R. Gallagher, and M. Patterson, "Turbulent momentum flux behavior above a fire front in an open-canopied forest," *Atmosphere*, vol. 12, no. 8, p. 956, 2021.

[92] M. T. Kiefer, W. E. Heilman, S. Zhong, J. J. Charney, and X. Bian, "Mean and turbulent flow downstream of a low-intensity fire: Influence of canopy and background atmospheric conditions," *Journal of Applied Meteorology and Climatology*, vol. 54, no. 1, pp. 42–57, 2015.

[93] M. R. Raupach, J. J. Finnigan, and Y. Brunet, "Coherent eddies and turbulence in vegetation canopies: the mixing-layer analogy," in *Boundary-Layer Meteorology 25th anniversary volume, 1970–1995*, pp. 351–382, Springer, 1996.

[94] X. Lee, W. Massman, and B. Law, *Handbook of micrometeorology: a guide for surface flux measurement and analysis*, vol. 29. Springer Science & Business Media, 2004.

[95] K. Clark, "AmeriFlux US-Ced Cedar Bridge," tech. rep., Lawrence Berkeley National Lab. (LBNL), Berkeley, CA, United States, 2016.

[96] K. Clark, "AmeriFlux US-Slt Silas Little-New Jersey," tech. rep., Lawrence Berkeley National Lab. (LBNL), Berkeley, CA, United States, 2016.

[97] D. Pereira, "Wind rose."

[98] E. Koo, P. J. Pagni, D. R. Weise, and J. P. Woycheese, "Firebrands and spotting ignition in large-scale fires," *International Journal of Wildland Fire*, vol. 19, no. 7, pp. 818–843, 2010.

[99] A. C. Fernandez-Pello, "Wildland fire spot ignition by sparks and firebrands," *Fire Safety Journal*, vol. 91, pp. 2–10, 2017.

[100] C. Thomas, J. J. Sharples, and J. Evans, "The terminal-velocity assumption in simulations of long-range ember transport," *Mathematics and Computers in Simulation*, vol. 175, pp. 96–107, 2020.

[101] C. B. Clements, A. K. Kochanski, D. Seto, B. Davis, C. Camacho, N. P. Lareau, J. Contezac, J. Restaino, W. E. Heilman, S. K. Krueger, *et al.*, "The FireFlux II experiment: a model-guided field experiment to improve understanding of fire–atmosphere interactions and fire spread," *International Journal of Wildland Fire*, vol. 28, no. 4, pp. 308–326, 2019.

[102] A. Desai, W. E. Heilman, N. S. Skowronski, K. L. Clark, M. R. Gallagher, C. B. Clements, and T. Banerjee, "Features of turbulence during wildland fires in forested and grassland environments," *Agricultural and Forest Meteorology*, vol. 338, p. 109501, 2023.

[103] S. L. Goodrick, G. L. Achtemeier, N. K. Larkin, Y. Liu, and T. M. Strand, "Modelling smoke transport from wildland fires: a review," *International Journal of Wildland Fire*, vol. 22, no. 1, pp. 83–94, 2012.

[104] V. Babrauskas, "Firebrands and embers," *Encyclopedia of Wildfires and Wildland-Urban Interface (WUI) Fires*, pp. 431–444, 2020.

[105] Y. Bebieva, J. Oliveto, B. Quaife, N. S. Skowronski, W. E. Heilman, and K. Speer, "Role of horizontal eddy diffusivity within the canopy on fire spread," *Atmosphere*, vol. 11, no. 6, p. 672, 2020.

[106] J. L. Dupuy, F. Pimont, R. R. Linn, and C. B. Clements, "FIRETEC evaluation against the FireFlux experiment: preliminary results," in *Advances in Forest Fire Research* (D. X. Viegas, ed.), ch. 1, pp. 261–274, Coimbra, Portugal: Coimbra University Press, 2014.

[107] R. Wadhwani, C. Sullivan, A. Wickramasinghe, M. Kyng, N. Khan, and K. Moinuddin, "A review of firebrand studies on generation and transport," *Fire Safety Journal*, p. 103674, 2022.

[108] K. L. Clark, W. E. Heilman, N. S. Skowronski, M. R. Gallagher, E. Mueller, R. M. Hadden, and A. Simeoni, "Fire behavior, fuel consumption, and turbulence and energy exchange during prescribed fires in pitch pine forests," *Atmosphere*, vol. 11, no. 3, p. 242, 2020.

[109] W. Gao, R. Shaw, and K. Paw U, "Observation of organized structure in turbulent flow within and above a forest canopy," *Boundary Layer Studies and Applications: A Special Issue of Boundary-Layer Meteorology in honor of Dr. Hans A. Panofsky (1917–1988)*, pp. 349–377, 1989.

[110] K. T. Paw U, Y. Brunet, S. Collineau, R. H. Shaw, T. Maitani, J. Qiu, and L. Hipps, "On coherent structures in turbulence above and within agricultural plant canopies," *Agricultural and Forest Meteorology*, vol. 61, no. 1-2, pp. 55–68, 1992.

[111] W. Gao and B. Li, "Wavelet analysis of coherent structures at the atmosphere-forest interface," *Journal of Applied Meteorology and Climatology*, vol. 32, no. 11, pp. 1717–1725, 1993.

[112] K. T. Paw U, J. Qiu, H.-B. Su, T. Watanabe, Y. Brunet, *et al.*, "Surface renewal analysis: a new method to obtain scalar fluxes," *Agricultural and Forest Meteorology*, vol. 74, no. 1-2, pp. 119–137, 1995.

[113] G. Katul, C.-I. Hsieh, R. Oren, D. Ellsworth, and N. Phillips, "Latent and sensible heat flux predictions from a uniform pine forest using surface renewal and flux variance methods," *Boundary-Layer Meteorology*, vol. 80, pp. 249–282, 1996.

[114] M. Fischer, G. Katul, A. Noormets, G. Pozníková, J.-C. Domec, M. Orság, Z. Žalud, M. Trnka, and J. S. King, "Merging flux-variance with surface renewal methods in the roughness sublayer and the atmospheric surface layer," *Agricultural and Forest Meteorology*, vol. 342, p. 109692, 2023.

[115] P. Kumar and E. Foufoula-Georgiou, "Wavelet analysis for geophysical applications," *Reviews of Geophysics*, vol. 35, no. 4, pp. 385–412, 1997.

[116] J. Liandrat and F. Moret-Bailly, "The wavelet transform-some applications to fluid dynamics and turbulence," *European Journal of Mechanics B Fluids*, vol. 9, no. 1, pp. 1–19, 1990.

[117] C. Meneveau, "Analysis of turbulence in the orthonormal wavelet representation," *Journal of Fluid Mechanics*, vol. 232, pp. 469–520, 1991.

[118] M. Farge, "Wavelet transforms and their applications to turbulence," *Annual Review of Fluid Mechanics*, vol. 24, no. 1, pp. 395–458, 1992.

[119] A. Rinoshika and H. Rinoshika, "Application of multi-dimensional wavelet transform to fluid mechanics," *Theoretical and Applied Mechanics Letters*, vol. 10, no. 2, pp. 98–115, 2020.

[120] S. Collineau and Y. Brunet, "Detection of turbulent coherent motions in a forest canopy part I: Wavelet analysis," *Boundary-Layer Meteorology*, vol. 65, no. 4, pp. 357–379, 1993.

[121] S. Collineau and Y. Brunet, "Detection of turbulent coherent motions in a forest canopy part II: Time-scales and conditional averages," *Boundary-Layer Meteorology*, vol. 66, no. 1-2, pp. 49–73, 1993.

[122] T. Watanabe, "Large-eddy simulation of coherent turbulence structures associated with scalar ramps over plant canopies," *Boundary-Layer Meteorology*, vol. 112, pp. 307–341, 2004.

[123] J. Qiu, K. T. Paw U, and R. H. Shaw, "Pseudo-wavelet analysis of turbulence patterns in three vegetation layers," *Boundary-Layer Meteorology*, vol. 72, no. 1, pp. 177–204, 1995.

[124] C. Schaller, M. Göckede, and T. Foken, "Flux calculation of short turbulent events–comparison of three methods," *Atmospheric Measurement Techniques*, vol. 10, no. 3, pp. 869–880, 2017.

[125] Y. Brunet and S. Collineau, "Wavelet analysis of diurnal and nocturnal turbulence above a maize crop," in *Wavelet Analysis and Its Applications*, vol. 4, pp. 129–150, Elsevier, 1994.

[126] B. Turner, M. Leclerc, M. Gauthier, K. Moore, and D. Fitzjarrald, "Identification of turbulence structures above a forest canopy using a wavelet transform," *Journal of Geophysical Research: Atmospheres*, vol. 99, no. D1, pp. 1919–1926, 1994.

[127] G. Katul and B. Vidakovic, "The partitioning of attached and detached eddy motion in the atmospheric surface layer using Lorentz wavelet filtering," *Boundary-Layer Meteorology*, vol. 77, no. 2, pp. 153–172, 1996.

[128] J. Chen and F. Hu, "Coherent structures detected in atmospheric boundary-layer turbulence using wavelet transforms at Huaihe River Basin, China," *Boundary-Layer Meteorology*, vol. 107, pp. 429–444, 2003.

[129] S. Dupont, F. Argoul, E. Gerasimova-Chechkina, M. R. Irvine, and A. Arneodo, "Experimental evidence of a phase transition in the multifractal spectra of turbulent temperature fluctuations at a forest canopy top," *Journal of Fluid Mechanics*, vol. 896, p. A15, 2020.

[130] M. Katurji, B. Noonan, J. Zhang, A. Valencia, B. Shumacher, J. Kerr, T. Strand, G. Pearce, and P. Zawar-Reza, "Atmospheric turbulent structures and fire sweeps during shrub fires and implications for flaming zone behaviour," *International Journal of Wildland Fire*, 2022.

[131] P. S. Addison, *The illustrated wavelet transform handbook: introductory theory and applications in science, engineering, medicine and finance*. CRC press, 2017.

[132] L. Hudgins, C. A. Friehe, and M. E. Mayer, "Wavelet transforms and atmopsheric turbulence," *Physical Review Letters*, vol. 71, no. 20, p. 3279, 1993.

[133] M. R. Gallagher, N. S. Skowronski, R. M. Hadden, E. V. Mueller, K. L. Clark, Z. J. Campbell-Lochrie, C. Walker-Ravena, R. L. Kremens, A. I. Everland, M. M. Patterson, *et al.*, "Multi-scale analyses of wildland fire combustion processes: Large-scale field experiments–burn layout and documentation," tech. rep., Fort Collins, CO: Forest Service Research Data Archive, 2023.

[134] J. M. Wallace, "Quadrant analysis in turbulence research: history and evolution," *Annual Review of Fluid Mechanics*, vol. 48, pp. 131–158, 2016.

[135] P. S. Addison, "Introduction to redundancy rules: the continuous wavelet transform comes of age," *Philosophical Transactions of the Royal Society A: Mathematical, Physical and Engineering Sciences*, vol. 376, no. 2126, p. 20170258, 2018.

[136] S. Mallat, *A wavelet tour of signal processing*. Elsevier, 1999.

[137] C. Thomas and T. Foken, "Detection of long-term coherent exchange over spruce forest using wavelet analysis," *Theoretical and Applied Climatology*, vol. 80, pp. 91–104, 2005.

[138] A. Grinsted, J. C. Moore, and S. Jevrejeva, "Application of the cross wavelet transform and wavelet coherence to geophysical time series," *Nonlinear Processes in Geophysics*, vol. 11, no. 5/6, pp. 561–566, 2004.

[139] C. Torrence and P. J. Webster, "Interdecadal changes in the ENSO–monsoon system," *Journal of Climate*, vol. 12, no. 8, pp. 2679–2690, 1999.

[140] W. M. Kays, M. E. Crawford, and B. Weigand, *Convective heat and mass transfer*, vol. 4. McGraw-Hill New York, 1980.

[141] D. Li, "Turbulent Prandtl number in the atmospheric boundary layer- where are we now?," *Atmospheric Research*, vol. 216, pp. 86–105, 2019.

[142] S. Chowdhuri and T. Banerjee, "Revisiting "bursts" in wall-bounded turbulent flows," *Physical Review Fluids*, vol. 8, no. 4, p. 044606, 2023.

[143] M. Allouche, E. Bou-Zeid, C. Ansorge, G. G. Katul, M. Chamecki, O. Acevedo, S. Thanekar, and J. D. Fuentes, "The detection, genesis, and modeling of turbulence intermittency in the stable atmospheric surface layer," *Journal of the Atmospheric Sciences*, vol. 79, no. 4, pp. 1171–1190, 2022.

[144] T. Fric and A. Roshko, "Vortical structure in the wake of a transverse jet," *Journal of Fluid Mechanics*, vol. 279, pp. 1–47, 1994.

[145] C. Cárdenas, R. Suntz, J. A. Denev, and H. Bockhorn, "Two-dimensional estimation of Reynolds-fluxes and-stresses in a Jet-in-Crossflow arrangement by simultaneous 2D-LIF and PIV," *Applied physics B*, vol. 88, pp. 581–591, 2007.

[146] K. Mahesh, "The interaction of jets with crossflow," *Annual Review of Fluid Mechanics*, vol. 45, no. 1, pp. 379–407, 2013.

[147] G. A. Briggs, "Plume rise and buoyancy effects," *Atmospheric Science and Power Production*, vol. 850, pp. 327–366, 1984.

[148] J. C. Weil, *Plume Rise*, pp. 119–166. Boston, MA: American Meteorological Society, 1988.

[149] G. Davidson, "Dimensionless correlations for bouyant plume behaviour in crossflows and scaling criteria for physical modelling of dispersion processes," *Journal of Wind Engineering and Industrial Aerodynamics*, vol. 51, no. 2, pp. 135–155, 1994.

[150] K. L. Pun and M. Davidson, "On the behaviour of advected plumes and thermals," *Journal of Hydraulic Research*, vol. 37, no. 4, pp. 519–540, 1999.

[151] A. Robins and D. Contini, "Water tank studies of the interactions between buoyant plumes emitted into a crossflow," *WIT Transactions on Ecology and the Environment*, vol. 42, 2000.

[152] J. H. W. Lee and V. H. Chu, *Plume in Crossflow: Advected Line Thermals*, pp. 249–291. Boston, MA: Springer US, 2003.

[153] D. Contini, A. Donateo, D. Cesari, and A. Robins, "Comparison of plume rise models against water tank experimental data for neutral and stable crossflows," *Journal of Wind Engineering and Industrial Aerodynamics*, vol. 99, no. 5, pp. 539–553, 2011.

[154] P. Huq and E. Stewart, "A laboratory study of buoyant plumes in laminar and turbulent crossflows," *Atmospheric Environment*, vol. 30, no. 7, pp. 1125–1135, 1996.

[155] C. B. James, N. Mingotti, and A. W. Woods, "On particle separation from turbulent particle plumes in a cross-flow," *Journal of Fluid Mechanics*, vol. 932, p. A45, 2022.

[156] H. Chung and J. R. Koseff, "Interaction of a buoyant plume with a turbulent canopy mixing layer," *Physical Review Fluids*, vol. 8, no. 6, p. 064501, 2023.

[157] W. E. Heilman, "Atmospheric turbulence and wildland fires: a review," *International journal of wildland fire*, vol. 32, no. 4, pp. 476–495, 2023.

[158] A. Desai, C. Guilloteau, W. E. Heilman, J. J. Charney, N. S. Skowronski, K. L. Clark, M. R. Gallagher, E. Foufoula-Georgiou, and T. Banerjee, "Investigating fire–atmosphere interaction in a forest canopy using wavelets," *Boundary-Layer Meteorology*, vol. 190, no. 5, p. 21, 2024.

[159] S. Wharton, M. J. Brown, D. Dexheimer, J. D. Fast, R. K. Newsom, W. W. Schalk, and D. J. Wiersema, "Capturing plume behavior in complex terrain: an overview of the Nevada National Security Site Meteorological Experiment (METEX21)," *Frontiers in Earth Science*, vol. 11, p. 1251153, 2023.

[160] J. A. Baijnath-Rodino, S. Li, A. Martinez, M. Kumar, L. N. Quinn-Davidson, R. A. York, and T. Banerjee, "Historical seasonal changes in prescribed burn windows in california," *Science of the Total Environment*, vol. 836, p. 155723, 2022.

[161] E. Strobach, W. Brewer, C. Senff, S. Baidar, and B. McCarty, "Isolating and investigating updrafts induced by wildland fires using an airborne doppler lidar during FIREX-AQ," *Journal of Geophysical Research: Atmospheres*, vol. 128, no. 14, p. e2023JD038809, 2023.

[162] B. J. Carroll, W. A. Brewer, E. Strobach, N. Lareau, S. S. Brown, M. M. Valero, A. Kochanski, C. B. Clements, R. Kahn, K. T. Junghenn Noyes, *et al.*, "Measuring coupled fire–atmosphere dynamics: The California Fire Dynamics Experiment (CalFiDE)," *Bulletin of the American Meteorological Society*, vol. 105, no. 3, pp. E690–E708, 2024.

[163] N. P. Lareau, N. J. Nauslar, E. Bentley, M. Roberts, S. Emmerson, B. Brong, M. Mehle, and J. Wallman, "Fire-generated tornadic vortices," *Bulletin of the American Meteorological Society*, vol. 103, no. 5, pp. E1296–E1320, 2022.

[164] E. V. Mueller, N. S. Skowronski, K. L. Clark, M. R. Gallagher, W. E. Mell, A. Simeoni, and R. M. Hadden, "Detailed physical modeling of wildland fire dynamics at field scale-an experimentally informed evaluation," *Fire Safety Journal*, vol. 120, p. 103051, 2021.

[165] J. T. Benik, A. Farguell, J. D. Mirocha, C. B. Clements, and A. K. Kochanski, "Analysis of fire-induced circulations during the FireFlux2 experiment," *Fire*, vol. 6, no. 9, p. 332, 2023.

[166] K. Shamsaei, T. W. Juliano, M. Roberts, H. Ebrahimian, B. Kosovic, N. P. Lareau, and E. Taciroglu, "Coupled fire-atmosphere simulation of the 2018 Camp Fire using WRF-Fire," *International Journal of Wildland Fire*, vol. 32, no. 2, pp. 195–221, 2023.

[167] M. Roberts, N. P. Lareau, T. W. Juliano, K. Shamsaei, H. Ebrahimian, and B. Kosovic, "Sensitivity of simulated fire-generated circulations to fuel characteristics during large wildfires," *Journal of Geophysical Research: Atmospheres*, vol. 129, no. 6, p. e2023JD040548, 2024.

[168] M. A. Finney, J. D. Cohen, S. S. McAllister, and W. M. Jolly, "On the need for a theory of wildland fire spread," *International Journal of Wildland Fire*, vol. 22, no. 1, pp. 25–36, 2012.

[169] K. Speer and S. Goodrick, *Wildland fire dynamics: fire effects and behavior from a fluid dynamics perspective*. Cambridge University Press, 2022.

[170] A. L. Sullivan, "Wildland surface fire spread modelling, 1990–2007. 1: Physical and quasi-physical models," *International Journal of Wildland Fire*, vol. 18, no. 4, pp. 349–368, 2009.

[171] T. B. Y. Chen, A. Yuen, G. H. Yeoh, V. Timchenko, S. C. Cheung, Q. N. Chan, W. Yang, and H. Lu, "Numerical study of fire spread using the level-set method with large eddy simulation incorporating detailed chemical kinetics gas-phase combustion model," *Journal of Computational Science*, vol. 24, pp. 8–23, 2018.

[172] M. M. Ahmed, A. Trouvé, J. Forthofer, and M. Finney, "Simulations of flaming combustion and flaming-to-smoldering transition in wildland fire spread at flame scale," *Combustion and Flame*, vol. 262, p. 113370, 2024.

[173] J. Lavelle, "Buoyancy-driven plumes in rotating, stratified cross flows: Plume dependence on rotation, turbulent mixing, and cross-flow strength," *Journal of Geophysical Research: Oceans*, vol. 102, no. C2, pp. 3405–3420, 1997.

[174] W. Thurston, K. J. Tory, R. J. Fawcett, and J. D. Kepert, "Large-eddy simulations of bushfire plumes in the turbulent atmospheric boundary layer," in *MODSIM2013, 20th International Congress on Modelling and Simulation*, pp. 284–289, Modelling and Simulation Society of Australia and New Zealand, 2013.

[175] C. Cintolesi, A. Petronio, and V. Armenio, "Turbulent structures of buoyant jet in cross-flow studied through large-eddy simulation," *Environmental Fluid Mechanics*, vol. 19, no. 2, pp. 401–433, 2019.

[176] M. Lappa, "On the highly unsteady dynamics of multiple thermal buoyant jets in cross flows," *Physics of Fluids*, vol. 31, no. 11, 2019.

[177] S. Behera, B. A. Khan, and A. K. Saha, "Characterization of the turbulent field behavior of an elevated jet-in crossflow investigated using direct numerical simulation," *Physics of Fluids*, vol. 35, no. 1, 2023.

[178] W. Quan, W. Sun, J. Zhang, and X. Tan, "Large-eddy simulations on flow structures and interaction mechanism of synthetic jets in a crossflow," *Journal of Applied Fluid Mechanics*, vol. 17, no. 4, pp. 756–769, 2024.

[179] Y. Cao, J. Philip, and A. Ooi, "Characteristics of a buoyant plume in a channel with cross-flow," *International Journal of Heat and Fluid Flow*, vol. 93, p. 108899, 2022.

[180] B. Maronga, S. Banzhaf, C. Burmeister, T. Esch, R. Forkel, D. Fröhlich, V. Fuka, K. F. Gehrke, J. Geletič, S. Giersch, *et al.*, "Overview of the palm model system 6.0," *Geoscientific Model Development*, vol. 13, no. 3, pp. 1335–1372, 2020.

[181] A. Arakawa and V. R. Lamb, "Computational design of the basic dynamical processes of the UCLA general circulation model," 1977.

[182] L. J. Wicker and W. C. Skamarock, "Time-splitting methods for elastic models using forward time schemes," *Monthly Weather Review*, vol. 130, no. 8, pp. 2088–2097, 2002.

[183] J. H. Williamson, "Low-storage Runge-Kutta schemes," *Journal of Computational Physics*, vol. 35, no. 1, pp. 48–56, 1980.

[184] B. Maronga, M. Gryschka, R. Heinze, F. Hoffmann, F. Kanani-Sühring, M. Keck, K. Ketelsen, M. O. Letzel, M. Sühring, and S. Raasch, "The Parallelized Large-Eddy Simulation Model (PALM) version 4.0 for atmospheric and oceanic flows: model formulation, recent developments, and future perspectives," *Geoscientific Model Development*, vol. 8, no. 8, pp. 2515–2551, 2015.

[185] J. W. Deardorff, "Stratocumulus-capped mixed layers derived from a three-dimensional model," *Boundary-Layer Meteorology*, vol. 18, no. 4, pp. 495–527, 1980.

[186] C. Q. Dias-Junior, E. P. Marques Filho, and L. D. Sa, "A large eddy simulation model applied to analyze the turbulent flow above amazon forest," *Journal of Wind Engineering and Industrial Aerodynamics*, vol. 147, pp. 143–153, 2015.

[187] E. G. Patton, P. P. Sullivan, R. H. Shaw, J. J. Finnigan, and J. C. Weil, "Atmospheric stability influences on coupled boundary layer and canopy turbulence," *Journal of the Atmospheric Sciences*, vol. 73, no. 4, pp. 1621–1647, 2016.

[188] R. H. Shaw and U. Schumann, "Large-eddy simulation of turbulent flow above and within a forest," *Boundary-Layer Meteorology*, vol. 61, no. 1, pp. 47–64, 1992.

[189] N. P. Lareau, C. B. Clements, A. Kochanski, T. Aydell, A. T. Hudak, T. R. McCarley, and R. Ottmar, "Observations of a rotating pyroconvective plume," *International Journal of Wildland Fire*, vol. 33, no. 3, 2024.

[190] T. S. Lund, X. Wu, and K. D. Squires, "Generation of turbulent inflow data for spatially-developing boundary layer simulations," *Journal of Computational Physics*, vol. 140, no. 2, pp. 233–258, 1998.

[191] R. Rotunno and H. B. Bluestein, "Recent developments in tornado theory and observations," *Reports on Progress in Physics*, 2024.

[192] A. Desai, S. Goodrick, and T. Banerjee, "Investigating the turbulent dynamics of small-scale surface fires," *Scientific Reports*, vol. 12, no. 1, p. 10503, 2022.

[193] C. R. Church, J. T. Snow, and J. Dessens, "Intense atmospheric vortices associated with a 1000 mw fire," *Bulletin of the American Meteorological Society*, vol. 61, no. 7, pp. 682–694, 1980.

[194] M. A. Finney *et al.*, "Role of buoyant flame dynamics in wildfire spread," *Proceedings of the National Academy of Sciences*, vol. 112, no. 32, pp. 9833–9838, 2015.

[195] T. Banerjee, T. Holland, K. Solander, M. Holmes, and R. Linn, "Identifying characteristics of wildfire towers and troughs," *Atmosphere*, vol. 11, no. 8, p. 796, 2020.

[196] K. Himoto and Y. Deguchi, "Temperature elevation and trajectory in the downwind region of rectangular fire sources in cross-winds," *Fire Safety Journal*, vol. 116, p. 103183, 2020.

[197] B. R. Morton, G. I. Taylor, and J. S. Turner, "Turbulent gravitational convection from maintained and instantaneous sources," *Proceedings of the Royal Society of London. Series A. Mathematical and Physical Sciences*, vol. 234, no. 1196, pp. 1–23, 1956.

[198] B. R. Morton, "Forced plumes," *Journal of Fluid mechanics*, vol. 5, no. 1, pp. 151–163, 1959.

[199] J. S. Turner, "Buoyant plumes and thermals," *Annual Review of Fluid Mechanics*, vol. 1, no. 1, pp. 29–44, 1969.

[200] G. R. Hunt and T. S. Van den Bremer, "Classical plume theory: 1937–2010 and beyond," *IMA Journal of Applied Mathematics*, vol. 76, no. 3, pp. 424–448, 2011.

[201] T. S. Van Den Bremer and G. R. Hunt, "Universal solutions for boussinesq and non-boussinesq plumes," *Journal of Fluid Mechanics*, vol. 644, pp. 165–192, 2010.

[202] J. Craske and M. van Reeuwijk, "Generalised unsteady plume theory," *Journal of Fluid Mechanics*, vol. 792, pp. 1013–1052, 2016.

[203] Z. Saeed, E. Weidner, B. A. Johnson, and T. L. Mandel, "Buoyancy-modified entrainment in plumes: Theoretical predictions," *Physics of Fluids*, vol. 34, no. 1, 2022.

[204] J. P. Webb, N. H. Wise, and G. R. Hunt, "Turbulent plumes above a heated plate," *Journal of Fluid Mechanics*, vol. 959, p. A29, 2023.

[205] A. J. Hogg, E. J. Goldsmith, and M. J. Woodhouse, "Unsteady turbulent line plumes," *Journal of Fluid Mechanics*, vol. 856, pp. 103–134, 2018.

[206] A. Skvortsov, T. C. DuBois, M. Jamriska, and M. Kocan, "Scaling laws for extremely strong thermals," *Physical Review Fluids*, vol. 6, no. 5, p. 053501, 2021.

[207] M. Kocan and A. Skvortsov, "Scaling laws of strong convective thermals: comparison with experimental data," *Environmental Fluid Mechanics*, vol. 22, no. 1, pp. 245–257, 2022.

[208] M. Raupach, "Similarity analysis of the interaction of bushfire plumes with ambient winds," *Mathematical and Computer Modelling*, vol. 13, no. 12, pp. 113–121, 1990.

[209] T. Hewett, J. Fay, and D. Hoult, "Laboratory experiments of smokestack plumes in a stable atmosphere," *Atmospheric Environment (1967)*, vol. 5, no. 9, pp. 767–789, 1971.

[210] V. H. Chu, "Turbulent dense plumes in a laminar cross flow," *Journal of Hydraulic Research*, vol. 13, no. 3, pp. 263–279, 1975.

[211] B. J. Devenish, G. G. Rooney, H. N. Webster, and D. J. Thomson, "The entrainment rate for buoyant plumes in a crossflow," *Boundary-Layer Meteorology*, vol. 134, no. 3, pp. 411–439, 2010.

[212] O. H. Jordan, G. G. Rooney, B. J. Devenish, and M. van Reeuwijk, "Under pressure: turbulent plumes in a uniform crossflow," *Journal of Fluid Mechanics*, vol. 932, p. A47, 2022.

[213] J. C. Gibbings, *Dimensional analysis*. Springer Science & Business Media, 2011.

[214] G. Katul, D. Li, and C. Manes, "A primer on turbulence in hydrology and hydraulics: The power of dimensional analysis," *Wiley Interdisciplinary Reviews: Water*, vol. 6, no. 2, p. e1336, 2019.

[215] M. Taherian and A. Mohammadian, "Buoyant jets in cross-flows: review, developments, and applications," *Journal of Marine Science and Engineering*, vol. 9, no. 1, p. 61, 2021.

[216] T. L. Clark, M. A. Jenkins, J. Coen, and D. Packham, "A coupled atmosphere fire model: Convective feedback on fire-line dynamics," *Journal of Applied Meteorology and Climatology*, vol. 35, no. 6, pp. 875–901, 1996.

[217] T. L. Clark, M. A. Jenkins, J. Coen, and D. R. Packham, "A coupled atmosphere-fire model: Role of the convective froude number and dynamic fingering at the fireline," *International Journal of Wildland Fire*, vol. 6, no. 4, pp. 177–190, 1996.

[218] A. L. Sullivan, "Convective froude number and byram's energy criterion of australian experimental grassland fires," *Proceedings of the Combustion Institute*, vol. 31, no. 2, pp. 2557–2564, 2007.

[219] B. GM, "Combustion of forest fuels," *Forest fire: control and use*, pp. 61–89, 1959.

[220] A. Monin and A. Obukhov, "Basic laws of turbulent mixing in the ground surface layer," *Tr. Geophiz. Inst. Akad. Nauk. SSSR*, vol. 151, pp. 163–187, 1954.

[221] K. A. McColl, C. C. van Heerwaarden, G. G. Katul, P. Gentine, and D. Entekhabi, "Role of large eddies in the breakdown of the reynolds analogy in an idealized mildly unstable atmospheric surface layer," *Quarterly Journal of the Royal Meteorological Society*, vol. 143, no. 706, pp. 2182–2197, 2017.

[222] J. A. Businger, J. C. Wyngaard, Y. Izumi, and E. F. Bradley, "Flux-profile relationships in the atmospheric surface layer," *Journal of the Atmospheric Sciences*, vol. 28, no. 2, pp. 181–189, 1971.

[223] A. Dyer, "A review of flux-profile relationships," *Boundary-Layer Meteorology*, vol. 7, pp. 363–372, 1974.

[224] J. C. Kaimal and J. J. Finnigan, *Atmospheric boundary layer flows: their structure and measurement*. Oxford University press, 1994.

Appendix A

Chapter 3

Sensitivity to Averaging Time Scale

In order to describe the sensitivity of the results to the use of different averaging time scales, we utilize data collected at the 20-m measurement height at the West Tower for the heading sub-canopy fire of 2019. There are two parts to the averaging process: obtaining the mean (and fluctuations) from the raw velocity components and then obtaining the turbulent fluxes and turbulent kinetic energy (TKE) budget equation terms. In answer to this question, we present the effect of using different averaging time scales on the turbulent streamwise momentum flux ($\overline{u'w'}$) and the buoyancy production and shear production terms of the TKE budget equation. We present statistical measures and time series of the quantities mentioned above during fire-front passage (FFP) at the West Tower, for four different time-averaging schemes.

The turbulent fluctuations (u_i') can be computed from the measured velocity components (u_i) during FFP as $u_i' = u_i - U_i$. We consider four methods to obtain the mean quantity, i.e. U_i, during FFP: (i) the 30-minute pre-FFP block mean, (ii) the 1-minute moving

Table A.1: Summary of the four "mean-removal" methods along with the mean (μ, m/s), standard deviation (σ, m/s), and skewness coefficient ($\tilde{\mu}_3$) of the histograms of turbulent fluctuations obtained from each method.

Method no.	Removed mean (U_i)	u' statistics	w' statistics
(i)	30-min. pre-FFP block mean	$\mu = 0.775$ $\sigma = 1.112$ $\tilde{\mu}_3 = -0.151$	$\mu = -0.053$ $\sigma = 0.856$ $\tilde{\mu}_3 = 0.799$
(ii)	1-min. moving mean	$\mu = 0.000$ $\sigma = 0.778$ $\tilde{\mu}_3 = -0.218$	$\mu = -0.003$ $\sigma = 0.737$ $\tilde{\mu}_3 = 0.557$
(iii)	10-min. moving mean	$\mu = -0.030$ $\sigma = 1.095$ $\tilde{\mu}_3 = -0.340$	$\mu = -0.003$ $\sigma = 0.847$ $\tilde{\mu}_3 = 0.720$
(iv)	60-min. moving mean	$\mu = 0.251$ $\sigma = 1.093$ $\tilde{\mu}_3 = -0.289$	$\mu = -0.017$ $\sigma = 0.855$ $\tilde{\mu}_3 = 0.795$

mean during FFP, (iii) the 10-minute moving mean during FFP, and (iv) the 60-minute moving mean during FFP. Since this mean is subtracted from the raw velocity component to obtain the turbulent fluctuations, we refer to these methods as "mean-removal" methods. Figures A.1(a) and A.1(b) present histograms for u' and w', respectively, for the four "mean-removal" methods and their corresponding statistics are summarized in Table A.1. Figure A.1(a) shows that the percentage of u' values obtained from method (ii) is higher close to zero as compared to distributions obtained from the other methods. This is also corroborated by the fact that the mean computed from this distribution is closest to zero as compared to the other methods (Table A.1). Furthermore, as seen from Table A.1, the standard deviation (σ) computed for this distribution is the lowest compared to other methods. This indicates that method (ii) underestimates the extreme values of u' induced by the presence of the fire. The higher percentage of u' values close to zero and the underestimation of the extreme values of u', obtained from method (ii) in contrast to other methods,

suggests that a large percentage of the strongest turbulent fluctuations induced by the flame are underestimated if we remove the 1-minute moving mean from the raw u signal to obtain u'. This makes method (ii) a less likely candidate as a suitable averaging scheme. Table A.1 also shows that the standard deviation of u' obtained from methods (i), (iii), and (iv) are similar, suggesting that the corresponding distributions have a similar "spread".

Next, it is seen from Fig. A.1(b) that the w' histograms obtained from methods (i), (iii), and (iv) are similar to a high degree: the corresponding bins have similar relative frequencies and modes occur at similar values of w'. The values of the standard deviation and the skewness coefficient for the w' distributions are also similar to their corresponding statistic across all three methods as seen in Table A.1. Similar to the corresponding histogram for u', a larger percentage of w' values is concentrated around zero in method (ii). This is also reflected in the fact that the mean of this distribution is closest to zero, compared to the other methods. Moreover, both the standard deviation and the skewness coefficient for the w' distribution obtained from method (ii) are lower compared to those obtained from the other methods. Again, this suggests that the strongest vertical fluctuations induced by the fire (extreme values in the w' distribution) are also underestimated when computed using method (ii).

If we compare the mean of the u' distributions (μ) for methods (i), (iii), and (iv), as depicted in Table A.1, we see that method (i) gives the highest mean, method (iv) gives an intermediate value, and method (iii) gives the lowest. As the averaging time scale increases, the moving means approach the block mean, i.e. their time series become "flatter" as seen in Fig. A.2(a). The overall energy contained in the streamwise turbulent fluctuations increases as the time series for the removed mean (U_i) "flattens"; hence, μ for method (i) is greater than μ for method (iv), which in turn is greater than μ for method (iii).

Additionally, we observe from Table A.1 that the distribution for u' is negatively skewed ($\tilde{\mu}_3 < 0$) whereas the distribution for w' is positively skewed ($\tilde{\mu}_3 > 0$) for all four methods. These are representative of the fact that the strongest turbulence events near the canopy top during FFP comprise sweep-like motions, which aligns with inferences drawn in previous studies (91). This dynamic is preserved for all four "mean-removal" methods.

We now consider the time-averaging schemes used to compute the turbulent fluxes (e.g., the overbar operator in $\overline{u'w'}$) and the terms of the TKE budget. These are summarized in Table A.2. Histograms for the values of $\overline{u'w'}$ attained during FFP are shown in Fig. A.1(c). It is seen that the "spread" (standard deviation, σ) of the distribution is highest for Case I (1-minute moving-average scheme along with "mean-removal" method (i)), decreases through Cases II and II, and is lowest for Case IV (60-minute moving-average scheme along with "mean-removal" method (iv)). This suggests that increasing the time-averaging window allows us to converge upon a value for $\overline{u'w'}$ during FFP, which is relatively stable with low uncertainty. A similar observation is made for the TKE buoyancy production term and the TKE shear production term from Figs. A.1(d) and A.1(e), respectively. This observation is also made more clearly from the statistical measures, viz. mean, standard deviation, and skewness, presented in Table A.2. It is noted that while the mean values (μ) computed from the distributions of $\overline{u'w'}$, TKE buoyancy production term, and TKE shear production term are similar in all four cases (I-IV), the uncertainty (as can be estimated from the standard deviations for these three quantities) is least in Case IV.

It is worth mentioning here that the main difference between analyzing quantities obtained from using shorter and longer averaging time scales is that important information pertaining to fire-induced effects is contained in the extreme values (tails of the corresponding distribution) in the former case and in the mean values in the latter. Constructing a vertical

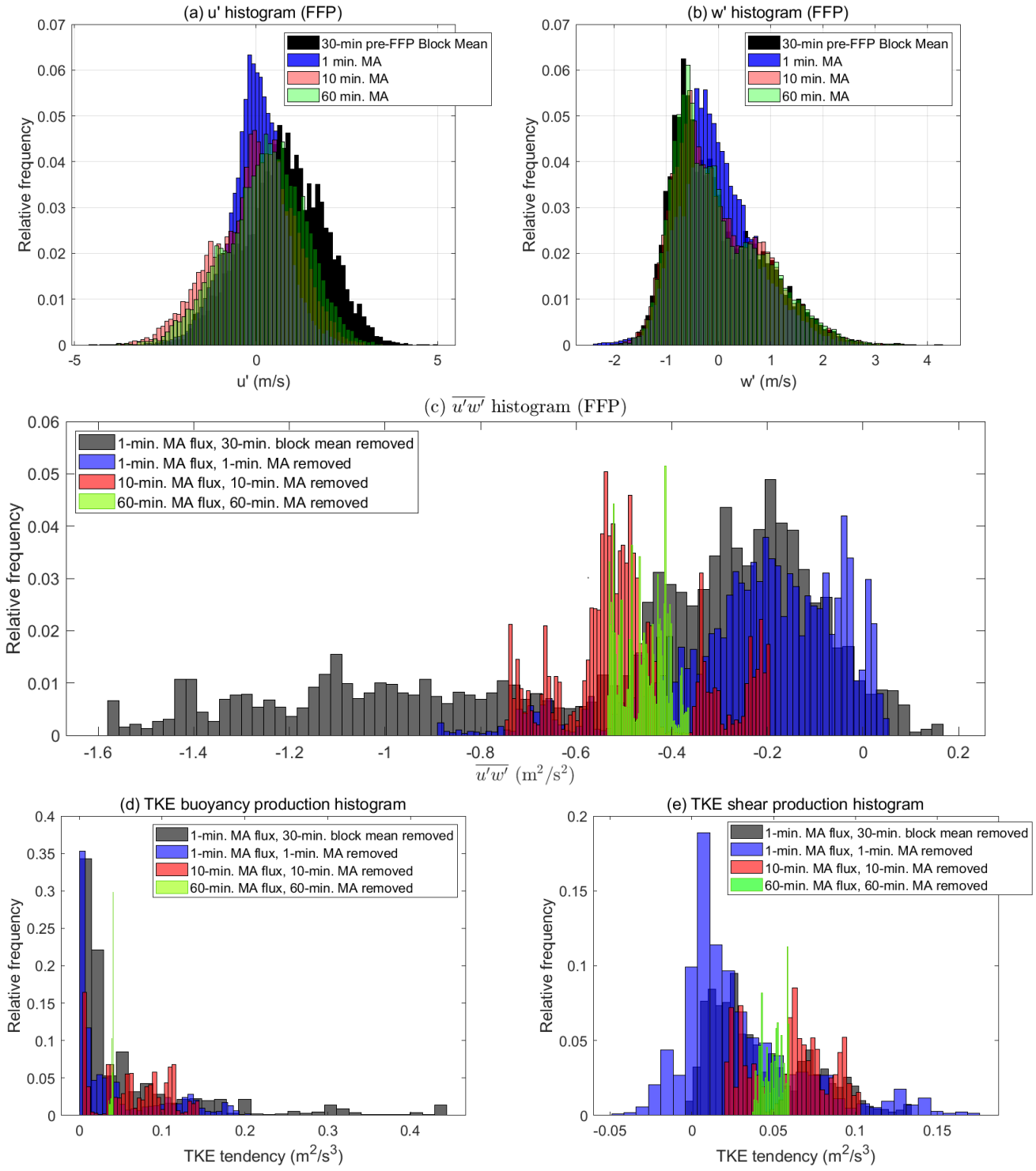


Figure A.1: For $h = 20\,\mathrm{m}$ during FFP at the West Tower of the 2019 heading fire: histograms of (a) u', (b) w', (c) $\overline{u'w'}$, (d) the TKE buoyancy production term, and (e) the TKE shear production term comparing multiple "mean-removal" methods and time-averaging schemes. MA stands for moving average.

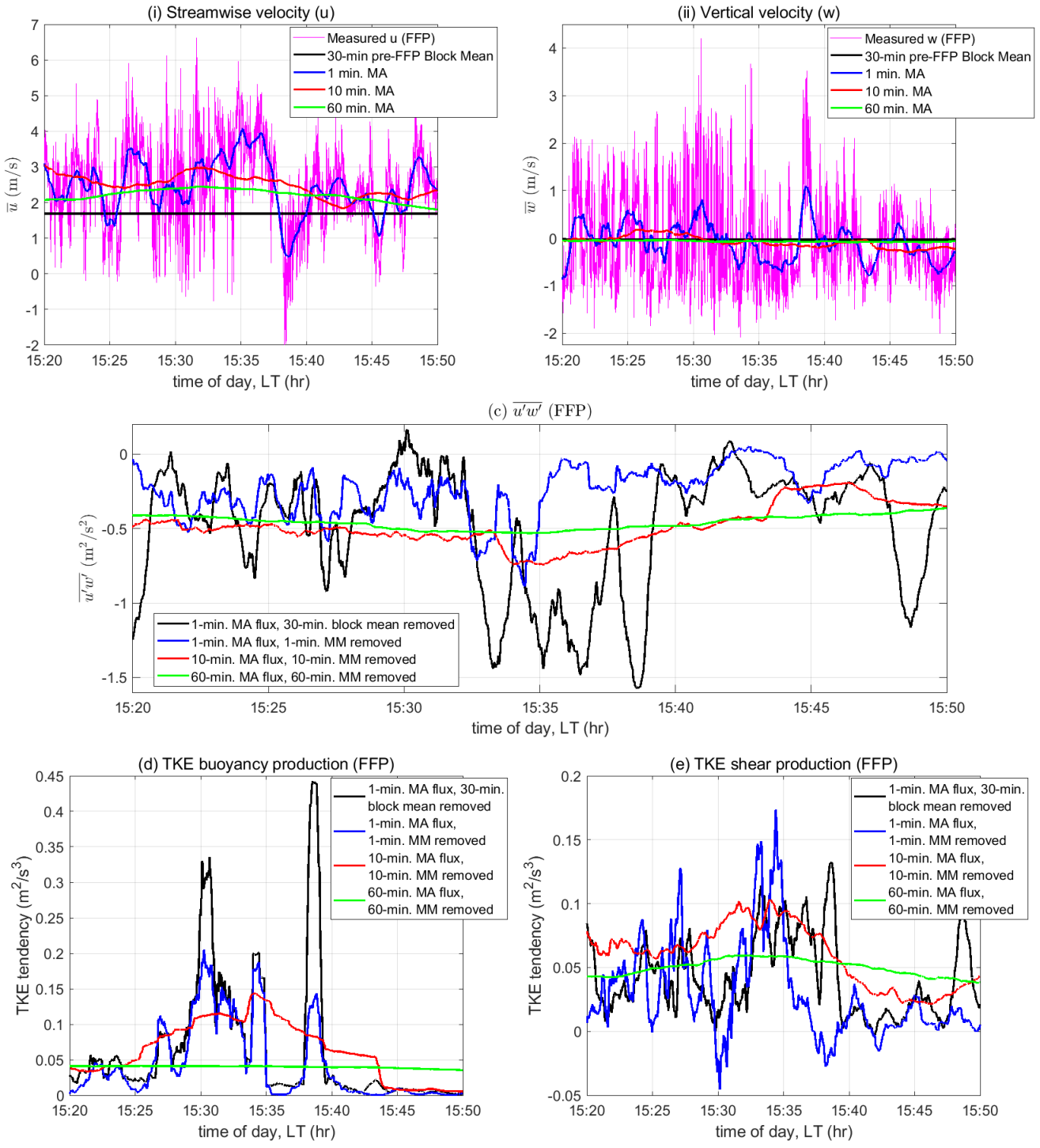


Figure A.2: For $h = 20\,\mathrm{m}$ during FFP at the West Tower of the 2019 heading fire: time series of (a) $\overline{u}$, (b) $\overline{w}$, (c) $\overline{u'w'}$, (d) the TKE buoyancy production term, and (e) the TKE shear production term comparing multiple methods to compute the mean and time-averaging schemes. MA stands for moving average; MM stands for moving mean.

profile for a TKE budget term (or the streamwise turbulent flux) is relatively easier from its mean value as compared to the multitude of extreme values taken from the long tails of its histogram. We, therefore, use longer averaging time scales for our analysis.

We now focus on plots of the time series, for these three quantities, presented in Fig. A.2. If we think of the mean velocity (U_i) as the "slowly-varying" component of the measured velocity, Case (ii) (1-minute moving mean) performs well in capturing such a "slowly-varying" component as seen from Figs. A.2(a)-(b). However, Fig. A.2(c) demonstrates that there is considerable variability in $\overline{u'w'}$ in Cases I and II (1-minute moving average along with "mean-removal" methods (i) and (ii), respectively), which is also reflected in the histograms for these cases (Fig. A.1(c)). Contrarily, Cases III and IV show a $\overline{u'w'}$ time series that has relatively approached a "plateau" during FFP, reducing the uncertainty in the estimation of $\overline{u'w'}$. Another point to note is that the $\overline{u'w'}$ time series is relatively smoother in Cases III and IV as compared to Cases I and II, in which there are noticeable "wiggles" in the series. Similar inferences can be drawn from the time series for the TKE buoyancy production and shear production terms (Figs. A.2(d)-(e)).

In our manuscript, we have taken to Case IV: the 60-minute moving mean to separate the mean from the fluctuations for the velocity components and then the 60-minute moving average to obtain the fluxes and TKE budget terms, for consistency. In other words, the meaning of the overbar in $u_i' = u_i - \overline{u}_i$ and in $\overline{u'w'}$, etc., remains the same. Furthermore, we have used a 60-minute time-averaging window to compute a "slowly-varying" component of the measured velocity (and temperature), in the hope that it would be devoid of fire-induced effects. This would have enabled us to treat the 60-minute moving mean ($\overline{u}_i$) as the larger-scale atmospheric flow upon which the fire-induced fluctuations "rode". However, it is seen from the mean kinetic energy (MKE) budget equation terms that the fire noticeably

Table A.2: Summary of the histogram statistics for four different averaging schemes used to compute $\overline{u'w'}$ (μ and σ in m^2/s^2) and terms of the TKE budget equation (μ and σ in m^2/s^3).

Case no.	Time-averaging scheme	Removed mean	$\overline{u'w'}$ statistics	TKE buoyancy prod. statistics	TKE shear prod. statistics
I	1-min. MA	30-min. pre-FFP block mean	$\mu = -0.488$ $\sigma = 0.411$ $\tilde{\mu}_3 = -0.926$	$\mu = 0.064$ $\sigma = 0.090$ $\tilde{\mu}_3 = 2.309$	$\mu = 0.042$ $\sigma = 0.031$ $\tilde{\mu}_3 = 0.770$
II	1-min. MA	1-min. moving mean	$\mu = -0.229$ $\sigma = 0.180$ $\tilde{\mu}_3 = -0.952$	$\mu = 0.044$ $\sigma = 0.054$ $\tilde{\mu}_3 = 1.248$	$\mu = 0.030$ $\sigma = 0.037$ $\tilde{\mu}_3 = 1.318$
III	10-min. MA	10-min. moving mean	$\mu = -0.484$ $\sigma = 0.135$ $\tilde{\mu}_3 = -0.409$	$\mu = 0.064$ $\sigma = 0.040$ $\tilde{\mu}_3 = 0.039$	$\mu = 0.060$ $\sigma = 0.024$ $\tilde{\mu}_3 = -0.108$
IV	60-min. MA	60-min. moving mean	$\mu = -0.460$ $\sigma = 0.046$ $\tilde{\mu}_3 = 0.178$	$\mu = 0.040$ $\sigma = 0.002$ $\tilde{\mu}_3 = -1.292$	$\mu = 0.050$ $\sigma = 0.006$ $\tilde{\mu}_3 = -0.110$

affects the mean flow (especially the MKE buoyancy production term) even if we use a time window as conservative as 60 minutes. This is the advantage of the 60-minute moving mean over using the pre-FFP mean: we are able to see how the FFP affects the larger scales after putting in our best efforts at separating the fire-induced turbulent effects.

Appendix B

Chapter 4

Wavelet Spectra and Co-spectra

In this section, we briefly comment on the appropriateness of the range of frequencies selected to obtain the reconstructed temperature signal within which the coherent ramp–cliff structures are tracked. This is done by analyzing the wavelet-based temperature spectra and the co-spectrum of w and T, on one hand, and that of u and w, on the other. Furthermore, we comment on the choice of the scale associated with the wavelet coefficients used to track ramp–cliff patterns (a_0).

The wavelet spectral energy density (E) as a function of scale (a) can be written using the following formula (131):

$$E(a) = \frac{1}{C_g} \int_{-\infty}^{\infty} |W(a,b)|^2 \mathrm{d}b \tag{B.1}$$

It follows that the spectral energy density can also be represented as a function of frequency (f), i.e. as $E(f)$; the spectral energy density pre-multiplied by the frequency, i.e. $fE(f)$, represents the pre-multiplied energy spectrum.

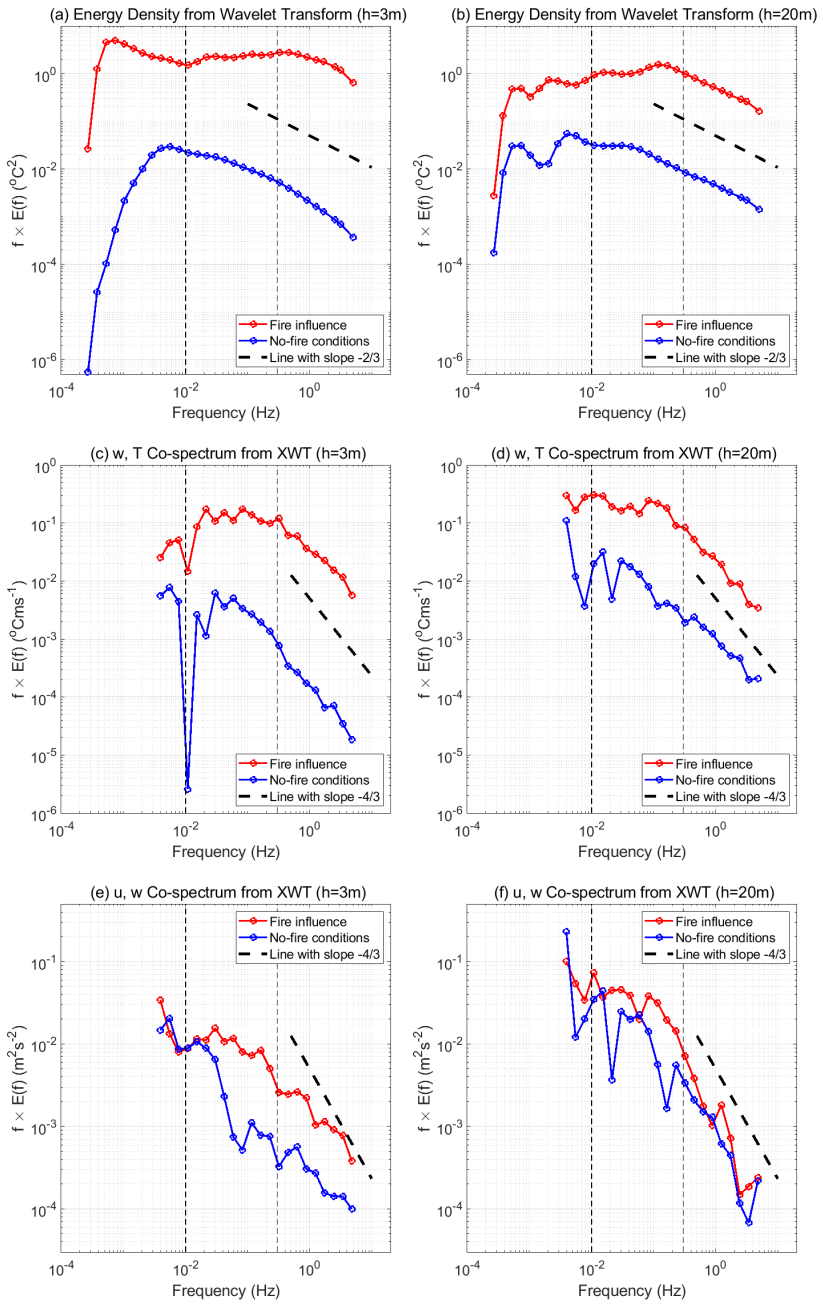


Figure B.1: Wavelet-based pre-multiplied energy spectra and co-spectra for the 30-minute period of 1520–1550 LT (5 min. pre-FFP, 20 min. during FFP, and 5 min. post-FF) at the West Tower (red) and Control Tower (blue). Pre-multiplied energy spectra (of T) at $h =$ (a) 3 m and (b) 20 m; w-T co-spectra at $h =$ (c) 3 m and (d) 20 m; u-w co-spectra at $h =$ (e) 3 m and (f) 20 m. Slanted thick black dashed lines have slope $-2/3$ in (a)–(b) and slope $-4/3$ in (c)–(f); vertical black dashed lines delineate the mid-to-high frequency band within which ramp–cliff structures are tracked

Figures B.1(a)–(b) depict the (pre-multiplied) energy spectra of the measured temperature obtained from the wavelet coefficients computed for the duration 1520–1550 LT (comprising 5 minutes pre-FFP, 20 minutes of the stipulated FFP time, and 5 minutes post-FFP at the West Tower) at both, the West and Control Towers. The range of frequencies, used to compute the reconstructed temperature signal to track ramp–cliff structures, is delineated using dashed black vertical lines. It is observed that the spectral energy associated with the West Tower is higher compared to that for the Control Tower, at both heights. This is attributed to the higher variability in the measured temperature during FFP as compared to the measured ambient temperature at both heights. Furthermore, the influence of the fire being stronger near the surface due to higher proximity, the spectral energy is relatively higher at $h = 3\,\mathrm{m}$ compared to at $h = 20\,\mathrm{m}$, at the West Tower.

We first focus on the peak frequencies for both towers at $h = 3\,\mathrm{m}$ (Fig. B.1(a)). At the West Tower, it is seen that the peak frequency (f_p) is approximately $6 \times 10^{-4}\,\mathrm{Hz}$, while $f_\mathrm{p} \approx 5 \times 10^{-3}\,\mathrm{Hz}$ at the Control Tower. The shift of f_p from a higher value in no-fire conditions to a lower value during FFP suggests that the most energetic turbulent eddies induced by the presence of the fire are associated with relatively lower frequencies (or longer time scales) compared to those affiliated with the background canopy turbulence near the surface. Moreover, a few additional peaks are observed within the range 10^{-2}–$0.3\,\mathrm{Hz}$, at the West Tower.

We now focus on the peak frequencies of the temperature spectra at $h = 20\,\mathrm{m}$ (Fig. B.1(b)). At both towers, it is seen that $f_\mathrm{p} \approx 5 \times 10^{-4}\,\mathrm{Hz}$. Furthermore, a secondary peak is seen at $f \approx 2 \times 10^{-3}\,\mathrm{Hz}$ at the West Tower, while a secondary peak is seen at $f \approx 4 \times 10^{-3}\,\mathrm{Hz}$, at the Control Tower. Again, a few additional peaks are observed within the range 10^{-2}–$0.3\,\mathrm{Hz}$, at the West Tower.

At the West Tower, the peak frequencies reported above can be used to compute peak time scales (t_p). Peak time scales are within the range 1600–2000 s for both T_3 and T_{20}, while

the secondary peak for T_{20} corresponds to 500 s. Each of these peak time scales is much longer compared to the durations of approximately 1–2 minutes that are typically associated with ramp–cliff structures in no-fire conditions (1). Since ramp–cliff structures are expected to have even shorter durations in the presence of a fire, we reconstruct the temperature signals using a range of periods (3 s–90 s) that encompass the additional peaks in the energy spectra of the temperature at the two heights, at the West Tower. These periods being much shorter than the peak time scales obtained from the energy spectra, it is difficult to use the wavelet coefficients at periods corresponding to $t_{\rm p}$ for the purpose of quantifying the durations and slopes of the ramp structures within the reconstructed temperature signal as described in Chapter 4. Therefore, in our analysis, we have chosen a_0 so that the wavelet coefficients associated with this scale are able to track the pattern of the coherent ramp–cliff structures from the local minima and zero-crossings as accurately as possible, as verified from a visual inspection ($a_0 \equiv 23.3$ s or $f_0 \approx 10/233$ Hz). Since this introduces some uncertainty in the estimates of the ramp durations and slopes, we conduct an analysis that explores the sensitivity of these quantities to different values of a_0 in the next section.

We now focus on the wavelet co-spectra. The wavelet co-spectrum between two time series $p(t)$ and $q(t)$ is computed from the cross-wavelet transform using the following formula:

$$E(a) = \frac{1}{C_g} \int_{-\infty}^{\infty} \Re \left[W_{pq}(a,b) \right] \mathrm{d}b \tag{B.2}$$

Figures B.1(c)–(f) depict the wavelet co-spectra computed for the duration 1520–1550 LT at both, the West and Control Towers. Figures B.1(c)–(d) represent the wavelet co-spectra of w and T, pre-multiplied with f, at h =3 m and 20 m, respectively. It is observed that the range of frequencies within which we track fire-modulated ramp–cliff structures in the (reconstructed) temperature signal encompasses the peak frequencies associated with the "energetic" heat fluxes under the influence of the fire (at the West Tower), prior to the onset of the inertial subrange. We then analyze momentum fluxes in the same range of frequencies

(delineated in Figs. B.1(e)–(f)) for consistency. Therefore, it is suitable to track the coherent ramp–cliff structures and explore their connection to the turbulent fluxes in the presence of a fire within this range of frequencies (10^{-2}–0.33 Hz).

Sensitivity Analysis of Ramp Durations and Slopes

The statistics of ramp durations and slopes for three different scale parameters (or frequencies) are analyzed here. Of these, we refer to the case for a_0 corresponding to $f_0 \approx 10/233$ Hz as Case (i), which serves as our reference case. The statistics corresponding to Case (i) are documented in Sect. 4.4.2 and are not repeated here. Cases (ii) and (iii) are summarized in Table B.1.

Table B.1: A summary of the time scales and frequencies used in the sensitivity analysis

Case no.	Scale parameter	Time scale (period)	Frequency (f_0)
(i)	$a_0^{(\mathrm{i})}$	23.3 s	10/233 Hz
(ii)	$a_0^{(\mathrm{ii})}$	16.6 s	10/166 Hz
(iii)	$a_0^{(\mathrm{iii})}$	32.7 s	10/327 Hz

Here, $a_0^{(\mathrm{ii})} < a_0^{(\mathrm{i})} < a_0^{(\mathrm{iii})}$. Figure B.2 depicts the reconstructed temperature signal at the West Tower for $h = 20$ m along with the time series of the wavelet coefficients ($W_T(a_0, b)$), for the three cases discussed in Table B.1, within a short time window. Dashed vertical lines indicate the locations of local minima and zero-crossings with negative slopes in $W_T(a_0, b)$ for each case. Two consecutive dashed vertical lines of the same colour delineate individual ramp-like structures as detected by the algorithm. It can be seen that in Case (ii), the algorithm is more likely to detect short-scale temperature increments and declines, which constitute coherent ramp–cliff structures, as individual ramp–cliff structures in themselves. On the contrary, in Case (iii), the relatively shorter-scale temperature increments and declines that characterize the shorter-scale coherent events during FFP are overlooked by the algorithm in favor of relatively longer-scale changes in temperature. The effects of the differences in

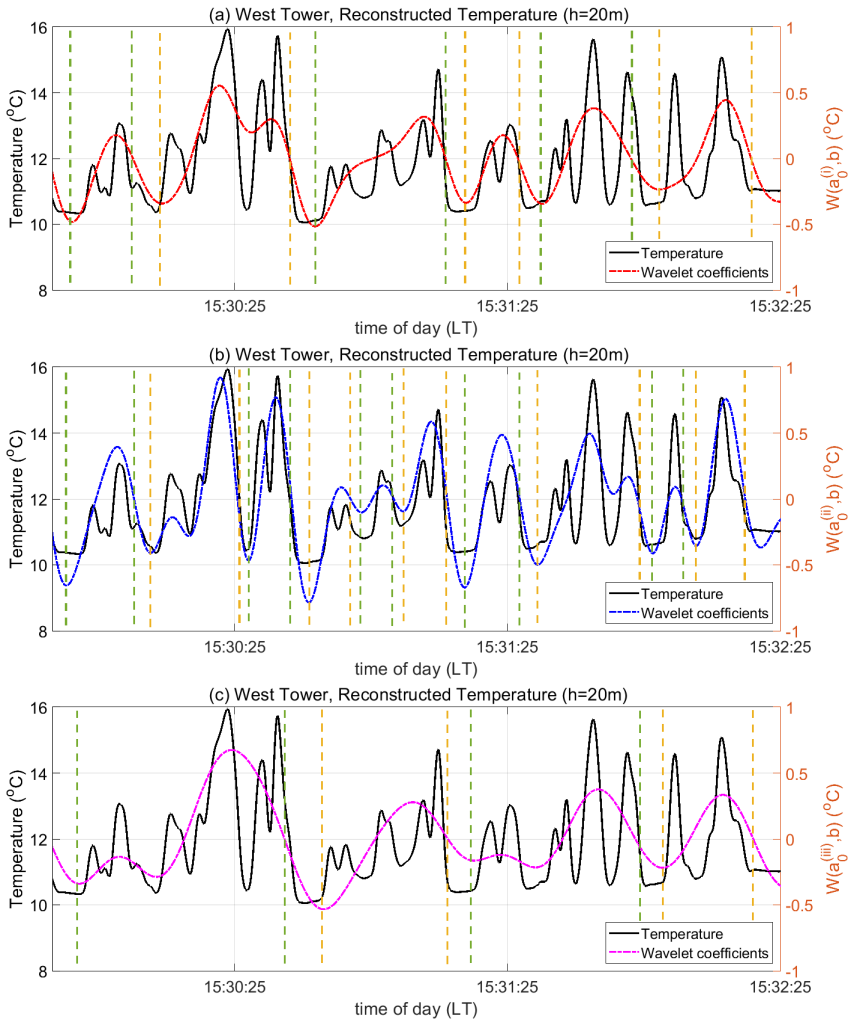


Figure B.2: Reconstructed temperature signal at $h = 20\,\text{m}$ in the mid-to-high frequency band (scales ranging from 3 s to 90 s) at the West Tower (where fire influence is experienced) along with the wavelet coefficients ($W_T(a_0, b)$) for (a) Case (i), (b) Case (ii), and (c) Case (iii). Dashed and dash-dotted vertical lines enclose examples of ramp-like structures: two consecutive vertical lines with the same colour and style enclose one such observed structure

ramp detection on the statistics of the ramp durations and slopes in each case are presented below.

Case (ii)

Figure B.3 depicts the histograms and empirical cumulative distribution functions (eCDFs) for Case (ii), while the associated summary statistics are shown in Table B.2. The modal

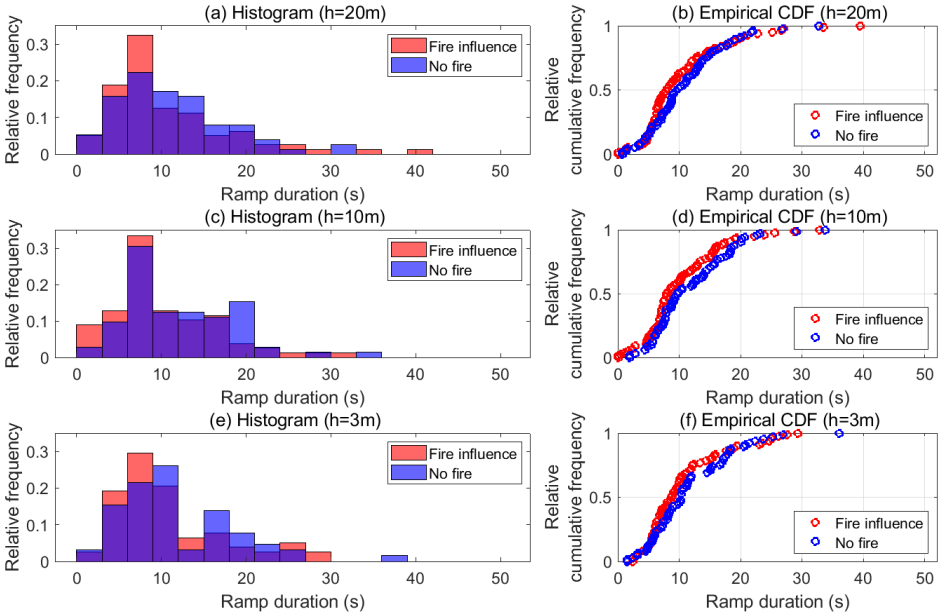


Figure B.3: Histograms and empirical cumulative distribution functions of ramp durations associated with both, fire influence and no-fire conditions at all three measurement heights for Case (ii) ($a_0^{(\mathrm{ii})} \equiv f_0 \approx 10/166\,\mathrm{Hz}$)

durations (as seen from the histograms in Fig. B.3) for fire-modulated ramps are shorter than 10 s at all heights. At all three heights, the percentage of both fire-modulated and no-fire ramps with durations not exceeding 10 s is higher compared to that in Case (i), as observed from the eCDFs. The modes of the histograms at $h = 10\,\mathrm{m}$, 20 m are shifted to the left compared to the histograms for Case (i), in both the presence of the fire and no-fire conditions. At $h = 3\,\mathrm{m}$, 20 m, the mean durations for fire-modulated ramps are approximately 3 s shorter compared to those in Case (i), while the mean durations for no-fire ramps are approximately 6 s shorter than those in Case (i), as seen from Table B.2. This difference is explained as follows. The caveat of using shorter-scale ($a_0^{(\mathrm{ii})}$) wavelet coefficients in Case (ii) is that shorter-scale temperature increments and declines, which "ride" (or constitute) the relatively longer-scale coherent ramp–cliff structures, are counted by the algorithm as individual ramp–cliff structures. This results in an underestimation of ramp durations compared to those obtained using relatively longer-scale wavelet coefficients in Case (i) (i.e. $W_T(a_0^{(\mathrm{i})}, b)$). This further explains why the median ramp durations as seen

from the eCDFs (Fig. B.3) are lower for both the fire-modulated and no-fire ramps at all heights in comparison with the median ramp durations for Case (i).

It would seem that the statistics for the ramp durations in Case (ii) provide some evidence to support our hypothesis that fire-modulated (West Tower) ramp durations are shorter compared to no-fire (Control Tower) ramps. At all three heights, the mean durations for fire-modulated ramps are shorter compared to those for no-fire conditions (Table B.2). While the histogram modes for fire-modulated and no-fire ramps appear to coincide near the canopy top and at the mid-canopy height (Fig. B.3), the most probable durations for fire-modulated ramps are shorter than those for no-fire ramps near the flame, i.e. at $h = 3\,\mathrm{m}$. The eCDFs show that there is a higher percentage of ramps with durations shorter than 10 s under fire influence in comparison with no-fire conditions at all three heights. The median fire-modulated ramp duration (where the relative cumulative frequency is 0.5) is shorter compared to the median no-fire ramp duration at all heights. While it appears that the durations of fire-modulated ramps are shorter than those of no-fire ramps, the difference is not as pronounced as in Case (i).

Table B.2: Height-wise summary statistics of fire-modulated ramps and ramps in no-fire conditions for Case (ii) ($a_0^{(\mathrm{ii})} \equiv f_0 \approx 10/166\,\mathrm{Hz}$). Modes are obtained directly from the data (not from the histograms)

	Fire-modulated ramps					No-fire ramps				
Height (h)	No. sampled	Mean duration (s)	Modal duration (s)	95$^{\mathrm{th}}$ percentile duration (s)	Mean slope ($^{\mathrm{o}}$C min.$^{-1}$)	No. sampled	Mean duration (s)	Modal duration (s)	95$^{\mathrm{th}}$ percentile duration (s)	Mean slope ($^{\mathrm{o}}$C min.$^{-1}$)
20 m	80	10.5	6.3	26.0	22.5	76	11.3	4.3	21.9	1.4
10 m	78	10.3	6.8	23.2	28.6	72	12.0	6.0	22.5	1.1
3 m	78	10.6	5.5	25.0	37.4	65	11.8	10.4	24.1	1.0

Next, Fig. B.4 shows the histograms and eCDFs of ramp slopes computed at all three heights. As seen from the eCDFs, the percentage of fire-modulated ramps exceeding $50\,^{\mathrm{o}}\mathrm{C\,min.}^{-1}$ is

higher for Case (ii) as compared to Case (i). This happens because the algorithm computes the slope of the shorter-scale temperature increments mentioned above instead of the slope of a more coherent ramp structure. Moreover, shorter-scale temperature increments are associated with shorter durations. Ramp slopes, therefore, have a tendency to be relatively overestimated. This is also reflected in the mean fire-modulated ramp slopes at all heights (Table B.2), which are overestimated compared to mean fire-modulated ramp slopes in Case (i). Ramp slopes in no-fire conditions are also slightly overestimated in comparison with those in Case (i). Nevertheless, in Case (ii), the mean fire-modulated ramp slope is an order of magnitude higher than the mean slope of a ramp in no-fire conditions (Table B.2), which is an inference similar to that obtained in Case (i).

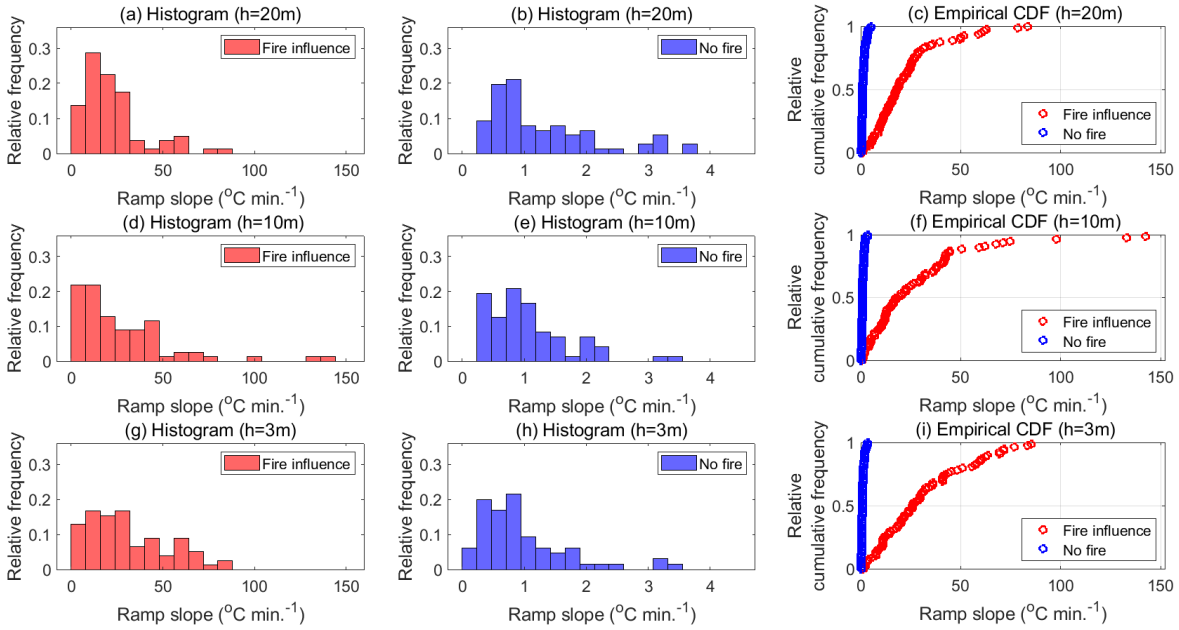


Figure B.4: Histograms of ramp slopes associated with both, fire influence and no-fire conditions, at all three measurement heights, along with the corresponding empirical cumulative distribution functions for Case (ii) ($a_0^{(\mathrm{ii})} \equiv f_0 \approx 10/166\,\mathrm{Hz}$)

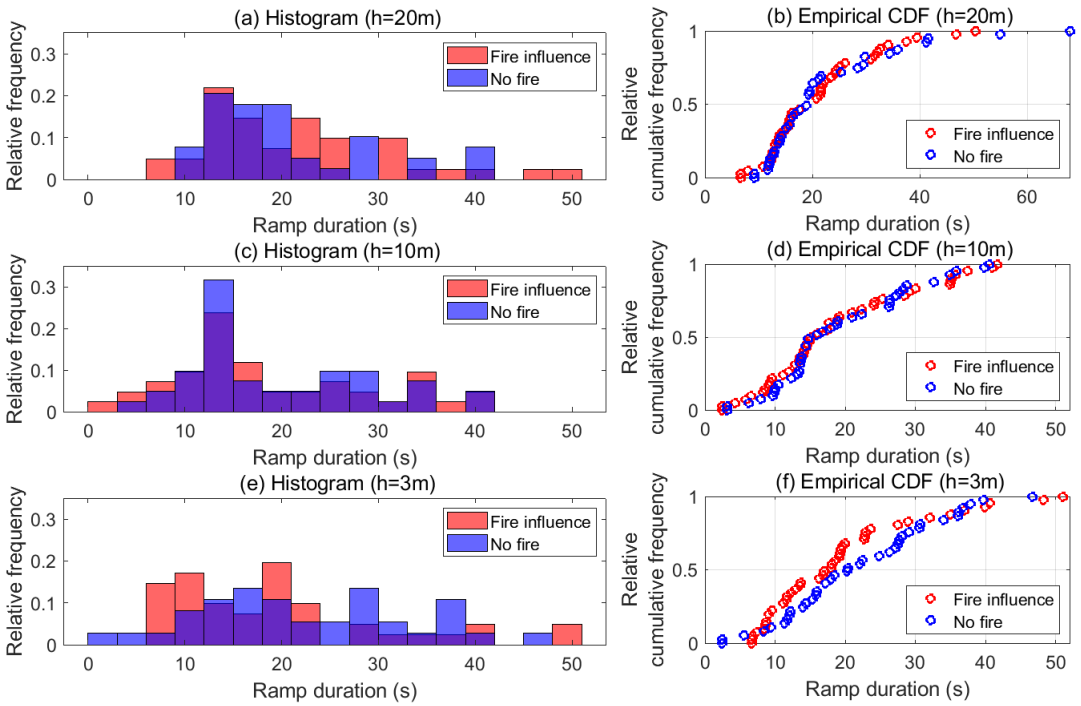


Figure B.5: Histograms and empirical cumulative distribution functions of ramp durations associated with both, fire influence and no-fire conditions at all three measurement heights for Case (iii) ($a_0^{(\mathrm{iii})} \equiv f_0 \approx 10/327\,\mathrm{Hz}$)

Case (iii)

Figure B.5 depicts the histograms and eCDFs of ramp durations at all three heights for Case (iii), while Table B.3 provides some of the associated summary statistics. It can be seen that the modes of these histograms are shifted to the right compared to histograms for Case (i). The most probable durations for fire-modulated ramps, as seen from the histograms, are longer than 10 s (and longer compared to that for Case (i)) at all heights. As seen from Table B.3, the mean durations for fire-modulated ramps are overestimated (longer) compared to those in Case (i). This difference is more palpable at $h = 3\,\mathrm{m}$ (approximately 6 s) and at $h = 20\,\mathrm{m}$ (approximately 7.5 s). Similarly, the mean durations for no-fire ramps are also overestimated compared to those in Case (i) at $h = 3\,\mathrm{m}$ and $20\,\mathrm{m}$ by approximately 5 s. This difference is explained as follows. The issue in using longer-scale wavelet coefficients

($W_T(a_0^{(\mathrm{iii})}, b)$), as in this case, is the opposite of that discussed in Case (ii) above: relatively shorter-scale ramp–cliff structures are overlooked by the algorithm. Consecutive coherent ramp–cliff structures are together counted as one structure resulting in an overestimation of the average duration of a ramp in both fire and no-fire conditions. This further explains why the median ramp durations as seen from the eCDFs (Fig. B.5) for both fire-modulated and no-fire ramps are longer than those observed for Case (i).

Table B.3: Height-wise summary statistics of fire-modulated ramps and ramps in no-fire conditions for Case (iii) ($a_0^{(\mathrm{iii})} \equiv f_0 \approx 10/327\,\mathrm{Hz}$). Modes are obtained directly from the data (not from the histograms)

	Fire-modulated ramps					No-fire ramps				
Height (h)	No. sampled	Mean duration (s)	Modal duration (s)	95$^{\mathrm{th}}$ percentile duration (s)	Mean slope ($^{\mathrm{o}}$C min.$^{-1}$)	No. sampled	Mean duration (s)	Modal duration (s)	95$^{\mathrm{th}}$ percentile duration (s)	Mean slope ($^{\mathrm{o}}$C min.$^{-1}$)
20 m	41	21.5	20.8	42.8	11.7	39	22.9	19.4	48.9	0.9
10 m	42	19.0	12.8	38.8	20.7	41	19.6	14.3	37.6	0.9
3 m	41	19.7	9.1	44.1	23.2	37	22.3	17.2	39.1	0.7

We now compare the statistics of the fire-modulated and no-fire ramp durations for Case (iii). The percentage of fire-modulated ramps with durations shorter than 20 s is higher than that of ramps in no-fire conditions at $h = 3$ m, i.e. near the flame (as seen from the eCDFs in Fig. B.5). Moreover, the median fire-modulated ramp duration is noticeably shorter compared to the median ramp duration in no-fire conditions, at this height. Similar to Case (i), the mean fire-modulated ramp duration is higher than the mean ramp duration in no-fire conditions at $h = 3$ m and 20 m (Table B.3). The difference, however, is less than 1.5 s and not as pronounced as in Case (i). Furthermore, the eCDFs for fire and no-fire conditions at higher heights, i.e. at $h = 20$ m and $h = 10$ m (Figs. B.5(b) and B.5(d)), overlap with each other to a considerable extent, such that the median ramp durations appear to be similar at each of those heights. The explanation for this is similar to that provided in the previous paragraph. Ramp–cliff structures are closely related to the updraft-downdraft events that occur near the

canopy top. Longer-scale wavelet coefficients ($W(a_0^{(\mathrm{iii})}, b)$) are unable to capture the effects of the more frequent, characteristic shorter-scale updraft–downdraft events that occur near the canopy top as a consequence of fire-front-passage (FFP). This results in the statistics of the fire-modulated ramp durations being very similar to those of the ambient, no-fire ramp durations.

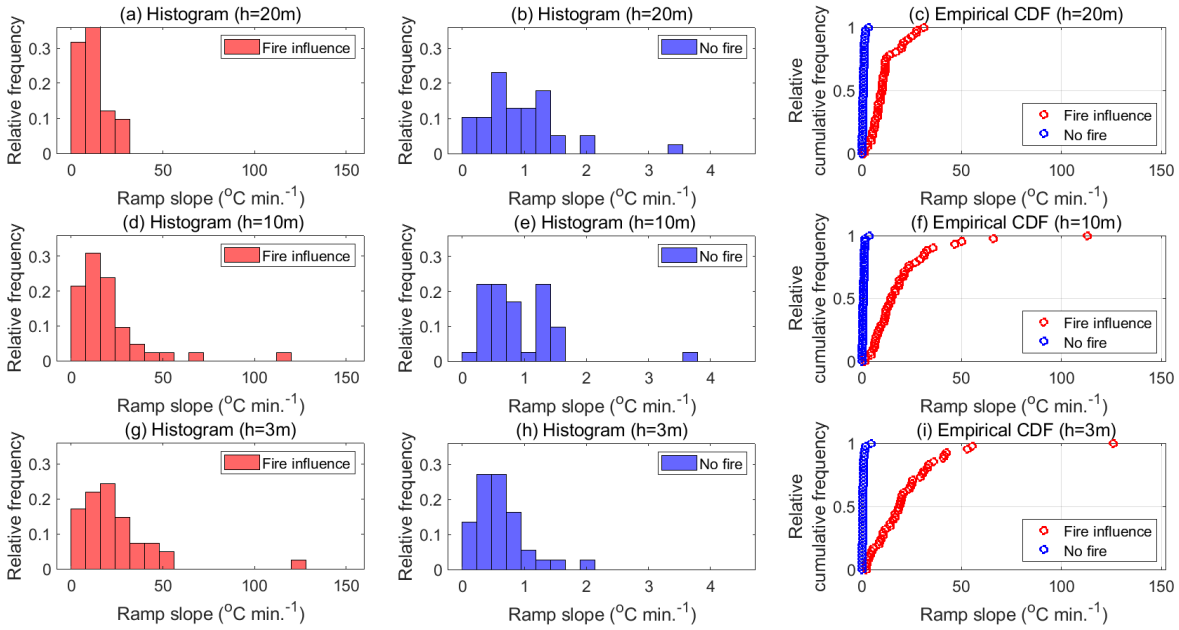


Figure B.6: Histograms of ramp slopes associated with both, fire influence and no-fire conditions, at all three measurement heights, along with the corresponding empirical cumulative distribution functions for Case (iii) ($a_0^{(\mathrm{iii})} \equiv f_0 \approx 10/327\,\mathrm{Hz}$)

Next, Fig. B.6 shows the histograms and eCDFs of ramp slopes computed at all three heights for Case (iii). It appears from the eCDF at $h = 3\,\mathrm{m}$ (Fig. B.6(i)) that the percentage of fire-modulated ramp slopes above $50\,^{\circ}\mathrm{C\,min.}^{-1}$ is lower compared to that in Case (i). As seen from Table B.3, both mean fire-modulated and no-fire ramp slopes are underestimated compared to those computed in Case (i). At $h = 10\,\mathrm{m}$, mean ramp slopes in both categories are underestimated by approximately 10%. Mean fire-modulated ramp slopes are underestimated by approximately 26% and mean no-fire ramp slopes by 18% at $h = 20\,\mathrm{m}$. Again, this is because the algorithm utilizes the temperature differences over longer time durations to compute the slope, while omitting the relatively shorter-scale increments that characterize

fire-modulated ramps. However, the mean fire-modulated ramp slope is an order of magnitude higher than that in no-fire conditions (Table B.3), which is an inference similar to that obtained in Case (i).

It appears that the choice of the scale parameter (or frequency) associated with the wavelet coefficients used to detect ramp-like structures influences the average ramp durations computed at all three heights. This appears to hold true for both fire-modulated as well as ambient (no-fire) ramps. In all the cases considered here, the mean duration is consistently found to be shorter for fire-modulated ramps as compared to ambient (no-fire) ramps both near the canopy top and near the flame. The difference, however, is most pronounced when wavelet coefficients corresponding to Case (i) are used. For instance, the mean fire-modulated ramp durations at $h = 3\,\mathrm{m}$ are shorter than ambient (no-fire) ramp durations by approximately 10% in Case (ii) and 12% in Case (iii). However, this difference corresponds to approximately 22% in Case (i). This is because longer-scale wavelet coefficients (Case (iii)) are unable to capture the shorter-scale updraft downdraft events that characterize the ramp–cliff structures modulated by the fire presence; on the other hand, shorter-scale wavelet coefficients (Case (ii)) detect (often erroneously) less coherent shorter-scale events as coherent ramp-like structures in both ambient conditions as well as in the presence of a fire. A more rigorous method may be needed for selecting a suitable scale parameter for analyzing ramp-like structures. Across all three cases, however, it must be noted that mean fire-modulated ramp slopes are higher by an order of magnitude than mean ambient (no-fire) ramp slopes. In all three cases, the ratio of the mean fire-modulated ramp slope to the mean ambient ramp slope is consistently above 30 at $h = 3\,\mathrm{m}$ and ranges from 13 to 17 at $h = 20\,\mathrm{m}$. Thus, while we need to be careful in selecting the appropriate scale for the wavelet coefficients being used to detect ramp-like structures in the temperature signal, the method shows considerable promise in estimating the important mean statistics that encapsulate the changes occurring in ramp–cliff structures (coherent motions beneath the canopy) due to the presence of the fire at the forest surface and the buoyant plume at the higher heights.

Estimating Sensible Heat Fluxes from Ramps

In this section, we demonstrate the applicability of ramp–cliff patterns observed in measured temperature signals to compute sensible heat fluxes in the presence of a fire, by invoking the surface renewal method (e.g., (112; 113; 114)). Sensible heat fluxes can be computed using the following formula (1):

$$H = \rho c_{\mathrm{p}} \frac{\mathrm{d}T}{\mathrm{d}t} \frac{V}{A}. \tag{B.3}$$

Here, $\mathrm{d}T/\mathrm{d}t$ is the time rate of temperature change from a Lagrangian perspective, c_{p} is the specific heat capacity of air (approximately $1004\,\mathrm{J\,kg^{-1}K^{-1}}$), V is the air-parcel volume (associated with the ramp) and A is the ground area. Furthermore, $\mathrm{d}T/\mathrm{d}t$ is given by (1):

$$\frac{\mathrm{d}T}{\mathrm{d}t} = \frac{\partial T}{\partial t} + u_i \frac{\partial T}{\partial x_i} = \frac{\partial T}{\partial t} + \frac{\partial u_i T}{\partial x_i} \approx \frac{\partial T}{\partial t}. \tag{B.4}$$

Here, the latter approximation is typically justified in no-fire conditions by arguing that the interaction between u_i and T is manifested at higher frequencies compared to those at which coherent structures (such as ramps) are observed in the temperature signal (T) (1; 114; 112). In the presence of a fire, however, it is difficult to ignore the advection term ($\partial(u_i T)/\partial x_i$) since gradients in $u_i T$ are expected to be stronger. For instance, $\partial(u_i T)/\partial x$ is expected to be substantial across the flame due to the fire-induced acceleration of the local wind (102). It is reasonable to assume that the contribution of both components of the Lagrangian derivative ($\mathrm{d}T/\mathrm{d}t$), i.e. the local time derivative ($\partial T/\partial t$) and the advection term, to the sensible heat fluxes, is significant. However, the absence of data collection in the horizontal direction in this experiment hinders the computation of some of these partial derivatives ($\partial/\partial x$ and $\partial/\partial y$ terms). Moreover, data collection may be needed at additional heights to quantify vertical derivatives ($\partial/\partial z$ terms) more accurately as well, at each height. Therefore, we focus on estimating the contribution due to local changes in temperature, at this stage.

The contribution to the sensible heat flux due to local changes in the temperature (H_{ramp}) can be estimated from the ramp slope ($\partial T/\partial t$) in the presence of a fire using the following formula:

$$H_{\mathrm{ramp}} = \rho c_{\mathrm{p}} \frac{\partial T}{\partial t} \frac{V}{A}. \tag{B.5}$$

Typically, it is assumed that V/A is proportional to the canopy height h_{c}, i.e. $V/A = \alpha h_{\mathrm{c}}$, where α is a scalar constant (114). The strongest turbulent eddies resulting in the steepest ramp–cliff patterns impacted by the fire (flame or plume) can be assumed to influence almost the entire canopy along the vertical axis, based on the warmest temperature isotherms shown in Fig. 9 of the main text. Therefore, it is reasonable to assume $\alpha = 1$, i.e. $V/A \approx h_{\mathrm{c}}$, at all heights within the canopy. Setting $\partial T/\partial t$ to the value of the mean ramp slope at each height, we obtain values for H_{ramp} as shown in Table B.4. In the presence of a fire, it can be observed that H_{ramp} is highest near the surface and decreases with height due to decreasing proximity with the heat source (the flame) with height. Contrarily, in the absence of a fire, H_{ramp} increases with height since the influx of ambient heat from the atmospheric surface layer aloft (and through incoming solar radiation) is highest near the canopy top.

Table B.4: Height-wise summary of sensible heat fluxes derived from fire-modulated ramps and ramps in no-fire conditions.

	Fire-modulated ramps			No-fire ramps		
Height (h)	Mean slope (°C min.$^{-1}$)	H_{ramp} (W m^{-2})	H_{turb} (W m^{-2})	Mean slope (°C min.$^{-1}$)	H_{ramp} (W m^{-2})	H_{turb} (W m^{-2})
20 m	15.8	5298	4869	1.1	369	289
10 m	18.8	6304	7135	1.0	335	185
3 m	27.2	9121	8476	0.8	268	51

For comparison, we have tabulated the turbulent sensible heat fluxes (H_{turb}) derived from

the kinematic heat fluxes ($\overline{w'T'}$) using the formula: $H_{\text{turb}} = \rho c_{\text{p}} \overline{w'T'}$ (Table B.4). The kinematic heat fluxes are obtained from 2-minute moving averages (represented by the overbar operator) within the corresponding time window during which fire-modulated ramps were tracked at each height. These are similar to the heat fluxes presented in Fig. 4.1. It can be observed that the values of H_{turb} and H_{ramp} are comparable under the influence of the fire, while these values diverge at lower heights within the canopy (by approximately 81% at $h = 10\,\text{m}$ and more than 400% at $h = 3\,\text{m}$) in the absence of a fire. One limitation of this comparison descends from the fact that the values of the kinematic heat flux ($\overline{w'T'}$) are sensitive to the averaging time window used to compute them. Moreover, as discussed above, we have not quantified the contribution to the sensible heat fluxes due to the advection terms. Nevertheless, our estimates capture the inversion in the vertical profile of the sensible heat flux (from no-fire conditions) under the influence of the surface fire within the canopy with an error of less than 12% at all heights. Thus, the analysis demonstrates that the application of ramp–cliff patterns in estimating sensible heat fluxes through the surface renewal method, in the presence of a fire within a forest canopy, is promising.

Deviation from the Reynolds Analogy

Adherence to the Reynolds analogy (140) is typically explored from values of the turbulent Prandtl number (Pr_{t}), where $Pr_{\text{t}} = \nu_{\text{t}}/\alpha_{\text{t}}$. Here, ν_{t} represents the turbulent momentum diffusivity and α_{t} represents the turbulent diffusivity of heat. When the Reynolds analogy holds, $Pr_{\text{t}} \to 1$, which suggests a similarity between turbulent momentum fluxes and turbulent heat fluxes. However, differences in the behaviour of heat and momentum fluxes manifest as a deviation of Pr_{t} from 1 and represent a distortion of the Reynolds analogy. Alternatively, Pr_{t} can also be expressed in terms of the stability correction functions, ϕ_{h}

and ϕ_{m}, conceived by Monin and Obukhov (220), as shown below (141):

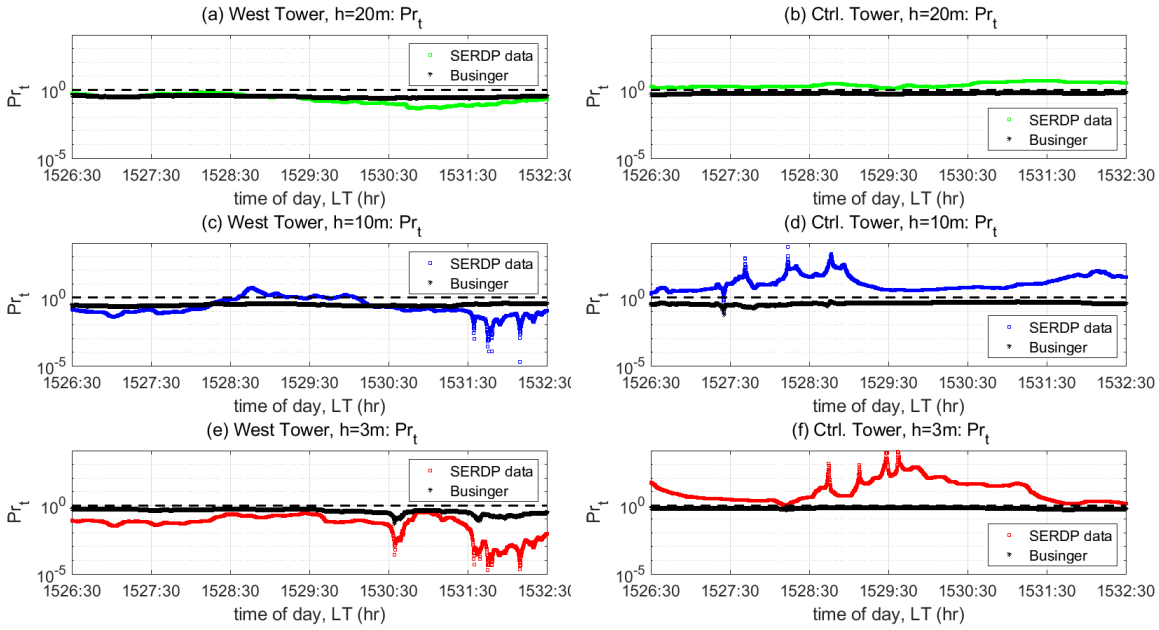
$$\phi_{\mathrm{m}} = \frac{\kappa z}{u_*}\frac{\partial \overline{u}}{\partial z}, \phi_{\mathrm{h}} = \frac{\kappa z}{T_*}\frac{\partial \overline{T}}{\partial z}, \text{where } u_*^2 = -\overline{u'w'} \text{ and } T_* = \frac{-\overline{w'T'}}{u_*}$$

$$Pr_{\mathrm{t}} = \frac{\phi_{\mathrm{h}}}{\phi_{\mathrm{m}}} = \frac{u_*}{T_*}\frac{\partial \overline{T}}{\partial z}\left(\frac{\partial \overline{u}}{\partial z}\right)^{-1} = \frac{\overline{u'w'}}{\overline{w'T'}}\frac{\partial \overline{T}}{\partial z}\left(\frac{\partial \overline{u}}{\partial z}\right)^{-1} \tag{B.6}$$

Here, the overbar operator represents a 2-minute moving mean, and κ is the von Kármán constant. Note that the right-hand side (RHS) of Eq. (B.6) is equivalent to the ratio of the turbulent diffusivities ($\nu_{\mathrm{t}}/\alpha_{\mathrm{t}}$) as discussed above. Previous studies (e.g., (221)) have alluded to deviation from the Reynolds analogy in unstable atmospheric conditions: Pr_{t} decreases ($Pr_{\mathrm{t}} < 1$) as atmospheric conditions become more strongly unstable (141), as would be expected in the presence of a fire. In that light, we explore the time series of Pr_{t} at each measurement height, at both the West and Control Towers, for deviations from unity within the two sub-durations (i) 1526:30–1532:30 LT (Fig. B.7(i)) and (ii) 1534–1540 LT (Fig. B.7(ii)). We have utilized the mean quantities and turbulent fluxes shown in Fig. 4.1 to compute Pr_{t} from Eq. (B.6). Note that we have taken the absolute value of the expression on the RHS of Eq. (B.6) to avoid negative values of Pr_{t} that arise from the non-monotonic nature of the mean temperature profile within the canopy subspace (Chapter 4).

In the earlier time window (as the fire-front approaches), deviations from the Reynolds analogy are observed near the canopy top ($h = 20\,\mathrm{m}$) at the West Tower (Fig. B.7(i)(a)). This is seen particularly after 1529:30 LT ($Pr_{\mathrm{t}} < 1$ and $Pr_{\mathrm{t}} \to 0.05$) as heat fluxes become stronger near the canopy top due to the influence of the tilted flame and buoyant plume. After 1530 LT, strong deviations from the Reynolds analogy are also observed at the mid-canopy height (Fig. B.7(i)(c)) for reasons akin to those near the canopy top, while the strong deviations near the surface (Fig. B.7(i)(e)) occur not only due to weak momentum

(i) 1526:30–1532:30 LT



(ii) 1534–1540 LT

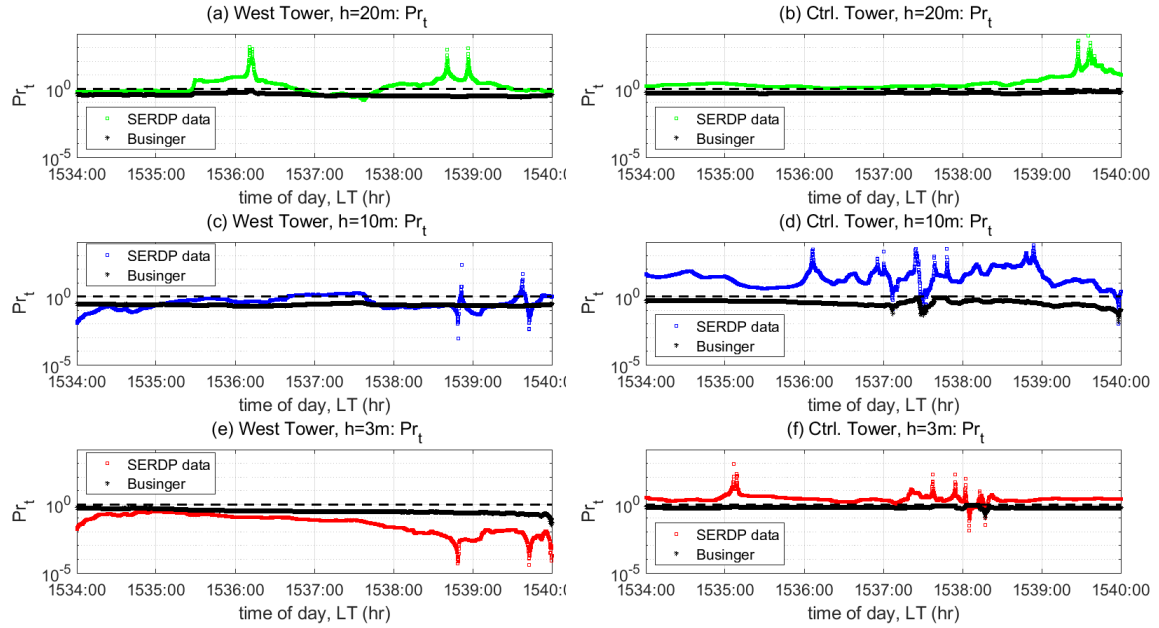


Figure B.7: Time series of Pr_{t} obtained from Eq. (B.6) and from the stability parameter (ζ) using the Businger relation at the three measurement heights, at both the West Tower (under fire influence) and the Control Tower (no-fire conditions) within (i) 1526:30–1532:30 LT and (ii) 1534–1540 LT

fluxes but also due to changes induced in the mean temperature profile within the canopy subspace ($\partial\overline{T}/\partial z \rightarrow 0$) by the approaching fire-front. In contrast, deviations from the

Reynolds analogy near the canopy top in no-fire conditions (Fig. B.7(i)(b)) are relatively weaker ($1 \leq Pr_t \leq 4.5$). Additionally, the behaviour of the time series of Pr_t near the surface and at the mid-canopy height in no-fire conditions (Figs. B.7(i)(d) and B.7(i)(f)), differs considerably from that at the West Tower, at these heights.

In the later time window (as the fire-front passes by), deviations from the Reynolds analogy are observed mid-canopy and near the surface at the West Tower (Figs. B.7(ii)(c) and B.7(ii)(e), respectively). At $h = 3\,\mathrm{m}$, deviations from the Reynolds analogy start to become stronger ($Pr_t << 1$) after 1536 LT as heat fluxes at this height become stronger due to maximum proximity to the flame. Deviations from the Reynolds analogy are observed earlier on at $h = 10\,\mathrm{m}$ ($Pr_t < 1$ before 1535:30 LT), which get weaker in time as the deviations at $h = 3\,\mathrm{m}$ continue to grow stronger. It appears that deviations at the mid-canopy height are weaker compared to those observed near the surface due to the competing effects of fire-induced heat fluxes and ambient momentum fluxes at the mid-canopy height. Near the canopy top (Fig. B.7(ii)(a)), deviations from the Reynolds analogy are observed from 1535:30–1536:30 LT; however, $Pr_t >> 1$, suggesting that this deviation is attributed to the relatively stronger momentum fluxes compared to heat fluxes during this time. Note that this time interval (1535:30–1536:30 LT) corresponds to the duration when persistent sweeping motions are observed and momentum-flux events gain prominence near the canopy top. In no-fire conditions (at the Control Tower), it is observed that $1 \leq Pr_t \leq 2.5$ for the most part (before 1538 LT) near the canopy top, suggesting that deviations from the Reynolds analogy are comparatively weaker here, in this time duration (Fig B.7(ii)(b)). Again, the behaviour of the time series of Pr_t near the surface and at the mid-canopy height in no-fire conditions (Figs. B.7(ii)(d) and B.7(ii)(f)), differs considerably from that at the West Tower, at these heights.

The Monin–Obukhov Similarity Theory (MOST) also allows us to express the correction functions in stably or unstably stratified conditions in the ASL as functions of the stability

parameter (e.g., (222; 223), etc.). Therefore, we can obtain Pr_{t} as a function of the stability parameter (thermal stratification) using the Businger relation as follows (222; 141):

$$\begin{aligned} Pr_{\mathrm{t}} &= 0.74\frac{(1-9\zeta)^{-\frac{1}{2}}}{(1-15\zeta)^{-\frac{1}{4}}}, \zeta < 0 \\ &= \frac{0.74+4.7\zeta}{1+4.7\zeta}, \zeta > 0 \end{aligned} \tag{B.7}$$

The stability parameter (ζ) in Eq. (B.7) can be expressed in terms of the Obukhov length (L) (224) as follows:

$$\zeta = \frac{z}{L}, \text{ where } L = \frac{-u_*^3}{\kappa}\frac{\overline{T}}{g\overline{w'T'}} \tag{B.8}$$

A comparison between predictions of Pr_{t} from the Businger relation (Eq. (B.7)) and values of Pr_{t} computed directly from the correction functions (Eq. (B.6)) can be accomplished in the Pr_{t}–ζ plane for unstable conditions ($\zeta < 0$) as well as stable conditions ($\zeta > 0$) within each time window (e.g., (141)). Our analysis (not shown here) revealed significant distortions from the predictions made by the Businger relation both in the absence and presence of a surface fire within the canopy; these distortions were notably significant during unstable conditions at all three heights at the West Tower, i.e. in the presence of the fire, in both time windows.

Here, we compare the predictions to computed values of Pr_{t} by representing them as a time series, as shown in Fig. B.7. It is observed that predictions from the Businger relation bear some resemblance to the values of Pr_{t} from Eq. (B.6), at $h = 20\,\mathrm{m}$, as the fire-front approaches (Fig B.7(i)(a)). However, the relation is unable to predict the diminished values of Pr_{t} ($Pr_{\mathrm{t}} \to 0.05$) attained when departures from the Reynolds analogy become stronger near the canopy top (after 1530 LT in Fig. B.7(i)(a)). Moreover, the Businger relation is unable to predict the large values of Pr_{t} attained within the later time window when

momentum fluxes become relatively stronger near the canopy top (1535:30–1536:30 LT in Fig. B.7(ii)(a)). In the absence of a fire (at the Control Tower), predictions from the Businger relation and computed values of Pr_{t} represented as a time series near the canopy top appear to be somewhat comparable in both time windows (Figs. B.7(i)(b) and B.7(ii)(b)).

Within the canopy subspace ($h = 3\,\mathrm{m},\ 10\,\mathrm{m}$), significant departures are observed between predictions made by the Businger relation and computed values of Pr_{t} represented as a time series, both in the presence and absence of a fire (West and Control Towers, respectively), in both time windows (Figs B.7(i)(c)–(f) and B.7(ii)(c)–(f)). Near the surface, predictions are substantially overestimated compared to computed values of Pr_{t} at the West Tower in both time windows (Figs B.7(i)(e) and B.7(ii)(e)). Contrarily, in the absence of a fire (at the Control Tower), predictions generally underestimate the computed values of Pr_{t} in both time windows, particularly within the canopy subspace.

This analysis reveals that predictions from the functional forms of the Pr_{t} in terms of the stability parameter (the Businger relation, in this case) are not always consistent with the values of Pr_{t} obtained from the turbulent fluxes and vertical gradients in the mean temperature and streamwise velocity (Eq. B.6) in the canopy sublayer, both in the presence and absence of a fire. These inconsistencies may emanate from the underlying assumptions involved in the MOST, which generally limits its application within plant canopies.

In summary, the Reynolds analogy is distorted by the presence of the fire. This occurs at different time instances near the surface, mid-canopy, and near the canopy top, attributed mainly to the increased strength of turbulent heat fluxes, as the fire-front advances towards and passes by the measuring tower. The Reynolds analogy is violated the most near the surface due to maximum proximity to the flame, particularly during the later stage of the fire-front passage. Deviations from the Reynolds analogy at the mid-canopy height are comparatively moderated by the competing interplay between fire-induced heat fluxes and ambient momentum fluxes. Deviations from the Reynolds analogy near the canopy top are

found to be the least intense compared to the lower heights within the canopy subspace. It must be noted that our analysis is based on the Monin–Obukhov Similarity Theory (MOST), which relies on certain assumptions so that its validity remains to be explored within plant canopies, both in the presence and absence of a surface fire. This constitutes a limitation of this analysis and presents a potential subject for future research.

Cross-wavelet Coherence in Canopy Subspace

Cross-wavelet coherence analysis allows us to comment on the degree of organization of turbulent eddies in the presence of a fire. We have already provided detailed insights on the association of the cross-wavelet coherence with the temperature isotherms and flow near the canopy top. Here, we extend the analysis to briefly explore changes in the organization of turbulent eddies at the mid-canopy height and near the surface in both time windows, based on the cross-wavelet coherence, associated with heat and momentum fluxes (R^2_{wT} and R^2_{uw}, respectively), depicted in Figs. B.8–B.11.

The presence of the fire results in the organization of flux-bearing eddies at the West Tower, particularly for heat flux, within a range of frequencies or periods. Such organization is observed in different time durations at different heights. The increased organization of heat-flux eddies within a range of periods (1 s–35 s and frequently up to 1 min.) is seen earliest near the canopy top (consistently within 1528:54–1531:18 LT) due to the tilting of the flame in the direction of the wind. Within the same range of periods, such behaviour is then chronologically observed at the mid-canopy height (intermittently within 1527:42–1531:18 LT and consistently within 1535:12–1536:24 LT as observed from Figs. B.8(a) and B.9(a), respectively), followed by the near-surface height (1536:24 LT onwards as observed from Fig. B.11(a)). The organized (coherent) heat-flux events comprise cool downdrafts or warm updrafts.

The organization of heat-flux eddies at the measurement heights, under the influence of a fire (at the West Tower), is more noticeable compared to momentum-flux eddies from the relatively more extensive regions of high R^2_{wT} within one of (or both) the time windows (depending on the height). This suggests two interrelated possibilities: the presence of the flame or the buoyant plume either (I) does not enhance the organization of momentum-flux eddies at shorter periods (below 35 s) as it does for the heat-flux eddies or (II) destroys pre-existing coherence, if any, in ambient momentum-flux events at shorter periods.

Possibility (II) can be explored via an analysis of R^2_{uw} in no-fire conditions. At the Control Tower, regions of high coherence (R^2_{uw}) are seen at relatively higher periods near the surface (35 s–60 s in Fig. B.10(d) and 17 s–60 s in Fig. B.11(d)). The (rightward-pointing) phase arrows in the regions of high R^2_{uw} at $h = 3$ m in both time windows indicate that u and w are not out of phase when the turbulent momentum-flux-bearing eddies are well-organized near the surface. This suggests that the most coherent momentum-flux events near the surface in the absence of the fire are counter-gradient motions ($\overline{u'w'} > 0$) rather than sweeps or ejections. In the presence of a fire (at the West Tower), however, coherent momentum-flux eddies associated with "in-phase" (counter-gradient) u–w motions are scarce near the surface (Figs. B.10(c) and B.11(c)). In fact, organized momentum-flux-bearing eddies, associated with the albeit fewer regions of high R^2_{uw} in the presence of a fire, are observed to manifest as either sweeps or ejections as discerned from the (leftward-pointing) phase arrows at the West Tower. Therefore, it appears that the presence of a fire disorganizes the pre-existing coherent momentum-flux events comprising counter-gradient motions near the surface, in this range of periods, and reorganizes them as sweeps or ejections, albeit relatively less extensively than heat-flux events.

Finally, it must be noted that regions of high coherence between heat fluxes, on one hand, and momentum fluxes, on the other, are found to be more extensive in no-fire conditions (at the Control Tower) compared to the West Tower, at the mid-canopy height and near the

surface. This is seen by comparing panel (e) to panel (f) in each of Figs. B.8–B.11. The higher coherence between heat and momentum fluxes across a range of periods suggests that these fluxes are comparatively more similar in behaviour, in no-fire conditions.

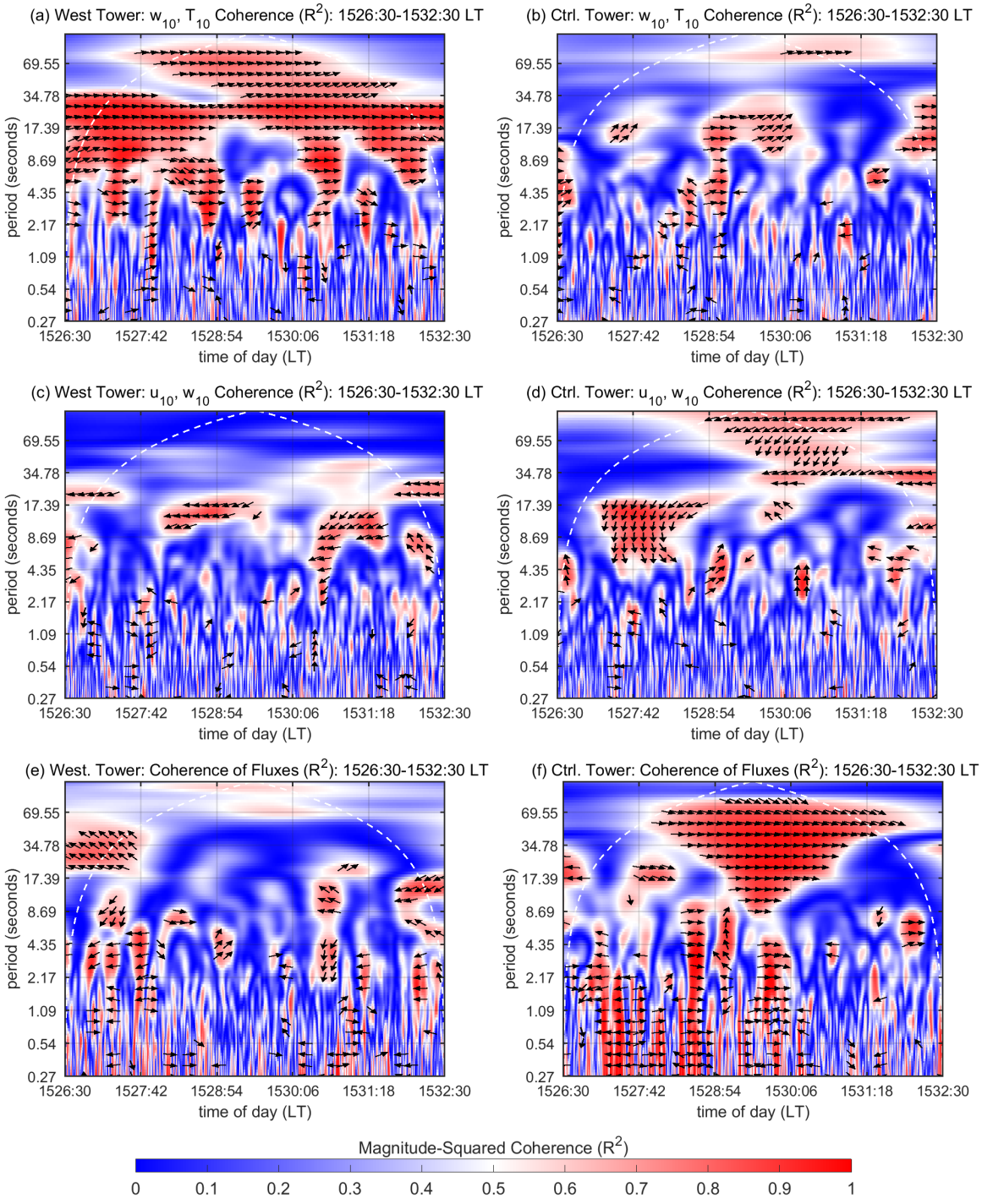


Figure B.8: Magnitude-squared coherence (R^2) at the mid-canopy height, i.e. at $h = 10\,\mathrm{m}$, within the 6-minute time window 1526:30–1532:30 LT. (a) R^2_{wT}, (c) R^2_{uw}, and (e) R^2 between $w'T'$ and $-u'w'$ at the West Tower. (b) R^2_{wT}, (d) R^2_{uw}, and (f) R^2 between $w'T'$ and $-u'w'$ at the Control Tower. Phase arrows are shown for $R^2 \geq 0.6$ in all cases: rightward-pointing arrows indicate in-phase motions; leftward-pointing arrows indicate motions out of phase by π radians. White dashed lines represent the cone of influence (COI) in all panels

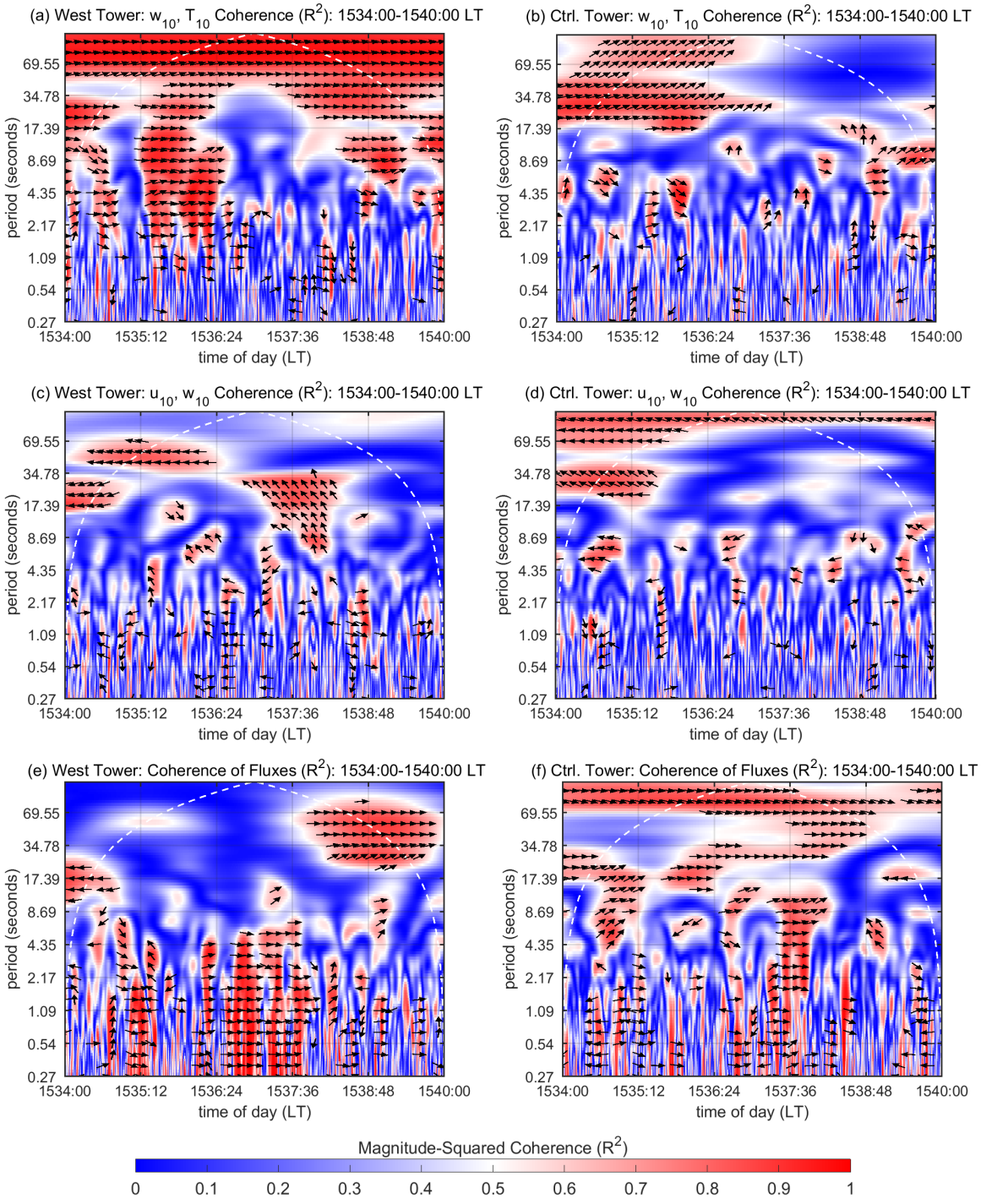


Figure B.9: Magnitude-squared coherence (R^2) at the mid-canopy height, i.e. at $h = 10\,\mathrm{m}$, within the 6-minute time window 1534–1540 LT. (a) R^2_{wT}, (c) R^2_{uw}, and (e) R^2 between $w'T'$ and $-u'w'$ at the West Tower. (b) R^2_{wT}, (d) R^2_{uw}, and (f) R^2 between $w'T'$ and $-u'w'$ at the Control Tower. Phase arrows are shown for $R^2 \geq 0.6$ in all cases: rightward-pointing arrows indicate in-phase motions; leftward-pointing arrows indicate motions out of phase by π radians. White dashed lines represent the cone of influence (COI) in all panels

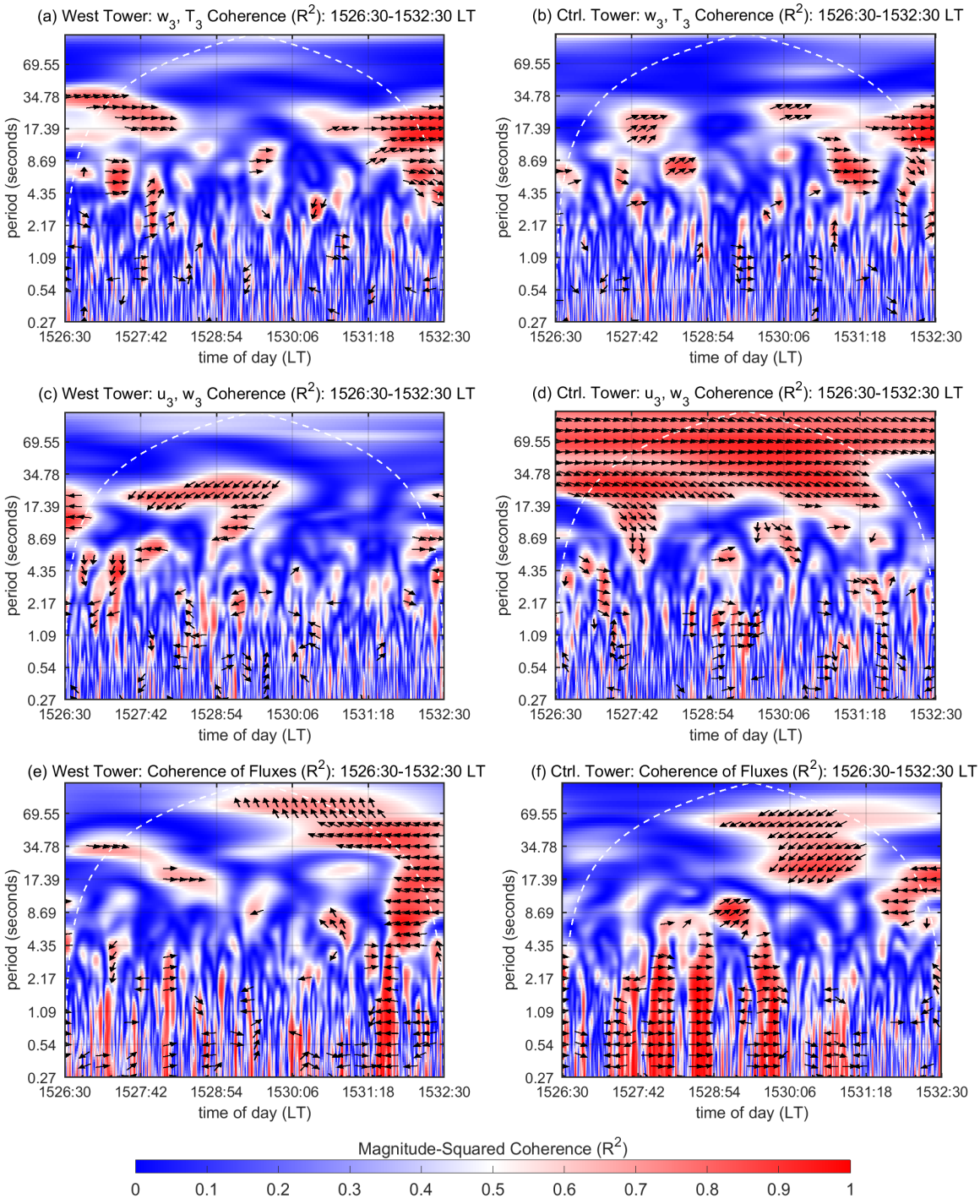


Figure B.10: Magnitude-squared coherence (R^2) near the surface, i.e. at $h = 3\,\mathrm{m}$, within the 6-minute time window 1526:30–1532:30 LT. (a) R^2_{wT}, (c) R^2_{uw}, and (e) R^2 between $w'T'$ and $-u'w'$ at the West Tower. (b) R^2_{wT}, (d) R^2_{uw}, and (f) R^2 between $w'T'$ and $-u'w'$ at the Control Tower. Phase arrows are shown for $R^2 \geq 0.6$ in all cases: rightward-pointing arrows indicate in-phase motions; leftward-pointing arrows indicate motions out of phase by π radians. White dashed lines represent the cone of influence (COI) in all panels

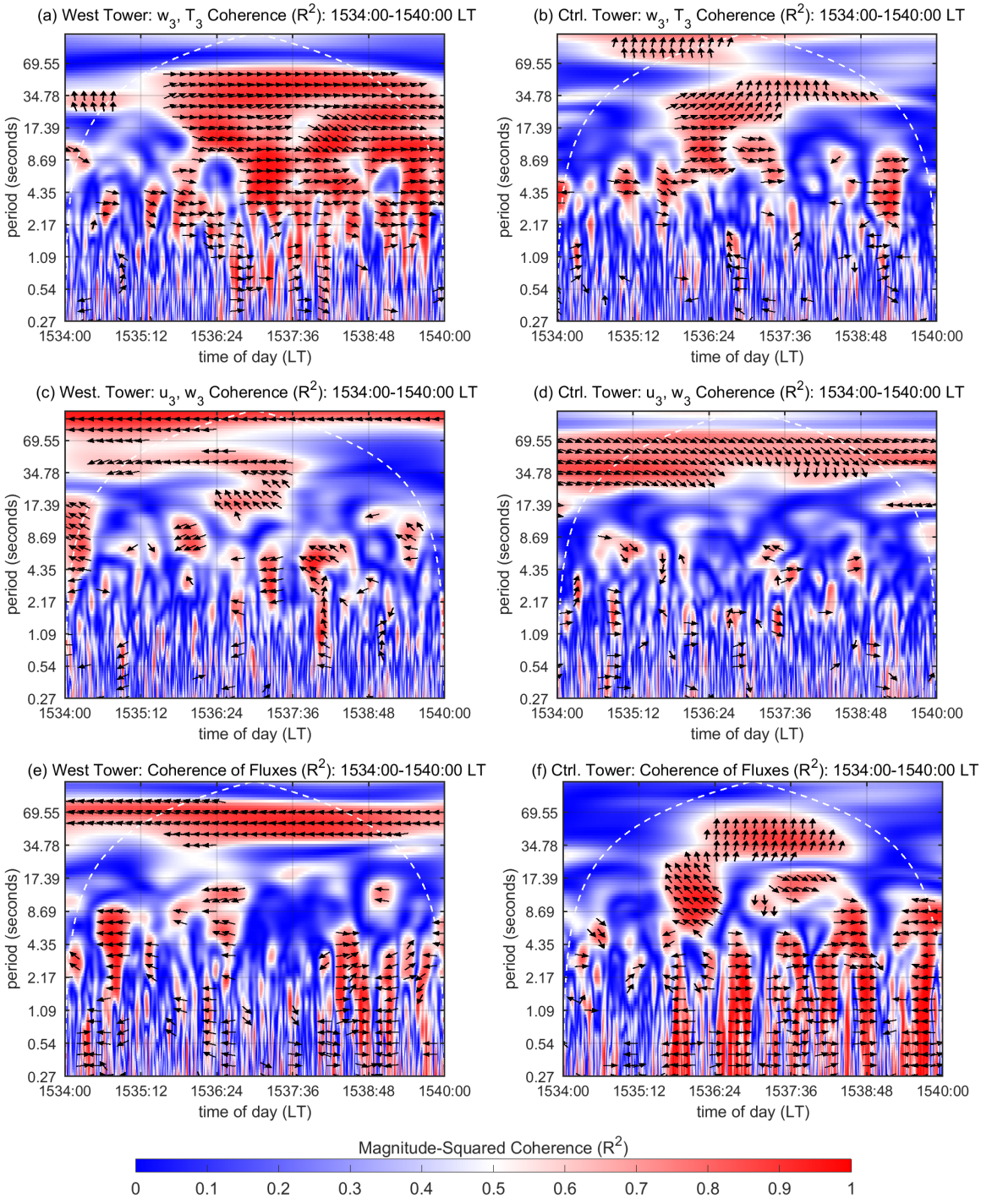


Figure B.11: Magnitude-squared coherence (R^2) near the surface, i.e. at $h = 3\,\mathrm{m}$, within the 6-minute time window 1534–1540 LT. (a) R^2_{wT}, (c) R^2_{uw}, and (e) R^2 between $w'T'$ and $-u'w'$ at the West Tower. (b) R^2_{wT}, (d) R^2_{uw}, and (f) R^2 between $w'T'$ and $-u'w'$ at the Control Tower. Phase arrows are shown for $R^2 \geq 0.6$ in all cases: rightward-pointing arrows indicate in-phase motions; leftward-pointing arrows indicate motions out of phase by π radians. White dashed lines represent the cone of influence (COI) in all panels

Appendix C

Chapter 6

Forming the π groups

Finding π_2 (ABL height)

$$\pi_2 = \delta R_{\mathrm{p}}^{a}\ \theta_{\mathrm{a}}^{b} U^{c}$$

Substituting the dimensions:

$$(\mathrm{L})(\mathrm{L}^{a})(\theta)^{b}(L\mathrm{T}^{-1})^{c}$$

Expanding and grouping like terms:

$$\mathrm{L}^{1+a+c}\Theta^{b}\mathrm{T}^{-c}$$

For dimensionless π, exponents must sum to zero:

1. Temperature: $b = 0$

2. Time: $-c = 0 \Rightarrow c = 0$

3. Length: $1 + a + c = 0 \Rightarrow 1 + a = 0 \Rightarrow a = -1$

So:

$$\pi_2 = \frac{\delta}{R_{\mathrm{p}}}$$

.

Finding π_3 (Buoyancy g)

$$\pi_3 = g R_{\mathrm{p}}^{a}\, \theta_{\mathrm{a}}^{b} U^{c}$$

Substituting the dimensions:

$$(\mathrm{LT}^{-2})(\mathrm{L}^{a})(\theta)^{b}(\mathrm{LT}^{-1})^{c}$$

. Expanding and grouping like terms:

$$\mathrm{L}^{1+a+c}\Theta^{b}\mathrm{T}^{-2-c}$$

For dimensionless π, exponents must sum to zero:

1. Temperature: $b = 0$

2. Time: $-2 - c = 0 \Rightarrow c = -2$

3. Length: $1 + a + c = 0 \Rightarrow 1 + a - 2 = 0 \Rightarrow a = 1$

So:

$$\pi_3 = g\frac{R_\mathrm{p}}{U^2}$$

.

Finding π_4 (Kinematic heat flux difference ΔH_s)

$$\pi_4 = \frac{\Delta H_\mathrm{s}}{\rho c_\mathrm{p}} R_\mathrm{p}^a \, \theta_\mathrm{a}^b U^c$$

Substituting the dimensions:

$$(\Theta L T^{-1})(L^a)(\Theta)^b(LT^{-1})^c$$

Expanding and grouping like terms:

$$\mathrm{L}^{1+a+c}\Theta^{1+b}\mathrm{T}^{-1-c}$$

For dimensionless π, exponents must sum to zero:

1. Temperature: $1 + b = 0 \Rightarrow b = -1$
2. Time: $-1 - c = 0 \Rightarrow c = -1$
3. Length: $1 + a + c = 0 \Rightarrow a = 0$

So:

$$\pi_4 = \frac{\Delta H_\mathrm{s}}{\rho c_\mathrm{p}} \frac{1}{\theta_\mathrm{a} U}$$

Finding π_5 (Friction velocity u_*)

$$\pi_5 = u_* \; R_{\mathrm{p}}^{a} \; \theta_{\mathrm{a}}^{b} U^{c}$$

Substituting the dimensions:

$$(\mathrm{LT}^{-1})(\mathrm{L}^{a})(\Theta)^{b}(\mathrm{LT}^{-1})^{c}$$

Expanding and grouping like terms:

$$\mathrm{L}^{1+a+c}\Theta^{b}\mathrm{T}^{-1-c}$$

For dimensionless π, exponents must sum to zero:

1. Temperature: $b = 0$
2. Time: $-1 - c = 0 \Rightarrow c = -1$
3. Length: $1 + a + c = 0 \Rightarrow a = 0$

So:

$$\pi_5 = \frac{u_*}{U}$$

Finding π_6 (Canopy height $h_{\mathbf{c}}$)

$$\pi_6 = h_{\mathrm{c}} R_{\mathrm{p}}^{a} \; \theta_{\mathrm{a}}^{b} U^{c}$$

Similar to above,

$$\pi_6 = \frac{h_\mathrm{c}}{R_\mathrm{p}}$$

Finding π_7 (Canopy drag length scale $L_\mathbf{c}$)

$$\pi_7 = L_\mathrm{c} R_\mathrm{p}^a \, \theta_\mathrm{a}^b U^c$$

Similar to above,

$$\pi_7 = \frac{L_\mathrm{c}}{R_\mathrm{p}}$$

Finding π_1 (Horizontal plume length scale $\lambda_\mathbf{pc}$) Finally, we consider the response variable, i.e. λ_pc).

$$\pi_1 = \lambda_\mathrm{pc} R_\mathrm{p}^a \, \theta_\mathrm{a}^b U^c$$

Similar to above,

$$\pi_1 = \frac{\lambda_\mathrm{pc}}{R_\mathrm{p}}$$